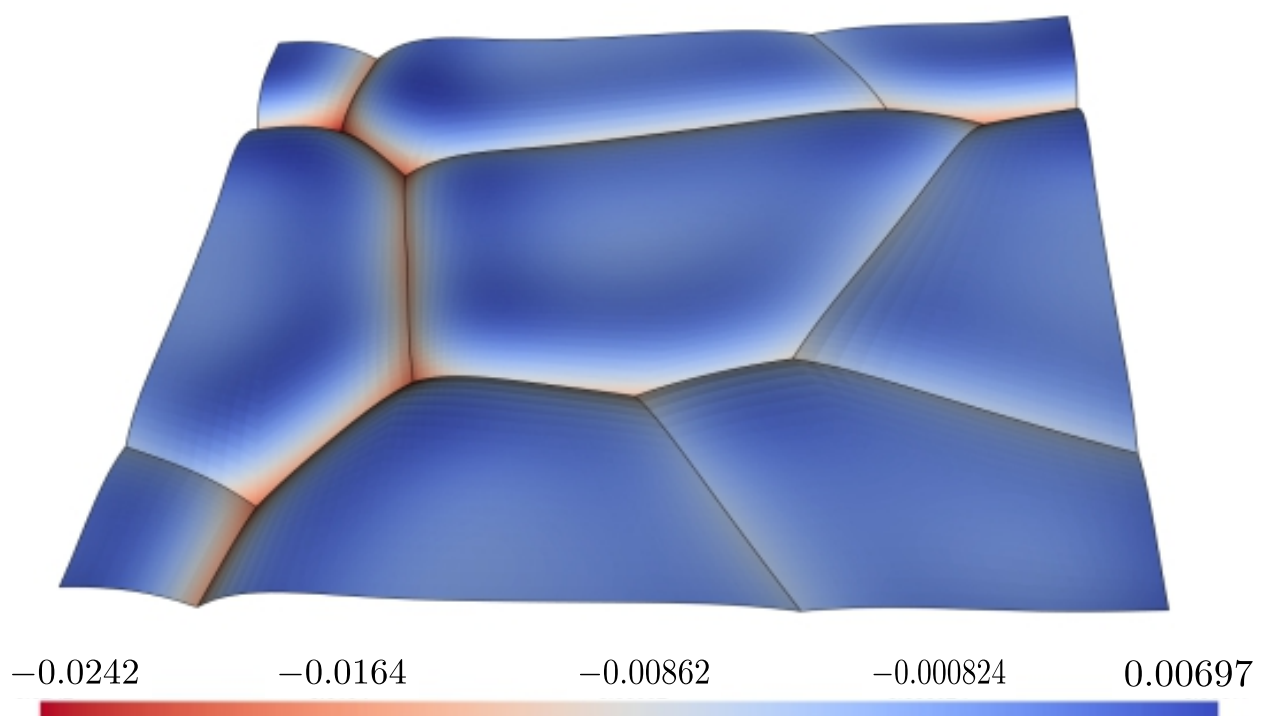


# Sharp interface modeling of anisotropic thermal grooving — Variational theory and numerical simulations

Asim ullah Khan





Fakultät Maschinenbau  
*fortschritt studieren*

RUHR  
UNIVERSITÄT  
BOCHUM

RUB

**Sharp interface modeling of  
anisotropic thermal grooving.  
Variational theory and numerical simulations.**

Dissertation  
zur  
Erlangung des Grades  
Doktor-Ingenieurin / Doktor-Ingenieur\*

der  
Fakultät für Maschinenbau  
der Ruhr-Universität Bochum

von

Asim ullah Khan

Aus Rawalpindi, Pakistan

Bochum 2019



Herausgeber (Publisher):

Institut für Mechanik  
— Schriftenreihe —  
Ruhr-Universität Bochum  
D-44780 Bochum

©2019 Asim ullah, KHAN, Institut für Mechanik, Ruhr-Universität Bochum

Printed in Germany

Einreichung der Dissertation: 11. April 2019

Tag der mündlichen Prüfung: 05. July 2019

Vorsitz:	Prof. Dr. Alexander Hartmaier
Erster Gutachter:	Prof. Dr. rer. nat. Klaus Hackl
Zweiter Gutachter:	Prof. Dr. Jörg Renner
Dritte Gutachter:	Prof. Dr. Thomas Antretter (Montanuni. Leoben, Österreich)



*To Saeeda,  
Fatima, Abdullah and Zainab*



*“Die besten von euch sind diejenigen, die den besten Charakter haben”*  
(The best amongst you are those who have the best manners and character.)

Saying of Prophet Muhammad (*peace be upon him*)

## Acknowledgements

I take this opportunity to express my sincere gratitude to all those who have supported and encouraged me during my time at the Institute of Mechanics of Materials at Ruhr university Bochum, Germany. It is certainly not possible to complete this work without the help in one or the other way of many persons, the most important of whom I would like to mention here.

Foremost, I express my utmost gratitude to my advisor who allowed me to work in his research group. I am thankful to Prof. Klaus Hackl. He introduced me with the thermodynamic extremal principle in the field of microstructures. His immense knowledge of the field and incomparable research skills are great source of motivation for me. He has always been kind and supportive during this stay in the university. Without his valuable discussions and focused guidance, it was not possible to reach up to this end today. I found him the best possible supervisor for my PhD study.

I would like to thank Prof. Matthias Baitsch for his guidance in implementing the finite element model in Java. His valuable support was always important in this study. I would also like to extend my gratitude to Prof. Jörg Renner and Prof. Thomas Antretter of Montan university Leoben, Austria for acting as referees for my dissertation. Their valuable comments helped me to improve this research work. I extend my thanks to all my friends and colleagues at the chair of Mechanics of Materials. In particular Dr.-Ing Ulrich Hoppe for providing me technical and non-technical support during this stay. I would like to thank Dr-Ing Philipp Junker for early discussion while writing the first draft of this dissertation. I like to mention other colleagues Taun Minh, Yinguang, Stephan, Johanna, Ghina, Golnaz, Dustin, Christopher and the others for healthy creative atmosphere and friendship.

Further more, I would like to acknowledge the financial support from the Higher Education Commission (HEC), Pakistan and also would like to thank Deutscher Akademischer Austauschdienst (DAAD) for supporting my research stay in Germany.

I am very much obliged to my parents and family for love and encouragement throughout my life to earn every achievement. My wife deserves a special thanks for being patience and thoughtful during all this time of my studies. I also acknowledge her efforts in the best upbringing of our children Fatima, Muhammad Abdullah and Zainab during my stay in Germany without my contribution.

## Summary

This thesis reports the research progress about the morphological evolution in the polycrystalline. Among the different transport processes in solids, the formation of thermal grooves along the free surface are predominately governed by the surface diffusion at a temperature below the melting temperature. The quadruple point is a geometrical identity, having an important role in the stability of thin sheets and protective coatings. There is not much more information available about its growth kinetics. We use finite element approach to solve the equations expressing the kinetics of thermal grooving in a three dimensional space, using the thermodynamic extremal principle for maximum dissipation. In this model, two coupled dissipation phenomena motion of matter along the free surfaces of the grains and motion of matter along the triple line channels are assumed taking place simultaneously. The finite element code is implemented in JAVA. The morphological evolutions and growth kinetics of grooves along the triple lines and pit formation at the quadruple points in a polycrystalline are analyzed in two different perspectives.

The grain boundary energies distribution are function of boundary plane inclination and misorientations between the neighboring grains. In the first part of this work, we discuss the grooves growth kinetics and their shapes using anisotropic grain boundary energies. Grain boundaries are inherently more complex than free surfaces, and they need more geometrical parameters to calculate relevant thermodynamics constant including the grain boundary energies. The complete description of these energies require eight independent parameters. In this work, we calculate grain boundary energies using an ansatz under the assumption of planar boundaries and negligible torque term at a boundary junction. With this approach, we have set of energies for  $\{100\}$  oriented boundaries in Cu. and Al. The surface energy is assumed constant over the distribution of grains. With this, the kinetics of thermal grooving over the range of scalar parameters in the ansatz function are studied. Comparative studies show the effect of diffusion coefficients on the shapes and kinetics of the process.

The second part of this report is based on some experimental observations during the secondary annealing process in the thin film coatings and the surface of the pure materials. For some particular oriented grains, we observe the formations of low energy planes along the thermal grooves. These singular faces formations are characterized due to the surface energy anisotropy. We use the analytical form of surface energy as a function of grain orientations in the normal direction. It is observed that growth kinetics are different in comparison with the normal grooves. Our model is stable even in the critical range of anisotropy. Within this particular settings, we have formation of singular grooves along the grain boundary and at the quadruple points. With an increasing anisotropy, we observe significant increase in the pit depths at the triple lines junctions. There is not much difference in the depth of grooves along the triple lines with the low anisotropy results. These studies effectively reproduce many experimentally observable phenomena.



## Contents

<b>1. Introduction</b>	<b>1</b>
<b>2. Thermodynamic Extremal Principle</b>	<b>5</b>
2.1. Introduction.	5
2.2. Local equilibrium and entropy flux.	8
2.3. Dissipation potential and dissipation functions.	12
2.4. Thermodynamic extremal principles (TEP).	13
<b>3. Thermal grooving</b>	<b>19</b>
3.1. Introduction.	19
3.2. Geometrical model and kinematics.	20
3.3. Conservation of matter.	23
3.4. Total energy of the system and its rate.	24
3.5. Dissipation functions.	25
3.6. TEP and phenomenological equation for grooving.	26
3.7. Finite element model for thermal grooving.	27
3.8. Dimensionless formulation.	34
<b>4. The role of grain boundary energy</b>	<b>35</b>
4.1. Introduction.	35
4.2. Grain boundary energy using an ansatz function.	37
4.3. Four grains periodic RVE.	39
4.3.1. Model geometry and kinetics parameters.	39
4.3.2. Simulation results and discussion.	39
<b>5. Singular grooves and surface energy anisotropy</b>	<b>51</b>
5.1. Introduction.	51
5.2. Gibbs and Wulff plots of surface energy.	54
5.3. Anisotropic surface energy function.	59
5.4. Three grains periodic RVE.	61
5.4.1. Model geometry and kinetics parameters.	61
5.4.2. Simulation results and discussion.	63
<b>6. Conclusion</b>	<b>101</b>
<b>Bibliography</b>	<b>105</b>
<b>A. Appendix.</b>	<b>115</b>
A.1. $\xi$ , surface energy vector.	115
A.2. Gaussian Curvature of a surface.	116



## List of symbols

$\mathbb{A}_{\Gamma_i}$	Set of all free surfaces intersecting at the triple line $\Gamma_i$ .
$\mathbb{A}_{P_i}$	Set of all triple lines meeting at quadruple point $P_i$ .
$a$	Area in current configuration.
$\mathbf{b}$	Mechanical body force per unit volume.
$c$	Scalar coefficient for setting the anisotropy in the surface energy.
$D_i$	Diffusion coefficient along the surface $\omega_i$ .
$D_{\Gamma_i}$	Diffusion coefficient along the line $\Gamma_i$ .
$E$	Total energy of a system.
$F$	Helmholtz free energy of the system.
$f$	Specific Helmholtz free energy.
$G$	Gibbs energy of the system.
$G_i$	Gibbs energy of the surface element $\omega_i$ .
$G_{\eta_i}$	Gibbs energy of the grain boundary $\eta_i$ .
$G_{\Gamma_i}$	Gibbs energy of the external triple line $\Gamma_i$ .
$G_{\Sigma_i}$	Gibbs energy of the internal grain boundary $\Sigma_i$ .
$g$	Specific Gibbs energy of the system.
$H$	Enthalpy of the system.
$h$	Specific enthalpy of the system.
$J_i$	Flux along the surface $\omega_i$ .
$\mathbf{J}$	General flux vector.
$j_{\Gamma_i}$	Flux along the triple line $\Gamma_i$ .
$K$	Kinetic energy of the system.
$\mathbf{K}$	Surface curvature tensor.
$K_i$	Mean curvature of the surface $\omega_i$ .
$K_{\Gamma_i}$	Curvature of the triple line $\Gamma_i$ .
$\mathbf{L}$	$n \times n$ coefficient matrix for linear flux to force relationship.
$M_i$	Mobility along the surface $\omega_i$ .
$M_{\Gamma_i}$	Mobility along the triple line $\Gamma_i$ .
$\mathbf{m}_{\Gamma_{ij}}$	Tangent vector from $\Gamma_i$ to the surface $\omega_j$ .
$\mathbf{n}$	Normal vector to the surface $\omega$ .
$\mathbf{n}_{\Gamma_i}$	Normal vector to the plane of the triple line $\Gamma_i$ .
$P_i$	Internal triple line formed at intersection of boundaries $\gamma_{\eta_{i,j,k}}$ .
$P$	Total mechanical power.
$Q$	Dissipation function.
$Q$	Total heat supplied or thermal power.
$q$	Heat supplied or removed from some part of the boundary.
$\mathbf{R}$	$n \times n$ coefficient matrix for linear force to flux relationship.
$r$	Heat source density.
$r$	Space vector / position vector.
$S$	Total entropy of the system.
$S_p$	Entropy production in the dissipative phenomena.
$S_s$	Entropy supplied to the system in the form of heat source $Q$ .
$\mathbb{S}$	Set of all surfaces in polycrystalline material.
$s$	Specific entropy of the system.
$\dot{s}$	Rate of change in arc length of the triple line $\Gamma_i$ .
$T$	Temperature field in the body at any instance $t$ .

$\mathbb{T}$	Set of all external triple lines in the polycrystalline material.
$\mathbf{t}$	Traction force acting on some parts of the boundary.
$\mathbf{t}_{\Gamma_i}$	Tangential vector along the triple line.
$\mathbf{t}_{\Sigma_i}$	Tangential vector to the internal grain boundary directed outward at quadruple point.
$t$	Time space.
$U$	Internal energy of the system.
$u$	Specific internal energy.
$v$	volume in the current configuration.
$\mathbf{v}$	Velocity vector.
$\mathbf{v}_{n,i}$	Velocity of the free surface $\omega_i$ in the normal direction.
$\mathbf{v}_{\Gamma_n,i}$	Velocity of triple line, $\Gamma_i$ in its normal direction.
$\mathbf{v}_{\Gamma t,i}$	Tangential velocity of the triple line $\Gamma_i$ .
$\mathbf{v}_{\Sigma_i}$	Velocity of the internal triple line $\Sigma_i$ in outward direction.
$\mathbf{X}$	General thermodynamics force vector.
$Y$	Internal variables of the thermodynamics system.

### Greek Symbols

$\beta, \lambda$	Lagrange parameters.
$\Gamma_i$	Triple line formed at an intersection of grain boundary $\eta_i$ with free surfaces $\omega_j$ & $\omega_k$ .
$\gamma_{\eta_i}$	Surface specific energy for $\eta_i$ .
$\gamma_{\Gamma_i}$	Specific line energy for $\Gamma_i$ .
$\gamma_{\Sigma_i}$	Specific line energy for $\Sigma_i$ .
$\dot{\epsilon}$	Strain rate in the body.
$\eta_i$	Grain boundary formed by intersection of two grains $\omega_j$ & $\omega_k$ .
$\kappa$	Thermal conductivity of the system.
$\mu$	Chemical potential given as $K\gamma$ .
$\rho$	Mass density of the system.
$\sigma$	Stress tensor.
$\Phi$	Dissipation flux expressed as a function of active fluxes only.
$\Psi$	Dissipation flux expressed as a function of active forces only.
$\omega_i$	Free surface of the grain $i$ .

## 1. Introduction

An intersection of a grain boundary with the free surfaces of the polycrystalline terminates with a groove formation. The precise measurements of these topographies are important in estimating the material characteristics parameters (e.g. strength of the material, crack resistance, and optical and electronic properties), surface diffusion coefficients, and mapping of relative grain boundary energies. These parameters vary with the grain orientation and boundary plane inclination (Hackl et al., 2017; Lin et al., 2016; Kelly et al., 2018). Hackl et al. (2013) establish the strong correlation between the boundary plane inclinations and groove shapes. This study also shows that kinetics parameters participating in the dissipation process, influence the topographical formations along the grooves. Alongside this, Fischer et al. (2012) give a detail study about the effect of moving triple points in the polycrystalline. In three dimensional space, we have quadruple points at the intersection of grain boundaries. With the progressing annealing time, thermal grooves deepen and widen, and the pit at the quadruple point grows at a faster rate due to the parallel diffusion processes along the constituting boundaries. In case of the thin sheets and coatings, these geometrical elements hold significant position. If these pits' depths extend below the thickness of the polycrystalline film, we observe the formations of the tiny holes and micro cracks. These defects cause the initiation of dewetting process with accelerated rate for any further increase in the temperature (Thompson, 2012; Amram et al., 2014). Altogether, the workability of micro-electronics and stability of thin films coatings are influenced by the thermal grooving shapes and growth rates. Among the different transport mechanism, the surface diffusion plays a major role in the groove formations and the dewetting phenomena well below the melting temperature. The prime objective of this work is to model the groove kinetics process for diffusion dominated phenomena in the three dimension space and study the effect of grain orientations and boundary plane inclinations using anisotropic driving forces.

The kinetics of grooving was first modeled by Mullins (1956) for small slope approximation. He studied different transport mechanisms including surface diffusion, evaporation–condensation, and bulk diffusion. According to his observations, the surface diffusion is the dominating transport mechanism below the roughening temperature. It was analytically shown that all dimensions for surface diffusion processes follow the same power law, while for the evaporation–condensation, the transport and morphological growth took place with  $1/2$  power law of the annealing time. Mullins model is based on some simplifications including isotropic surface energy and the assumption for the bisection of dihedral angle at the groove root. Cahn and Taylor (1994) modeled the thermal grooving with coupled surface and interface motion. They included the surface energy as single driving force governing the kinetics of the system. The normal motion of the surface for diffusion dominated process was calculated from the gradient of the total surface energy in the  $H^{-1}$  inner product, and the motion of grain boundary was modeled as function of the mean curvature, calculated by the gradient of the total surface energy on the moving surface in  $L^2$  inner product. They suggested several methods to solve these sets of differential equations under the two limiting cases ranging from the surface diffusion controlled to grain boundary mobility dominated evolution. Their model satisfied the conditions for the conservation of mass and volume. This brief overview encompassed anisotropy in the surface energy and diffusion coefficients. The extreme anisotropy in the surface energy causes

the formation of planer grooves along the grain boundary. It was proposed that these formations can disappear with the creations of the new faces at different locations with the progressing annealing time. These alternative formations induced the maximization of total dissipation in the system (Suo, 1997).

Afterwards, Klinger and Rabkin extensively studied the kinetics of the thermal grooves based on the experimental observations for moving and stationary grain boundaries in different materials. They coupled the previous grooving models with other concurrent phenomena including both surface and interface diffusion, and surface diffusion with moving grain boundaries. Formations of singular faces at groove roots were characterized due to the variations in surface energy with grain orientation. These facets formations slowed down the overall dissipation process, due to decrease in the diffusion kinetics (Klinger and Rabkin, 2001). In case of moving grain boundaries, the amount of sliding was determined as function of the boundary plane inclination. In some experiments, they also observed diffusional humps without particularly attached grain boundaries. They also correlated these formations with the anisotropy in the surface energy. The rates of decay in boundary-free grooves were evaluated as  $1/4$  exponent of the annealing time (Rabkin et al., 2001, 2004). In contrast with the Mullins model under symmetry conditions, Klinger (2002) extended approach is applicable to the bi-grain structure. In their model, the bulk diffusion due to concentration gradient was responsible for the flow of net flux between the grains. The mass deficit in the multilayer thin film was attributed to interface diffusion between the layers. For the case of anisotropic surface energy and diffusion coefficient, they observed a decrease in the growth rate of the diffusion humps (Amram et al., 2014).

Surface diffusion also plays important role in the production of ordered nanoparticles. The overall decrease in the energy of system is governed by the coupled surface and the interface diffusions, causing the grain boundary sliding. It was observed in thin film experiments that some regions showed accelerated grooving with moving boundaries. These expedite phenomena were also correlated with the anisotropic surface energy (Barmak et al., 2013; Kosinova et al., 2014; Jiang and Zhao, 2018). Based on the Mullins model for the inclined grain boundaries, Zhang and Wong studied coupled surface grooving and grain boundary migration to measure the mobility of particular grain boundaries. They used Sun and Bauer method in these measurements. It was concluded that the grain boundaries with small inclination remain attached with the groove tips. Under these conditions, the boundary motions took place with two different rates influenced by the grain boundary plane inclination (Zhang and Wong, 2002; Zhang et al., 2002). Beck et al. (2010) solved coupled problems using the traveling wave solution.

Xin and Wong (2003); Min and Wong (2006a,b); Du and Wong (2006) used the shooting method to solve the differential equations for self similar and singular grooves profiles. They studied the evolution kinetics for different energy functions and equilibrium crystal shapes. Any singularity at critical anisotropy, was homogenized by using the Dirac  $\delta$  function in the surface stiffness function. Hackl et al. (2013) used the similar approach with posing the initial conditions within the flat region out side the groove and employing the matching conditions at the groove root. With these configurations, the solution was stable subject to the initial guess. A linear homotopy method was implemented to find solution independent of the initial guess over the range of the boundary inclination. Ramasubramaniam and Shenoy used the variational approach to model a thermal grooving process. By using the analytical form of anisotropic surface energy, the limiting cases for the planer grooves were studied as function of grain boundary plane inclination and grain orientations. They established a correlation between boundary orientation and the dihedral angle for the two dimension only.

Ogurtani et al. (2008) simulated grooving models for the singular facet formations under a strong anisotropic Gibbs surface energy. They found good estimates of the diffusion coefficients in Aluminum and Tungsten. Thermal grooving under the combined effect of capillary forces, and tensile stresses (Akyildiz et al., 2012), and additional stresses due to the electric field (Akyildiz and Ogurtani, 2011) are in the range of numerical experiments with additional driving forces, which were also contributing to the overall entropy production of the system. Derkach et al. (2014) simulation experiments for micro pinning and groove shapes for a regular hexagonal structure provide the overview for grain size effects on the pit growth at the quadruple points and surface kinetics for the particular polycrystalline geometry.

Phase field modeling is not a new approach in the research field, but it is widely used for material process simulations due to the availability of high speed computational power. With some additional regularization for the sharp grain boundaries, there are some scientific works in the literature studying the kinetics of the thermal grooving processes. Schiedung et al. (2017) used a multi-phase field modeling approach to study the vanishing hill and valley structure along the free surface both in two and three dimensions with isotropic surface energy. The polycrystalline model and the energetic arguments for the process kinetics were evaluated in CALPHAD. Chakraborty et al. (2018) studying the phase-field model for grooving due to thermal and electric current, and Joshi et al. (2017) investigating the stability of a membrane with cylindrical nanopores due to surface diffusion produced curvature dependent profiles with the center of curvature in the smallest grain. Using a finite element modeling approach for sintering and surface grooving, Barrett et al. (2010a) showed an accelerated growth kinetics for anisotropic surface energies.

In addition to these numerical methods, there are other models based on variational theory. Thermodynamics extremal principles are excellent tools for modeling the irreversible processes. Using these principles, we describe the kinetics of the system with rather simple set of coupled equations. These equations replace the classical phenomenological relations (Svoboda et al., 2005; Fischer et al., 2014). Irreversible processes, diffusional control grain growth with sharp interfaces (Svoboda and Riedel, 1992; Svoboda et al., 2002; Fischer et al., 2003), bulk diffusion through the interfaces (Svoboda et al., 2004), non-isothermal coupled, and non-coupled processes in materials (Hackl, 1997; Hackl and Heinen, 2008; Hackl et al., 2011; Kochmann and Hackl, 2011; Klinge et al., 2015) were effectively modeled by engaging these principles. The prime benefits of these principles are no need to define any additional boundary condition at the free boundaries, and no additional constraints at the intersecting boundaries. All conditions include in the Lagrange formulations satisfied by these set of coupled evolution equations.

A variational model for thermal grooving in two dimensions (Hackl et al., 2013), and model for the motion of triple junctions and grain boundaries (Fischer et al., 2012) successfully explain the effect of boundary inclinations on surface morphologies and grain boundaries mobility as a function of grain size and shape. Both of these models are based on the principle of maximum dissipation.

In the present chapter, the general introduction of the previous existing models for thermal grooving process are discussed in brief with their limitations. There is no model to the author knowledge that work unconditionally over the complete range of anisotropy for the static grain boundaries. This research work is based on Hackl et al. (2017) three dimensions model for thermal grooving, which is modeled using the principle of maximum dissipation potential with additional constraints for the conservation of mass and continuity of domain at the meeting boundaries. We will study the morphological evolution in a polycrystal using anisotropic sur-

face energy, and orientation dependent grain boundary energies. This model is stable over the complete range of anisotropy in the surface energy function without introducing any homogenization or linearization.

In chapter (2), we will discuss the equilibrium criteria for the irreversible processes. We will also explain some thermodynamic extremal principles and their applications in modeling the material processes with additional constraints. This brief introduction will be helpful in understanding the effectiveness of TEPs in modeling the irreversible processes with and without additional constraints.

Chapter (3) will explain the model for thermal grooving in three dimensions. In this model, the dissipation is considered due to the motion of flux along the free surface. Additionally, the diffusion along a triple line channel is balanced with the fluxes of the neighboring grains. The vertical motion of the surface is modeled as vector Laplacian of the chemical potential. These curvature dependent equations enable us to use this model for both an isotropic and anisotropic surface energy function without any homogenization and limitations for the stationary grain boundaries. Finite element modeling is done to solve these coupled equations. Identification and calculation of process parameters are primary factors in numerical experiments. Thermodynamic forces, specific Gibbs energies of the geometrical elements and diffusion coefficients are identified as basic parameters influencing the thermal grooving process.

We will work in two different regimes. In the first part, we will study the morphological evolution in the polycrystalline with isotropic surface energy. Other forces, grain boundary energies will be calculated as a function of grain misorientation. Chapter (4) starts with the motivation for analyzing the effect of anisotropic grain boundary energies for the thermal grooving. We will calculate the energy distributions for selected RVE using an ansatz function. We will also study the effect of scalar coefficients in the ansatz function for the groove's shape and overall process kinetics. The material characteristics parameters, diffusion coefficients along the surface and along the triple line channels also influence the overall grooving phenomena. We will make comparisons between the groove geometries and growth rates over the range of diffusion coefficients.

In the second part of this research work, we will study the effects of surface energy anisotropy on the morphologies of a periodic representative volume element (RVE). Chapter (5) will start with brief review of the previous experimental and simulation work from the literature as an inspiration of this study. We will explain about the Wulff-plot for the anisotropic surface energy function. This is important to develop understanding for the cause and effect of any anisotropy on the surface morphology and thermal grooves. Other forces grain boundary energies will be constant. We will study the effects of grain orientations on the groove's shapes and growth kinetics. The grooving phenomena will be discussed for three different orientations in highly textured RVE. Effects of moderate to critical anisotropy in surface energy will be discussed for each particular set of orientations. We will make the comparisons for varying relative diffusion coefficients. We will identify the causes for the formation of many experimentally observed groove shapes with these simulation experiments.

## 2. Thermodynamic Extremal Principle

A constitutive modeling of the non-equilibrium process establishes the relationships between internal state variables and material characteristic parameters (e.g. diffusion coefficient, thermal conductivity). With these set of equations, we develop our understanding about the conditions and constraints for the equilibrium state of the system. We are also able to identify the key process controlling parameters. In general, these models are combinations of algebraic and differential equations. The modeling of any irreversible process using a thermodynamic extremal principle starts with the phenomenological model interrelating the contributing forces and fluxes. Identification of driving forces and corresponding fluxes determine the complexity of the model. Thermodynamic extremal principles use variational approaches to find explicit evolution equations for the process parameters. The objective of this chapter is to discuss the thermodynamic extremal principles in relation with the entropy production and establish the interrelationships between them.

### 2.1. Introduction.

In many of the processes of engineering and physics, we have to consider both mechanical and thermal energy, participating actively in governing the kinetics of the system. These systems establish the equilibrium state by dissipating some part of the mechanical energy in form of heat and contributing in entropy production of the system. It is important to find the relationship for law of conservation of energy and entropy production for a generic process as it will be helpful in identification of process parameters participating actively in the dissipation phenomena. Let us assume a body  $\Omega$  with a current volume  $v$  subjected to both mechanical and thermal energy. It is acted upon by a body force  $\mathbf{b}$  and surface traction  $\mathbf{t}$  along the part of its boundaries,  $\partial\Omega$ . In addition to these forces, the body includes a heat source  $r$  and heat flux  $\mathbf{q}$  in the non-overlapping parts of the boundary. The total energy of the system,  $E = U + K$  must be conserved. We have

$$\frac{d}{dt}(U + K) = P + Q, \quad (2.1)$$

with  $P$  and  $Q$ , total power of the system, including both mechanical and thermal contributions from the external sources. Equation (2.1) is referred as the balance of energy (mechanical and thermal), and is also termed as first law of thermodynamics. In this equation, the rate of internal energy,  $\dot{U}$  germinates from the part of energy supplied that is not converted into kinetic energy,  $K$  of the system. The quantitative measurements of these state variables in integral form are given as

$$U = \int_{\Omega} \rho u \, dv, \quad (2.2a)$$

$$K = \int_{\Omega} \frac{1}{2} \rho \mathbf{v} \cdot \mathbf{v} \, dv, \quad (2.2b)$$

$$P = \int_{\Omega} \rho \mathbf{b} \cdot \mathbf{v} \, dv + \int_{\partial\Omega} \mathbf{t} \cdot \mathbf{v} \, da, \quad (2.2c)$$

and

$$Q = \int_{\Omega} \rho r \, dv + \int_{\partial\Omega} \mathbf{q} \cdot \mathbf{n} \, da. \quad (2.2d)$$

Combining equations (2.1) and (2.2), and after simplifications, the local form for the balance of energy is given as

$$\rho \dot{u} = \boldsymbol{\sigma} : \dot{\boldsymbol{\varepsilon}} + \rho r - \nabla \cdot \mathbf{q}, \quad (2.3)$$

with  $\boldsymbol{\sigma}$  and  $\dot{\boldsymbol{\varepsilon}}$  are stress and strain tensor respectively. Thus according to equation (2.3), any increase in the internal energy of the system is caused by the contribution from the potential energy, due to the relative positions or increase in the kinetic energy, due to the thermal agitations (Holzapfel et al., 2002; Hackl and Heinen, 2008). The internal energy may have contributions due to chemical reactions. We can include these contributions as product of chemical potential and rate of concentration for each constituent.

Equation (2.3) is a mathematical expression for the first law of thermodynamics. This relation expresses the conversion of energy from one state to another, but does not include any information about the direction of a process. Clausius by introducing the concept of entropy explained the second law of thermodynamics. This law enable us to determine the directional flow of the energy to attain the state of equilibrium. According to this principle, the total entropy production per unit time of the system must be positive. The total entropy,  $S$  of the system can be divided into two parts.

$$S = \int_{\Omega} \rho s \, dv = S_s + S_p, \quad (2.4)$$

with  $s$ , the specific entropy per unit volume of the system. The internal variables  $S_s$  and  $S_p$  are entropy transferred, and total entropy production in the system respectively. Mathematically, the rate of entropy transferred into a certain region of a continuum body is given by the heat transferred across its surface boundary and the heat generated or annihilated inside the volume. With this, we have

$$\dot{S}_s = \int_{\Omega} \rho \frac{r}{T} \, dv - \int_{\partial\Omega} \frac{\mathbf{q} \cdot \mathbf{n}}{T} \, da. \quad (2.5)$$

Substituting equation (2.5) in the rate form of equation (2.4) for the total entropy production per unit time, we have

$$\dot{S}_p = \int_{\Omega} \rho \dot{s} \, dv - \int_{\Omega} \rho \frac{r}{T} \, dv + \int_{\partial\Omega} \frac{\mathbf{q} \cdot \mathbf{n}}{T} \, da \geq 0. \quad (2.6)$$

For reversible processes equation (2.6) hold equal sign and the total entropy of the system is equal to the heat supplied to the body as given in equation (2.5). The entropy production rate for the irreversible processes can be calculated indirectly using equation (2.6). This production corresponds to the heat generated during the energy transformation. This contribution in the

total entropy give indirect measurement for the total dissipation in the system. Using the divergence theorem for the area integral in equation (2.6) and combining volume terms, the local form of the entropy production is

$$\dot{s}_p = \rho \dot{s} + \nabla \cdot \frac{\mathbf{q}}{T} - \rho \frac{r}{T} \geq 0. \quad (2.7)$$

In this equation, the entropy flux is related to the heat sources and fluxes proportionality to the temperature  $T$ . After the work of Coleman and Noll (1963), the combine form of first and second law, i.e. Clausius-Duhem inequality is used to calculate the entropy production in solid mechanics. Combing equations (2.3) and (2.7) gives

$$\dot{s}_p = \boldsymbol{\sigma} : \dot{\boldsymbol{\varepsilon}} + \rho (T\dot{s} - \dot{u}) + \frac{1}{T} \mathbf{q} \cdot \nabla T \geq 0. \quad (2.8)$$

Under the assumption of constant temperature, using equation (2.8) we can define different energy potentials. For reversible processes, there is no entropy production and we have a condition for the conservation of energy given as

$$\frac{1}{\rho} \boldsymbol{\sigma} : \dot{\boldsymbol{\varepsilon}} + T\dot{s} - \dot{u} = 0. \quad (2.9)$$

Equation (2.9) defines the specific internal energy  $u$  in term of state variables  $u(\boldsymbol{\varepsilon}, s)$ . Since entropy is not direct measurable quantity, we use the Legendre transformation to define potentials as function of measurable independent quantities.

- Defining a linear relationship between internal energy and entropy, the specific Helmholtz free energy  $f = u - Ts$ , equation (2.8) defines the entropy production rate as

$$\dot{s}_p = \boldsymbol{\sigma} : \dot{\boldsymbol{\varepsilon}} - \rho (s\dot{T} + \dot{f}) + \frac{1}{T} \mathbf{q} \cdot \nabla T \geq 0. \quad (2.10)$$

Using the criterion of reversible processes, we do not have any dissipative phenomenon, and equation (2.10) hold the equality. Under the condition of constant temperature, we define the Helmholtz free energy as a function of independent measurable state variables  $T$  and  $\boldsymbol{\varepsilon}$ . With  $\dot{f} = \rho^{-1}(\boldsymbol{\sigma} : \dot{\boldsymbol{\varepsilon}}) - s\dot{T}$ , using the chain rule we have  $\boldsymbol{\sigma} = \rho (\partial f / \partial \boldsymbol{\varepsilon})$  and  $s = -\partial f / \partial T$ . We can write the rate of Helmholtz free energy as

$$\dot{f}(\boldsymbol{\varepsilon}, T) = \left( \frac{\partial f(\boldsymbol{\varepsilon}, T)}{\partial \boldsymbol{\varepsilon}} \right)_{\mathbf{T}} : \dot{\boldsymbol{\varepsilon}} + \left( \frac{\partial f(\boldsymbol{\varepsilon}, T)}{\partial T} \right)_{\boldsymbol{\varepsilon}} \dot{T} \quad (2.11)$$

- Another thermodynamics potential is defined based on the internal energy from equation (2.9), as

$$\dot{u}(\boldsymbol{\varepsilon}, s) = \boldsymbol{\sigma} : \dot{\boldsymbol{\varepsilon}} + T\dot{s} = \left( \frac{\partial u(\boldsymbol{\varepsilon}, s)}{\partial \boldsymbol{\varepsilon}} \right)_{\mathbf{s}} : \dot{\boldsymbol{\varepsilon}} + \left( \frac{\partial u(\boldsymbol{\varepsilon}, s)}{\partial s} \right)_{\boldsymbol{\varepsilon}} \dot{s}. \quad (2.12)$$

Equation (2.11), Helmholtz free energy at constant temperature, and equation (2.12) internal energy at constant entropy are equal to the strain energy of the system. These two type of energy functions are useful in modeling thermoelastic material behaviors without any memory or plastic strains.

- Gibbs free energy potential is used for a process with controlled pressure and temperature. By defining specific Gibbs energy,  $g = f - \frac{1}{\rho} \boldsymbol{\sigma} : \boldsymbol{\varepsilon}$ , the rate of Gibbs energy for reversible processes after using  $\dot{f}$  from equation (2.10) for constant temperature, becomes

$$\dot{g}(\boldsymbol{\sigma}, T) = -\boldsymbol{\varepsilon} : \dot{\boldsymbol{\sigma}} - s\dot{T} = - \left( \frac{\partial g(\boldsymbol{\sigma}, T)}{\partial \boldsymbol{\sigma}} \right)_{\mathbf{T}} : \dot{\boldsymbol{\sigma}} - \left( \frac{\partial g(\boldsymbol{\sigma}, T)}{\partial T} \right)_{\boldsymbol{\sigma}} \dot{T}. \quad (2.13)$$

- Another thermodynamic potential enthalpy,  $h = u - \boldsymbol{\sigma} : \boldsymbol{\varepsilon}$  is useful in establishing a relationship between temperature, pressure and entropy. Using equation (2.12), the rate of specific enthalpy for non dissipative processes with zero temperature gradient is

$$\dot{h}(\boldsymbol{\sigma}, s) = T\dot{s} - \boldsymbol{\varepsilon} : \dot{\boldsymbol{\sigma}} = \left( \frac{\partial h(\boldsymbol{\sigma}, s)}{\partial s} \right)_{\boldsymbol{\sigma}} \dot{s} - \left( \frac{\partial h(\boldsymbol{\sigma}, s)}{\partial \boldsymbol{\sigma}} \right)_{s} : \dot{\boldsymbol{\sigma}}. \quad (2.14)$$

It is concluded from the above discussion, that with the Legendre transformations, we can define useful potentials as a function of measurable state variables. The selection of particular energy potential is based on the process parameters that influenced the kinetics of the system.

## 2.2. Local equilibrium and entropy flux.

In the previous section, different energy potentials were defined using the assumption of equilibrium thermodynamics. There is hardly any system in the universe without irreversibility. We have dissipation in the system contributing to the total entropy as additional value given by entropy production. Equation (2.8) gives the quantitative measurement of the dissipation in the system. Modeling of irreversible processes is a difficult task due to the lack of information about the dissipative processes contributing in entropy production. We can use the Clausius-Duhem inequality to model irreversible processes. All classical formulations for irreversible processes are based on a local equilibrium hypothesis. The basic assumption in modeling irreversible processes are in intuitive discretization of the system into small cells, such that each cell is considered as a macroscopic thermodynamic subsystem. Every cell is to be considered in a state of local equilibrium (Balluffi et al., 2005; Kreuzer, 1981; Jou et al., 2010).

Other assumptions for modeling the processes for irreversible thermodynamics are

1. All variables in a reversible process are equally significant in the modeling in the modeling of irreversible process. The state parameters e.g. temperature, entropy are accurately defined as they are in equilibrium. The local values of these quantities are constant in each cell, but they can have different values from cell to cell. They are allowed to change as a function of time  $t$  and space  $r$  over a complete domain.
2. The definition of energy potentials (e.g. equations (2.11) to (2.14)), defined for reversible processes are also valid for the irreversible processes. For the irreversible process, we have additional contribution from the internal variable participating in the entropy production of the system due to the dissipative phenomenon.

Based on these assumptions, we explain the general dissipation phenomena for any process using certain energy potentials defined previously and the Clausius-Duhem inequality. The choice of energy potential depends upon the process constraints being modeled. In case of plastic strains and control temperature, we can define the dissipation function by incorporating the Helmholtz free energy and Clausius-Duhem inequality, equations (2.8) and (2.11), respectively.

For irreversible processes with non-zero entropy production rate, it is assumed that the free energy potential has additional contributions from the internal state variables, participating actively in the dissipative process. The identification and classification of these parameters is not straightforward. We define the Helmholtz free energy,  $f = f(\boldsymbol{\varepsilon}^e, T, Y)$ , with  $Y$  being the vector

of additional internal variables contributing to the entropy production. The rate of Helmholtz free energy  $\dot{f}$  using the chain rule is

$$\dot{f}(\boldsymbol{\varepsilon}^e, T, Y) = \frac{\partial f(\boldsymbol{\varepsilon}^e, T, Y)}{\partial \boldsymbol{\varepsilon}} : \dot{\boldsymbol{\varepsilon}}^e + \frac{\partial f(\boldsymbol{\varepsilon}^e, T, Y)}{\partial T} \dot{T} + \frac{\partial f(\boldsymbol{\varepsilon}^e, T, Y)}{\partial Y} \bullet \dot{Y}. \quad (2.15)$$

Equation (2.15) has additional contributions due to the internal variables participating in the entropy production flux. The  $\bullet$  operator represents an appropriate operation between the extensive quantity,  $\partial f(\boldsymbol{\varepsilon}^e, T, Y)/\partial Y$  and conjugate flux of intensive variable,  $\dot{Y}$  with single scalar output. In case of plastic strains in a system, we split up the total strain,  $\boldsymbol{\varepsilon} = \boldsymbol{\varepsilon}^e + \boldsymbol{\varepsilon}^p$ , with  $\boldsymbol{\varepsilon}^e$  and  $\boldsymbol{\varepsilon}^p$  are elastic and plastic strains respectively. Using this expression in the Clausius-Duhem inequality gives a general expression for entropy production rate as

$$\left( \boldsymbol{\sigma} - \rho \frac{\partial f}{\partial \boldsymbol{\varepsilon}} \right) : \dot{\boldsymbol{\varepsilon}}^e + \boldsymbol{\sigma} : \dot{\boldsymbol{\varepsilon}}^p - \rho \left( s + \frac{\partial f}{\partial T} \right) \dot{T} - \rho \frac{\partial f}{\partial Y} \cdot \dot{Y} - \frac{1}{T} \mathbf{q} \cdot \nabla T \geq 0. \quad (2.16)$$

Using the state equations for reversible processes in equation (2.11), the quantitative measurement of the dissipation in irreversible inelastic evolution simplifies to

$$\dot{s}_p = Q_{mech} + Q_{thermal} = \boldsymbol{\sigma} : \dot{\boldsymbol{\varepsilon}}^p - \rho \frac{\partial f}{\partial Y} \cdot \dot{Y} - \frac{1}{T} \mathbf{q} \cdot \nabla T \geq 0. \quad (2.17)$$

With reference to equation (2.17), the total dissipation includes the contributions from internal heat generation  $Q_{thermal} = T^{-1} \mathbf{q} \cdot \nabla T$ , and dissipation in irreversible strains  $Q_{mech} = \boldsymbol{\sigma} : \dot{\boldsymbol{\varepsilon}}^p - \rho (\partial f / \partial Y) \cdot \dot{Y}$ . Hackl et al. (2011) evaluated similar dissipation functions for both coupled, and non-coupled non isothermal processes. They included an additional contribution due to the concentration,  $C$  of each constituent in a multicomponent system. This assumption modifies the Helmholtz-free energy potential as  $f = f(\boldsymbol{\varepsilon}, T, C, Y)$ . Using the Clausius-Duhem inequality, the dissipation includes an additional contribution due to the motion of fluxes. The relation for total entropy production per unit time, by using the chain rule is

$$\begin{aligned} \dot{s}_p &= \boldsymbol{\sigma} : \dot{\boldsymbol{\varepsilon}}^p - \rho \frac{\partial f}{\partial Y} \cdot \dot{Y} - \frac{1}{T} \mathbf{q} \cdot \nabla T - \frac{1}{T} \sum_{i=1}^n J_i \cdot \nabla \mu_i \geq 0, \\ &= Q_{mech} + Q_{thermal} + Q_{chemical}. \end{aligned} \quad (2.18)$$

The additional contribution,  $Q_{chemical}$  is regarded as a dissipation due to motion of matter as flux  $J_i$ , controlled by the force vector  $\nabla \mu_i$ . The magnitude of these fluxes are calculated using some constitutive law, that express a relationship between the flux and the contributing forces. Intuitively if we observed each contribution in equation (2.18), it is a scalar product between force and corresponding flux. For example in case of thermal dissipation, the gradient of temperature field,  $\nabla T$  acts as thermodynamics force and  $T^{-1} \mathbf{q}$  is a conjugate flux. The positive definitiveness of  $Q_{thermal}$  can be proved by using Fourier law,  $\mathbf{q} = -\boldsymbol{\kappa} \cdot \nabla T$  with  $\boldsymbol{\kappa}$  being the thermal conductivity tensor, we have

$$Q_{thermal} = \frac{1}{T} (\nabla T \cdot \boldsymbol{\kappa} \cdot \nabla T) \quad (2.19)$$

Similarly,  $Q_{mech}$ , the mechanical dissipation is also a function of force like quantities,  $\boldsymbol{\sigma}$  and  $\rho(\partial f / \partial Y)$  and conjugate rate terms  $\dot{\boldsymbol{\varepsilon}}^p$  and  $\dot{Y}$  are correlated as fluxes. The convexity of this dissipation is ensured by using appropriate flow rules for respective quantities. For the dissipation due to non-elastic strains, we need a rule to calculate the plastic strain. In the literature, we can find these principles. For example, for a finite strain elastoplasticity rule see Hackl (1997), for

an evolution principle with elasto-plastic deformation in a laminate, see [Kochmann and Hackl \(2011\)](#), for a general constitutive relation for coupled and non-coupled processes, see [Hackl et al. \(2011\)](#). Conclusively, we can write a general equation for the entropy production flux or the total dissipation in any system as summation of scalar product between thermodynamic forces, which are in general related with the gradient of thermodynamic intensive variables and conjugate fluxes, generally expressed in time derivatives of extensive quantities. Thus we can write a general expression of the dissipation in the system as

$$Q = \mathbf{X} \bullet \mathbf{J}. \quad (2.20)$$

Here  $\mathbf{X}$  is the vector of forces and  $\mathbf{J}$  is the vector of fluxes participating in the dissipative phenomena. We can have different pairs of tensorial quantities contributing in it. The  $\bullet$  represents a general scalar product operator necessary for the respective force-flux couple to obtain the single scalar output.

**Remark 1.** *The above derivation for total entropy production per unit time is done using the Helmholtz free energy potential. We have defined other free potentials in equations (2.11) to (2.14). For the sake of completeness, we express the criterion for the entropy production rate using Gibbs energy potential for processes with controlled pressure and temperature. In case of irreversibility, the additional internal variables vector,  $Y$  also contributes to the dissipation. The modified Gibbs potential is written as non-linear function of  $\boldsymbol{\sigma}$ ,  $T$ , and  $Y$ ,  $g = g(\boldsymbol{\sigma}, T, Y)$ . The rate of specific Gibbs energy,  $\dot{g}(\boldsymbol{\sigma}, T, Y)$  using the chain rule is expressed as*

$$\dot{g}(\boldsymbol{\sigma}, T, Y) = \frac{\partial g(\boldsymbol{\sigma}, T, Y)}{\partial \boldsymbol{\sigma}} : \dot{\boldsymbol{\sigma}} + \frac{\partial g(\boldsymbol{\sigma}, T, Y)}{\partial T} \dot{T} + \frac{\partial g(\boldsymbol{\sigma}, T, Y)}{\partial Y} \bullet \dot{Y}. \quad (2.21)$$

In case of processes with constant  $\boldsymbol{\sigma}$  and  $T$ , the total non-thermal entropy production rate is given by the product of forces,  $\partial g(\boldsymbol{\sigma}, T, Y)/\partial Y$  and rate of intrinsic variables,  $\dot{Y}$  acting as fluxes in the system. With this simplification, we can develop a correlation between the expression of entropy production rate using the Gibbs energy potential and equation (2.20). The thermodynamic forces are  $\mathbf{X} \rightarrow \partial g(\boldsymbol{\sigma}, T, Y)/\partial Y$ , a vector of forces and  $\mathbf{J} \rightarrow \dot{Y}$ , a vector of fluxes.

$$\dot{s}_p = \frac{\partial g(\boldsymbol{\sigma}, T, Y)}{\partial Y} \bullet \dot{Y} = \mathbf{X} \bullet \mathbf{J} \geq 0 \quad (2.22)$$

These dissipation potentials, equations (2.20) and (2.22) ensure the positive definitiveness under the assumption that there exist linear constitutive relationships between these fluxes and forces. These quadratic forms are known as Rayleigh-Onsager dissipation potentials. In the next sections, we will discuss these dissipative potentials and dissipative functions based on [Onsager \(1931\)](#) and [Fischer et al. \(2014\)](#) respectively.

### 2.2.1. Linear phenomenological relationships.

After formulating the functional form of total dissipation as scalar tensor product of force and flux, it is important to establish the constitutive relations between them to ensure convexity. Usually for the set of independent forces, we can use well established empirical laws, but these laws are not available in every case. [Onsager](#) postulated two theorems to formulate linear constitutive relationships between dissipative forces and fluxes. These formulations can be used for coupled and uncoupled processes. To model these constitutive equations, the selection of

force and the flux is at one's own choice. In general, these decisions are based on the cause and effects observed in the experiments. It is found experimentally that for the coupled processes, forces and fluxes are interwoven with each other. We need some phenomenological relationships between these forces and relative extensive quantities along with the externally imposed constraints. These constraints are related to the process requirements or external loadings. **Onsager** defined the reciprocal relations in coherence with the Thompson reciprocal functions. According to his statement, for any number of independent fluxes, each flux is related through a linear relationship with the coupled forces and vice versa. Using this postulate with set of forces  $\mathbf{X}$ , and conjugate fluxes  $\mathbf{J}$ , we can include the contribution of each flux in the individual force with linear relationship to first order near the equilibrium. Thus each force,  $X_i$  as a function of all participating fluxes is given as

$$X_i = X_i(\mathbf{J}) = X_i(J_1 \cdots J_n). \quad (2.23)$$

By using Taylor expansion to the first order differential with vanishing values of conjugate fluxes near to the equilibrium, we have

$$\begin{aligned} X_1(J_1 \cdots J_n) &= \frac{\partial X_1}{\partial J_1} J_1 + \frac{\partial X_1}{\partial J_2} J_2 + \cdots + \frac{\partial X_1}{\partial J_n} J_n \\ X_2(J_1 \cdots J_n) &= \frac{\partial X_2}{\partial J_1} J_1 + \frac{\partial X_2}{\partial J_2} J_2 + \cdots + \frac{\partial X_2}{\partial J_n} J_n \\ &\vdots \\ X_n(J_1 \cdots J_n) &= \frac{\partial X_n}{\partial J_1} J_1 + \frac{\partial X_n}{\partial J_2} J_2 + \cdots + \frac{\partial X_n}{\partial J_n} J_n. \end{aligned} \quad (2.24)$$

Equation (2.24) is written as

$$\mathbf{X} = \mathbf{R}\mathbf{J}, \quad (2.25)$$

where  $\mathbf{R}$  is a symmetric  $n \times n$  matrix. The diagonal components,  $R_{ii} = \partial X_i / \partial J_i$  are coefficients, expressing relationships between the forces and conjugate fluxes. Non-diagonal components,  $R_{ij} = \partial X_i / \partial J_j$  are coupling coefficients, which are adding cross effects of other participating fluxes  $J_j$  to the active force  $X_i$ .

It is not possible to make the direct measurements of the individual fluxes participating during the laboratory experiments, which are contributing in the dissipation phenomena. Conversely, it is more convenient to express each flux as a function of measurable participating forces in the system. Using the assumption of linear relationship between the flux  $J_i$  to all forces,  $X_j$  with  $j = [1, 2 \cdots, n]$ , the inverse relations for active fluxes under the condition of vanishing forces near the equilibrium are

$$\begin{aligned} J_1(X_1 \cdots X_n) &= \frac{\partial J_1}{\partial X_1} X_1 + \frac{\partial J_1}{\partial X_2} X_2 + \cdots + \frac{\partial J_1}{\partial X_n} X_n \\ J_2(X_1 \cdots X_n) &= \frac{\partial J_2}{\partial X_1} X_1 + \frac{\partial J_2}{\partial X_2} X_2 + \cdots + \frac{\partial J_2}{\partial X_n} X_n \\ &\vdots \\ J_n(X_1 \cdots X_n) &= \frac{\partial J_n}{\partial X_1} X_1 + \frac{\partial J_n}{\partial X_2} X_2 + \cdots + \frac{\partial J_n}{\partial X_n} X_n. \end{aligned} \quad (2.26)$$

Equation (2.26) in an abbreviated form is written as

$$\mathbf{J} = \mathbf{L}\mathbf{X}, \quad \text{with } L_{ij} = \frac{\partial J_i}{\partial X_j}. \quad (2.27)$$

$\mathbf{L}$  is  $n \times n$  symmetric matrix with  $\partial J_i / \partial X_j = \partial J_j / \partial X_i$ . The diagonal coefficients,  $\partial J_i / \partial X_i$  are direct coupling terms, and can be replaced with constants in the constitutive relations, if they exist for the particular case. The off-diagonal coefficients,  $\partial J_i / \partial X_j$  are adding coupling effects due to secondary participating forces,  $X_j$  in the primary flux,  $J_i$ . The coefficient matrices  $\mathbf{R}$  and  $\mathbf{L}$  are related with each other through an invertible kinetic. The product of these two coefficients matrices is  $R_{ik}L_{kj} = \delta_{ij}$ , with  $\delta_{ij}$  representing the Kronecker delta function.

By using these linear force–flux relationships, we can ensure the positive definiteness of total entropy production per unit time of the system. Substituting equations (2.25) and (2.27) in equation (2.22), a expression for quantitative dissipation measurement, we have

$$\dot{s}_p = R_{ij}J_iJ_j = L_{ij}X_iX_j \geq 0. \quad (2.28)$$

If we rewrite the above equations as summation of a symmetric and an anti-symmetric coefficient matrix. We have

$$\begin{aligned} \dot{s}_p &= R_{ii}J_iJ_i + \frac{1}{2}(R_{ij} + R_{ji})J_iJ_j \\ &= L_{ii}X_iX_i + \frac{1}{2}(L_{ij} + L_{ji})X_iX_j \geq 0. \end{aligned} \quad (2.29)$$

Equation (2.29) expresses a general condition for the coupling coefficients in the matrices as

$$R_{ii}R_{jj} > \frac{1}{4}(R_{ij} + R_{ji})^2 \text{ and } L_{ii}L_{jj} > \frac{1}{4}(L_{ij} + L_{ji})^2. \quad (2.30)$$

### 2.3. Dissipation potential and dissipation functions.

The total dissipation in the system is measured from the total entropy production rate as stated in the previous section. Thus, the quantitative measurement is given by equation (2.6) with respective constraints for positive definiteness. [Onsager](#) defined two dissipation potentials based on the quadratic form of entropy flux, equation (2.28). The first dissipation potential is defined as a function of fluxes. It is given as

$$\Phi(J, J) = \frac{1}{2} \sum_{i,j} J_i R_{ij} J_j. \quad (2.31)$$

Equation (2.31) defines a quadratic form as a function of fluxes only. Complementary to this, a second dissipation potential is defined as a function of forces only. It is given as

$$\Psi(X, X) = \frac{1}{2} \sum_{i,j} X_i L_{ij} X_j. \quad (2.32)$$

In order to ensure the positive definiteness of these potentials, the coefficients matrices of these two potentials must also satisfy the conditions given by equation (2.30) for coupling coefficients. Using these potentials in conjunction with equation (2.28) define the relationships to the entropy flux of the system.

$$\dot{s}_p = 2\Phi = 2\Psi \geq 0, \quad (2.33)$$

provided the linear kinetic relations, equations (2.25) and (2.27) are also satisfied. The inequality condition also add additional constraint of positive definiteness of both matrices  $\mathbf{R}$  and  $\mathbf{L}$  ( $R_{ii} \geq 0$  and  $L_{ii} \geq 0$ ).

The Onsager linear relations and dissipation potentials are based on the assumption that forces and fluxes are related under linear kinetics. In most of the practical problems, it is not possible to define these dissipation potentials. Hackl et al. (2011) overcome this setback by introducing a functional form of the dissipation in the system. This function is considered as a quadratic form of measurable extensive quantities. Similar dissipation functions were also used in Hackl and Fischer (2008); Hackl et al. (2011). For example, plasticity is modeled as a function of deviatoric stress and strain, whereas diffusion is modeled as a function of fluxes or rates of mass transfer along the surfaces. Fischer et al. (2014) described a general form of dissipation function  $Q(\mathbf{J}, Y)$  in relation with entropy flux as

$$Q(\mathbf{J}, Y) = T\dot{s}_p. \quad (2.34)$$

$Q$  is the dissipation function and depends on the fluxes,  $J_i$  and state variables  $Y$ . In reference to the second law of thermodynamics, the condition of an irreversible process, that total entropy of the system must be positive, holds true for equation (2.34). The positive definiteness of the dissipation function is ensured by assuming that it is twice differentiable with respect to  $\mathbf{J}$ .

**Remark 2.** A comparison of equation (2.33) and equation (2.34) establishes a necessary equivalence criterion between dissipation functions and dissipation potentials:

$$Q(\mathbf{J}, Y) = 2\Phi(\mathbf{J}, \mathbf{J}) = 2\Psi(X, X). \quad (2.35)$$

## 2.4. Thermodynamic extremal principles (TEP).

In the previous sections, general relations for dissipation functions and potentials were discussed in the general framework of thermodynamics. Thermodynamic extremal principles (TEPs) are an excellent tool widely used in many fields as an alternative to determine the kinetics of the system. TEPs are also helpful in formulating the evolution equations of the system with coupled dissipative mechanisms. These principles employ the variational formulations to find the phenomenological equations expressing the equilibrium state of the system for the set of dissipative phenomena and boundary constraints. The general statement for TEPs can be formulated as

*“ For all admissible fluxes  $J_i$ , with the conditions for conservation, and boundary and contact conditions at the edges and interfaces, only the fluxes that maximize the total dissipation are selected, subject to the conditions that all dissipation potentials ( $\Phi(J_i, J_j)$ ,  $\Psi(X_i, X_j)$ ) or dissipation functions ( $Q(\mathbf{J})$ ,  $Q(\mathbf{J}, Y)$ ) obey the equivalence condition given by equation (2.35)”* (Hackl and Fischer, 2008)

There are different formulations of TEPs in the literature. These principles differ from each other on the basis of Lagrange formulation and the methods to include process constraints. Detailed descriptions of these principles will be discussed in the forthcoming parts of this section.

### 2.4.1. Onsager’s extremal principle of maximum dissipation.

Onsager defined a variational principle in irreversible thermodynamics with the name “*The principle of least dissipation of energy*”. According to its statement, for an isolated system,  $\Omega$

with no net flow of flux across its boundaries,  $\partial\Omega$  the Lagrangian of the system is written as

$$\begin{aligned} L_{Ons} &= \dot{s}_p - \Phi(J_i, J_j) \\ &= X_i J_i - \frac{1}{2} \sum_{i,j} J_i R_{ij} J_j. \end{aligned} \quad (2.36)$$

Variation of equation (2.36) with respect to fluxes  $\mathbf{J}$ , provides a stationary point. Under the assumption of positive definiteness of dissipation potential  $\Phi$ , a stationary point represents the maximum point value of the dissipation for selected process variables  $X_i$ . The general evolution equations after variation w.r.t fluxes is

$$\frac{\partial L_{Ons}}{\partial J_i} = X_i - R_{ij} J_j = 0. \quad (2.37)$$

Equation (2.37) is written in a matrix form, and is expressing the linear relationship between the force vector,  $\mathbf{X}$  and all participating fluxes  $J_j$ . A condition for the maximum dissipation holds true only for the case that  $R_{ij}$  is symmetric and positive definite. Additionally, equation (2.37) satisfies this relation, in accordance with equation (2.25). Using an equivalence criterion between dissipation potentials and dissipation function, equation (2.35) with equation (2.37), the alternative form of a stationary condition is given as

$$X_i - \frac{1}{2} \frac{\partial Q}{\partial J_i} = 0. \quad (2.38)$$

It is important to mention that the unique value of the force vector  $X_i$  is subject to the positive definiteness of the dissipation function  $Q(J_i, Y)$  and the constraint of vanishing fluxes at the equilibrium, which is also the basic assumption of Onsager's force–flux linear relationships.

#### 2.4.2. Ziegler's thermodynamic extremal principle.

Ziegler's extremal principle is often termed as “*maximum entropy production principle*”. This principle is a modified form of the Onsager Lagrange function. According to this principle,

*“If irreversible force,  $X_i$  is prescribed, the actual flux,  $J_i$  maximizes the entropy production if and only if, the relation for the entropy production flux equivalence criterion,  $\dot{s}_p = \sum_i X_i J_i$ ” is satisfied (Martyushev and Seleznev, 2006).*

The Ziegler Lagrangian function with the dissipation function is written as:

$$L_{Zie} = Q(J_i, \dots) - \lambda \{Q(J_i, \dots) - \dot{s}_p\}. \quad (2.39)$$

Here,  $\lambda$  is Lagrange multiplier and its value is calculated using a variational formulation. The variation of equation (2.39) with respect to the participating fluxes  $\mathbf{J}$  gives

$$\frac{\partial L_{Zie}}{\partial J_i} = (1 - \lambda) \frac{\partial Q}{\partial J_i} + \lambda X_i = 0, \quad (2.40)$$

here  $X_i$  is the collection of conjugate force vectors relevant to the participating fluxes. Multiplying equation (2.40) with  $J_i$ , and using the equivalence criterion for dissipation function and entropy flux, we have

$$\frac{1 - \lambda}{\lambda} = - \frac{Q}{\frac{\partial Q}{\partial J_i} \cdot J_i}. \quad (2.41)$$

Using equation (2.41) with equation (2.40) for the Lagrange parameter, the steady state force vector  $X_i$  is given as

$$X_i - \frac{1}{T} \frac{Q}{\frac{\partial Q}{\partial J_i} \cdot J_i} \frac{\partial Q}{\partial J_i} = 0. \quad (2.42)$$

Usually,  $Q(J_i, \dots)$  is homogeneous function of order  $n$ , ( $(\partial Q/\partial J_i) \cdot J_i = nQ$ ). So, we can also evaluate  $\lambda = n/(n-1)$ . With this, equation (2.42) becomes

$$X_i - \frac{1}{T} \frac{1}{n} \frac{\partial Q}{\partial J_i} = 0. \quad (2.43)$$

If we compare equation (2.43) with equation (2.33), there exists a linear relationship between these two principles. Ziegler and Onsager extremal principles are analogous for  $n = 2$ , subject to the constraints satisfying the boundary and interface conditions. Ziegler's variational principle is the more general form of the extremal principle. For many problems in real life, we have additional constraints and these restrictions can be included in the Lagrangian along with basic TEPs formulations. As dissipation function and entropy production rate are functions of  $J$ , it is more convenient if the additional constraints are first formulated as linear function of the corresponding flux  $J_i$ . Thus, for a system with ' $m$ ' number of additional constraints, defined as  $\sum_{i=1}^N a_{ik} J_i = 0$  with  $k = 1, 2, \dots, m$  and  $a_{ik}$  as function of state variables other than  $J$ . The modified Lagrangian with additional constraints reads

$$L_{Zie} = Q(J_i, \dots) - \lambda \{Q(J_i, \dots) - \dot{s}_p\} + \beta_k a_{ik} J_i, \quad (2.44)$$

with  $\beta_k$  as the Lagrange parameters for the additional constraints. Now the modified Lagrangian is function of fluxes only. Variation of equation (2.44) w.r.t.  $J_i$  gives the steady state condition for  $X_i$  as

$$X_i - \frac{1}{n} \frac{\partial Q}{\partial J_i} + \beta_k a_{ik} = 0. \quad (2.45)$$

Equation (2.45) represents the matrix form with  $N$  number equations for  $J_N$  fluxes. After multiplying each with  $J_i$ , we have  $(N+m)$  number of equations with constraints ( $\sum_{j=1}^N a_{jk} J_j = 0$ ). After this appropriate operation, we have  $(N+m)$  number of equations with  $(N+m)$  number of unknowns,  $X_i$  with ( $i = 1, \dots, N$ ) and  $\beta_k$  with ( $k = 1, \dots, m$ ). This system of equations is easy to solve using ordinary methods of linear algebra.

**Remark 3.** *Hackl et al. (2011) modeled the system of equations for both coupled and non-coupled processes. In contrast to the Ziegler's principle, they did not assume an orthogonality condition between dissipation surface and forces (see Fig. (2.1)). Hackl et al.'s model is valid for any homogeneous dissipation function. Additionally, in case of non-coupled processes, the total dissipation function is the summation of all individual dissipative function, expressed as pairs of respective forces and fluxes (see chap. 9 DeHoff, 2006). We have modified Lagrangian with  $\lambda_i$  Lagrange parameters, where  $i$  is the number of individual dissipation processes in the system. For every  $i$ th process, equation (2.41) becomes*

$$\frac{1 - \lambda_i}{\lambda_i} = - \frac{Q_i}{\frac{\partial Q_i}{\partial J_i} \cdot J_i}, \quad (2.46)$$

and the condition for the balance of forces, equation (2.42) takes the following form

$$X_i - \frac{1}{T} \frac{Q_i}{\frac{\partial Q_i}{\partial J_i} \cdot J_i} \frac{\partial Q_i}{\partial J_i} = 0. \quad (2.47)$$

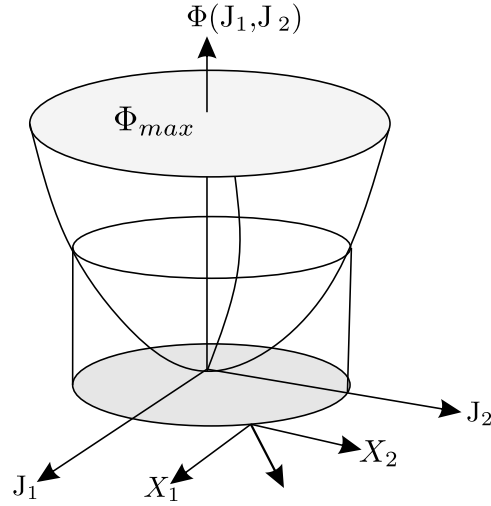


Figure 2.1.: A simple dissipation potential,  $\Phi(J_1, J_2)$  shown as quadratic function of fluxes  $J_1, J_2$  under linear theory. At the maximum dissipation, we have state of vanishing fluxes.

**Remark 4.** As it is assumed in the previous section that  $Q(J, \dots)$  is of order  $n > 1$ , than we can define two identities that are useful in defining the relations in linear irreversible kinetics.

$$\sum_j \frac{\partial Q}{\partial J_j} J_j = \frac{\partial Q}{\partial \mathbf{J}} \cdot \mathbf{J} = nQ \quad (2.48)$$

similarly another related useful identity,

$$\sum_j \frac{\partial^2 Q}{\partial J_j \partial J_j} J_j = (n-1) \frac{\partial Q}{\partial J_i} \quad (2.49)$$

equation (2.49) is useful in defining Onsager symmetry matrix. Using equation (2.49) with equation (2.43) gives  $\mathbf{X}$

$$\begin{aligned} \mathbf{X} &= \frac{1}{n(n-1)} \frac{\partial^2 Q}{\partial J_i \partial J_i} J_i, \\ &= \mathbf{R}(J_i) \cdot \mathbf{J}, \quad \mathbf{R}(J_i) = \frac{1}{n(n-1)} \frac{\partial^2 Q}{\partial J_i \partial J_i}, \end{aligned} \quad (2.50)$$

with  $\mathbf{R}$  being a symmetric matrix. Equation (2.50) enables us to define the coefficient matrix as a function of the dissipation function, subject to the condition that  $Q$  must be twice differentiable w.r.t. fluxes. If we are able to find  $\mathbf{L}(J) = (\mathbf{R})^{-1}$ , this enables us to establish the relationship for an individual flux with the force vector  $X_j$  ( $J_i = L_{ij}(J_i) X_j$ ). Conclusively, the Ziegler's principle is considered as a more general form of the TEPs, and it is capable of formulating the system kinetics with additional constraints (Fischer et al., 2014).

### 2.4.3. The minimum principle for the dissipation potential (MDPD).

There is no single individual person or research group associated with the formulation of this principle. Cocks and Gill (1996) distinguishably contributed in establishing this theory for material processes with a particular emphasis in powder metallurgy. Hackl and Fischer (2008)

discussed this principle in detail for inelastic materials and compared it with Ziegler and Onsager thermodynamic extremal principles for establishing the equivalence between dissipation functions and dissipation potentials. For the cases, where the equivalence criterion does not hold true, a reconstruction of the dissipation function enables us to re-establish these relations. Hackl (1997) used this principle for microstructure evolution modeling. A generalized definition of this principle is

*“For all admissible fluxes  $J_i$ , with the conditions for the conservation, boundary and contact conditions at edges and interfaces, only these fluxes are taken which minimize  $\dot{E} + \Phi$ .”*

Here  $\dot{E}$  is rate of the total energy of the system and  $\Phi$  is dissipation potential defined in the previous section. Thus, the Lagrange, according to this principle is written as

$$L_{MPDP} = \dot{E} + \Phi. \quad (2.51)$$

The energy  $E(Y)$  is function of state variables. Thus minimization with respect to these state variables yields

$$\frac{\partial E}{\partial Y} + \frac{\partial \Phi}{\partial \dot{Y}} = 0 \quad (2.52)$$

This principle is a true minimization principle. In comparison with equation (2.36), if the energy rate  $\dot{E}$  is replaced with  $-\dot{s}_p$ , it is the conjugate inverse of the Onsager principle of maximum dissipation.

#### 2.4.4. Prigogine’s principle of minimum entropy production.

In comparison with the maximization principles discussed earlier, Prigogine principle seems contradictory to maximum entropy production for an isolated system. The previously cited extremal principles are based on maximization of the entropy production in a closed system but this principle is valid for stationary processes with some unconstrained forces. So the scope of this principle is limited in comparison with other TEPs. The system establishes a steady state condition with minimum entropy production for external constraints. These restricted state parameters prevent the system to achieve the equilibrium state. This principle states

*“In the stationary non equilibrium system, which is consistent with the external restrictions (constant irreversible forces  $X_\zeta \forall \zeta = 1, \dots, j; j < n$  with  $n$  being the total number of forces in the system), the entropy production is minimum, if the fluxes are expressed as a function of forces with an additional constraint for the symmetry condition of the coefficient matrix  $L$ ”.*

According to this statement, the variational form of Prigogine’s principle is

$$\dot{s}_p(\mathbf{X}) \rightarrow \min_{X_\Upsilon} \forall \Upsilon = j + 1, \dots, n \quad \text{for constant forces, } X_\zeta. \quad (2.53)$$

We can express the entropy production in the form of forces by using an equivalence criterion with dissipation potentials. Hence, Combining equation (2.28) with equation (2.53),  $\dot{s}_p(\mathbf{X}) = L_{ij}X_iX_j$ , the Lagrange is a function of forces only. Hence, the variation of this potential w.r.t free forces  $X_\Upsilon$  expresses the stationary condition for steady state as

$$\frac{\partial}{\partial X_\Upsilon} \dot{s}_p(\mathbf{X}) = \frac{\partial}{\partial X_\Upsilon} (L_{i\Upsilon}X_iX_\Upsilon) = 2 \sum_{i=1}^N L_{i\Upsilon}X_i = 0, \quad (2.54)$$

Thus, from the linear relationship between forces and fluxes (equation (2.27)),  $J_\gamma$  vanishes under the stationary condition with external constraints. which from the Onsager's potential for forces, gives  $J_\gamma = L_{i\gamma} X_i = 0$ . From this condition, it is clear that for the system with constraint forces, we have a steady state with the vanishing fluxes for unconstrained forces.

**Remark 5.** *Prigogine's extremal principle can be considered as a corollary of Onsager TEP within the framework of linear thermodynamics relationship between force and flux. Alternative derivation of this principle can also be done using the Gyarmati's formulation of Onsager's TEP with free forces and fixed fluxes, which is valid for stationary processes in the presence of free forces. It is also worth mentioning that Prigogine's TEP is not applicable to all steady state systems, limiting to linear nonequilibrium irreversible processes. There are several examples e.g. Peltier element, Benard effect and structure instability during biochemical evolution that shows the condition for vanishing fluxes, and equation (2.54) is not satisfied (Fischer et al., 2014; Martyushev and Seleznev, 2006).*

### 3. Thermal grooving

The grain boundary interactions with the free surface minimizes total energy of the system by different mechanisms. Surface diffusion, bulk diffusion, and evaporation–condensation are active transport mechanisms participating develop the surface topography at the different temperature regions. These processes minimize the total energy of the system due to mass transfer. Among these, surface diffusion participates actively below the roughening temperature in the solids, above which the facets disappears from the crystal surfaces. It is dominant process for the thermal grooves formations along the grain boundaries (Blakely, 1963; Stone et al., 2005; Akyildiz and Ogurtani, 2017). There are different models in the literature, discussing the kinetics and shapes of the thermal grooves with different coupled transport mechanisms. In most of these models, contact conditions at the interfaces and intersecting points, and boundary conditions along the edges are expressed by using the additional set of equations/constraints. These relations are defined based on the assumptions for numerical homogenization and limitations. Hackl et al. (2017) engaged the thermodynamic extremal principle to model thermal grooving in three dimensions. The dissipation function includes the contributions from two parallel transport mechanisms over the domain. Along the side, a finite element model is also formulated using the thermodynamic extremal principle. The objective of this chapter is to discuss this model and its implementation for the polycrystal.

#### 3.1. Introduction.

The study of thermal grooving is not only useful in evaluating the grain boundary energies distribution using relative value of the grain boundary energies from the equilibrium dihedral angle but is also important to develop understanding of the kinetics of processes occurring at the free surface, such as grain growth due to bulk diffusion, dewetting with increasing temperature, and sintering. Mullins's (1961) analytical model for thermal grooving is used in many research works to evaluate the processes parameters, e.g. grain boundary energy and diffusion coefficients. He showed that the thermal grooving causes stagnation in the grain growth due to the boundaries pinning at the free surfaces up to the critical range of boundary plane inclination. Later on, Allen (1982) proved that depth of the groove decreases for moving grain boundary and shape of such groove differ significantly from the stationary grooves. There are many other models (for references, see section (5.1)) and improvements after the Mullins initial work, but they have not considered any contribution from the diffusion along a triple line channel, which plays an important role in micro structure morphology. Hoffman and Cahn (1972), while discussing equilibrium condition for three meeting boundaries at the free surface in private discussion with Nielsen, accepted that the role of the triple line energy in morphological evolution is subject to the existence of equilibrium relations between the boundaries and the interface line energy, which was unidentified in the scientific community till that time. The experimental works of Gottstein et al. (2010) discussed the importance and existence of triple line energy for the first time, and they explained the methods to measure these energies. The effects of triple line energy on the groove kinetics and equilibrium dihedral angle are discussed

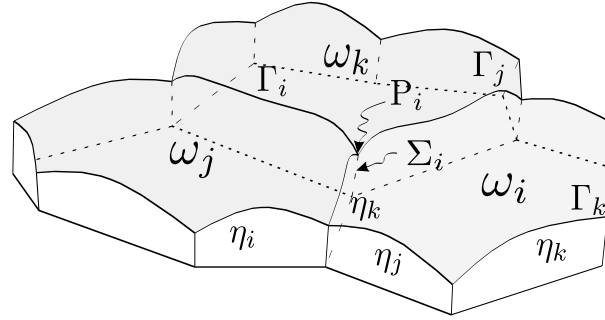


Figure 3.1.: Top thin layer of a polycrystal with three grains meeting at the common quadruple point  $P_i$ . Other geometrical elements grain boundaries  $\eta_i$ , triple lines  $\Gamma_i, \Sigma_i$ , are also shown.

with peculiarity (see Fortier et al., 1991; Zhao et al., 2010, 2012a,b).

Thermodynamic extremal principles have proved their effectiveness in modeling the diffusion dominated processes (for interface and bulk diffusion, see Svoboda et al., 2001; Fischer et al., 2003, 2012). For thermal grooving in two dimensions, Hackl et al. (2013) model is based on the principle of maximum dissipation. The effect of boundary plane inclinations on the groove shapes were discussed in detail for different diffusion coefficients. They established a relationship between the actual and measured dihedral angle for exact estimation of grain boundary orientation and energy.

In three dimensions, in addition to grain boundary inclination, the misorientation between the grains also influences the groove shape and overall kinetics in the polycrystalline. In order to understand the kinetics of grooving in three dimensions for multi-grains, Hackl et al. (2017) used the principle of maximum dissipation to formulate the set of phenomenological equations of the thermal grooving. This model includes coupled dissipation processes with additional constraints for the conservation of mass and consistent contact between the boundaries. The model includes

- . the specific surface energy ( $\gamma$ ),
- . the specific grain boundary energy ( $\gamma_\eta$ ),
- . the specific external triple line energy ( $\gamma_\Gamma$ ),
- . the specific internal triple line energy ( $\gamma_\Sigma$ )

The dissipation is considered due to two coupled transport mechanisms,

- . mass diffusion along the free surface,
- . mass diffusion along the groove channel at the triple line.

### 3.2. Geometrical model and kinematics.

To model the grooving at the free surface, we consider only the upper half of a polycrystal. Grain boundaries between these grains are assumed planar to exclude the torque effects at the

boundary junctions. Figure (3.1) shows the element of three grains.  $\omega_i$  is representing a free surface of each grain. A grain boundary  $\eta_i$  is formed at intersection of two grains  $\omega_j$  and  $\omega_k$  ( $\eta_i = \omega_j \cap \omega_k$ ). A triple line  $\Gamma_i$  is a geometrical element coexisting at the intersection of grain boundaries, a internal grain boundary and free surfaces ( $\Gamma_i = \omega_j \cap \omega_k \cap \eta_i$ ). An internal triple line,  $\Sigma_i$  is a geometrical element at an intersection of all three internal grain boundaries. A quadruple point  $P_i$  is characterized as an intersection point of  $\Gamma_i$  and  $\Sigma_i$  lines at the free surface ( $P_i = \Gamma_i \cap \Gamma_j \cap \Gamma_k \cap \Sigma_i$ )<sup>1</sup>.

In general, we can have more than three grains in the polycrystalline periodic structure. So here onward, set  $\mathbb{S}$  represents a collection of all surfaces, set  $\mathbb{T}$  represents a collection of all triple lines, and set  $\mathbb{Q}$  is a collection of all quadruple points in the array. In this model, the free surface  $\omega_i$  of each grain is defined using the surface normal vector  $\mathbf{n}_i$ . Similarly, each triple line  $\Gamma_i$  is ascribed to a normal vector  $\mathbf{n}_{\Gamma_i}$ , and a tangent vector  $\mathbf{t}_{\Gamma_i}$ . It is also assumed that each line lies in the respective grain boundary  $\eta_i$  plane and vertical motion of this line is within this plane. Thus, both of these elements share a common normal vector  $\mathbf{n}_{\Gamma_i}$ . An additional unit vector,  $\mathbf{m}_{\Gamma_{ij}}$  is tangent to the surface  $\omega_j$ , such that the orthogonality condition

$$\mathbf{m}_{\Gamma_{ij}} = \pm \mathbf{t}_{\Gamma_i} \times \mathbf{n}_j. \quad (3.1)$$

with neighboring triple lines  $\Gamma_i$  must be satisfied. The direction of  $\mathbf{m}_{\Gamma_{ij}}$  is chosen in such a way that it must be directed away to  $\Gamma_i$ . The motion of internal triple line,  $\Sigma_i$  is considered in the tangential direction  $\mathbf{t}_{\Sigma_i}$ , a unit vector pointing outward for the positive motion. Figure (3.2) shows the graphical representation of these vectors.

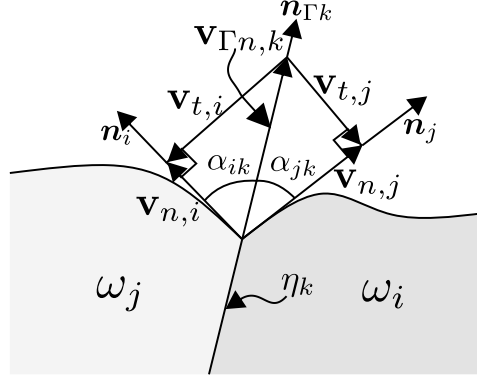


Figure 3.2.: Condition for the continuity along the grain boundary  $\eta_k$ . The triple line velocity along the grain boundary plane,  $\mathbf{v}_{\Gamma n,k}$  must be in the state of an equilibrium with surface velocities in accordance with equations (3.2) and (3.3)

With these,  $\mathbf{v}_{n,i}$  is the velocity of surface points in the normal,  $\mathbf{n}_i$  direction. As the triple line and grain boundary motion is restricted in the common plane, thus the triple line  $\Gamma_i$  moves in the grain boundary plane with normal velocity  $\mathbf{v}_{\Gamma n,i}$ , directed in  $\mathbf{n}_{\Gamma_i}$  direction. To ensure the contact condition between all boundaries along the triple line, the compatibility condition reads

$$\mathbf{v}_{n,j} = \mathbf{v}_{\Gamma n,i} \sin \alpha_{ij}, \quad (3.2)$$

with  $\sin \alpha_{ij}$  is a angle between  $\mathbf{n}_j$  and  $\mathbf{n}_{\Gamma_i}$ . Subsequent motion of the triple line  $\Gamma_i$  within grain boundary  $\eta_i$  causes reductions in the areas  $A_j$  of the forming surfaces  $\omega_j$ . These reductions are

<sup>1</sup>A quadruple point is considered to be formed at an intersection of three grains. So in principle, it is a junction point at a free surface between four triple lines, and six grain boundaries meeting together.

related with tangential velocities of the free surfaces  $\mathbf{v}_{t,j}$ . This velocity is given as

$$\mathbf{v}_{t,j} = -\frac{\mathbf{v}_{n,j}}{\tan \alpha_{ij}} = -\mathbf{v}_{\Gamma n,i} \cos \alpha_{ij}. \quad (3.3)$$

The vertical motion of the surface is attributed to the motion of matter along it. Additionally, the motion of matter along different triple lines channels along the boundary edges contribute to increase or decrease in the total surface area of the forming grains. Thus, the time rate of area of the free surface,  $\dot{\omega}_i$  includes the additional contributions due to the motion of quadruple points,  $P_i$  at the corners. With this

$$\dot{A}_i = \frac{d}{dt} \int_{\omega_i} dA_i = \int_{\omega_i} d\dot{A}_i + \sum_{j, \omega_i \in \mathbb{A}_{\Gamma_j}} \int_{\Gamma_j} \mathbf{v}_{t,j} ds_j \quad \forall \mathbb{A}_{\Gamma_j} = \{\omega_i \in \mathbb{S} | \Gamma_j \subset \partial\omega_i\}. \quad (3.4)$$

$\mathbb{A}_{\Gamma_j}$  is a set of external triple lines at the free boundaries of the grain  $\omega_i$ . Combining equation (3.4) and equation (3.3) yields

$$\dot{A}_i = \int_{\omega_i} K_i \mathbf{v}_{n,i} dA_i - \sum_{j, \omega_i \in \mathbb{A}_{\Gamma_j}} \int_{\Gamma_j} \mathbf{v}_{\Gamma n,j} \cos \alpha_{ji} ds_j. \quad (3.5)$$

Here,  $K_i$  is twice the mean curvature and is equal to the trace of curvature tensor given by equation (3.56) and  $ds_j$  is small arc length of the triple line.

At both ends of the triple lines, it is assumed that the quadruple points  $P_i$  move along  $\Sigma_i$ . If  $\mathbf{v}_{\Sigma_i}$  is the velocity vector of  $P_i$  in  $\mathbf{t}_{\Sigma_i}$  direction, than the condition for coupled motion of the triple lines in contact with free surfaces is

$$\mathbf{v}_{\Gamma n,j} = \mathbf{v}_{\Sigma_i} \sin \alpha_{\Gamma ij}, \quad (3.6)$$

with  $\alpha_{\Gamma ij}$  is the angle between  $\mathbf{n}_{\Gamma_j}$  and  $\mathbf{t}_{\Sigma_i}$ . The positive motion of  $P_i$  in  $\mathbf{t}_{\Sigma_i}$  direction engenders the variations in the lengths of adjoining lines with tangential velocity  $\mathbf{v}_{\Gamma t,j}$ . In relation with the relative inclination between internal and external triple lines, we have

$$\mathbf{v}_{\Gamma t,j} = -\frac{\mathbf{v}_{\Gamma n,j}}{\tan \alpha_{\Gamma ij}} = -\mathbf{v}_{\Sigma_i} \cos \alpha_{\Gamma ij}. \quad (3.7)$$

The rate of change in the length of each triple line has contribution from the motion of line, governed by the curvature and additional contribution from the motion of each quadruple point,  $P_i$  at both ends. With these two concatenated phenomena, the overall rate is

$$\dot{s}_i = \frac{d}{dt} \int_{\Gamma_i} ds_i = \int_{\Gamma_i} d\dot{s}_i + \sum_{j, \Gamma_i \in \mathbb{A}_{P_j}} \mathbf{v}_{\Gamma t,j} \quad \forall \mathbb{A}_{P_j} = \{\Gamma_i \in \mathbb{T} | P_j \subset \partial\Gamma_i\}. \quad (3.8)$$

$\mathbb{A}_{P_j}$  is a set of triple lines meeting at  $P_j$ . Using equation (3.7)<sub>2</sub> and the definition of the line integral from basic calculus, equation (3.8) yields

$$\dot{s}_i = \int_{\Gamma_i} K_{\Gamma_i} \mathbf{v}_{\Gamma n,i} ds_i - \sum_{j, \Gamma_i \in \mathbb{A}_{P_j}} \mathbf{v}_{\Sigma_j} \cos \alpha_{\Gamma ji}. \quad (3.9)$$

Here  $K_{\Gamma_i}$  is the curvature of  $\Gamma_i$ . Next step is to calculate the rate of growth of the internal triple line. As stated earlier that motion of  $\Sigma_i$  is only along the tangential direction, thus

$$\dot{s}_i = \mathbf{v}_{\Sigma_i}. \quad (3.10)$$

### 3.3. Conservation of matter.

This model is based on the diffusional based dissipation processes. Thus the total mass of the system must be conserved at all the time. In this model, the morphology of the polycrystal is considered due to two types of motion.

- (i) motion of matter along the free surface  $\omega_i$ .
- (ii) motion of matter in the triple line channel  $\Gamma_i$  along the grain boundary.

Figure (3.3) illustrates these fluxes along the free surface. Flux  $J_i$  relevant to each surface  $\omega_i$ , is a vector quantity, and is measured in the unit  $m^3/m \text{ sec} = m^2/sec$ . The motion of free surface in normal direction is directly proportional to the flux. So, according to the balance condition for the conserved quantities, there must be state of equilibrium without any production density. It is expressed as

$$\mathbf{v}_{n,i} + \nabla_s \cdot \mathbf{J}_i = 0, \quad (3.11)$$

with  $\nabla_s \cdot$  is the surface divergence operator. The second flux,  $j_{\Gamma_i}$  in  $\mathbf{t}_{\Gamma_i}$  direction is a flow of matter in the triple line channel between the two surfaces  $\omega_{j,k}$  and is measured in the unit  $m^3/sec$ .

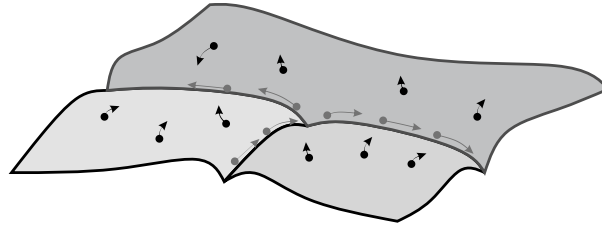


Figure 3.3.: Motion of flux,  $J_i$  along the grains surfaces is governed in accordance with the linear force and flux relationship, equation (3.29). The thermodynamics forces,  $\nabla_s \mu$  determine their direction to maximize the dissipation. Conditions for balance of matter, equations (3.13) and (3.14) must be satisfied along the triple lines,  $\Gamma_i$  and at quadruple point  $P_i$  respectively.

In order to establish the condition for the conservation of matter along these channels, we assume a small line element  $ds_i$  between the grains  $\omega_{j,k}$ . Net flow of matter is the difference of fluxes between the ends of this line element,  $j_{\Gamma_i}(s_i + ds_i) - j_{\Gamma_i}(s_i)$ . The surfaces fluxes also contribute in it. If  $(J_j \cdot \mathbf{m}_{\Gamma_{ij}} + J_k \cdot \mathbf{m}_{\Gamma_{ik}})ds_i$  expresses the net flow of flux from the neighboring grains  $\omega_j$  and  $\omega_k$ , than the balance condition along  $ds_i$  is

$$j_{\Gamma_i}(s_i + ds_i) - j_{\Gamma_i}(s_i) + (J_j \cdot \mathbf{m}_{\Gamma_{ij}} + J_k \cdot \mathbf{m}_{\Gamma_{ik}})ds_i = 0. \quad (3.12)$$

For the limit  $ds_i \rightarrow 0$ , equation (3.12) in derivative form is given as

$$\frac{dj_{\Gamma_i}}{ds_i} + \sum_{j, \omega_j \in \mathbb{A}_{\Gamma_i}} J_j \cdot \mathbf{m}_{\Gamma_{ij}} = 0. \quad (3.13)$$

In addition to this, the net flow of fluxes at the point of meeting triple lines,  $P_i$  must satisfy the zero flux condition. Thus the continuity of mass flux at  $P_i$  implies

$$\sum_{j, \Gamma_j \in \mathbb{A}_{P_i}} S_{\Sigma_{ij}} j_{\Gamma_j} = 0. \quad (3.14)$$

Here  $S_{\Sigma_{ij}} = \pm 1$ , taken as positive, when flux is flowing away at  $P_i$  and vice versa.

### 3.4. Total energy of the system and its rate.

In order to establish the Lagrange formulation for the principle of maximum dissipation in accordance with equation (2.51), we calculate the rate of total energy of the system. In our polycrystalline model, the total energy,  $G$  includes the contribution from the geometrical elements, free surfaces  $\omega_i$ , grain boundaries  $\eta_i$ , triple lines  $\Gamma_i$ , and internal triple lines  $\Sigma_i$ .

$$G = \sum G_i + \sum G_{\eta_i} + \sum G_{\Gamma_i} + \sum G_{\Sigma_i}. \quad (3.15)$$

Here  $G_i$  is the surface Gibbs energy of grain  $\omega_i$ , and is given as

$$G_i = \int_{\omega_i} \gamma_i dA_i, \quad (3.16)$$

with  $\gamma_i$  is the specific surface energy. It is assumed that this energy is independent of time, therefore the rate of this quantity,  $\dot{G}_i$  has only contribution from the time derivate of  $dA$ . Using equation (3.5) in coordination with equation (3.16), we have

$$\dot{G}_i = \int_{\omega_i} \gamma_i K_i \mathbf{v}_{n,i} dA_i - \sum_{j, \omega_i \in \mathbb{A}_{\Gamma_j} \Gamma_j} \int \gamma_i \mathbf{v}_{\Gamma n, j} \cos \alpha_{ij} ds_j. \quad (3.17)$$

Grain boundary energy of each boundary,  $G_{\eta_i}$  is given as

$$G_{\eta_i} = \int_{\eta_i} \gamma_{\eta_i} dA_i, \quad (3.18)$$

with  $\gamma_{\eta_i}$  is the specific grain boundary energy and is also independent of time. As the motion of triple line and grain boundary are in the same direction, thus the rate of area of the boundary is expressed with the normal velocity and triple line length. The rate of equation (3.18) is given as

$$\dot{G}_{\eta_i} = \int_{\Gamma_i} \gamma_{\eta_i} \mathbf{v}_{\Gamma n, i} ds_i, \quad (3.19)$$

with  $\mathbf{v}_{\Gamma n, i}$  is the velocity in  $\mathbf{n}_{\Gamma_i}$  direction. Similarly,  $G_{\Gamma_i}$  is the line energy of external triple lines  $\Gamma_i$ , and is given as

$$G_{\Gamma_i} = \int_{\Gamma_i} \gamma_{\Gamma_i} ds_i, \quad (3.20)$$

with  $\gamma_{\Gamma_i}$  is the specific line energy. The rate  $\dot{G}_{\Gamma_i}$ , in association with equation (3.9) becomes

$$\dot{G}_{\Gamma_i} = \int_{\Gamma_i} \gamma_{\Gamma_i} K_{\Gamma_i} \mathbf{v}_{\Gamma n, i} ds_i - \sum_{j, \Gamma_i \in \mathbb{A}_{P_j}} \gamma_{\Gamma_i} \mathbf{v}_{\Sigma_j} \cos \alpha_{\Gamma_j i}, \quad (3.21)$$

and the Gibbs energy of the internal triple line,  $G_{\Sigma_i}$  is given as

$$G_{\Sigma_i} = \int_{\Sigma_i} \gamma_{\Sigma_i} ds_i, \quad (3.22)$$

with  $\gamma_{\Sigma_i}$  is the specific line energy for  $\Sigma_i$ . The rate  $\dot{G}_{\Sigma_i}$  is given as

$$\dot{G}_{\Sigma_i} = \gamma_{\Sigma_i} \mathbf{v}_{\Sigma_i}. \quad (3.23)$$

The rate of total Gibbs energy of the system,  $\dot{G}$  in reference with equation (3.15) becomes

$$\begin{aligned} \dot{G} &= \sum_{\omega_i \in \mathbb{S}} \int_{\omega_i} \mu_i \mathbf{v}_{n,i} dA_i \\ &\quad - \sum_{\Gamma_i \in \mathbb{T}} \int_{\Gamma_i} \left( \sum_{j, \omega_j \in \mathbb{A}_{\Gamma_i}} \gamma_j \cos \alpha_{ij} - \gamma_{\eta_i} - \gamma_{\Gamma_i} K_{\Gamma_i} \right) \mathbf{v}_{\Gamma_i, i} ds_i \\ &\quad - \sum_{P_i \in \mathbb{Q}} \left( \sum_{j, \Gamma_j \in \mathbb{A}_{P_i}} \gamma_{\Gamma_j} \cos \alpha_{\Gamma_j i} - \gamma_{\Sigma_i} \right) \mathbf{v}_{\Sigma_i}, \end{aligned} \quad (3.24)$$

with  $\mu_i = \gamma_i K_i$  is representing the chemical potential in usual meaning of thermodynamics. Equation (3.24) expresses the rate of thermodynamic potential as a product of forces and fluxes. As there is no contribution from the rate term of extensive variables, thus conjugate rate term ( $-\dot{G}$ ) is congruent with the entropy production rate in the irreversible thermodynamics (Fischer et al., 2014).

### 3.5. Dissipation functions.

In this model, the dissipation is considered due to two types of mass transfer processes, coupled with each other under the constraint for the conservation of mass.

- (i) Diffusion along the surface.
- (ii) Diffusion along the triple line channel.

The diffusion along the surface is characterized with the motion of flux  $J_i$ , while the diffusion in the triple line channel is linked with the motion of flux  $j_{\Gamma_i}$ , tangential to the grain boundaries. If  $D_i$ , the diffusion coefficient along the free surface and  $D_{\Gamma_j}$ , the line diffusion coefficient are two material characteristics parameters. We can define the dissipation function as the sum of total diffusion along the surface and total diffusion along the triple line channel. With this, we define a dissipation function in accordance with the constraint given in Fischer et al. (2014) as a quadratic function of fluxes. The total dissipation,  $Q$  is given as

$$Q = \sum_{\omega_i \in \mathbb{S}} \frac{1}{M_i} \int_{\omega_i} |J_i|^2 dA_i + \sum_{\Gamma_i \in \mathbb{T}} \frac{1}{M_{\Gamma_i}} \int_{\Gamma_i} |j_{\Gamma_i}|^2 ds_i. \quad (3.25)$$

Here,  $M_i = (\Omega D_i)/(R_g T)$  and  $M_{\Gamma_i} = (\Omega D_{\Gamma_i})/(R_g T)$  are termed as surface and line mobilities respectively.  $T$  is the absolute temperature,  $R_g$  is the gas constant and  $\Omega$  is molar volume. To this point, we have defined all basic model parameters for thermodynamic extremal principle. The next section engage the variational formulation for modeling the kinetics of the thermal grooves.

### 3.6. TEP and phenomenological equation for grooving.

In accordance with the principle of maximum dissipation for coupled processes in remark (3), the dissipation function,  $Q$  and  $-\dot{G}$  must be in a state of equilibrium. Thus

$$Q + \dot{G} = 0. \quad (3.26)$$

According to Fischer et al. (2014); Hackl et al. (2011), we can add additional constraints in the Lagrange formulation for TEP with additional Lagrange parameters. According to equation (2.44), we include additional constraints for conservation of matter along the surface, conservation of matter along the boundaries, continuity condition along the grain boundary, and contact condition at a quadruple point. With these, the final form of the Lagrange is

$$L = L_1 + L_2 + L_3 \quad (3.27)$$

with

$$L_1 = Q + \lambda_1 (Q + \dot{G}), \quad (3.28a)$$

$$L_2 = \sum_{\omega_i \in \mathbb{S}} \int_{\omega_i} \beta_{1,i} (\mathbf{v}_{n,i} + \nabla_s \cdot \mathbf{J}_i) dA_i + \sum_{\Gamma_i \in \mathbb{T}} \int_{\Gamma_i} \beta_{2,i} \left( \frac{dj_{\Gamma_i}}{ds_i} + \sum_{j, \omega_j \in \mathbb{A}_{\Gamma_i}} \mathbf{J}_j \cdot \mathbf{m}_{\Gamma_{ij}} \right) ds_i, \quad (3.28b)$$

$$L_3 = \sum_{\Gamma_i \in \mathbb{T}} \int_{\Gamma_i} \beta_{3,ij} (\mathbf{v}_{n,j} - \mathbf{v}_{\Gamma_{n,i}} \cdot \sin \alpha_{ij}) ds_i + \sum_{P_i \in \mathbb{Q}} \left[ \sum_{j, \Gamma_j \in \mathbb{A}_{P_i}} \beta_{4,ij} (\mathbf{v}_{\Gamma_{n,j}} - \mathbf{v}_{\Sigma_i} \cdot \sin \alpha_{\Gamma_{ij}})_{P_i} \right]. \quad (3.28c)$$

In above set of equations (3.28a) to (3.28c), description of Lagrange multipliers are

- $\lambda_1$  is the Lagrange multiplier related to the equilibrium relation between the dissipation function  $Q$  and entropy flux  $-\dot{G}$ .
- $\beta_{1,i}$  are functions for each surface  $\omega_i$ , relating the surface motion in  $\mathbf{n}_i$  direction, and flux  $\mathbf{J}_i$ .
- $\beta_{2,i}$  are functions for the balance of fluxes along the boundaries.
- $\beta_{3,ij}$  are functions for the compatibility conditions between the set of surfaces  $\mathbb{A}_{\Gamma_i}$  along the triple line  $\Gamma_i$
- $\beta_{4,ij}$  are constants for compatibility condition between set of triple lines  $\mathbb{A}_{P_i}$  meeting at  $P_i$ .

$\mathbf{J}_i$ ,  $j_{\Gamma_i}$ ,  $\mathbf{v}_{n,i}$ ,  $\mathbf{v}_{\Gamma_{n,i}}$ , and  $\mathbf{v}_{\Sigma_i}$  are the kinetic variables with respect to them variation are carried out. After some simplifications, the stationary conditions of the process states:

on  $\omega_i \in \mathbb{S}$  :

$$\mathbf{J}_i = -M_i \nabla_s \mu_i, \quad (3.29)$$

$$\mathbf{v}_{n,i} + \nabla_s \cdot \mathbf{J}_i = 0; \quad (3.30)$$

equation (3.29) gives the constitutive relation between force and flux along the surface. The rate of flow of matter along the surface is equal to product of gradient of chemical potential and surface diffusion factor,  $M_j$ . So we have a relation similar to the Fick's law of diffusion. The second relation express the condition for the conservation of mass. The steady state conditions along the external triple lines state

on  $\Gamma_i \in \mathbb{T}$  :

$$\mathbf{j}_{\Gamma_i} = -M_{\Gamma_i} \frac{d\mu_{\Gamma_i}}{ds_i}, \quad (3.31)$$

$$\mu_{\Gamma_i} = \mu_i = \mu \quad \text{for } \omega_j \in \mathbb{A}_{\Gamma_i}, \quad (3.32)$$

$$\gamma_{\eta} i + \gamma_{\Gamma_i} K_{\Gamma_i} = \sum_{j, \omega_j \in \mathbb{A}_{\Gamma_i}} \gamma_j \cos \alpha_{ij}. \quad (3.33)$$

Here, equation (3.31) expresses the Fick's law for diffusion along the triple line channel. According to equations (3.29) and (3.31), we have a condition of vanishing flux at constant chemical potential in the system. Equation (3.32) express the condition of constant potential along the grain boundaries. Gamsjäger (2007) also formulated such condition for the migrating sharp interfaces using TEPs. Equation (3.33) defines the condition for energy balance between the thermodynamic forces. Nielsen also discussed the role of triple line energy in the surface evolution in Hoffman and Cahn (1972) but accepted unawareness about the method to measure these forces. Later Gottstein and Shvindlerman (Gottstein et al., 2005; Barrales Mora et al., 2008) discussed conscientiously about the existence and role of the triple line energy in establishing the equilibrium dihedral angle and developing the surface morphology in the polycrystalline. For each quadruple point, we have

at  $P_i \in \mathbb{Q}$  :

$$\sum_{j, \Gamma_j \in \mathbb{A}_{P_i}} S_{\Sigma ij} \mathbf{j}_{\Gamma_j} = 0, \quad S_{\Sigma ij} \pm 1, \quad (3.34)$$

$$\gamma_{\Sigma i} = \sum_{j, \Gamma_j \in \mathbb{A}_{P_i}} \gamma_{\Gamma_j} \cos \alpha_{\Gamma_{ij}}. \quad (3.35)$$

Equation (3.34) is *zero flux* condition at  $P_i$  for steady state, which satisfy the null gradient condition for the chemical potential. Secondly equation (3.35) establishes the relation between triple lines energies at  $P$ . Equations (3.29) to (3.35) are set of coupled differential equations, that cannot be solved using ordinary methods. In the next section, a finite element formulation for solving these set of equations will be discussed.

### 3.7. Finite element model for thermal grooving.

In this section, the finite element model using thermodynamic extremal principle is discussed based on the formulation already done by Hackl et al. (2017). For this modeling process, we start by defining the Lagrange function in the reference configuration and reduce the characteristics parameters by using previously derived relations for extensive variables. As per author knowledge, the thermodynamic extremal principle was not previously used for the finite element modeling.

### Relation between current to reference configuration.

Let us consider the polycrystalline grain structure in the reference configuration. All free surfaces are represented as  $\omega_{i0} \in \mathbb{S}_0$ . Similarly,  $\Gamma_{i0} \in \mathbb{T}_0$ , and  $P_{i0} \in \mathbb{Q}_0$  are sets of triple lines, and quadruple points in the reference configuration respectively. The model is setup in a quasi two-dimensional space with Cartesian coordinates  $(x_1, x_2, x_3)$ , such that the geometry is defined in  $(x_1, x_2)$  plane and  $x_3$  is a continuous displacement field along the geometry. This parameter also represents the displacement of triple lines and quadruple points. With these assumptions, the geometries of the free surfaces  $\omega_i$  are defined as

$$\omega_i = \{(x_1, x_2, x_3) | x_3 = u(x_1, x_2) \forall (x_1, x_2) \in \omega_{i0}\} \quad \text{for } \omega_i \in \mathbb{S}. \quad (3.36)$$

Similarly, for all triple lines  $\Gamma_i$ , we have

$$\Gamma_i = \{(x_1, x_2, x_3) | x_3 = u_{\Gamma_i}(x_1, x_2) \forall (x_1, x_2) \in \Gamma_{i0}\} \quad \text{for } \Gamma_i \in \mathbb{T}. \quad (3.37)$$

It is important to mention here that  $u(x_1, x_2) = u_{\Gamma_i}(x_1, x_2)$ , due to the continuity in displacement field. Thus, here onward a single variable  $u(x_1, x_2)$  defines the displacement field over the complete domain. Now, a relation between small area element  $dA_i$  to  $dA_{i0}$ , a area in reference configuration is given as

$$dA_i = J_i(u) dA_{i0}, \quad \text{with } J_i(u) = \sqrt{1 + |\nabla u|^2}. \quad (3.38)$$

$\nabla u$ , gradient of displacement field is calculated in the reference configuration. A relation between  $ds_i$  and  $ds_{i0}$  for line element  $\Gamma_i$  is

$$ds_i = J_{\Gamma_i}(u) ds_{i0}, \quad \text{with } J_{\Gamma_i}(u) = \sqrt{1 + (u')^2}. \quad (3.39)$$

$u' = du/ds_i$  is derivative in the direction of  $\Gamma_i$ . The rate of the Jacobians  $\dot{J}_i$ , and  $\dot{J}_{\Gamma_i}$  are calculated by taking time derivatives of equation (3.38)<sub>2</sub> and equation (3.39)<sub>2</sub> respectively.

$$\frac{d}{dt} J_i(u) = \frac{\nabla u \cdot \nabla \dot{u}}{J_i(u)}, \quad (3.40)$$

and

$$\frac{d}{dt} J_{\Gamma_i}(u) = \frac{u' \cdot \dot{u}'}{J_{\Gamma_i}(u)}, \quad (3.41)$$

with  $\cdot$  represents a dot product and upper dot,  $\dot{\cdot}$  represents a time derivative. With these basic definitions, we write the total Gibbs energy, equation (3.15) in reference configuration as

$$\begin{aligned} G = & \sum_{\omega_{i0} \in \mathbb{S}_0} \int \gamma_i J_i(u) dA_{i0} + \sum_{\Gamma_{i0} \in \mathbb{T}_0} \int_{\Gamma_{i0}} (\gamma_{\eta_i} u + \gamma_{\Gamma_i} J_{\Gamma_i}(u)) ds_{i0} + \\ & \sum_{P_{i0} \in \mathbb{Q}_0} \gamma_{\Sigma_i} u(P_{i0}), \end{aligned} \quad (3.42)$$

and its rate  $\dot{G}$

$$\begin{aligned} \dot{G} = & \sum_{\omega_{i0} \in \mathbb{S}_0} \int_{\omega_{i0}} \gamma_i \nabla u \cdot \nabla \dot{u} \frac{1}{J_i(u)} dA_{i0} + \\ & \sum_{\Gamma_{i0} \in \mathbb{T}_0} \int_{\Gamma_{i0}} (\gamma_{\eta_i} \dot{u} + \gamma_{\Gamma_i} u' \cdot \dot{u}' \frac{1}{J_{\Gamma_i}(u)}) ds_{i0} + \\ & \sum_{P_{i0} \in \mathbb{Q}_0} \gamma_{\Sigma_i} \dot{u}(P_{i0}). \end{aligned} \quad (3.43)$$

The dissipation function  $Q$ , equation (3.25) in reference configuration is expressed as

$$Q = \sum_{\omega_i \in \mathbb{S}} \frac{1}{M_i} \int_{\omega_{i0}} |J_i|^2 J_i(u) dA_{i0} + \sum_{\Gamma_i \in \mathbb{T}} \frac{1}{M_{\Gamma_i}} \int_{\Gamma_{i0}} |j_{\Gamma_i}|^2 J_{\Gamma_i}(u) ds_{i0}. \quad (3.44)$$

In addition to above, other required relations in reference configuration are

$$v_{n,i} = \frac{1}{J_i(u)} \dot{u}, \quad (3.45)$$

and

$$\frac{dj_{\Gamma_i}}{ds_i} = \frac{1}{J_{\Gamma_i}(u)} j'_{\Gamma_i}. \quad (3.46)$$

Using equation (3.45), relation for conservation of matter along  $\omega_i$ , equation (3.11) becomes

$$\frac{1}{J_i(u)} \dot{u} + \nabla_s \cdot J_i = 0, \quad (3.47)$$

and using equation (3.46), balance of matter along  $\Gamma_i$ , equation (3.13) is written as

$$\frac{1}{J_{\Gamma_i}(u)} j'_{\Gamma_i} + \sum_{j, \omega_j \in \mathbb{A}_{\Gamma_i}} J_j \cdot \mathbf{m}_{\Gamma_{ij}} = 0. \quad (3.48)$$

With the condition of continuity of chemical potential from equation (3.32), the modified Lagrange in reference configurations is

$$\begin{aligned} L_{u,\mu} = & \frac{1}{2} \left( Q + \lambda_1(Q + \dot{G}) \right) \\ & - \sum_{\omega_i \in \mathbb{S}} \int_{\omega_i} \mu \left( \frac{1}{J_i(u)} \dot{u} + \nabla_s \cdot J_i \right) dA_i - \\ & \sum_{\Gamma_i \in \mathbb{T}} \int_{\Gamma_i} \mu \left( \frac{1}{J_{\Gamma_i}(u)} j'_{\Gamma_i} + \sum_{j, \omega_j \in \mathbb{A}_{\Gamma_i}} J_j \cdot \mathbf{m}_{\Gamma_{ij}} \right) ds_i. \end{aligned} \quad (3.49)$$

Applying the Gauss-Theorem and integration by parts for equation (3.49), we have

$$\begin{aligned} L_{u,\mu} = & \frac{1}{2} \left( Q + \lambda_1(Q + \dot{G}) \right) - \\ & \sum_{\omega_i \in \mathbb{S}} \int_{\omega_i} \mu \left( \frac{1}{J_i(u)} \dot{u} \right) dA_i + \sum_{\Gamma_i \in \mathbb{T}} \int_{\Gamma_i} \mu \left( \sum_{j, \omega_j \in \mathbb{A}_{\Gamma_i}} J_j \cdot \mathbf{m}_{\Gamma_{ij}} \right) ds_i + \\ & \int_{\omega_i} \nabla_s \mu \cdot J_i dA_i - \mu \sum_{j, \Gamma_j \in \mathbb{A}_{P_i}} S_{\Sigma_{ij}} j_{\Gamma_j} + \\ & \sum_{\Gamma_i \in \mathbb{T}} \int_{\Gamma_i} \frac{1}{J_{\Gamma_i}(u)} \mu' j_{\Gamma_i} ds_i - \sum_{\Gamma_i \in \mathbb{T}} \int_{\Gamma_i} \mu \left( \sum_{j, \omega_j \in \mathbb{A}_{\Gamma_i}} J_j \cdot \mathbf{m}_{\Gamma_{ij}} \right) ds_i \end{aligned} \quad (3.50)$$

In equation (3.50),  $\mu$  is introduced as the Lagrange parameter due to the fact that it is continuous function and factor of 1/2 is used to simplify the calculations in further steps. Secondly, if we

go through the previous variational derivation, we can use  $\lambda_1 = -2^2$ . The remaining terms after simplification and using equations (3.38) and (3.39) give

$$\begin{aligned} L_{u,\mu} = & -\dot{G} - \frac{1}{2}Q \\ & - \sum_{\omega_{i0} \in \mathbb{S}_0} \int_{\omega_{i0}} (\mu \dot{u} - J_i(u) \nabla_s \mu \cdot \mathbf{J}_i) dA_{i0} \\ & + \sum_{\Gamma_{i0} \in \mathbb{T}_0} \int_{\Gamma_{i0}} \mu' j_{\Gamma_i} ds_{i0}. \end{aligned} \quad (3.51)$$

Equation (3.51) has  $\mu$ ,  $J_i$ ,  $j_{\Gamma_i}$ , and  $\dot{u}$  as kinetic variables. We can eliminate the fluxes,  $J_i$  and  $j_{\Gamma_i}$  using relative definitions in reference configuration. Thus combining equations (3.43), (3.44) and (3.51), and using respective relation for both fluxes, we get

$$\begin{aligned} L_{u,\mu} = & - \sum_{\omega_{i0} \in \mathbb{S}_0} \int_{\omega_{i0}} \gamma_i \nabla u \cdot \nabla \dot{u} \frac{1}{J_i(u)} dA_{i0} \\ & - \sum_{\Gamma_{i0} \in \mathbb{T}_0} \int_{\Gamma_{i0}} (\gamma_{\eta_i} \dot{u} + \gamma_{\Gamma_i} u' \cdot \dot{u}' \frac{1}{J_{\Gamma_i}(u)}) ds_{i0} - \sum_{P_{i0} \in \mathbb{Q}_0} \gamma_{\Sigma_i} \dot{u}(P_{i0}) \\ & + \sum_{\omega_{i0} \in \mathbb{S}_0} \frac{1}{2} \int_{\omega_{i0}} M_i |\nabla_s \mu|^2 J_i(u) dA_{i0} + \sum_{\Gamma_{i0} \in \mathbb{T}_0} \frac{1}{2} \int_{\Gamma_{i0}} M_{\Gamma_i} |\mu'|^2 \frac{1}{J_{\Gamma_i}(u)} ds_{i0} \\ & - \sum_{\omega_{i0} \in \mathbb{S}_0} \int_{\omega_{i0}} \mu \dot{u} dA_{i0}. \end{aligned} \quad (3.52)$$

$L_{u,\mu}$  is now function of  $\dot{u}$  and  $\mu$  only. Calculation of  $\nabla_s \mu$  can be transformed to alternative, mathematically simple relation as

$$\nabla_s \mu = \nabla \mu - (\mathbf{n}_i \cdot \nabla \mu) \mathbf{n}_i, \quad (3.53)$$

with  $\nabla \mu = (\mu_x, \mu_y, 0)$ , is a vector holding derivative of  $\mu$  along the planer axis.  $\mathbf{n}_i$  is surface normal vector, can be calculated using simple calculus (Struik, 1961)

$$\mathbf{n}_i^T = \frac{1}{J_i(u)} (-u_x, -u_y, 1), \quad (3.54)$$

with  $u_x$  and  $u_y$  are derivatives with respect to principle axis. Now using equation (3.53) with equation (3.54) for  $|\nabla_s \mu|^2$  gives

$$|\nabla_s \mu|^2 = \frac{1}{J_i(u)} \nabla \mu \cdot \mathbf{K}(u) \cdot \nabla \mu, \quad (3.55)$$

with  $\mathbf{K}(u)$  is the curvature tensor, and is expressed as

$$\mathbf{K}(u) = \begin{pmatrix} 1 + u_y^2 & -u_x u_y \\ -u_x u_y & 1 + u_x^2 \end{pmatrix}. \quad (3.56)$$

<sup>2</sup>The value is derived in equation 54 in Hackl et al. (2017)

Combining equations (3.52) and (3.55), gives

$$\begin{aligned}
L_{u,\mu} = & - \sum_{\omega_{i0} \in \mathbb{S}_0} \int_{\omega_{i0}} \gamma_i \nabla u \cdot \nabla \dot{u} \frac{1}{J_i(u)} dA_{i0} \\
& - \sum_{\Gamma_{i0} \in \mathbb{T}_0} \int_{\Gamma_{i0}} \left( \gamma_{\eta_i} \dot{u} + \gamma_{\Gamma_i} u' \cdot \dot{u}' \frac{1}{J_{\Gamma_i}(u)} \right) ds_{i0} - \sum_{P_{i0} \in \mathbb{Q}_0} \gamma_{\Sigma_i} \dot{u}(P_{i0}) \\
& + \sum_{\omega_{i0} \in \mathbb{S}_0} \frac{1}{2} \int_{\omega_{i0}} M_i \nabla \mu \cdot \mathbf{K}(u) \cdot \nabla \mu dA_{i0} + \sum_{\Gamma_{i0} \in \mathbb{T}_0} \frac{1}{2} \int_{\Gamma_{i0}} M_{\Gamma_i} |\mu'|^2 \frac{1}{J_{\Gamma_i}(u)} ds_{i0} \\
& - \sum_{\omega_{i0} \in \mathbb{S}_0} \int_{\omega_{i0}} \mu \dot{u} dA_{i0} \tag{3.57}
\end{aligned}$$

Now, variation of equation (3.57) with respect to  $\dot{u}$  gives

$$\begin{aligned}
& - \sum_{\omega_{i0} \in \mathbb{S}_0} \int_{\omega_{i0}} \gamma_i \nabla u \cdot \nabla \delta \dot{u} \frac{1}{J_i(u)} dA_{i0} \\
& - \sum_{\Gamma_{i0} \in \mathbb{T}_0} \int_{\Gamma_{i0}} \left( \gamma_{\eta_i} \delta \dot{u} + \gamma_{\Gamma_i} u' \cdot \delta \dot{u}' \frac{1}{J_{\Gamma_i}(u)} \right) ds_{i0} \\
& - \sum_{P_{i0} \in \mathbb{Q}_0} \gamma_{\Sigma_i} \delta \dot{u}(P_{i0}) \\
& - \sum_{\omega_{i0} \in \mathbb{S}_0} \int_{\omega_{i0}} \mu \delta \dot{u} dA_{i0} = 0. \quad \forall \delta \dot{u}. \tag{3.58}
\end{aligned}$$

Equation (3.58) gives the condition for balance of thermodynamic forces, which are in this case, Gibbs energies of the geometrical elements. Now variation of equation (3.57) with respect to  $\mu$  gives

$$\begin{aligned}
& \sum_{\omega_{i0} \in \mathbb{S}_0} \int_{\omega_{i0}} M_i \nabla \mu \cdot \mathbf{K}(u) \cdot \nabla \delta \mu \frac{1}{J_i(u)} dA_{i0} + \\
& \sum_{\Gamma_{i0} \in \mathbb{T}_0} \int_{\Gamma_{i0}} M_{\Gamma_i} \mu' \delta \mu' \frac{1}{J_{\Gamma_i}(u)} ds_{i0} - \\
& \sum_{\omega_{i0} \in \mathbb{S}_0} \int_{\omega_{i0}} \delta \mu \dot{u} dA_{i0} = 0 \quad \forall \delta \mu \tag{3.59}
\end{aligned}$$

Equation (3.59) gives steady state condition of fluxes in the system. The kinetic parameter  $\dot{u}$  in equation (3.59) is approximated as

$$\dot{u} = \frac{u^{n+1} - u^n}{\Delta t}. \tag{3.60}$$

Here,  $\Delta t = t^{n+1} - t^n$  is used. We use semi implicit scheme for numerical experimentations in equations (3.58) and (3.59). In this configurations, all Jacobian's and normal vectors are calculated at current time  $t^n$ , whereas  $u$  and  $\mu$  are calculated at  $t^{n+1}$ . Substituting equation (3.60) for

steady state conditions gives

$$\begin{aligned}
& - \sum_{\omega_{i0} \in \mathbb{S}_0} \int_{\omega_{i0}} \gamma_i \nabla u^{n+1} \cdot \nabla \delta u \frac{1}{J_i(u^n)} dA_{i0} \\
& - \sum_{\Gamma_{i0} \in \mathbb{T}_0} \int_{\Gamma_{i0}} (\gamma_{\Gamma_i} \delta u + \gamma_{\Gamma_i} (u^{n+1})' \cdot \delta u' \frac{1}{J_{\Gamma_i}(u^n)}) ds_{i0} \\
& - \sum_{P_{i0} \in \mathbb{Q}_0} \gamma_{\Sigma_i} \delta u (P_{i0}) \\
& - \sum_{\omega_{i0} \in \mathbb{S}_0} \int_{\omega_{i0}} \mu^{n+1} \delta u dA_{i0} = 0, \quad \forall \delta u.
\end{aligned} \tag{3.61}$$

and

$$\begin{aligned}
& \sum_{\omega_{i0} \in \mathbb{S}_0} \int_{\omega_{i0}} M_i \nabla \mu^{n+1} \cdot \mathbf{K}(u^n) \cdot \nabla \delta \mu \frac{1}{J_i(u^n)} dA_{i0} + \\
& \sum_{\Gamma_{i0} \in \mathbb{T}_0} \int_{\Gamma_{i0}} M_{\Gamma_i} (\mu^{n+1})' \delta \mu' \frac{1}{J_{\Gamma_i}(u^n)} ds_{i0} \\
& \sum_{\omega_{i0} \in \mathbb{S}_0} \frac{1}{\Delta t} \int_{\omega_{i0}} \delta \mu (u^{n+1} - u^n) dA_{i0} = 0 \quad \forall \delta \mu
\end{aligned} \tag{3.62}$$

Now for the finite element space, we introduce  $\phi$ , set of shape function in  $(x_1, x_2)$  plane given as

$$\phi(x_1, x_2) = \begin{matrix} & N_1 & N_1 & N_2 & N_2 & N_3 & N_3 & N_4 & & N_m \\ x_1 & \left( \begin{array}{cccccccc} \phi_1 & 0 & \phi_2 & 0 & \phi_3 & 0 & \phi_4 & \cdots & 0 \\ 0 & \phi_1 & 0 & \phi_2 & 0 & \phi_3 & 0 & \cdots & \phi_m \end{array} \right), & \end{matrix} \tag{3.63}$$

with  $m$  is the total number of the nodes of each element in discretized space. For variables  $u^n$ ,  $u^{n+1}$ ,  $\delta u$ ,  $\delta \mu$ , and  $\mu^{n+1}$  approximated value with shapes functions are

$$f(x_1, x_2) = \sum_{I \rightarrow 1}^m \hat{f}_I \phi_I(x_1, x_2) = \hat{\mathbf{f}} \cdot \phi, \tag{3.64}$$

where  $\hat{\mathbf{f}} = \hat{f}$  is vector of state variables at each node in finite element approximation. Substituting equation (3.64) in the variational forms, equations (3.61) and (3.62) for the respective

variables. We have discretized form in the finite element space as

$$\begin{aligned}
& -\delta\hat{u} \left( \sum_{\omega_{i0} \in \mathbb{S}_0} \int_{\omega_{i0}} \gamma_i \nabla \phi_I \cdot \nabla \phi_J \frac{1}{J_i(u^n)} dA_{i0} \right) \hat{u}^{n+1} \\
& -\delta\hat{u} \left( \sum_{\Gamma_{i0} \in \mathbb{T}_0} \int_{\Gamma_{i0}} \left( \gamma_{\Gamma_i} \phi_I' \phi_J' \frac{1}{J_{\Gamma_i}(u^n)} \right) ds_{i0} \right) \hat{u}^{n+1} \\
& -\delta\hat{u} \left( \sum_{\omega_{i0} \in \mathbb{S}_0} \int_{\omega_{i0}} \phi_I \phi_J dA_{i0} \right) \hat{\mu}^{n+1} = \\
& \delta\hat{u} \left( \sum_{\Gamma_{i0} \in \mathbb{T}_0} \int_{\Gamma_{i0}} \gamma_{\eta_i} \phi_I ds_{i0} + \sum_{P_{i0} \in \mathbb{Q}_0} \gamma_{\Sigma_i} \phi_I(P_{i0}) \right) \forall \delta\hat{u}. \tag{3.65}
\end{aligned}$$

and

$$\begin{aligned}
& \delta\hat{\mu} \left( \sum_{\omega_{i0} \in \mathbb{S}_0} \Delta t \int_{\omega_{i0}} M_i \nabla \phi_I \cdot \mathbf{K}(u^n) \cdot \nabla \phi_J \frac{1}{J_i(u^n)} dA_{i0} \right) \hat{\mu}^{n+1} + \\
& \delta\hat{\mu} \left( \sum_{\Gamma_{i0} \in \mathbb{T}_0} \Delta t \int_{\Gamma_{i0}} M_{\Gamma_i} \phi_I' \phi_J' \frac{1}{J_{\Gamma_i}(u^n)} ds_{i0} \right) \hat{\mu}^{n+1} - \\
& \delta\hat{\mu} \left( \sum_{\omega_{i0} \in \mathbb{S}_0} \int_{\omega_{i0}} \phi_I, \phi_J dA_{i0} \right) \hat{u}^{n+1} = \\
& -\delta\hat{\mu} \left( \sum_{\omega_{i0} \in \mathbb{S}_0} \int_{\omega_{i0}} \phi_I \phi_J dA_{i0} \right) \cdot \hat{u}^n \quad \forall \delta\hat{\mu} \tag{3.66}
\end{aligned}$$

Rearranging equations (3.65) and (3.66) in suitable form for numerical implementation gives

$$\mathbf{K}_{IJ}^n = \begin{pmatrix} \mathbf{K}_{AA}^n & \mathbf{K}_{AB}^n \\ \mathbf{K}_{BA}^n & \mathbf{K}_{BB}^n \end{pmatrix}, \tag{3.67}$$

with

$$\mathbf{K}_{AA}^n = \begin{pmatrix} \sum_{\omega_{i0} \in \mathbb{S}_0} \int_{\omega_{i0}} \gamma_i \nabla \phi_I \cdot \nabla \phi_J \frac{1}{J_i(u^n)} dA_{i0} \\ - \sum_{\Gamma_{i0} \in \mathbb{T}_0} \int_{\Gamma_{i0}} \gamma_{\Gamma_i} \phi_I' \phi_J' \frac{1}{J_{\Gamma_i}(u^n)} ds_{i0} \end{pmatrix} \tag{3.68}$$

$$\mathbf{K}_{AB}^n = \mathbf{K}_{BA}^n = \sum_{\omega_{i0} \in \mathbb{S}_0} \int_{\omega_{i0}} \phi_I, \phi_J dA_{i0} \tag{3.69}$$

$$\mathbf{K}_{BB}^n = \Delta t \begin{pmatrix} \sum_{\omega_{i0} \in \mathbb{S}_0} \int_{\omega_{i0}} M_i \nabla \phi_I \cdot \mathbf{K}(u^n) \cdot \nabla \phi_J \frac{1}{J_i(u^n)} dA_{i0} \\ + \sum_{\Gamma_{i0} \in \mathbb{T}_0} \int_{\Gamma_{i0}} M_{\Gamma_i} \phi_I' \phi_J' \frac{1}{J_{\Gamma_i}(u^n)} ds_{i0} \end{pmatrix} \tag{3.70}$$

and

$$\mathbf{U}^{n+1} = \begin{pmatrix} \hat{\mathbf{u}}^{n+1} \\ \hat{\boldsymbol{\mu}}^{n+1} \end{pmatrix}, \quad (3.71)$$

and

$$\mathbf{P}^n = \begin{pmatrix} \sum_{\Gamma_{i0} \in \mathbb{T}_0} \int_{\Gamma_{i0}} \gamma_{\eta_i} \phi_I \, ds_{i0} + \sum_{P_{i0} \in \mathbb{Q}_0} \gamma_{\Sigma_i} \phi_I (P_{i0}) \\ - \left( \sum_{\omega_{i0} \in \mathbb{S}_0} \int_{\omega_{i0}} \phi_I \phi_J \, dA_{i0} \right) \cdot \hat{\mathbf{u}}^n \end{pmatrix}. \quad (3.72)$$

Here  $\mathbf{K}_{IJ}^n$  is global stiffness matrix, with all Jacobin calculated at  $t^n$ ,  $\mathbf{P}^n$  is Global load vector and  $\mathbf{U}^{n+1}$  is vector of state functions. The equation with global stiffness matrix reads

$$\mathbf{K}_{IJ}^n \cdot \mathbf{U}^{n+1} = \mathbf{P}^n \quad (3.73)$$

These set of equations are implemented in open source finite element code in JAVA for numerical experimentation. Results of different parametric studies will be discussed in the next chapters.

### 3.8. Dimensionless formulation.

The dimensionless formulation is helpful in understanding the evolution kinetics in relatively easy way. It also make it convenient to identify the parameters influencing the kinetics of the process.

For our thermal grooving model, we have two process parameters,  $u$  and  $\mu$ . If all material parameters are constant within the geometrical elements. Then, the displacement field is written as

$$u = f(a, b, t, \gamma, \gamma_\eta, \gamma_{\Gamma_i}, \gamma_{\Sigma_i}, M_i, M_{\Gamma_i}). \quad (3.74)$$

For our formulation of surface energy,  $\gamma_i = \gamma_0 = \gamma$ , is constant factor representing isotropic surface energy and  $M_i = M$  is constant mobility factor for all grains in the polycrystalline. This enable us to write equation (3.74) in the dimensionless state as

$$\bar{u} = \bar{f}(\bar{b}, \bar{t}, \bar{\gamma}_{\eta_i}, \bar{\gamma}_{\Gamma_i}, \bar{\gamma}_{\Sigma_i}, \bar{M}_\Gamma), \quad (3.75)$$

with following definitions:

$$\begin{aligned} \bar{u} = \frac{u}{a}, \quad \bar{b} = \frac{b}{a}, \quad \bar{t} = \frac{M\gamma}{a^4} t, \quad \bar{\gamma}_{\eta_i} = \frac{\eta_i}{\gamma}, \\ \bar{\gamma}_{\Gamma_i} = \frac{\Gamma_i}{\gamma a}, \quad \bar{\gamma}_{\Sigma_i} = \frac{\gamma_{\Sigma_i}}{\gamma a}, \quad \bar{M}_\Gamma = \frac{M_{\Gamma_i}}{Ma}. \end{aligned} \quad (3.76)$$

Similarly, the chemical potential the dimensionless state is define as

$$\bar{\mu} = \frac{a}{\gamma} \mu \quad (3.77)$$

We will express our results in the dimensionless space for the morphological evolution and growth kinetics.

## 4. The role of grain boundary energy

In chapter (3), we explained our model for the thermal grooving along the free surface and its finite element formulation for numerical simulations. The thermodynamics forces, grain boundary and surface energies have prime role in establishing the equilibrium dihedral angles along the grooves. It was observed that grain boundary energy varies with the boundary plane inclination and misorientation between the neighboring grains. The changes in the grain boundary energy effect the materials behavior including intergranular brittleness and creep. Any variation in these forces also influence the groove shapes and dissipation rates. The objective of this work is to study the effect of change in grain boundary energy on the groove growth kinetics and morphology of the polycrystalline.

### 4.1. Introduction.

A grain boundary separates the two regions of different orientations from the same crystals structure. The grain boundary energies are function of boundary inclination and grains misorientation. In two dimensions, we need four parameters, misorientation between two grains  $\varphi$ , spatial orientation of grain boundary plane  $\Psi$ , and translation vector  $\mathbf{t}(t_1, t_2)$  of two crystals for its identification. Whereas in three dimensions, we need eight parameters, three Euler angles ( $\varphi_1, \Phi, \varphi_2$ ) for orientation relationship between grains, two parameters for grain boundary plane using a normal vector  $\mathbf{n}$ , and a translation vector  $\mathbf{t}(t_1, t_2, t_3)$  to distinguish a grain boundary. The properties, in particular the energy and the mobility of a grain boundary depend upon these parameters. Among the eight parameters, five of them, orientation relationship and spatial orientation of the boundary plane are influenced by the external processes during the production where are translation vector is evaluated during the crystals growth or grain boundary motion for achieving the state of minimum energy (chap. 2 in [Gottstein and Shvindlerman, 2009](#)).

We usually classify the grain boundaries into two general types, based on the rotation angle with constant crystallographic orientation of the boundary plane. If grain boundary and rotation axis are parallel, the grain boundary is classified as tilt grain boundary. In contrast to it, if the grain boundary plane is perpendicular to the rotation axis, it is referred as twist grain boundary. Based on misorientation angles between the grains, we have different set of grain boundary energies for different tilt angles. In order to find the energies for unknown set of Euler angle, [Sutton and Balluffi \(2009, sec. 5 therein\)](#) established a linear interpolation for tilt and twist set of grain boundary energies using experimental measured set of data from [Wolf \(1990a,b,c\)](#). According to these findings, Grain boundaries with  $\{111\}$  orientations have minimum energy.

There are different methods for measuring the grain boundary energies using the experimental setups but these data sets are limited due to difficulty in measuring the accurate interfacial energies and steady state conditions ([Amouyal et al., 2005](#); [Olmsted et al., 2009](#); [Ratanaphan et al., 2015](#)). Alternative to these, there are numerical methods to calculate the grain boundary energies using computational schemes. These results have good correlation with experimentally calculated grain boundary energies ([Saylor and Rohrer, 2004](#); [Rohrer et al., 2010](#); [Holm](#)

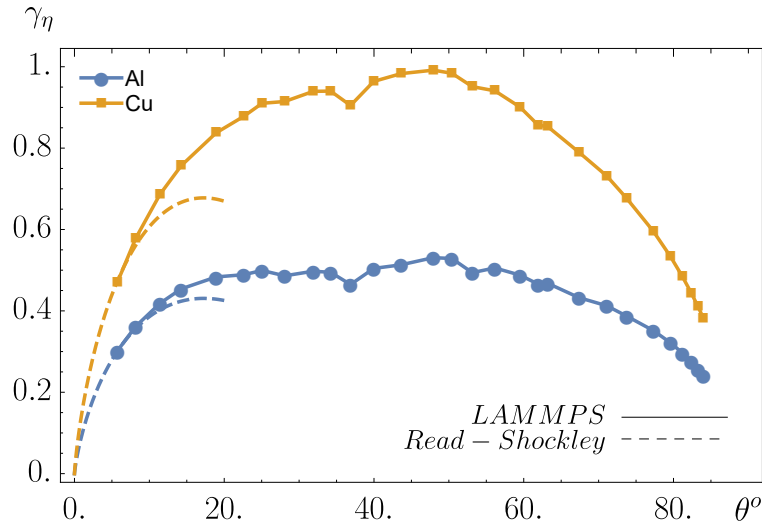


Figure 4.1.: A comparison between **Read and Shockley** model and computed grain boundary energies in LAMMPS for  $\langle 1\ 0\ 0 \rangle$  tilt grain boundaries in Cu. and Al. The analytical model provide good approximation up to  $15^\circ$  tilt angle.

et al., 2011; Rohrer, 2011b; Bulatov et al., 2013). There is no single method that expresses the excellent correlation between the experimental and computationally calculated grain boundary energies for all materials. **Read and Shockley** used dislocation based model to calculate the grain boundary energies. This formulation is

$$\gamma_\eta = E_0\theta(A - \ln \theta), \quad (4.1)$$

with

$$E_0 = \frac{\mu b}{4\pi(1 - \nu)}, \quad \text{and} \quad A = \frac{4\pi(1 - \nu)E_c}{\mu b^2} - \ln \alpha. \quad (4.2)$$

$E_0$  is function of only elastic parameters with  $\mu$  as shear modulus and  $\nu$  is a Poisson ratio and  $b$  is a radius of the dislocation core. Additional parameter  $A$  is the function of dislocation core energy,  $E_c$ . The principle parameter in equation (4.1) is misorientation angle  $\theta$ . This model is widely accepted as providing a good prediction of energies for the low angle grain boundaries. Figure (4.1) shows the grain boundary energy plot using equation (4.1) for Al and Cu. This formulation gives good approximation for  $\theta < 15^\circ$ . For grain boundaries with  $\theta \geq 15^\circ$ , the model predicts decrease in the grain boundary energies but both in experiments, and computed grain boundary energies, there is no such decrease. Thus this dislocation based model cannot predict high angle grain boundary energies. **Wolf (1989); Shekhawat et al. (2016)** generalized the Read and Shockley model, by replacing  $\theta$  with  $\sin \theta$ . These extended models predict good approximation of the energy for high angle grain boundary. There does not appear any theoretical justification for this replacement (**Sutton and Balluffi, 2009**). **Weins et al. (1969); Ashby et al. (1978); Gleiter (1982)** hard sphere models calculate the grain boundary energies based on the assumption that all grain boundaries (symmetric, and asymmetric tilt and twist grain boundaries) are made up of eight fundamental polyhedrons. Thus, the grain boundary energy is summation of assigned energies for each polyhedron constructing the particular boundary in the polycrystalline structure. **Wolf** models for zero-temperature energies, (**Wolf, 1989, 1990a,b**) were based on the atomistic simulations for broad crystallographic domains. They showed that

grain boundary energies strongly depends on the misorientation between the grains. It was suggested that symmetrical grain boundaries have higher energies than asymmetrical grain boundaries (Wolf, 1990c). Bulatov et al. (2014) calculated the grain boundary energies only for f.c.c. materials. They fitted the data in completed five dimensions using a function of 43 numerical parameters.

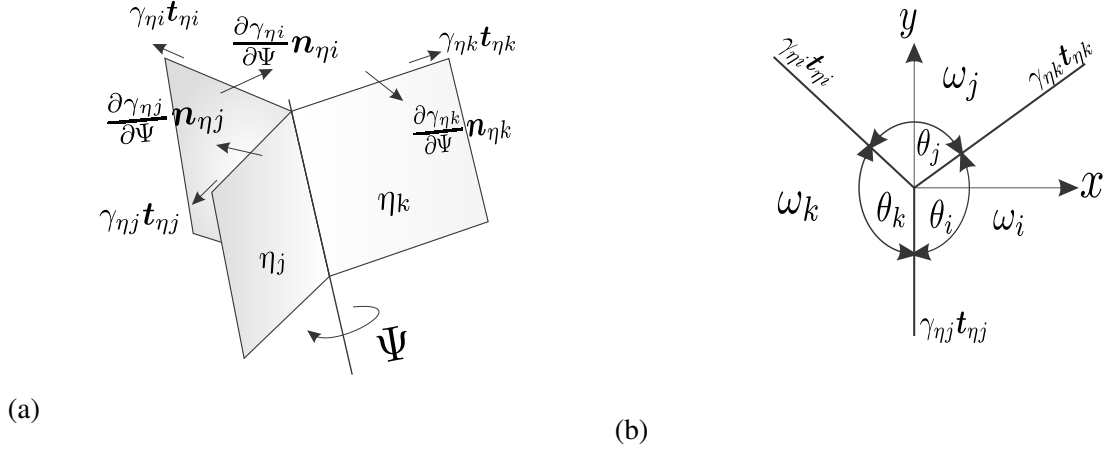


Figure 4.2.: Illustration of balance of the boundary energies at the triple junction. It explains the quantities used in equations (4.3) and (4.4). (a) Contribution of grain boundary energies in normal, ( $\mathbf{n}$ ) and tangential, ( $\mathbf{t}_{\eta_j}$ ) directions in accordance with the **Herring** relation. (b) Balance of grain boundary energies in the tangential directions for the cases, when torque terms contributions are too small.

In addition to these, there are some other models that calculate the grain boundary energy distributions from the geometries of the triple junctions in the polycrystalline. These models are based on the criterion of a local equilibrium. Rohrer et al. (Barmak et al., 2006; Saylor and Rohrer, 2001; Holm et al., 2011; Ratanaphan et al., 2015) calculated the grain boundary distribution in different materials from the constructions of triple junctions as a function of five macroscopic state parameters. Similarly Adams et al. (1998); Archibald et al. (2004) used statistical multi-scale approach to calculate the grain boundaries energies distribution from the shapes of thermal grooves. They used two different trial functions to approximate the relative grain boundary energies over the range of distribution angles. We find it an optimum method to calculate relative grain boundary energies under the assumption of constant surface energy. We will use an disorientation dependent ansatz function. The limitation and application of this method will be discussed in the next section.

## 4.2. Grain boundary energy using an ansatz function.

In the polycrystalline, triple junctions are in the state of equilibrium. The grain boundary energies in tangential direction, and torque terms due to the anisotropy acting in the normal direction to its plane are balancing each other. The equilibrium condition for each grain boundary junction is expressed by the **Herring**'s relation.

$$\sum_{i=1}^3 (\gamma_{\eta_i} \mathbf{t}_{\eta_i} + \frac{\partial \gamma_{\eta_i}}{\partial \Psi} \mathbf{n}_{\eta_i}) = \mathbf{0}. \quad (4.3)$$

Figure (4.2a) shows vector balance of forces at the triple junction. In case of moving boundaries, the interface with a higher energy pulls itself in the tangential direction and ultimately break it down into two low energy interfaces. Contrary to this,  $\partial\gamma_{\eta_i}/\partial\Psi$  is the contribution of torque due to the anisotropy in grain boundary energy. This factor defines the capability of the grain boundary to rotate about the central axis  $\Psi$ . In case of anisotropic grain boundaries, the system lowers its energy either by twisting or in some cases by forming the serrated grain boundaries of lower energy in the particular orientation. Equation (4.3) stands for the balance of forces at the triple junction. In our model, we have no dissipation due to the motion of the triple junction and there is no bulk or interface diffusion. Thus the planar grain boundaries remain flat during the thermal grooving process. Hence, the contribution due to the torque term in the Herring's relation can be neglected, and we only need an expression for the balance of forces in the tangential direction. Under these circumstances, the balance condition is expressed by a Young's relation at each triple point in the domain.

$$\frac{\gamma_{\eta_i}}{\sin \theta_i} = \frac{\gamma_{\eta_j}}{\sin \theta_j} = \frac{\gamma_{\eta_k}}{\sin \theta_k}, \quad (4.4)$$

with  $\theta_i$  is the angle opposite to  $\gamma_{\eta_i}$ . Figure (4.2b) shows the state of equilibrium at the triple junction with negligible torque. Now, we have three forces that establish the state of an equilibrium. We will use an ansatz function to find the grain boundary energies as a function of misorientation angle. The ansatz function reads

$$\gamma_{\eta_i} = A + B \sin(\psi_{jk}), \quad (4.5)$$

with  $A$  and  $B$  are scalar parameters and  $\psi_{jk}$  is the minimum misorientation angle between  $\omega_j$  and  $\omega_k$  lattice without any consideration for the misorientation of grains axis. Wolf has used similar expression with the concept of burger vector and dislocation core energy. He has calculated the grain boundary energies over the complete range of misorientation for different types of grain boundaries in different materials (Sutton and Balluffi, 2009).

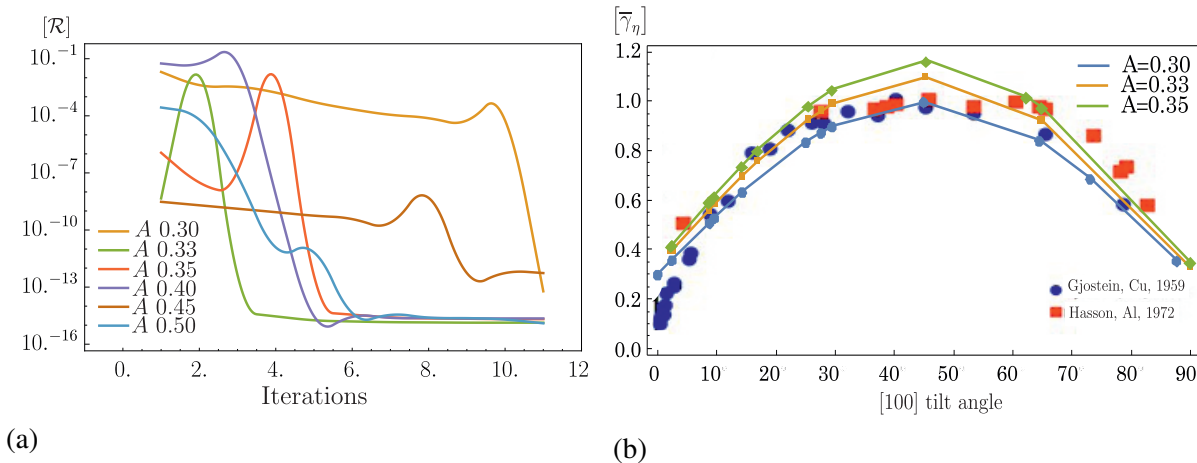


Figure 4.3.: Residuals and relative grain boundary energies calculated for four grains geometry, Fig. (4.4). (a) Evolution of residuals  $\mathcal{R}$  with different values of  $A$  in the energy potential using the condition for negligible torque at each  $P_i$ , equation (4.4). (b) Grain boundary energies distribution fitted to experimental data for relative grain boundary energies, Rohrer (2011a, see fig.8a therein). For Cu.,  $A = 0.30$ , and for Al.,  $A = 0.35$ , we have good fit for  $[1\ 0\ 0]$  tilt grain boundaries.

With this, we write grain boundary energy potential for the set of grain boundaries in the polycrystalline. This matrix has two set of equation for each triple point, and grain boundary ansatz

function. In this model, the surface energy is assumed isotropic for all surfaces. So, we have a constant factor  $\gamma_i = \gamma$  for every boundary,  $\eta_i$ . Equation (4.5) can be written as a multiple of constant surface energy. Thus we have the modified form as

$$\gamma_{\eta_i} = \gamma(A + B \sin(\psi_{jk})). \quad (4.6)$$

For our four grains periodic model (Fig. (4.4)), we have 10 grain boundaries and 8 junctions. Consequently, we have 28 set of equations with 10 unknown energies. This over determine system of equations can be solved using least square method with minimizing the residual function. In order to have a positive value of  $\gamma_{\eta_i}$ , we impose an additional constraint between two scalar parameters. In these calculations, we use  $A - 3B = 0$ . For each value of  $A$ , we have a set of energies with minimum residual. These sets can be correlated with the grain boundary energies of different materials at constant boundary inclination and different misorientations. Figure (4.3a) shows the residuals for limiting values of  $A$ . According to Wolf (1990c), we can fit experimentally observed grain boundary energies with different set of parameters. For  $A = 0.30$  and  $A = 0.35$ , our calculated grain boundary energies are congruent with the experimental results for  $\{100\}$  oriented grains for Al and Cu taken from the literature (see Fig. (4.3b)).

### 4.3. Four grains periodic RVE.

#### 4.3.1. Model geometry and kinetics parameters.

In this section we will explain about the geometry of our model for this particular problem. We will use four grains periodic RVE. This structure is created using Voronoi tessellation with random distribution of points. This method has been used for generating RVE for finite element simulations in materials sciences and also in the phase-field modelings (see Barbe and Quey, 2011; Barrales Mora et al., 2012; Głowiński, 2015). This modeling approach provides us realistic physical representation of the microstructures.

Periodic grains structure shown in Fig. (4.4) includes four irregular hexagonal grains. Each grain is made up of unequal sides. The central grain,  $\omega_1$  is alternatively surrounded by other three grains  $\omega_2$ ,  $\omega_3$ , and  $\omega_4$ . This periodic RVE incorporate eight quadruple points and twelve grain boundaries. The domain is discretized with regular quadrilateral elements. The meshing is done in such a way that no element intersect with the grain boundaries. Also, the nodal distribution along the opposite sides are congruent. This discretization is convenient in apply the periodic boundary conditions without any additional linearization. We have total 5244 nodes with 5688 quadrilateral elements. In the next sections, we present the results for thermal grooving for different values of grain boundary energies and varying relative diffusion coefficient  $\bar{M}_\Gamma$ .

#### 4.3.2. Simulation results and discussion.

##### 4.3.2.1. Anisotropic grain boundary energy with $A = 0.30$ .

After setting up the model with quadrilateral mesh, we applied periodic boundary conditions for the state variables  $\bar{u}$  and  $\bar{\mu}$ . The value of surface energy was assumed constant and isotropic.

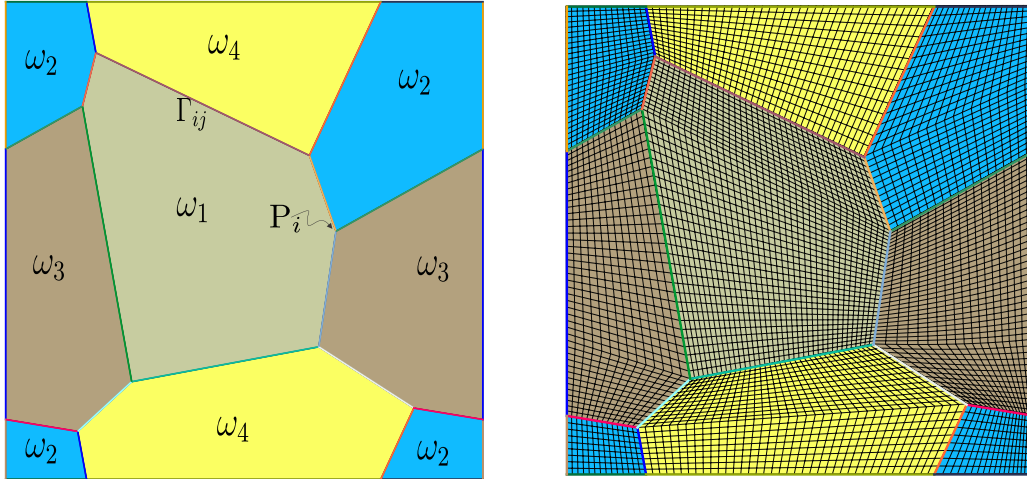


Figure 4.4.: Four grains periodic RVE with irregular hexagons. The model is created using Voronoi tessellations for a unit dimensions. RVE includes eight quadruple points  $P_i$  and twelve boundaries  $\Gamma_{ij}$ . On the right, a discretized domain of total 5688 quadrilateral. There are equal number of boundaries on the opposite sides. This discretization is helpful in engaging the periodic boundary condition.

Other parameters, relative internal and external triple line energies were kept constant and have same numerical values as in Hackl et al. (2017). With these numerical settings, we started our simulations with exponential time stepping due to the fact that diffusion is faster in the beginning and slows down with the proceeding time. In all these finite element simulations, linear shape function was used for both state parameters.

We started with a flat surface. Initially all quadruple points and grain boundaries were at high chemical potential. We ignored some initial steps and consider them as settling time. During these steps, the flux vectors orientated them in the appropriate directions in accordance with equations (3.29) and (3.31). Figure (4.5) shows evolution of  $\bar{u}$  and  $\bar{\mu}$  fields along the free surface at different instance of  $\bar{t}^n$ . The formations of grooves started at the quadruple points and along the triple lines. These sites have high chemical potential in comparison with the rest of the RVE. Directions of the fluxes were determined by the vector functions  $-\nabla_s \mu$  along the surfaces and  $d\mu_\Gamma/ds$  along the triple lines. Additionally, the fluxes magnitudes were influenced by the diffusion coefficients for two dissipation processes. We observed formation of pits with varying depths at quadruple points. The groove profiles along the grain boundaries exhibited different growth rates. As diffusion coefficients were constant, thus only controlling parameter was relative grain boundary energy. As system proceeded towards the state of an equilibrium, we had condition of vanishing fluxes with constant chemical potential over the entire domain ( see Fig. (4.5h)).

From these observations, it is important to discuss the evolution along different cross sections in the polycrystalline. Figure (4.6) shows  $\bar{u}$  along chosen cross sections with the progressing time  $\bar{t}^n$ . Morphological evolutions along  $\overline{AA}$  are shown in figures (4.6a) and (4.6b). We have groove profiles with exponential growth kinetics. The process started with the formation of diffusional humps along the grain boundaries. The grooves depths along the triple lines, increased with the progressing time. There was also widening in the groove width with increasing depth. Similarly, figures (4.6c) and (4.6d) show evolutions of surface along  $\overline{BB}$ . This cross section includes a quadruple point. It was observed in many experiments in the literature that growth of the pit

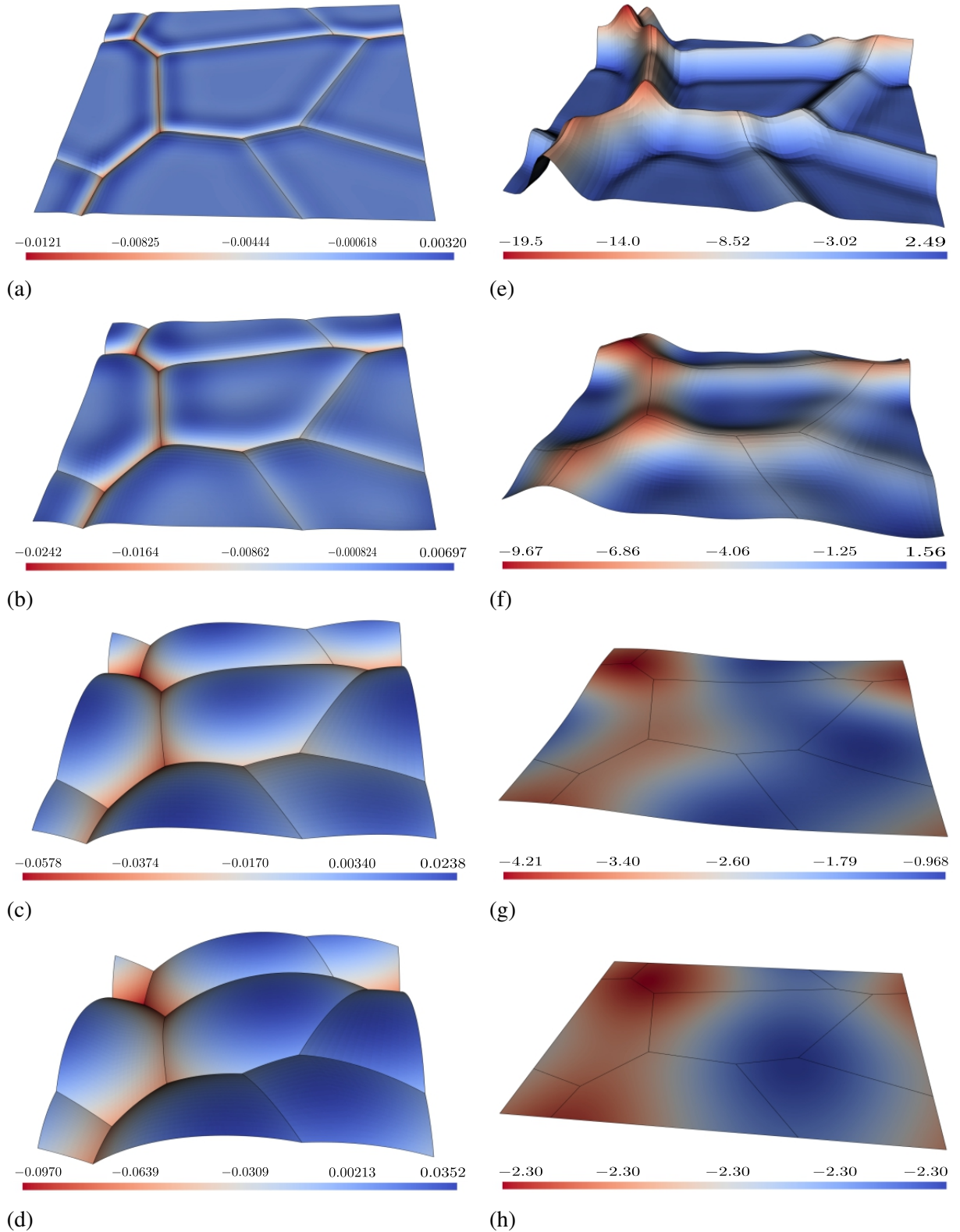


Figure 4.5.: Morphological evolution of four grains RVE using a set of grain boundary energies for  $A = 0.30$  in equation (4.6). In this simulations  $\bar{M}_\Gamma = 2.5 \times 10^{-2}$ . Figures (4.5a–d) show distribution of  $\bar{\mu}$ , and figures (4.5e–h) show  $-\bar{\mu}$  field along the surface at  $\bar{t}^{20}, \bar{t}^{35}, \bar{t}^{55}$  and  $\bar{t}^{75}$ , the equilibrium state. The surface proceed towards the constant curvature profile with the progressing time. In (e), at  $\bar{t}^{20}$ ,  $-\bar{\mu}$  is maximum along the boundaries. The grooves increase in depths with diminishing differentials of  $\bar{\mu}$ . (h) shows a constant distribution of  $\bar{\mu}$  at  $\bar{t}^{75}$  along the surface. It expresses the state of an equilibrium in the system.

is faster in comparison with the grooves in the rest part of the geometry. We had congruent behavior in these numerical experiments. The left groove in Fig. (4.6c) shows the depth of the quadruple point and it is faster than the grooves along the boundary. Groove on the right between  $\omega_3$  and  $\omega_4$  shows anomalous growth kinetics. Figure (4.6d) shows this shallow groove. Initially, we observed formation of less deep groove in comparison with the area of diffusional humps surrounding it. These mass accumulations were due to influx of matters from the rest parts of the geometry. We also observed the variation in the groove kinetics. Initially, the groove formation was taking place at a slower rate but after  $\bar{t}^{50}$ , the influx of material dominates the grooving process along this triple line, and we had increase in the dihedral angle at the groove pit. Such positive motions along the grain boundaries were also observed in some experiments (see [Sachenko et al., 2002](#)).

In other parts of the RVE, we also observed positive influx of matter to maximize the dissipation. Figures (4.6e) and (4.6f) show evolution along the  $\overline{CC}$  for progressive  $\bar{t}^n$ . These plots show groove profiles after initial settling steps. We observed grooves growth with relatively slower rates. Formation of diffusion plateaus along the grain boundaries represent the removal of material along the triple line with the reduction in the total grain boundary energy. Although, we had constant diffusion coefficients for all grains, the grain boundary at the right between  $\omega_2$  and  $\omega_3$  evolve with slower growth kinetics. At the later stage, it was observed that due to high influx of material, increase in dihedral angles took place. These reverse motion of the fluxes conduced to increase in the dihedral angle. With these topographical observations, it is concluded that the variations in equilibrium dihedral angles observed in the experiments reflect steady-state measurements and when the external constraints removed, the system try to establish a new steady state with the motion of fluxes favorable to minimize the total energy.

In addition to these, it is necessary to compare the growth kinetics of quadruple points in the RVE. This study is helpful in marking out the critical locations in the polycrystalline, effecting its workability and expected life. Figure (4.7) shows growth rates of all quadruple points  $P_i$ 's and some points on the triple lines. The overall growth took place with  $\bar{t}^{1/4}$  with different coefficients. This power law express the analytical solution for diffusion controlled process along the surface given by [Mullins](#). The pit depths increased at the higher rates. Thus the quadruple points have faster increase in depth than the triple lines. In some parts of the geometry, we also observed variations in growth rates. Initially, one of the triple line growth followed  $0.3578\bar{t}^{0.25}$  but after ward due to relatively high chemical potential in this region, the flux moved at higher rate ( $0.4705\bar{t}^{0.25}$ ). This faster decrease in the depth of groove is due to influx of matter towards the site of low chemical potential.

#### 4.3.2.2. Effect of $\overline{M}_\Gamma$ on groove shapes and growth kinetics.

In our model, the rates of matter ( $J_i, j_{\Gamma i}$ ) are function of chemical potential and material diffusion coefficients. The objective of this section is to elaborate the effect of  $\overline{M}_\Gamma$ , which is the ratio between line diffusion and surface diffusion coefficients.

The change in  $\overline{M}_\Gamma$ , effects the polycrystalline morphology. The increasing value of this dimensionless parameter interprets surface diffusion dominating process. With relatively low value of surface diffusion coefficients, the groove shape have narrow-downing of dihedral angle. Contrary to this, at low value of  $\overline{M}_\Gamma$ , material along the surface moves with relative ease in comparison to the converse problem. This causes the widening of the dihedral angle and we

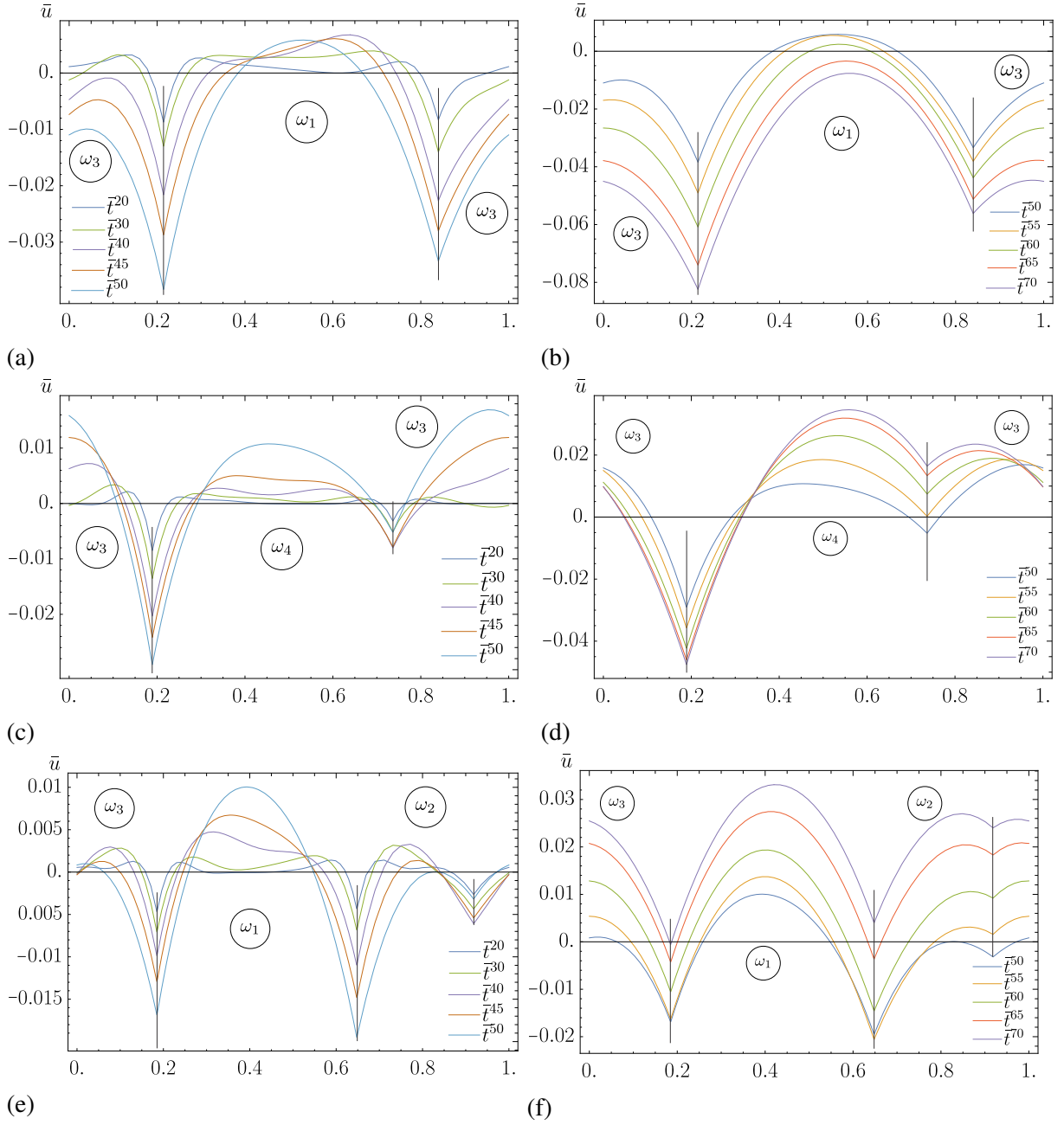


Figure 4.6.: Evolution along different cross sections for the anisotropic factor  $A = 0.30$  and  $\overline{M}_\Gamma = 2.5 \times 10^{-2}$ . (a),(b) surface profiles along  $\overline{AA}$ . Deepening of the grooves start along the boundaries. We observe variations in the growth kinetics in some parts of the RVE. (c),(d) shows evolution along the cross section  $\overline{BB}$ . Left groove is at the quadruple point and growth rate is faster with deeper depth. The groove on the right side is along the triple line. At this site, we observe slow growth kinetics with bulging of surface near to the equilibrium. (e),(f) illustrate evolution along  $\overline{CC}$ . Formation of diffusional humps are visible along this cross section with formation of the grooves along the triple line. We have different growth kinetics with formation of planer face along the free surface at this value of  $\overline{M}_\Gamma$ .

observe grooves with continuous curvatures.

Figure (4.8) plots the evolution of  $\overline{u}$  at different instances of  $\overline{t}^n$  for different values  $\overline{M}_\Gamma$ . It

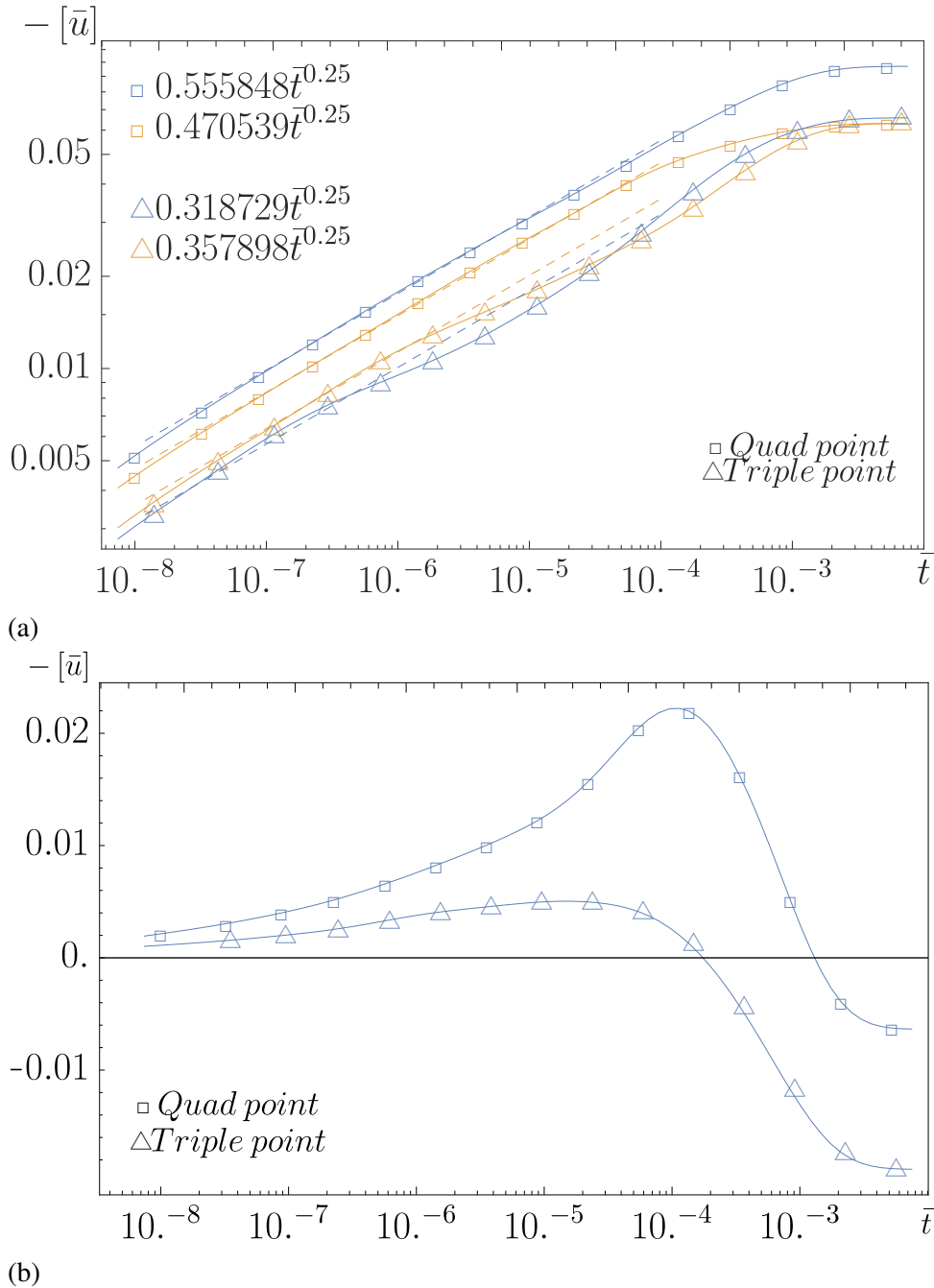


Figure 4.7.: Growth rates of quadruple points,  $P_i$  and points on the triple lines  $\Gamma_i$ . (a) shows depths on log-log scale. These depths are fitted for  $\bar{t}^{1/4}$  power law. Overall, P's depths increase at the faster rates. Some fluctuations at pits depth are also evident for the system near to the equilibrium. Triple lines grow with faster growth rates in the second phase. (b) shows depth evolutions using log-linear scale. Initially, we observed normal formation of grooves and pit at very slow rates in this particular region. At the later stage, the influx of mater to minimize the energy caused formation of the protrusions at these regions.

shows the deepening of grooves with an increasing value of surface diffusion coefficient. For low value of it, there was formation of flat region along the free surface with the steeping of the dihedral angle. Formation of diffusional humps were not evident in these numerical experiments. Contrary to this, In the experiments with the higher surface diffusivity coefficients,

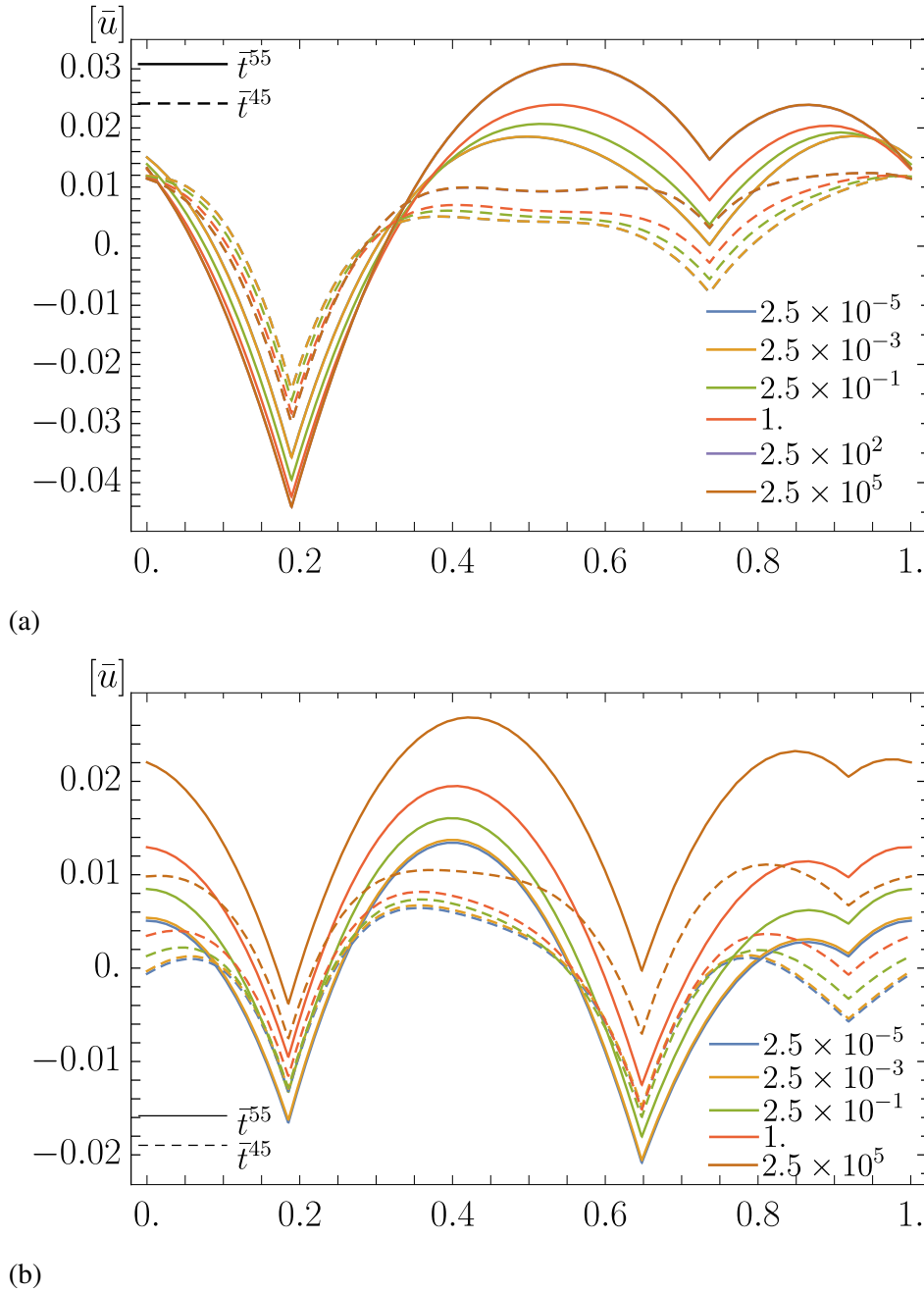


Figure 4.8.: Effect of  $\bar{M}_\Gamma$  on surface cross sections. (a) is the evolution of surface along  $\overline{BB}$ , (b) is the evolution of surface along  $\overline{CC}$  at  $\bar{t}^{45}$ , and  $\bar{t}^{55}$ . For any increase in  $\bar{M}_\Gamma$ , there are accelerated increase in depths at the quadruple points, and we have diffusion humps with relatively low profiles. The groove shapes and kinetics are governed by P growth. At lower value of  $\bar{M}_\Gamma$ , we have wider grooves with larger dihedral angles.

material is relaxed to flow along the free surface and we have widening of grooves with faster kinetics. Alongside this, the heights of the diffusional humps were also prominent on both sides of the groove. Variations in the diffusion coefficients not only effect the growth kinetics of the surface morphologies but also the growth kinetics of the quadruple points. Figure (4.9) shows plots for growth rates of different quadruple and triple points. With the change in the diffusion coefficients, we observed variations in the growth kinetics, but the steady state positions of the

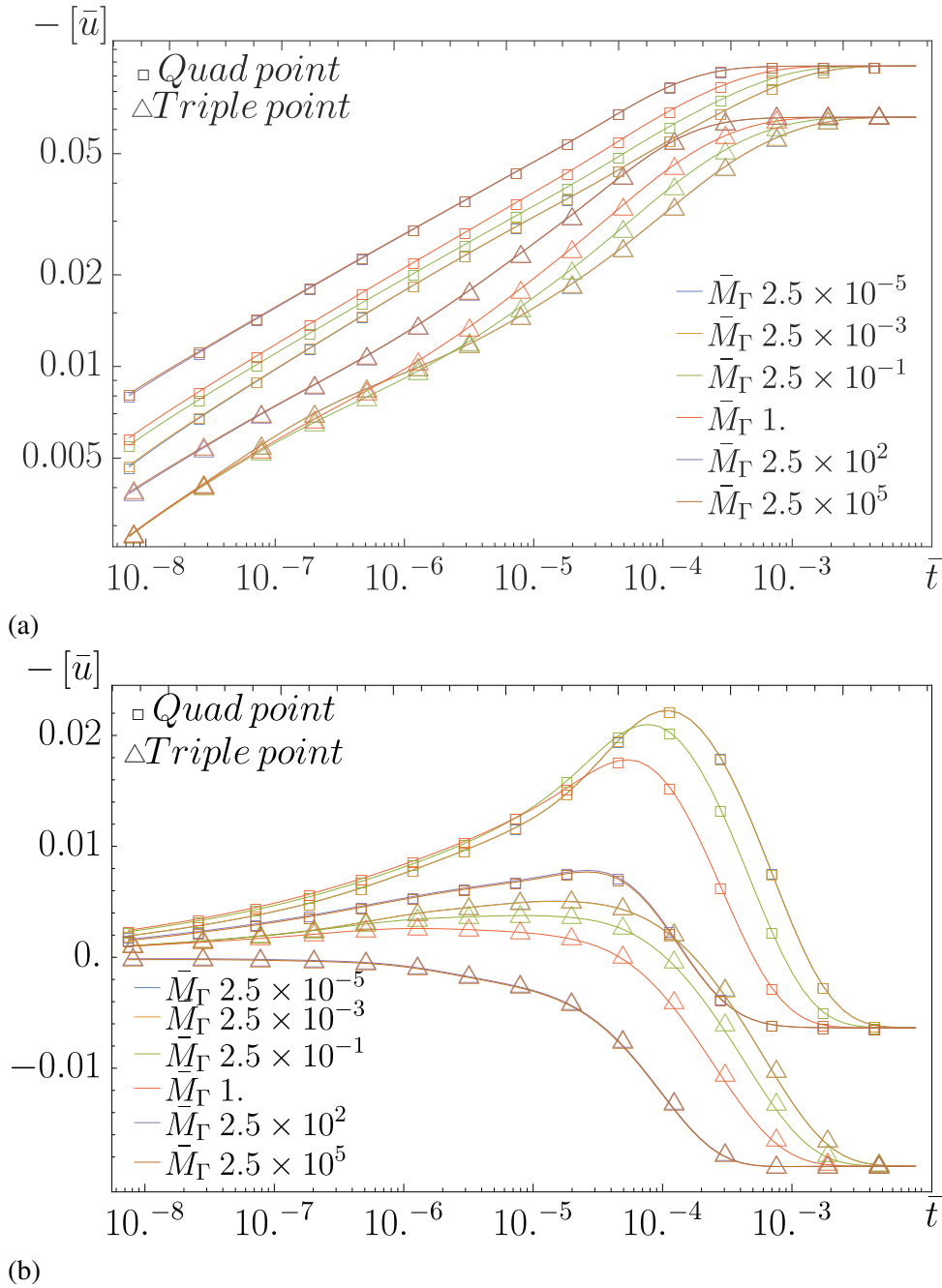


Figure 4.9.: Over all effect of change in  $\bar{M}_\Gamma$  on depths of pits and triple points at grooves bases. (a) evolutions on log-log scale. (b) evolutions on log-linear scale for extruded points. Increase in  $\bar{M}_\Gamma$ , increases the quadruple points  $P_i$  growth rates. With different kinetics path, the system attains constant state of the equilibrium.

system remained constant. Likewise, the geometrical parts with the positive influx to maximize the dissipation, behaved in the congruent way, followed by variations in overall kinetics.

#### 4.3.2.3. Effect of varying $A$ in an ansatz function.

Grain boundary energies of different materials are correlated under the linear relationship. They are scaled under material parameters. There are many studies in the literature establishing the relationship between the material characteristics parameters and grain boundary energies based on the basic crystal structure. For example in case of f.c.c materials, see [Holm et al. \(2010, 2011\)](#), for b.c.c materials, see [Ratanaphan et al. \(2015\)](#), for the grain size correlation with material properties specifically grain boundary energies, see [Kim et al. \(2012\)](#). In our ansatz function, different set of parameters  $A$  and  $B$  in equation (4.5) we have sets of grain boundary energies for common polycrystalline structure. These sets are portraying the thermodynamics forces for different materials. Simulation results with these sets enable us to select the best material for the maximum workability under the design constraints (in this particular case, we have constraint of the geometry). With these perspectives, this section compares results for the different set of relative grain boundary energies with different diffusion coefficients and factor  $A$  in the ansatz function. There can be infinite number of different grain boundaries forces depending upon the orientation relationship between the grains ([Kim et al., 2011](#); [Cantwell et al., 2014](#)), but here we will assume that the one with the minimum residual of the grain boundary energy potential, and it represents the steady state structure.

Figure (4.10) illustrates comparative morphological study of the polycrystalline at the different instances of  $\bar{t}^n$ . In these simulations, we had constant surface diffusion coefficients and triple lines energies. A comparison is made for the three different sets of grain boundary energies calculated for varying scalar factor  $A$  in the ansatz function. An increasing value of this factor for a constant geometry, represents grain boundary energies for stiffer materials. Morphological kinetics of the surface showed that with an increasing value of  $A$  we had dominating surface diffusion due to high value of grain boundary energies. It is also evident from the height of diffusional hump in the neighborhood of the grooves along the grain boundaries. With an increasing value of  $A$ , the height of the humps increased.

The quadruple junctions kinetics are important in determining the workability of the polycrystalline materials. Figure (4.11) illustrates the comparative study for the evolution of  $P_i$  for three sets of grain boundary energies at different  $\bar{M}_\Gamma$ . With an increase in the scalar factor  $A$  in the ansatz function, the depths of the quadruple points increased linearly. This behavior is in accordance with the observation in [Kim et al. \(2012\)](#). Also the growth rate varied linearly with constant diffusion coefficients. Secondly, this plot also compares the evolution kinetics for different diffusion coefficients. For the surface diffusion dominating process (with high value of  $\bar{M}_\Gamma$ ), we have faster rate of increase in pit depths. As per previous observations, the overall behavior is congruent regarding the equilibrium positions of the quadruple points and surface morphologies.

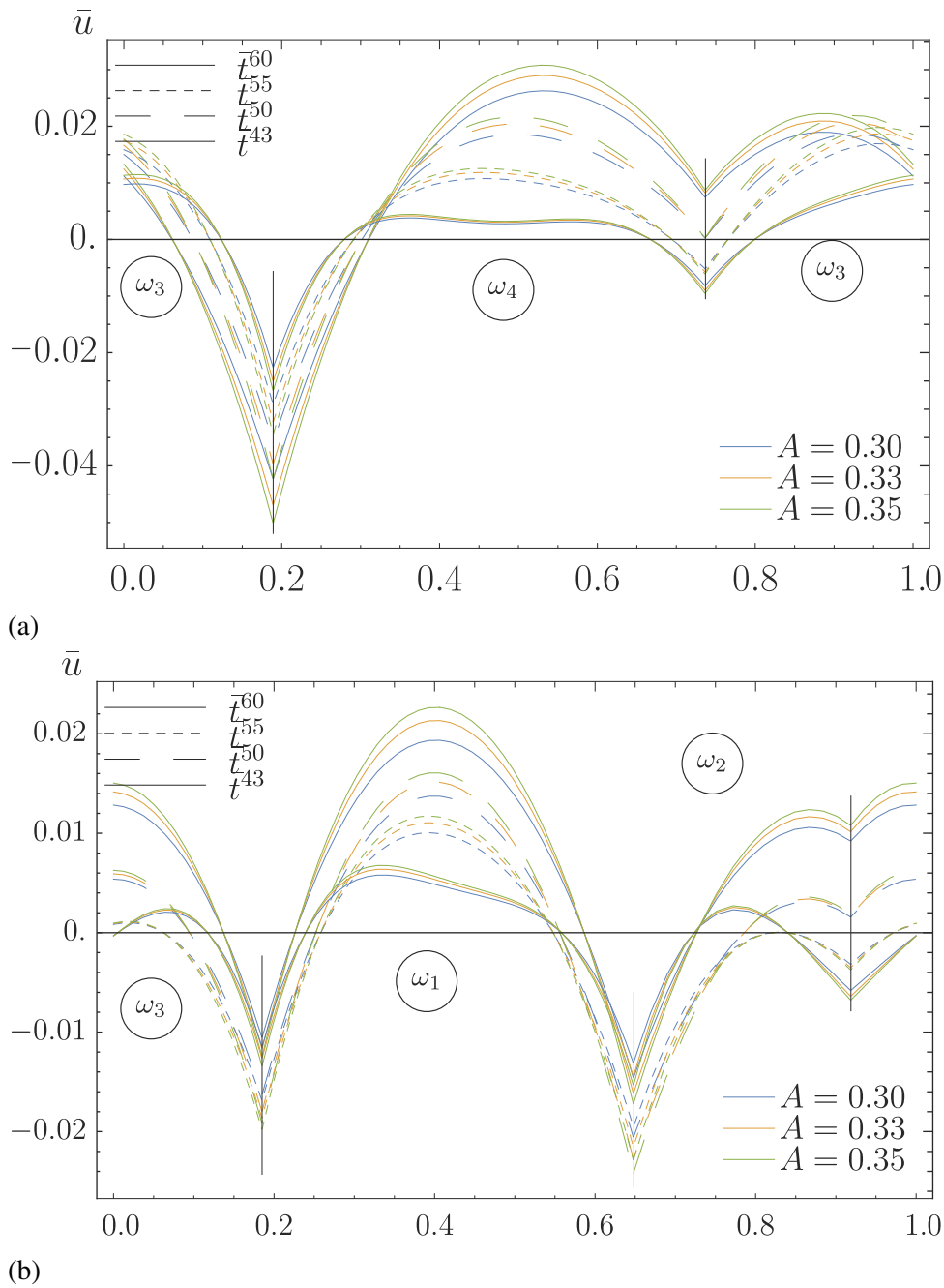


Figure 4.10.: Comparison of surface morphologies and grooves shapes for sets of grain boundary energies at different values of  $A$  in equation (4.6). (a) evolution along  $\overline{BB}$ , (b) evolution along  $\overline{CC}$  at different instances of  $\overline{t}^n$ . In these simulations surface energy is constant and  $\overline{M}_\Gamma = 2.5 \times 10^{-2}$ . With an increasing value of  $A$  in an ansatz function, we have sets of higher energy grain boundaries. Conclusively, steeper grooves are formed with decreasing dihedral angles. Also the height of diffusional humps increase due to conservation of matter in the system.

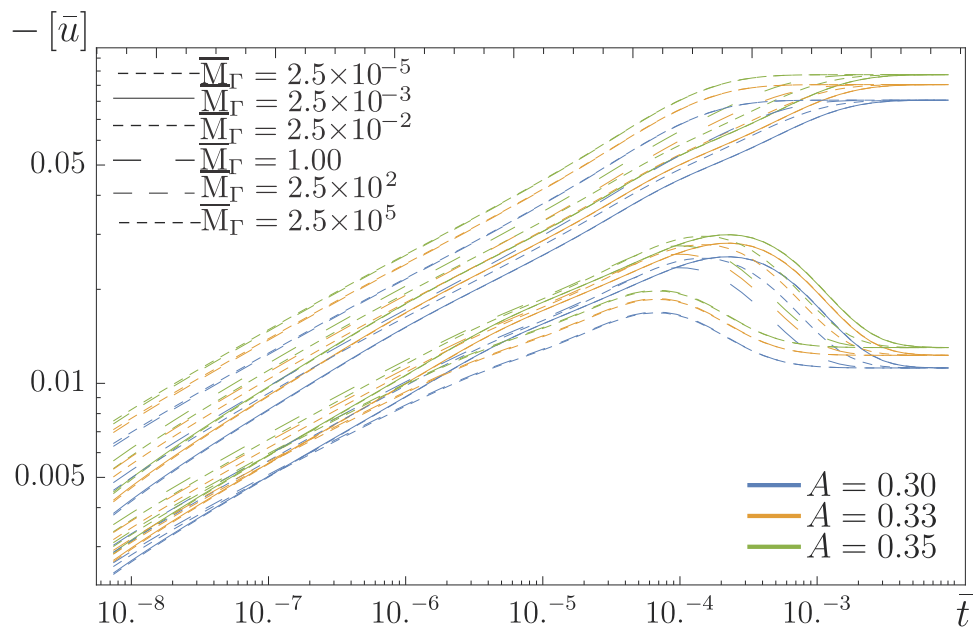


Figure 4.11.: Comparison for growth kinetics at quadruple points for the sets of grain boundary energies at different values of  $A$ . The pit depths are plotted against  $\bar{t}$  using log-log scale. With the increasing values of  $A$ , we observed linear relationship between pit depths and boundary energies. For each set, any increase in  $\bar{M}_\Gamma$ , increases the diffusion kinetics along the triple lines. Ultimately, the system reach at the constant equilibrium state.



## 5. Singular grooves and surface energy anisotropy

Shapes and growth rates of the thermal grooves are focus of research in material sciences and other scientific fields form several decades. These grooves develop at the expense of mass transfer and energy dissipation. The topographies of the polycrystallines are due to coupled or uncoupled processes including bulk diffusion, surface diffusion, and evaporation-condensation. The bulk diffusion is accompanied by grain growth with moving grain boundaries. In case of stationary grain boundaries, the thermal grooves express the steady state conditions between grain boundaries and surface energies with the equilibrium dihedral angles. We can also calculate the grain boundaries characteristics distributions, grain boundary energies, and diffusion coefficients under the assumption of constant surface energy.

From the Mullins's model, it was shown that we have formations of self similar symmetric grooves profiles under the assumption of isotropic surface energy, but many experiments in the literature reported asymmetric groove profiles due to parallel dissipation processes, and moreover in some cases there are planar facets of unequal lengths along the grain boundaries. Grooves with these planer facets on either or both faces are termed as singular grooves due to the non existence of measurable curvature, and they were indicating their singular character. These formations are characterized due to change in the surface energy with the orientations. The diffusional humps of small amplitudes were also attached to the planer faces, indicating low diffusional activities in these areas. Using these planar grooves shapes for the calculating the material parameters, we are not able to predict the correct value of the relative grain boundary energy and diffusion coefficients. Additionally, we can have symmetric or asymmetric profiles for the grains with different orientations along the grain boundary. Keeping in views these, the prime objective of this work is to study the morphological evolutions in the polycrystalline using orientation dependent surface energy for the diffusion control processes. We will use the same set of equations for thermal grooving already discussed in chapter (3). The effect of grain orientations and diffusion coefficients on growth kinetics and shapes of the grooves will be discussed in detail.

### 5.1. Introduction.

Thermal grooving has a key role in the morphological evolution and the stability of a thin layer coating as well as at micro scale in micro electromechanical systems (MEMS). With the miniaturization of materials, we gain high strength at the expense of decrease in the fracture resistance (Kozic et al., 2018). Different topographical structures, for example hill and valley formations at free surfaces, groove profiles with secondary diffusional humps, oscillations at the groove roots, asymmetric groove profiles and singular surfaces along the grain boundaries (see Fig. (5.1)) are reported during secondary annealing processes in literature. These phenomena have strong correlation with the anisotropic surface energy (Klinger and Rabkin, 2001; Munoz et al., 2004; Shaffir et al., 2009; Zhao et al., 2012b; Stamelou et al., 2017). Some of these observations are also considered as a consequence of anisotropic diffusion coefficient (Sachenko

et al., 2002; Schiedung et al., 2017; Saylor and Rohrer, 2004; Amram et al., 2014). In overall, thermal grooving effects the efficacy and workability of many electronic components, protective coatings and epitaxial layer in the thin films. During the processes well below the roughening temperature (secondary annealing, high working temperature), tiny holes are formed due to the diffusion phenomena, which is dominating transport mechanism in these temperature regions. These micro holes are suitable sites for cracks initiation and degradation of thin films (Keneffick and Raj, 1989; Miller et al., 1990; Nemetz et al., 2019) and failure of microelectronics (Lee et al., 1987; Kozic et al., 2018). Additionally, it was also observed that in the absence of external driving forces, grooves formations cause the pinning of the grain boundaries (Mullins, 1958; Frost et al., 1990; Génin et al., 1992; Lou and Player, 2002; Ma et al., 2017) and grain growth under the limiting conditions of the dihedral angles (Svoboda et al., 1991; Svoboda and Riedel, 1992; Fischer et al., 2012). Thus it is important to understand the kinetics of these processes for different orientations. We use anisotropic surface energy to explain these grooves formations, combined with different set of material characteristics parameters.

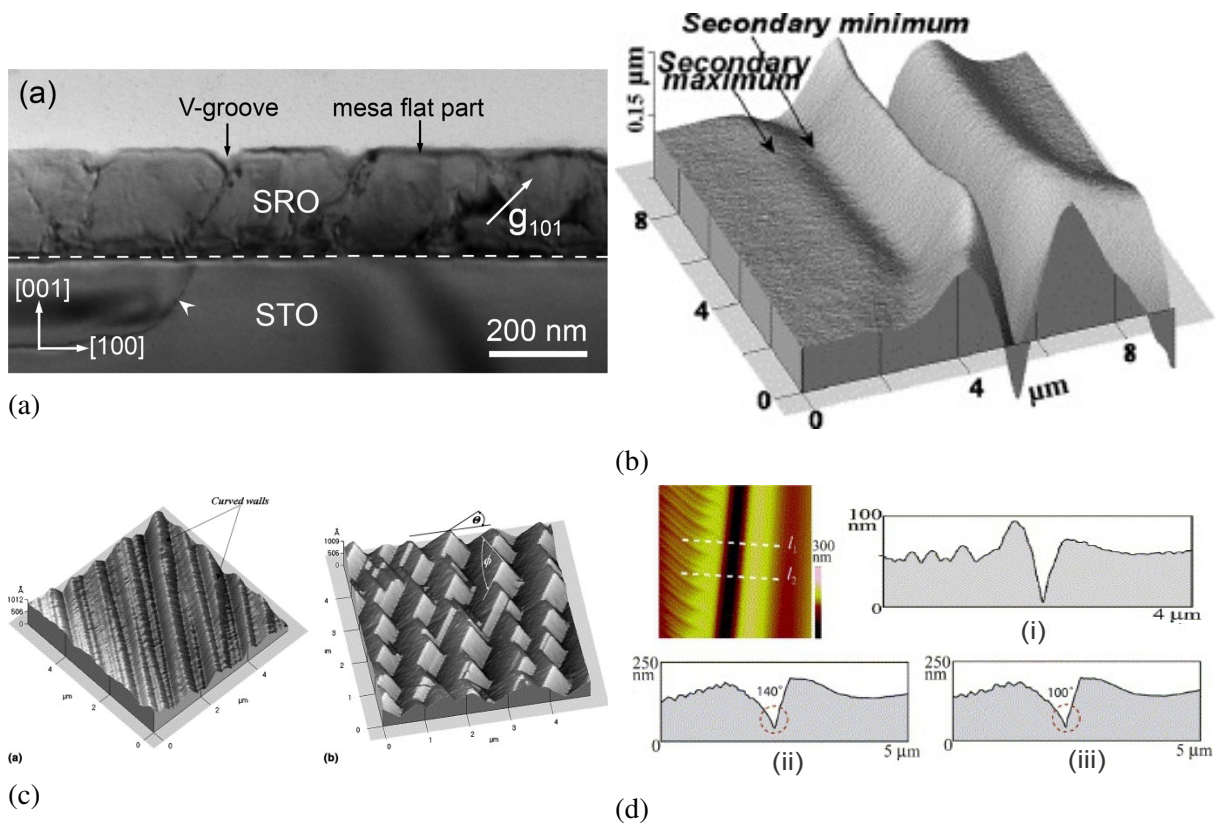


Figure 5.1.: Morphological evolutions due to surface energy anisotropy varying with grains orientations for different materials. (a): cross section of TEM image with V grooves along the free surface of SrRuO<sub>3</sub> with the depth of 17nm to 55nm grown over SrTiO<sub>3</sub> and annealed for 20 min. (Liu et al., 2016). (b): AFM image of the grain boundary groove in tungsten sample after 128 hr. annealed at 1350 °C. Image shows secondary diffusional hump along the grain boundary (Sachenko et al., 2004). (c): AFM image of hill and valley structure along the free surface, annealed at 1350 °C, after 128 hr. (Zhang et al., 2004). (d): AFM image of cross sections at different time steps, (i) is the groove profile after 60min annealing at 1650 °C with asymmetric groove profile, (ii) and (iii) in this figure are groove profiles along two different sections  $l_1$  and  $l_2$ , after 120min at 1650°C with planar groove profiles on the right side and normal profile on the left side (Munoz et al., 2004).

Gibbs and Herring (1951) models on the growth kinetics of a single crystal are the pioneering works that explain the singular facets formations using anisotropic surface energy. Later on Hoffman and Cahn (1972) developed the comprehensive modeling approach for diffusion control growth in two dimension using anisotropy surface energy. In addition to this, Mullins (1961); Brailsford and Gjostein (1975) explained the formation of linear facet along the grain boundary for symmetric grooves. It was concluded that under the anisotropic surface energy grooves growth, the over all kinetics took place with  $1/4$  power law of the annealing time with relatively faster rates. In case of moving grain boundaries, there are possibilities of emergence as well as fading out of the singular facets at the expense of new planar faces formations (Carter et al., 1995). Cahn and Taylor (1994) model for morphological changes along the free surface is based on the coupled diffusional processes for minimizing the total energy of the system. This model can be used for both isotropic and anisotropic surface energy due to curvature based formulation.

Sachenko et al. (2002) modeled two dimensional grooving to simulate the serrated topography along the free surface of Tungsten. These formations were characterized with the anisotropy in the surface diffusion coefficient. Zhang et al. (2002) simulated the problem with time varying surface energy. In this case, the overall kinetics took place at faster rate. An extended three dimensional model, Zhang and Gladwell (2005) simulated the thermal grooving process for a symmetric groove shape of a single square grain. In case of moderate anisotropy, they accepted the results for  $\{1\ 1\ 1\}$  orientations as a quasi-steady state. They found the termination of simulations due high numerical error. Savina et al. (2003) simulated the thermal grooving due to coupled surface diffusion and evaporation-condensation. The model is based on higher-order Cahn-Hilliard equation. The coarsening due to coupled process varied inversely with increasing effect of evaporation-condensation.

The numerical simulations Amouyal et al. (2008); Derkach et al. (2016) are based on the experimental observations for thermal grooving and dewetting in solids. They effectively used numerical experiments to measure the diffusion coefficients within a tolerance. Rabkin et al. (2006) observed the formation of secondary diffusional humps during annealing process. They established a relationship between grain boundary migration and surface energy anisotropy for blunted and singular grooves.

Ogurtani and Oren (2005); Ogurtani (2007); Ogurtani et al. (2008) used the principle of maximum entropy production to develop the thermal grooving models with additional external forces in two dimension. The flux along a surface includes the contributions from electric and magnetic forces in accordance with Onsager first principle. Afterwards, Akyildiz et al. (2011) included anisotropic surface energy model (Ramasubramaniam and Shenoy, 2005) to study the asymmetric groove shapes in the annealing experiments.

Simulation experiments, Zhang and Wong (2002); Xin and Wong (2004); Min and Wong (2006a,b) included the anisotropic surface stiffness to study the effect of grain boundary orientation on grooves shapes and growth kinetics. In these two dimensional model, they used non-linear shooting method to solve the set of coupled differential equations to establish the condition for formation of singular faces along the groove with moving grain boundaries.

Diffusion based single crystal models, Zhang (2006, 2009a) explain the effect of surface energy anisotropy on the equilibrium shapes. It was concluded that for the crystals with  $\{1\ 1\ 1\}$  orientations, steady states were achieved at comparatively faster rates. Also for similar orientations, vanishing serrated topographies were observed along the free surface. Other research works,

Barrett et al. (2008, 2010b) are finite element based models for thermal grooving and sintering. They expressed the evolution kinetics for both isotropic and anisotropic grooving with moving grain boundaries.

Based on this review, there is no work in literature to the author knowledge that includes unconditionally anisotropic surface energy for thermal grooving. Derkach et al. (2014) work in three dimension expressed results only for isotropic surface energy. So, to explain the thermal grooving in complete three dimensions for any general shape of polycrystalline, we use Hackl et al. (2017) thermal grooving model with anisotropic surface energy function. Since, the model parameters are geometry dependent (see equations (3.57) and (3.59) ), and are function of surface mean curvature along the free surface. Therefore, this model can be unconditionally used for both isotropic and anisotropic surface energy function. The main reason of the stability of this model is the fact that in case of critical to severe anisotropy, any discontinuity in the curvatures of the surface is countered with the continuity of chemical potential, which is the basic requirement of the under laying physics for the motion of flux, equation (3.29). The contents of this chapter start with a brief explanation of Wulff-Gibbs energy plot. In next section, we will explain analytical form of the anisotropic surface energy that is use in these simulations. Finally, the effect of grain orientations on grooves shapes and kinetics of the geometrical elements will be discussed for a chosen polycrystalline geometry.

## 5.2. Gibbs and Wulff plots of surface energy.

The surface energy,  $\gamma$  is a scalar quantity and is assumed isotropic in most of the simulations. However, It is experimentally evident that there are variations in it with the crystal orientations. So, it can be modeled as a function of surface geometry in coordination with the crystal reference system. A free surface can be considered as a geometrical entity formed by cutting the crystal along a line inclined at some angle  $\theta$ . Figure (5.2) shows a two dimensional cross section of a free surface. The rectangular elements represent the atoms with the dimension  $a$  separated by breaking bonds between them.

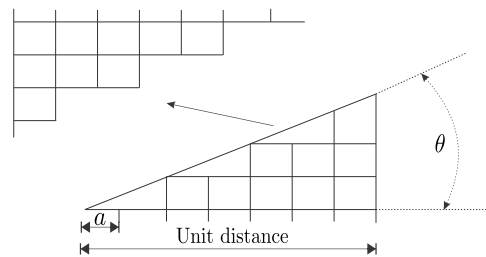


Figure 5.2.: A representative surface in the two dimensions. Each atom is illustrated with a square of dimension ‘ $a$ ’ and is inclined at an angle  $\theta$  with the horizontal. The upper half represent the remaining atoms to form the complete crystal of unit dimensions (Meier, 2014, fig. 4.1 ).

The total number of broken bonds in the vertical direction per unit length are determined as

$$N_V = \frac{1}{a}. \quad (5.1)$$

and number of bonds in the horizontal direction per unit projected length are calculated as

$$N_H = \frac{\tan \theta}{a}. \quad (5.2)$$

So surface-free energy density is the summation of bond energy of these free atoms per unit length of the surface. Hence, with total number of bonds  $1/a + \tan \theta/a$ , we have

$$\begin{aligned} \gamma(\theta) &= \frac{E_{aa}}{2} \frac{(1/a + \tan \theta/a)}{1/\cos \theta}, \\ &= \frac{E_{aa}}{2} (\cos \theta + \sin \theta) \end{aligned} \quad (5.3)$$

Equation (5.3) is an equation of a circle. It can be plotted for all four quadrants as shown in Fig. (5.3)

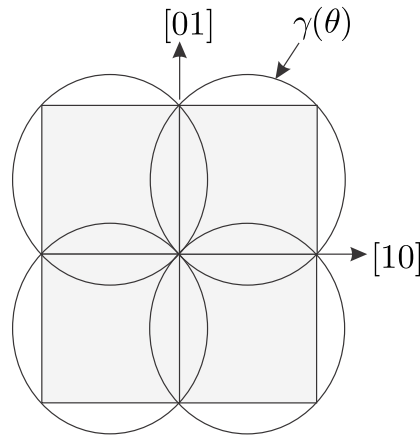


Figure 5.3.: A polar plot of surface energy function using equation (5.3) for all four quadrants. The inner rectangle represents the equilibrium shape of the crystal (Meier, 2014)

This construction of surface energy is termed as Wulff-plot. The extension of this plot in three dimensions is generated by rotating a vector of magnitude of surface energy through all  $hkl$  orientations in the crystal reference system (Meier, 2014). Cahn and Hoffman (1974) introduced the vector function,  $\xi$  as an alternative method to plot the scalar surface energy. This model plots the scalar surface energy function in such a way that we can find the crystal shape over the range of orientations in two and three dimensions. With these formulations, one can also explain the range of orientations for which there exist a set of normal vectors expressing the state of an equilibrium with minimum surface energy. The surface energy vector,  $\xi$  is defined as

$$\xi \cdot \mathbf{n} = \gamma, \quad (5.4)$$

$$\xi \cdot d\mathbf{n} = d\gamma. \quad (5.5)$$

Equation (5.4) expresses a normal component.  $\xi_n$  shows the tendency of surface to minimize its energy by contraction. Equation (5.5) gives a relation for a change in the surface energy with orientations ( $\partial\gamma/\partial\theta$ , See equation (A.7)). This component contributes to the torque term along the central axis, which is given by a relation  $\mathbf{n} \times \mathbf{t}$ , with  $\mathbf{t}$  is parallel to  $d\mathbf{n}$ . The  $\xi$  must satisfy an auxiliary condition  $\mathbf{n} \cdot d\xi = 0$  (equation (A.6)<sub>1</sub>), defining the orthogonality condition. Cahn and Hoffman (1974) related this term with the minimization of chemical potential at constant

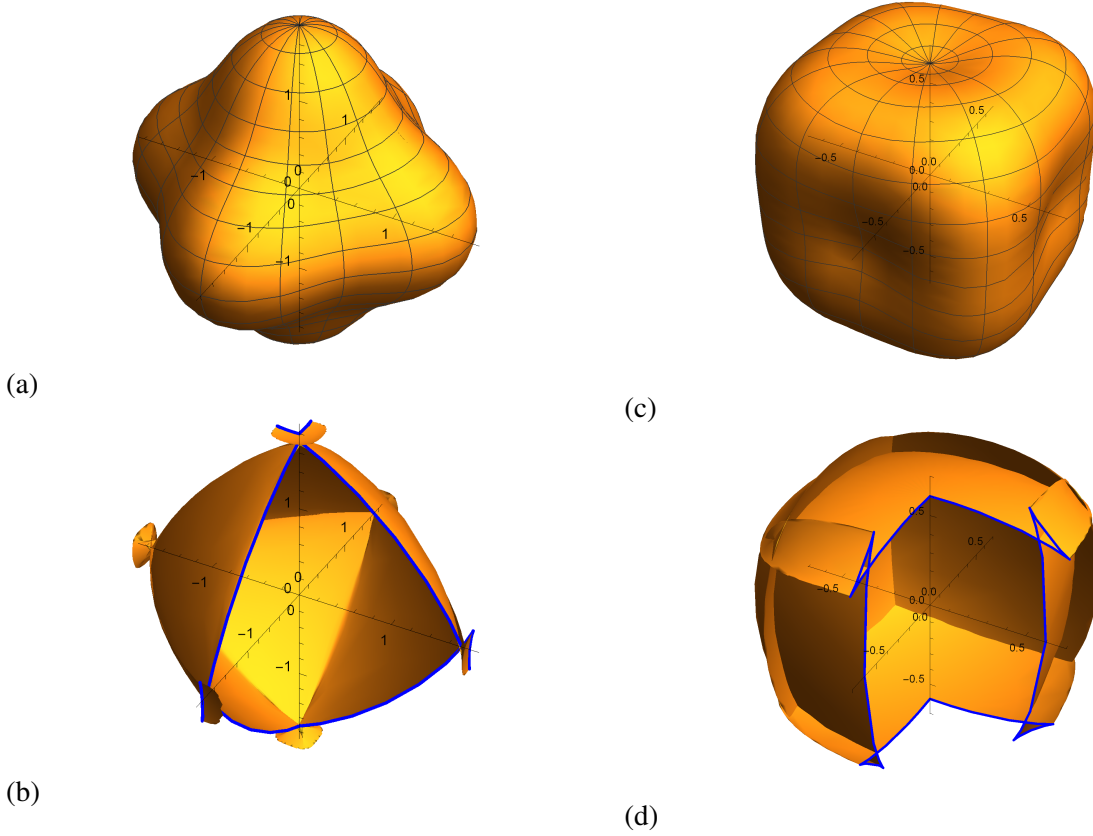


Figure 5.4.:  $\gamma$  and  $\xi$  plots for two different energy functions. (a):  $\gamma$ -plot over complete orientations in  $hkl$  directions, using anisotropic surface energy function,  $\gamma = 1 + c(n_1^4 + n_2^4 + n_3^4)$  with  $c = 0.4$ . The surface has maximum energy,  $(1 + c)$  along the principle axis of the crystal. (b):  $\xi$ -plot for (a) with cross sections. (c) and (d) are  $\gamma$  and  $\xi$  plots respectively. These are plotted using the anisotropic surface energy,  $\gamma = 1 - c(n_1^4 + n_2^4 + n_3^4)$  with  $c = 0.4$ . The surface has minimum energy,  $(1 - c)$  along the principle axis of the crystal.

temperature and pressure in coherence with Gibbs-Duhem equation of classical thermodynamics.

With these definitions, for any surface element of area  $A$ , the total energy is  $\gamma A = \xi \cdot \mathbf{A}$ . Any change in the area and its energy is given as

$$\begin{aligned}
 d(\gamma A) &= d(\xi \cdot \mathbf{A}) = \xi \cdot d\mathbf{A} + \mathbf{A} \cdot d\xi \\
 &= \xi \cdot d\mathbf{A} \quad (\because \mathbf{n} \cdot d\xi = 0) \\
 &= \xi \cdot (n dA + A d\mathbf{n})
 \end{aligned} \tag{5.6}$$

The first term ( $\xi_n \cdot n dA$ ) is amount of work required to minimize the total surface energy with reducing area and the second term ( $A \xi_t \cdot d\mathbf{n} = \mathbf{A} (\partial\gamma/\partial\theta) d\theta$ ) is amount of torque required to rotate the crystal in the direction, which minimizes the total surface energy. Faceting along the free surface during crystal growth or grooves with planar faces appear due to anisotropy in surface energy. With these facets formations, overall area of the surface of the crystal increases but there is reduction in the surface energy contribution by splitting high orientation surface into low orientation surfaces. Formation of these low energy facets can be explained using  $\xi$  vector plot.

Figure (5.4) shows  $\gamma$  and  $\xi$  plots of the single crystal in three dimensions. These two  $\gamma$ -plots are plotted using two different energy functions. In figures (5.4b) and (5.4d),  $\xi$  plots show formations of ears like protrusions along the edges. If a crystal surface orientation lies in these ranges, probabilities of facets formations along the grooves and free surfaces are relatively high. Formation of small facets along the free surface is explained graphically in Fig. (5.5). For the range of vectors,  $m_1$  to  $m_n$ , we have a limiting range of orientation due to intersecting boundaries. All  $\xi$  in these ranges have minimum value of surface energy, given as

$$\xi(0) = \xi(1) = \xi(2) \cdots = \xi(n) \quad (5.7)$$

This equilibrium condition restrict surface normal vectors of different orientations to  $\xi(0)$  energy. Thus, high  $\gamma$  orientation will break up into a set of facets of lower  $\gamma$  orientation. Range of these orientations are categorized under unstable, missing or forbidden orientations (Einstein, 2015; Sekerka, 2015).

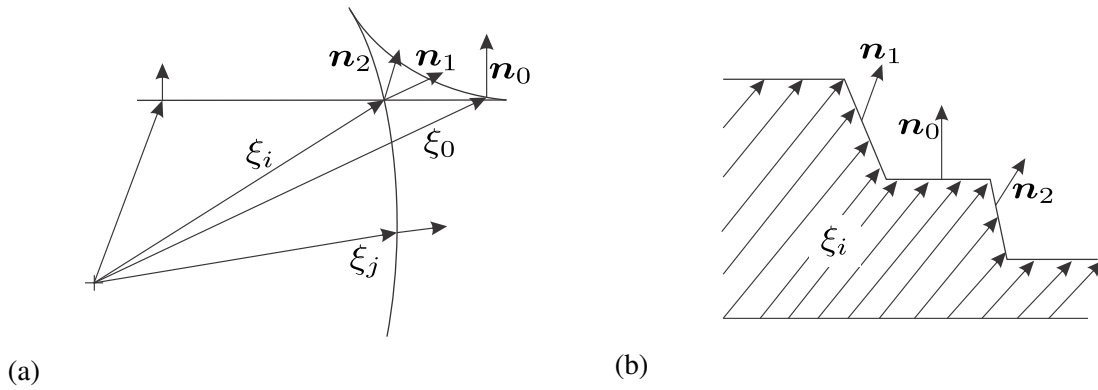


Figure 5.5.: An illustrative explanation of planar facets formations at surface. The surfaces with different orientations  $n_i$  have constant minimum value of  $\xi$ . (a) explains that for the orientations over the range of self intersecting region, there are existence of surfaces with different orientations having minimum energy in accordance with equation (5.7). (b) shows the formation of planar facets for the orientations lies in the self intersecting region. Each surface with different orientation has minimum energy  $\xi_0$

It was observed that in some cases we do not have formations of flat or singular faces in the limiting case of these orientations. It is complex to precisely pinpoint the orientation for the appearance of singular faces along the surface. Sekerka modeled a condition for the formation of planar facets as a function of Gaussian curvature. In two dimensions, if we plot a circle of diameter  $\xi$  over the  $\gamma$ -plot, with one end of diameter at origin, and rotate it over the range of orientations. The inclination angles for which the circle is not tangent to the  $\gamma$ -plot and intersect it, lies over the range of missing orientation. Elegantly, in  $1/\gamma$ -plot, the tangent circle becomes a tangent line at the outer side of it. In a similar way in three dimensions, the intersecting spheres become the intersecting planes over  $1/\gamma$  plot.

Figure (5.6a) shows  $\gamma$ -plot with an intersecting Herring's circle at point  $P$ . If the orientation  $RP$  is a point of tangency, it will appear at orientation  $RQ$  in  $\xi$  plot, and if it is intersecting than this orientation will be missing on the equilibrium shape. Figure (5.6b) shows  $1/\gamma$  plot. The tangent line at point  $P$  lies outside the plot boundaries. In the range of missing orientations, this tangent line lies inside the region. The range of orientation angles between  $A$  and  $B$  shown by dotted, express the range for intersecting circle. We observe the formations of extended regions

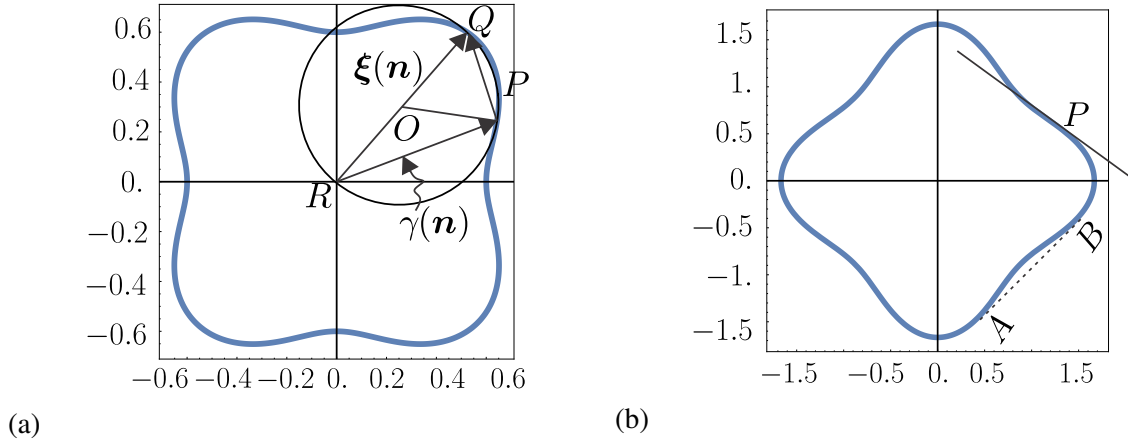


Figure 5.6.: Polar plots of surface energy in two dimension. **(a)**:  $\gamma$  plot for  $c = 0.5$ . A circle of diameter  $\xi$  is tangent at point  $P$ . Hence, surface energy vector  $\gamma(\mathbf{n})$  at point  $P$  appears at point  $Q$  on  $\xi(\mathbf{n})$  plot. **(b)**:  $1/\gamma$  plot in two dimension for the same energy function. For the corresponding point  $P$ , we have tangent line at the inner side of the close region. The orientation lies in  $\xi$  plot and if this tangent line is outside of the plot region, we have that orientation in the intersection region. With this, the orientation range  $A$  to  $B$  shown by dotted line shows missing orientation in  $\xi$  plot for the equivalent anisotropy. These missing orientations lies inside the intersecting region formed at the edges of the  $\xi$  plot.

over these angles in  $\xi$  plot. It follows that if  $1/\gamma$ -plot is convex, then all of these orientations will be on the equilibrium crystal and if it is not convex, then the orientation will be categorize as missing and will not appear on the equilibrium crystal shape. It concludes that when the system is at verge of missing orientation, the curvature of  $1/\gamma$ -plot changes from convex to concave and in case of three dimensions, one of the principle curvatures or both change their signs. This condition is calculated using a Gaussian curvature ( $G$ ) of  $1/\gamma$ -plot, which can be calculated using the normal vector of the surface.

The normal vector of  $1/\gamma$ -plot, in term of  $\xi$  vector is

$$\mathbf{N}_{\gamma^{-1}} = \frac{\xi(\mathbf{n})}{|\xi|}. \quad (5.8)$$

We can calculate principle curvatures from the derivative of normal vector (Dietz and Iseri; Weatherburn, 1927). Based on derivation in appendix (A.2), the Gaussian curvature of the surface in term of  $\xi$  is calculated using equations (5.8) and (A.14).

$$G = K_1 K_2 = \frac{\xi \cdot \xi_x \times \xi_y}{H |\xi|^3}. \quad (5.9)$$

With this, the limit of missing orientation is given by the condition  $\xi \cdot \xi_x \times \xi_y = 0$ . The portion between these two tangent planes and the origin correspond to the restricted orientations in the equilibrium crystal structure.

### 5.3. Anisotropic surface energy function.

In most of the numerical simulations, we assume isotropic surface energies in the model, but was reported in many experimental observations that surface energy of the crystal varies with the orientations. There are many method to calculate the anisotropic distribution of the surface energy in the single crystal. We can use the experimentally evaluated surface energy from *zero-creep technique*, or from *multiphase-equilibrium (MPE) technique*. Saylor and Rohrer (2001) reconstructed anisotropic surface energy distribution of the range of orientation from thermal grooving data. For the numerical simulations, there are analytical anisotropic surface energy models that are also symmetric. McFadden et al. (2000) modeled dendrite growth using analytical form of anisotropic surface energy. Zhang (2009b) used positive coefficient anisotropic surface energy function for simulating the behavior of single crystal. Dantzig analytical model is best suited for amorphous crystals shapes. For numerical simulations in this literature, we will use anisotropic surface energy model with negative coefficient. The mathematical form of this cubic symmetric energy model is

$$\gamma(\mathbf{n}) = \gamma_0(1 - c(n_1^4 + n_2^4 + n_3^4)), \quad (5.10)$$

with  $\gamma_0$  is constant isotropic surface energy and  $\mathbf{n}_i$  are surface normal vectors. The scalar parameter,  $c$  has a value  $[0, 1]$ . For  $c = 0$ , the surface energy is isotropic. With an increasing value of  $c$ , we have anisotropy in the surface energy. It has minimum value,  $\gamma_0(1 - c)$  along the principle axis,  $\{1\ 0\ 0\}$  directions in the crystal reference system as shown in figures (5.7a–d). For  $c \leq 2/9$ , we observed no formations of ear like edges along the diagonal of  $\xi$ -plot (see Fig. (5.7e)). For  $2/9 < c < 1/3$ , we have formation of ears along the diagonals, in  $\{1\ 1\ 0\}$  directions in crystal reference system (see Fig. (5.7f)). For  $c < 1/3$ , these extended areas extend in  $\{1\ 1\ 1\}$  directions (see figures (5.7g) and (5.7h)). Zhang (2006) used equation (5.10) in single crystal growth simulations to study the effect of anisotropy. It was also revealed in these simulations that formations of singular facets depend upon the grain orientations and anisotropy factor. We use this energy function to study the effect of anisotropy on surface morphology and growth kinetics in three grains periodic RVE (Fig. (5.8)).

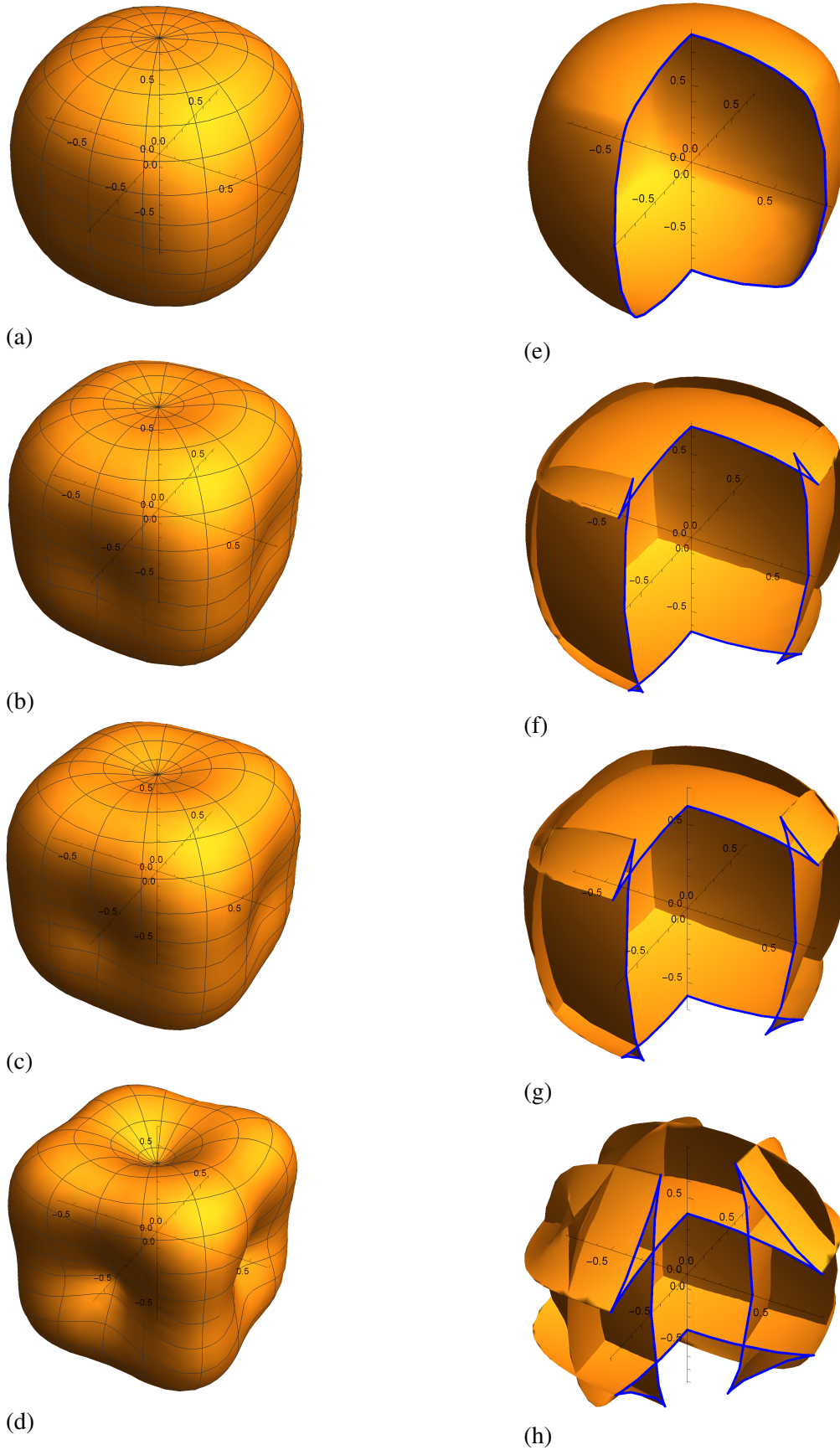


Figure 5.7.: Polar plot for anisotropic surface energy function,  $\gamma(n) = 1 - c(n_1^4 + n_2^4 + n_3^4)$  for different values of  $c$ . (a)  $c = 0.2$ , (b)  $c = 0.35$ , (c)  $c = 0.4$ , (d)  $c = 0.6$ . Figures (5.7e–h) are  $\xi$ -plots. (e) for  $c = 0.2$  shows smooth vector surface without any overlapping region. (f) for  $c = 0.35$  shows self intersection regions along the edges in  $\{110\}$  directions. (g) for  $c = 0.4$  & (h) for  $c = 0.6$  have overlapping extended regions in  $\{111\}$  direction. The surface energy anisotropy is characterized as critical anisotropy for  $c > 0.6$ .

## 5.4. Three grains periodic RVE.

### 5.4.1. Model geometry and kinetics parameters.

In this section, a model geometry and method to calculate the grain boundary energies will be discussed. Although our variational model (Hackl et al., 2017) and software code implemented in Java, are capable of handling the multi grains models with an equal ease, we decided to work with three grains periodic structure. The prime concern of using this model is to develop a better understanding for the effects of surface energy anisotropy on the growth kinetics and evolutions of dihedral angles with the morphological changes.

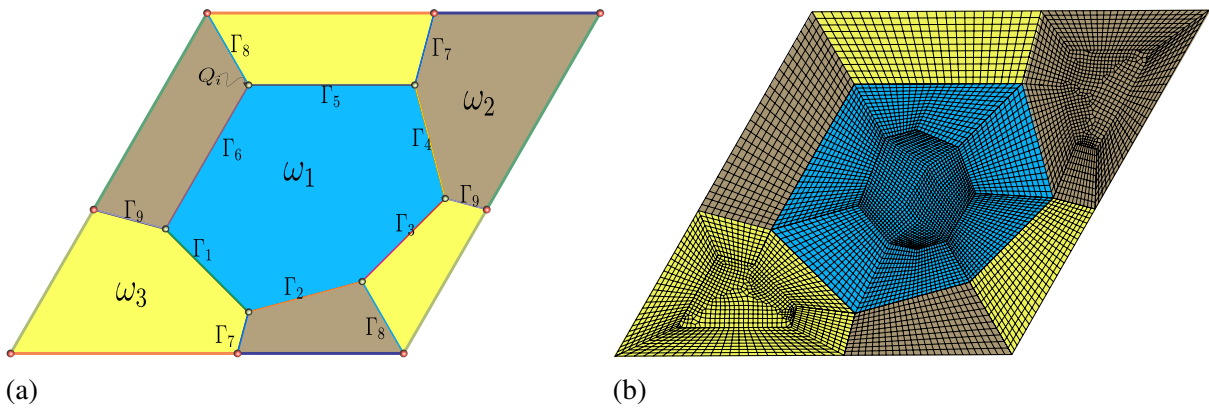


Figure 5.8.: Three grains periodic model with regular hexagons. The model has two types of quadruple points, one with rotational symmetry about the meeting internal triple line i.e. with all grain boundaries  $120^\circ$  far apart, and second with mirror symmetry of the lattice about the internal triple line i.e. two of the boundaries have  $150^\circ$  include angle. The model is discretized using both rectangular and triangular elements.

Simulation model shown in Fig. (5.8) includes three regular hexagonal grains of unequal sides. The central grain  $\omega_1$  is surrounded by  $\omega_2$  and  $\omega_3$  alternatively. The length of this RVE is  $a$  and height is  $b = \sqrt{3}/2a$ . This model has mirror symmetry about the minor diagonal. There are in total six quadruple points ( $P_1$  to  $P_6$ ), at  $\omega_1$  edges. We have two types of configurations at these quadruple points. In the first configuration, all three grain boundaries are  $120^\circ$  far apart and in the second configuration, two of the grain boundaries are separated with  $150^\circ$ , hence making an angle of  $105^\circ$  with the third grain boundary. There are total six grain boundaries, ( $\eta_1$  to  $\eta_6$ ) formed at intersections between  $\omega_1$  with  $\omega_2$  and  $\omega_3$  alternatively. Corresponding external triple lines ( $\Gamma_1$  to  $\Gamma_6$ ) are assumed to lie in the planes of respective boundaries. Additionally, there are three common grain boundaries between  $\omega_2$  and  $\omega_3$ . These are labeled from  $\eta_7$  to  $\eta_9$  with relevant triple lines ( $\Gamma_7$  to  $\Gamma_9$ ). Internal triple lines ( $\Sigma_1$  to  $\Sigma_6$ ) at six quadruple points are also there.

Internal and external triple lines energies are assumed constant for these simulations. For each triple line, the energy is  $\gamma_\Gamma = 16.8 \times 10^{-9}\gamma_0$  and for each quadruple point, internal triple line energy is  $\gamma_\Sigma = 6.3 \times 10^{-9}\gamma_0$ . These relative energy values are taken from Hackl et al. (2017), which are based on experimental data from the literature. For specific grain boundary energies, it is assumed that all grain boundaries are planar and their energies have no dependence on boundary plane inclination. Under these assumptions, Herring's (1951) relation at meeting

grain boundaries reduces to the Young's relation at each quadruple point. The balance equation at each  $P_i$  reads

$$\sum_i^3 \gamma_{\eta_i} \mathbf{t}_{\Gamma_i} = 0, \quad (5.11)$$

with  $\mathbf{t}_{\Gamma_i}$  is a vector tangent to grain boundary. The direction of  $\mathbf{t}_{\Gamma_i}$  is chosen such that the triple line vector at each junction must satisfy the relation,  $\mathbf{t}_{\Sigma_i} = \mathbf{n}_{\Gamma_j} \times \mathbf{t}_{\Gamma_j}$  and directed outward for all three boundaries (*as grain boundary and triple line are in common plane thus  $\mathbf{t}_{\eta_i} = \mathbf{t}_{\Gamma_i}$* ) (Adams et al., 1999; Rohrer, 2011a).

With six quadruple points, we have twelve equations for nine unknown grain boundary energies. This is an over determine system of equations. In order to calculate unknown grain boundary energies with a constraint to satisfy the equation (5.11) at each  $P_i$ , we define an objective function that minimize the residual  $\mathcal{R}$  (equation (5.12)). It is written as

$$\min_{\mathcal{R}} \frac{1}{2} \sum^P \left| \sum_i^3 \gamma_{\eta_i} \mathbf{t}_{\Gamma_i} \right|_2^2. \quad (5.12)$$

**Wolfram Mathematica® 11** is used to calculate these unknown energies with *Minimization* function. It converges to a global minimum for the linear system of equations. We get two different types of grain boundary energies. The relative value of these energies are  $\gamma_{\eta_1} = 0.4376\gamma_0$  and  $\gamma_{\eta_2} = 0.2265\gamma_0$ , with  $\mathcal{R} = 4.76852 \times 10^{-21}$ . The other parameters, diffusion coefficient along the surface and diffusion coefficient along the triple lines are taken isotropic in all these simulations.

The surface energy of each grain is calculated using equation (5.10). Each grain is considered, having fix orientation with respect to the flat surface. These orientations are given by the set of Euler angles  $(\phi_1, \Phi, \phi_2)$  for each grain. Set of normal vectors ( $\mathbf{m}$ ) in crystal reference system are calculated using transformation matrix, equation (5.13). In each simulation, we assign a fix value of  $c$  to each grain. The orientation angles are defined such that we have highly textured grain structure. In these arrangements, all grains belong to a same family with different orientations as shown in figures (5.9a) and (5.9b).

$$\begin{bmatrix} m_1 \\ m_2 \\ m_3 \end{bmatrix} = \begin{bmatrix} \cos \phi_2 & \sin \phi_2 & 0 \\ -\sin \phi_2 & \cos \phi_2 & 0 \\ 0 & 0 & 1 \end{bmatrix} \begin{bmatrix} \cos \Phi & 0 & \sin \Phi \\ 0 & 1 & 0 \\ -\sin \Phi & 0 & \cos \Phi \end{bmatrix} \begin{bmatrix} \cos \phi_1 & \sin \phi_1 & 0 \\ -\sin \phi_1 & \cos \phi_1 & 0 \\ 0 & 0 & 1 \end{bmatrix} \begin{bmatrix} n_1 \\ n_2 \\ n_3 \end{bmatrix} \quad (5.13)$$

The model is discretized using combination of four node quad and three node triangular elements, see Fig. (5.8b). Division of nodes at the boundary edges are kept constant with reference to the relevant grains boundaries on both sides. This discretization is helpful in implementing the periodic grain boundary conditions for the state variables. Simulations were tested for mesh independence. In the final version, we have 6566 quadrilateral and 62 triangular elements with in total 6496 nodes. Linear shape functions are used in finite element calculations. In the next sections, we will discuss the morphological evolutions for anisotropy surface energy in different orientated textured model.

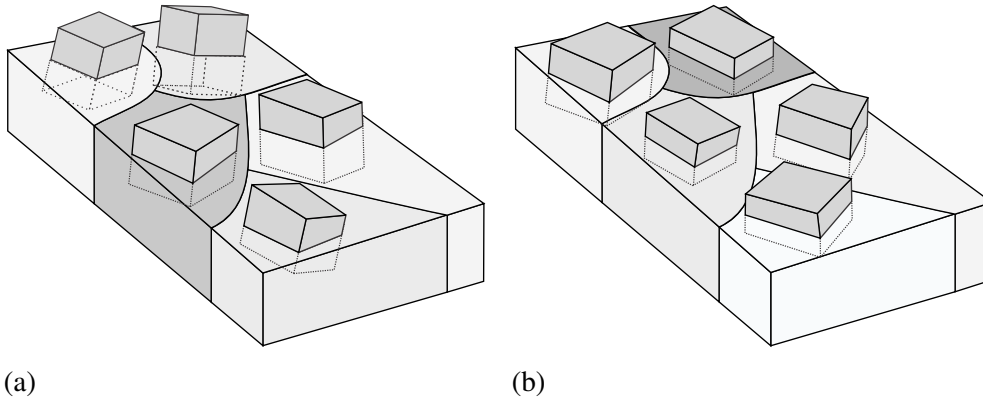


Figure 5.9.: The thin sheet of polycrystalline material with constituent grains. (a) is made up of crystalline with no preferred orientation. Such random orientations are quite rare in the solid materials. (b) represents a polycrystalline with oriented texture. These structured are often observed in rolled sheets. The existence of anisotropy in metals properties can be attributed to grains orientations.

#### 5.4.2. Simulation results and discussion.

##### 5.4.2.1. Three grains with $\{100\}$ orientation.

In order to orientate the grains for  $\{100\}$  with the planar surface in these simulations, Euler angles for three grains are tabulated in the surface energy function, table (5.1). For each grain, we set different anisotropy in the surface energy function and this was achieved by setting different value of  $c$  in equation (5.10) for each grain. In this set of simulations, central grain,  $\omega_1$  had  $c_{\omega_1} = 0.8$  and other two grains  $\omega_2$  and  $\omega_3$  had  $c_{\omega_2} = 0.7$  and  $c_{\omega_3} = 0.75$  respectively. Reference to section (5.3),  $\omega_1$  had minimum surface free energy in the principle direction,  $(1 - 0.8)\gamma_0$  in comparison with the neighboring grains. Thus, most of the matter moved towards the central grain based on the energetic arguments.

Table 5.1.: Three grains orientation

Grain	Angle		
	$\phi_1$	$\Phi$	$\phi_2$
$\omega_1$	$-45.0^\circ$	$0.0^\circ$	$-10.0^\circ$
$\omega_2$	$45.0^\circ$	$0.0^\circ$	$30.0^\circ$
$\omega_3$	$45.0^\circ$	$0.0^\circ$	$-30.0^\circ$

We started with a flat surface. The chemical potential was maximum at P's and along the grain boundaries. Figure (5.10) shows  $\bar{u}$  and  $J_i$  contours at different instant of time  $\bar{t}^n$ . Initially in a settling phase, fluxes orientated them in the appropriate directions. Overall gradient of chemical potential in the system was very high. It determined the directions of the fluxes in accordance with equation (3.29) for diffusion along the surfaces, and equation (3.31) for diffusion along the triple lines.

Onward after the settling of fluxes, the grooves started forming along the sites of intersecting boundaries. It is evident in figures (5.10a–c), that the grooves emerged along the grain boundaries and at quadruple points. It was observed that the material removed from the surfaces at these sites due to grooving, moved equally in both directions. As the system proceeded towards

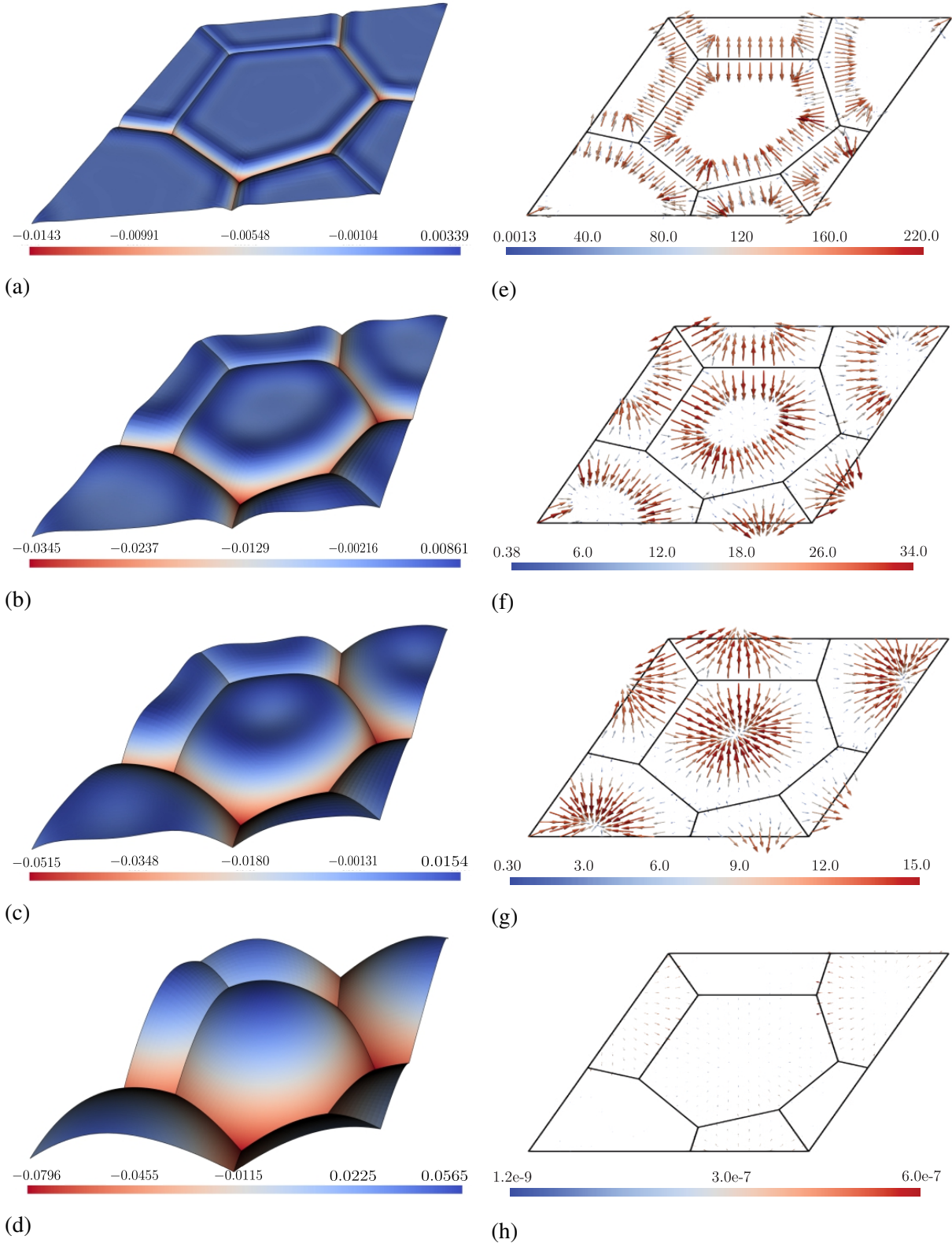


Figure 5.10.: Contour plots of  $\bar{u}$  and  $J_i$  fields for  $\{100\}$  oriented grains. In these results  $c_{\omega_{1,2,3}} = \{0.8, 0.7, 0.75\}$  respectively, and  $\bar{M}_\Gamma = 2.5 \times 10^5$ . Figures (5.10a–d) are  $\bar{u}$  contours at  $\bar{t}^{20}$ ,  $\bar{t}^{40}$ ,  $\bar{t}^{50}$ , and at the equilibrium, ( $\bar{t}^{70}$ ). We have groove of varying growth rates and relatively deeper grooves at the quadruple points. Figures (5.10e–h) show surface flux vectors,  $J_i$  at  $\bar{t}^{20}$ ,  $\bar{t}^{40}$ ,  $\bar{t}^{50}$ , and near to an equilibrium at  $\bar{t}^{65}$ . Initially these fluxes have higher magnitude along the grain boundaries and matter flows are directed in both sides along the grooves (see (f)). We have vanishing fluxes with subsiding thermodynamics forces in accordance with equation (3.29).

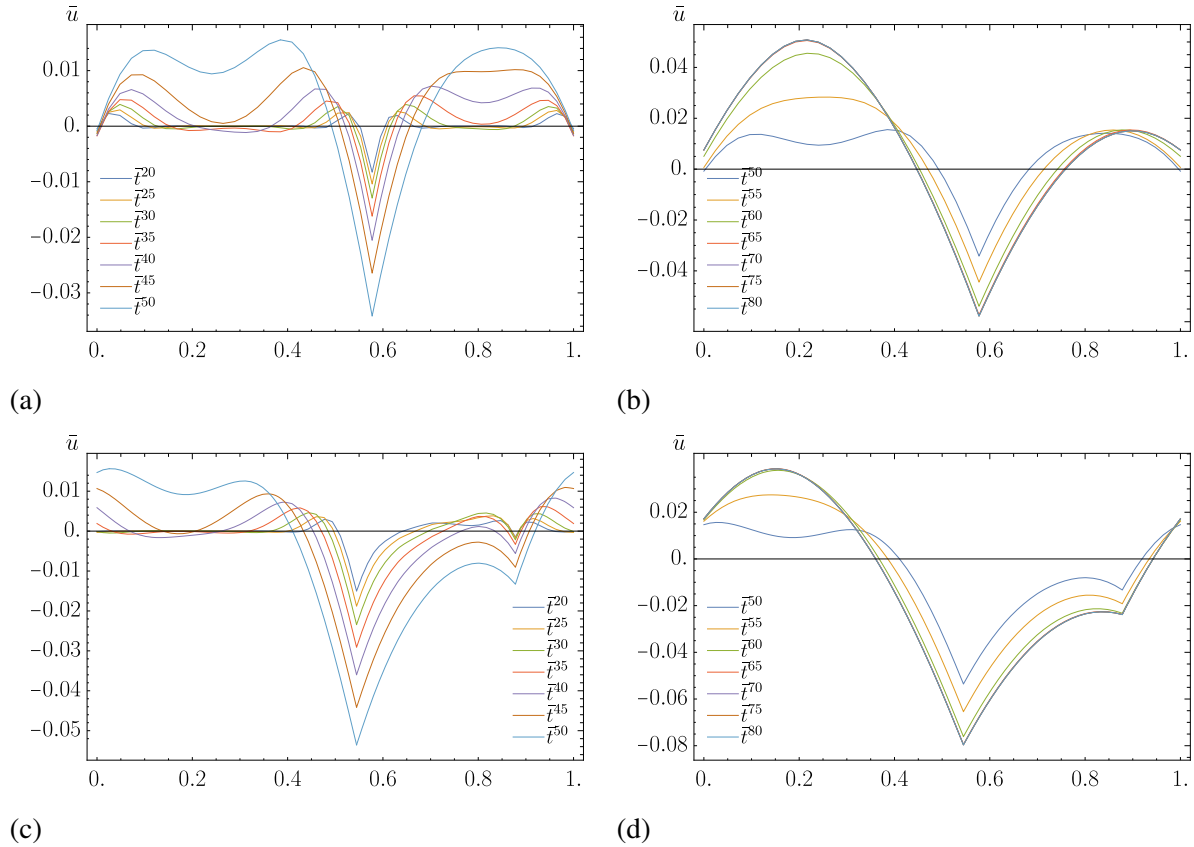


Figure 5.11.: Evolution of surface along two different cross sections at proceeding  $\bar{t}^n$ . In this simulation grains are oriented in  $\{100\}$  direction and  $\bar{M}_\Gamma = 2.5 \times 10^{-5}$ . With these configurations (a), and (b) shows evolution along the lower horizontal periodic boundary. Whereas, (c) and (d) show evolution of surface along section  $\overline{AA}$  in the RVE. The dissipation starts with the formations of grooves along the grain boundaries. We have groove profiles of constant mean curvatures with two different dissipation phenomena.

the equilibrium condition, the diffusion humps increased in their volumes and traveled towards the geometrical center of the grains. Overall directions of the fluxes along a surface were directed toward a central grain. This was due to the lowest surface energy in it. Figure (5.10h) shows a state of vanishing flux near to the equilibrium at  $\bar{t}^{65}$ . It is clear in this figure that we observed vanishing differential in the chemical potential. Figure (5.10d) is a contour plot for  $\bar{u}$  at  $\bar{t}^{70}$  with constant mean curvature. This shows the surface morphology due to the thermal grooving with nonzero constant chemical potential over the entire domain.

In order to explain the evolution kinetics of the grooving process and motion of the fluxes, Fig. (5.11) shows line views along two different cross sections. Initially, diffusional humps formations were along the grain boundaries with the plateaus in the middle region of each grain. As the process proceeds, these flat regions converged towards the surfaces of constant mean curvatures. In both cross sections, we had surface morphology with the constant mean curvature satisfying the relation  $\mu_i = \gamma_i K_i$ .

According to the analytical solution for growth of triple point Mullins (1956), and analytical solution for the growth rate of quadruple points Génin et al. (1992), the growth rates of  $P_i$ 's must be faster than  $\Gamma_i$ 's. These growth rates are expected to obey  $\bar{t}^{\frac{1}{4}}$  law together with anisotropic

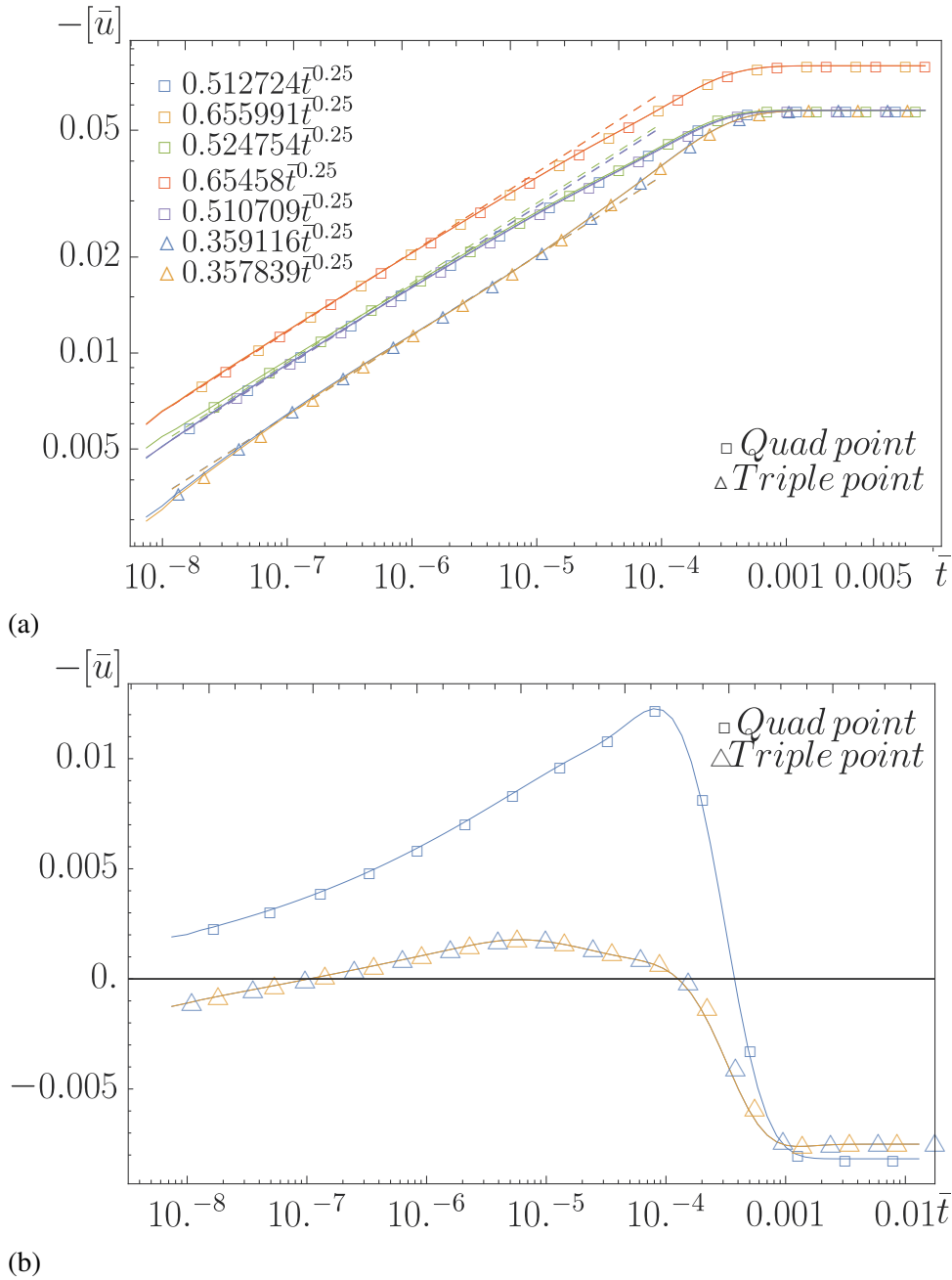


Figure 5.12.: Rate of the growth of  $P_i$  and points on the  $\Gamma_j$  for  $\{100\}$  oriented grains with  $\bar{M}_\Gamma = 2.5 \times 10^{-5}$ . (a) shows growth rates of these points using log-log scale. Although we have anisotropic surface energy, we have symmetric growth kinetics. The depth is fitted for  $1/4$  power law. These curves have similar coefficients. (b) shows growth rates of points showing the protrusion formation. These evolutions are plotted on semi-log scale. The fluctuations are due to influx of the matter to achieve the state of minimum energy.

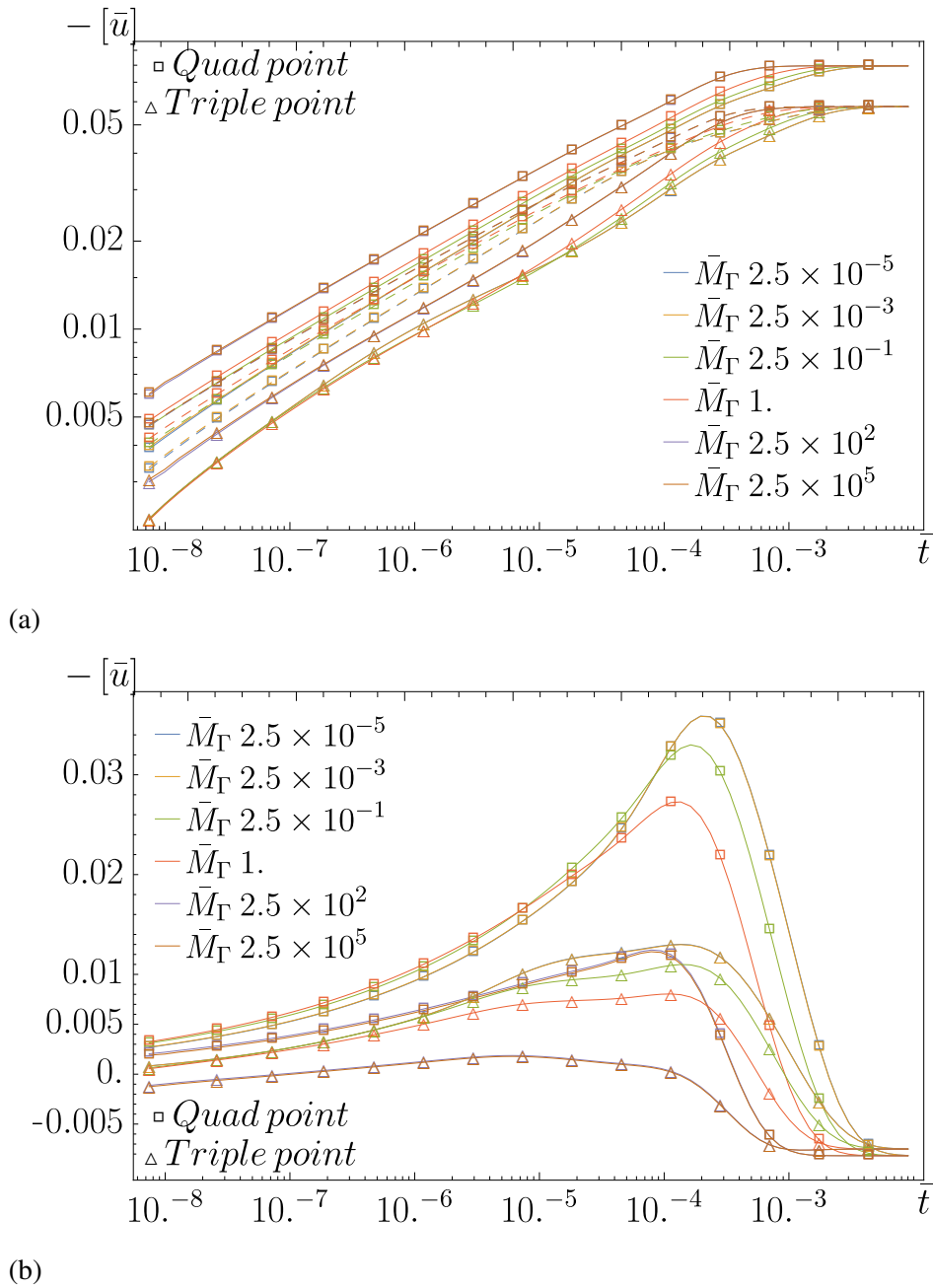


Figure 5.13.: Effect of  $\bar{M}_\Gamma$  on growth kinetics of  $P_i$ 's and points on  $\Gamma$ 's for  $\{100\}$  oriented RVE. Figure (5.13a) shows growth of quadruple points and triple points with increasing depths on log-log scale. Figure (5.13b) shows evolution of points depicting backpedal behavior due to influx of matter. With an increasing value of  $\bar{M}_\Gamma$ , we have relaxation in the motion of matter along the triple line due to relative increase in  $M_{\Gamma_i}$ , mobility along the triple line. The ultimate effects are fast growth kinetics along the triple line and comparatively slow growth in groove depths due to the surface diffusion.

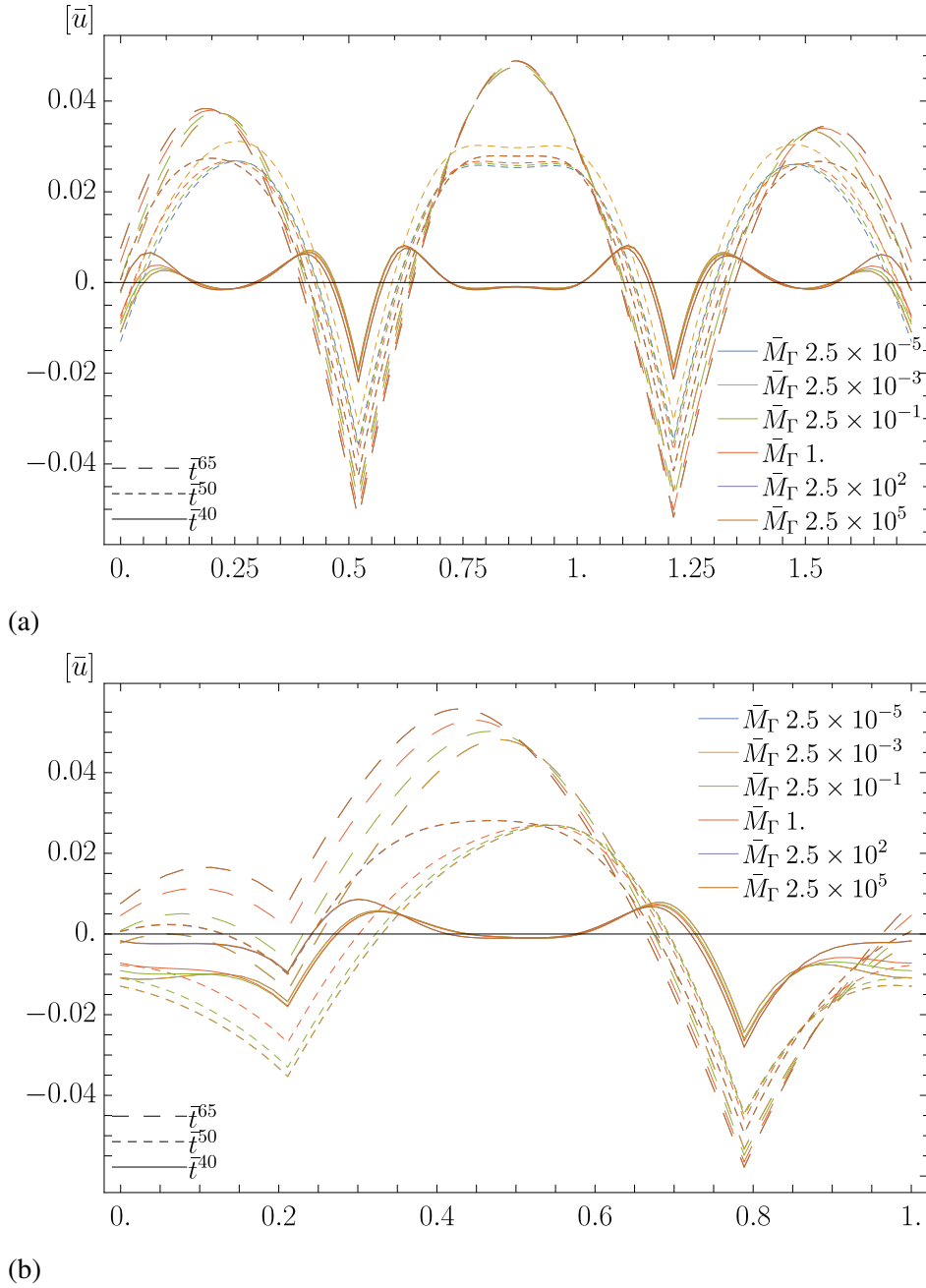
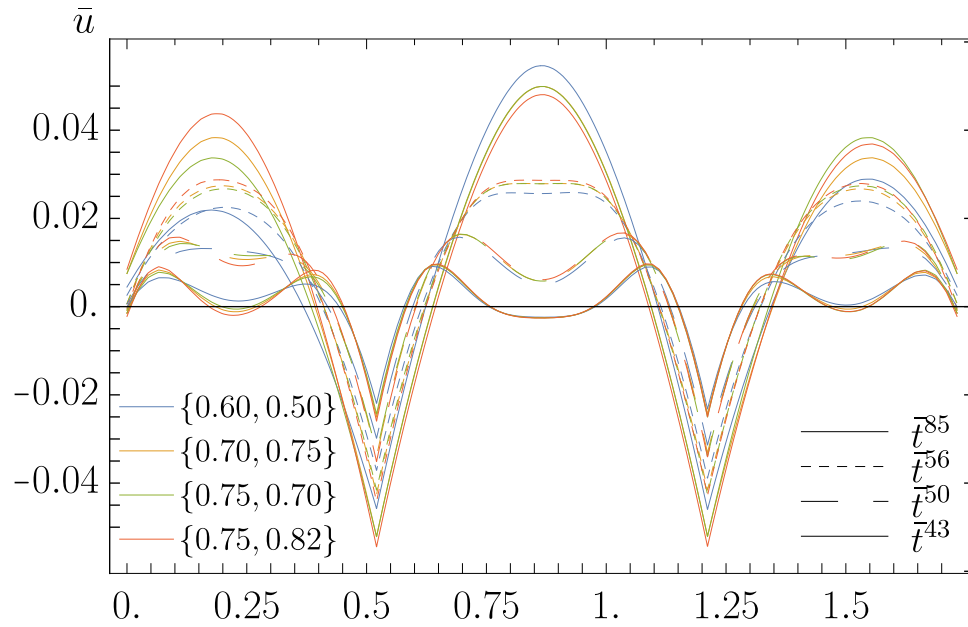
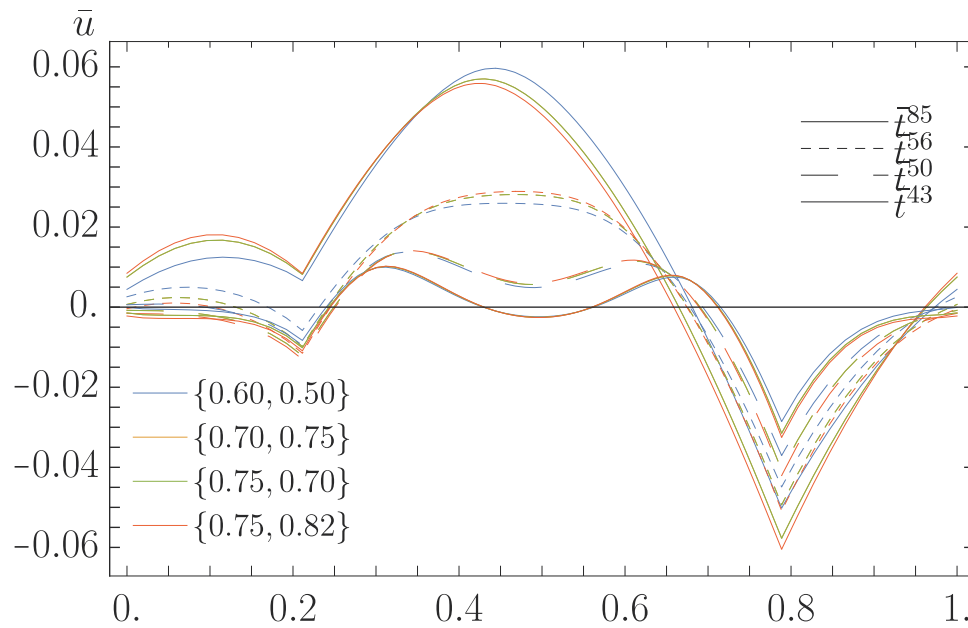


Figure 5.14.: Effect of  $\bar{M}_\Gamma$  on surface profiles and grooves growth rates at different time  $\bar{t}$ . (a): surface profiles along the major diagonal. (b): surface profiles along the minor diagonal. For higher value of  $\bar{M}_\Gamma$ , the groove growth is determined by the diffusion along the surface, and we have deeper grooves along the quadruple points and increase of the equilibrium dihedral angles.



(a)



(b)

Figure 5.15.: Evolution of surface with  $c_{\omega_1} = 0.8$  and varied  $c_{\omega_{2,3}}$  in the peripheral grains at different instants of  $\bar{t}^n$ . (a) shows evolution along the major diagonal and (b) gives evolution along the minor diagonal. We observe thermodynamically consistent behavior. Any increase in surface energies, due to decrease in the value of  $c$  in equation (5.10), increase the volume of diffusional hump at a middle grain.

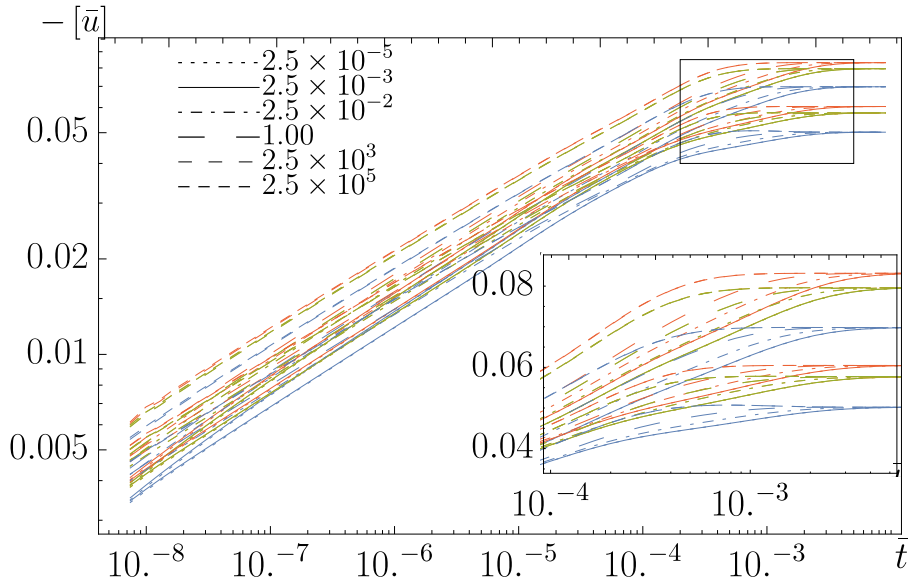


Figure 5.16.: Evolution of  $P_i$ 's, with constant  $c_{\omega_1} = 0.8$ , and varying set of  $\{c_{\omega_{2,3}}\}$  using log-log scale. The figure shows evolution of quadruple points depth for decreasing anisotropy in the peripheral grains. We observe a linear relationship with anisotropic factor  $c$  in equation (5.10). The plot also compares the effect of  $\bar{M}_\Gamma$  on pit growth. We observe consistent behavior in reference with Fig. (5.13).

surface energy in the model.

In Fig. (5.12), depth evolution of quadruple and triple points (these points are taken at an intersection of  $\Gamma$  with RVE boundaries.) are plotted. The maximum growth rate of quadruple point is  $0.65458\bar{t}^{\frac{1}{4}}$ , which is almost double of the growth rate of the points on  $\Gamma$ 's. It is also evident that there is not much difference between the growth rates of the quadruple points. We also observe slight variations in the growth rate as the system reached towards an equilibrium. The growth rate of quadruple points reduced down whereas triple lines demonstrated increase in the growth rate kinetics in the later stage. It was also observed that one of the quadruple points showed negative diffusion with progressivity. Initially, there was a removal of the material at this junction but at later stage, some fluxes directed towards this node, and caused accumulation of material at this junction. We found decrease in the depth of quadruple point. Figure (5.12b) shows depth evolution of these points on semi-log scale. In the beginning, depth of the quadruple point decreases up to  $-0.015$ . Later on, a plateau of an apex height  $0.007$ , was formed.

Simulations with different values of  $\bar{M}_\Gamma$ , a ratio between  $M_{\Gamma_i}/M_i$  explain the effects of diffusion coefficients on the grooves growth kinetics and morphological characteristics. It was observed that with the changes in this parameter, kinetics of the overall grooving process varies, but finally these solutions attained the constant equilibrium state. The growth rates of quadruple and triple points are compared for different values of  $\bar{M}_\Gamma$  in Fig. (5.13). These points followed separate paths with different growth rate, but ultimately reached to constant depth.

In Fig. (5.14), evolution of surface along major and minor diagonals are plotted at  $\bar{t}^{40}$ ,  $\bar{t}^{50}$ , and  $\bar{t}^{65}$ . These results reveal the limiting ranges of  $\bar{M}_\Gamma$ . The values for this parameter range between  $2.5 \times 10^{-3}$  to  $2.5 \times 10^3$ . These approximations are helpful in determining the surface diffusion coefficients for different materials at particular temperatures. For the small value of  $\bar{M}_\Gamma$ , the surface diffusion dominates and growth rate was higher along the pit. This high rate was due

high diffusion coefficient along the triple line channel. From Fig. (5.14a), kinetics of chosen triple points show that initial dominance of line diffusion caused slow growing surface profiles, but at the later stage the surface diffusion dominated and growth kinetics accelerated with the widening of dihedral angle.

We simulated our model for different set of anisotropies in  $\{100\}$  oriented model. Here, we are reporting the results for the cases with constant value of  $c_{\omega_1} = 0.8$  on the central grain and different anisotropies in the peripheral grains  $[c_{\omega_2}, c_{\omega_3}]$ . Figure (5.15) shows the evolution of surface along the diagonals of the RVE. Growth kinetics minimized the total energy of the system by establishing the thermodynamic equilibrium. Overall growth behavior was function of the difference in the surface energies. The grains with the higher energy potentials minimized their energies at the expense of maximum dissipation through the motion of matter, and ultimately producing deeper grooves. This behavior caused production of diffusion humps with higher plateau in the grains of comparatively lower energies.

Figure (5.16) shows growth rates of  $P_i$ 's for different sets of  $[c_{\omega_2}, c_{\omega_3}]$ . It was observed that increase in  $c_{\omega_i}$  of peripheral grains produced deeper grooves pits. Accumulated with the effect of varying  $\overline{M}_\Gamma$ , process kinetics demonstrated analogous behavior as discussed in the previous case shown in Fig. (5.13). Thus, the growth rate of each point varied with change in the diffusion coefficients but it attained the constant depth of the equilibrium.

### 5.4.2.2. Three grains with $\{110\}$ orientation.

It has been shown in the Fig. (5.7) that with an increasing anisotropy in surface energy, we observed formation of intersecting regions along the edges in  $\xi$  plots. These formations excluded the range of orientations from a equilibrium crystal shape. Thus, if crystals/grains lie in the vicinity of these orientations, we observe discontinuity in the gradient function of  $\xi$  and it is expected that we have formations of lower energy planes along the grain boundary in thermal grooving or serrated facets at the free surface. These low energy planes can appear in different configurations with rough grooves as explained by Ramasubramaniam and Shenoy (see Fig. (5.17)). In section (5.4.2.1), we observed groove for  $\{100\}$  textured RVE with normal profiles for constant mean curvature along the surface of each grain, and even with critical values of  $c$  in the surface energy function we had normal groove shapes facilitating the growth kinetics along the quadruple points. A General representation of these profiles is shown in Fig. (5.17a).

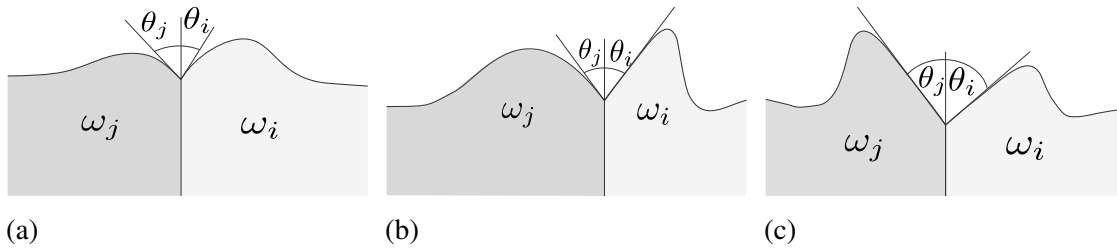


Figure 5.17.: A schematic description of different grooves profiles observed in the annealing. (a) shows a groove with continuous curvature on its both edges. (b) illustrates groove with planar face on one of its forming edge. (c) illustrates the groove with planar faces on both of its forming edges. The dihedral angle includes by these boundaries are function of boundary plane inclination and grains misorientation.

Table 5.2.: Three grains orientation

Grain \ Angle	$\phi_1$	$\Phi$	$\phi_2$
$\omega_1$	$-30.0^\circ$	$-45.0^\circ$	$0.0^\circ$
$\omega_2$	$0.0^\circ$	$45.0^\circ$	$45.0^\circ$
$\omega_3$	$30.0^\circ$	$45.0^\circ$	$0.0^\circ$

For the numerical simulations results that we will discuss in this section, we assumed that all grains were oriented in such a way that they all belongs to  $\{110\}$ . Set of Euler angles used for three grains are given in table (5.2) to fix the orientations with the normal. Although we simulated our numerical experimentation over the complete range of an anisotropy factor  $c$ , but we will discuss two cases in particular for the kinetics of grooving in the following sections.

**{110} oriented grains with low to moderate anisotropy.**

In order to study the kinetics of thermal grooving under low to moderate anisotropy in the polycrystalline, the scalar factors in surface energy function equation (5.10) for three grains were fixed to  $c_{\omega\{1,2,3\}} = \{0.3, 0.4, 0.6\}$  respectively. In this configuration, the circumferential grains had mild anisotropy, whereas the central grain,  $\omega_1$  had no anisotropy. Conclusively, the central grain energy vector plot did not have any intersecting volume. We started our simulations with initially flat surfaces. At the beginning, all the fluxes orientated themselves in accordance with the relations given by equations (3.29) and (3.31). We exclude some initial steps as settling time from the plotting and afterwards the dissipation processes proceeded with pits and thermal grooves formations due to mass transport along the surface geometry and the triple line channels.

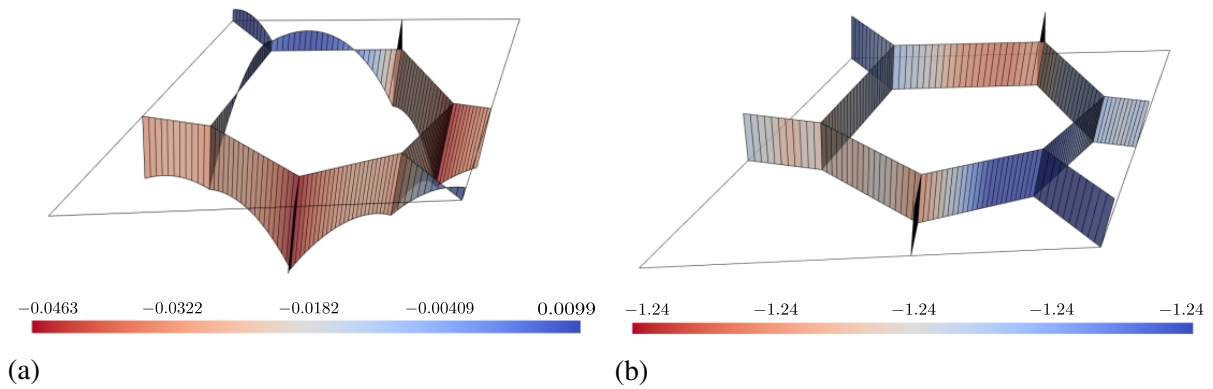


Figure 5.18.: Distribution of process parameters along the grooves roots at the equilibrium state. (a) shows  $\bar{u}$  profiles along the grooves roots. We have groove profiles with varying depths along the boundaries. Quadruple points have deeper depths. (b) shows constant  $\bar{\mu}$  along the  $\Gamma_i$  at equilibrium, which is the conditions for vanishing fluxes in the system in accordance with equations (3.29) and (3.31).

Figure (5.19) shows displacement,  $\bar{u}$  and chemical potential,  $\bar{\mu}$  fields along the free surface with progressing time. Figure (5.19e) exhibits  $\bar{\mu}$  at  $\bar{t}^{20}$ . It is evident that the chemical potential was maximum values along the grain boundaries. Consequently, the material must removed form these sites to minimize the total energy of the system. The process started with the formations of grooves and pits along the triple lines and at quadruple points respectively. The rates of pits formations were faster at the quadruple points in comparison with the grooves in the geometry. The diffusional humps formations along the boundary grooves showed ordinary shapes with constant mean curvatures. Figures (5.19a–d) show  $\bar{u}$  field in quasi two dimensions. We observed surfaces with varying groove profiles. Also, figures (5.19e–h) show  $\bar{\mu}$  field distribution along the free surface. As system progressed towards the equilibrium, we had the state of constant chemical potential with the vanishing fluxes. For the sake of completeness, Fig. (5.18) shows the overall groove profiles along the surface (Fig. (5.18a)) and constant chemical potential along the triple lines (Fig. (5.18b)). With these plots, it is ensured that our simulation model satisfied the condition of constant chemical potential over the complete domain as stated in equation (3.32). With the increasing anisotropy, we expect the formation of singular faces due to splitting of the high energy surfaces into low energy faces, but we did not observe such profiles for these configurational settings. To elucidate this claim, figures (5.20–22) show morphological growths along the different cross sections in the RVE. Grooving along the surface

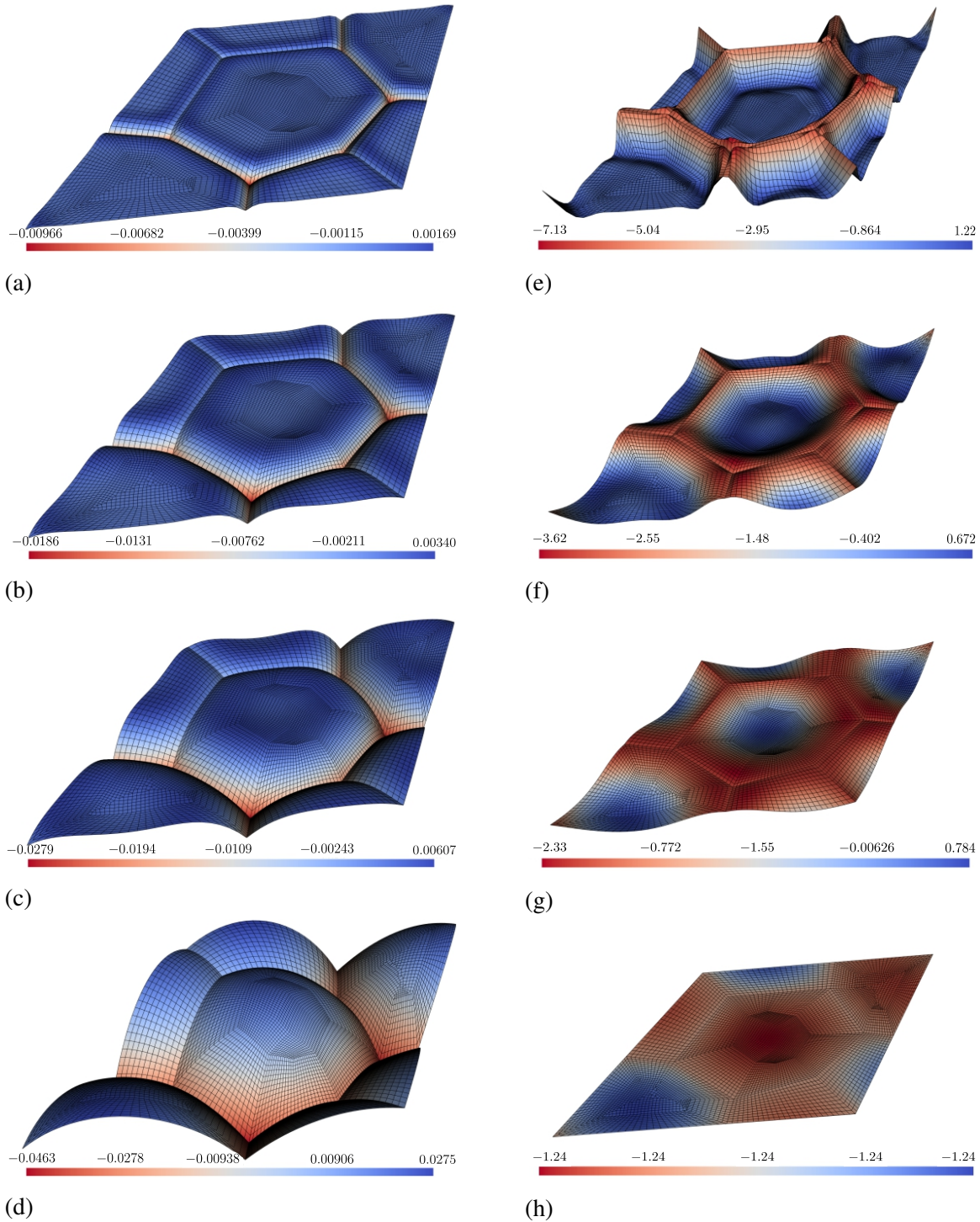


Figure 5.19.: Thermal grooving with moderate anisotropic surface energies. In this configurations  $c_{\omega_{1,2,3}} = \{0.3, 0.4, 0.6\}$  and  $\bar{M}_\Gamma = 2.5 \times 10^5$ . Figures (5.19a–d) show field values of  $\bar{u}$  and we have formation of groove profiles with continuous surface curvatures. Figures (5.19e–h) show evolution of  $\bar{\mu}$  at  $\bar{t}^{20}, \bar{t}^{35}, \bar{t}^{45}$  and  $\bar{t}^{70}$ . Initially with high gradient, the diffusion proceeds to establish the constant distribution of  $\bar{\mu}$  along the surface.

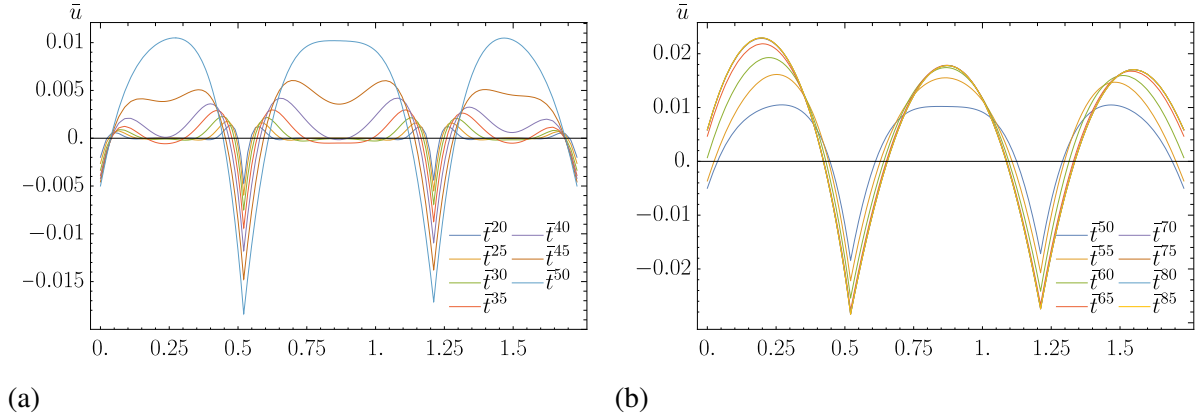


Figure 5.20.: Evolution of  $\bar{u}$  along the major diagonal. (a) shows evolution of grooves with the diffusional humps along the grain boundaries. We do't observe any secondary diffusional hump with low to moderate anisotropy. (b) shows evolution of groove with single diffusional hump. The humps formations are in accordance with the surface energy model.

showed normal growth kinetics. Based on energetic arguments, there must be maximum flow of flux towards  $\omega_3$  due to its lowest energy, and maximum flow of matter must be from the central grain  $\omega_1$ . In figures (5.20a) and (5.20b), evolution of surface along the major diagonal consolidate this statement. We observed different groove profiles, e.g. surfaces with secondary diffusional humps, flat region on the grain free surface. All these formations are due to difference in anisotropy of the surface energy function.

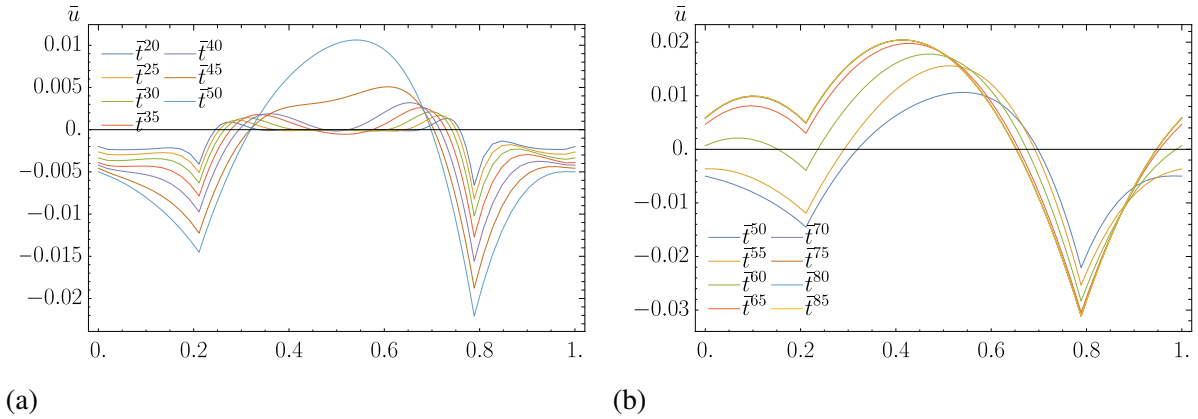


Figure 5.21.: Evolution of  $\bar{u}$  along the minor diagonal. The three grain have low to moderate anisotropy with  $\bar{M}_\Gamma = 2.5 \times 10^{-3}$ . In (a), a deeper pits are formed at  $P_1$ . Also we have formation of high curvature plane along the free surface of the central grain. (b) shows the formation of raised plateau with comparatively lower height with the other orientations of same anisotropy.

Figures (5.21a) and (5.21b) show evolution along the minor diagonal. The central diffusional hump depicts the growth along the free surface of  $\omega_1$ , whereas lines on both sides depict the growth along the triple line  $\Gamma_8$  in accordance with Fig. (5.8a). The quadruple points at triple line junctions show different behavior. Initially we observed development of pit at left quadruple point. At the stage near to equilibrium, we observed positive motion at this region. A hump with increase in the dihedral angle was formed and consequently width of the groove also increased.

Asymmetric shapes of  $\omega_1$  surface during the evolution corresponded to difference in the surface energies of neighboring grains.

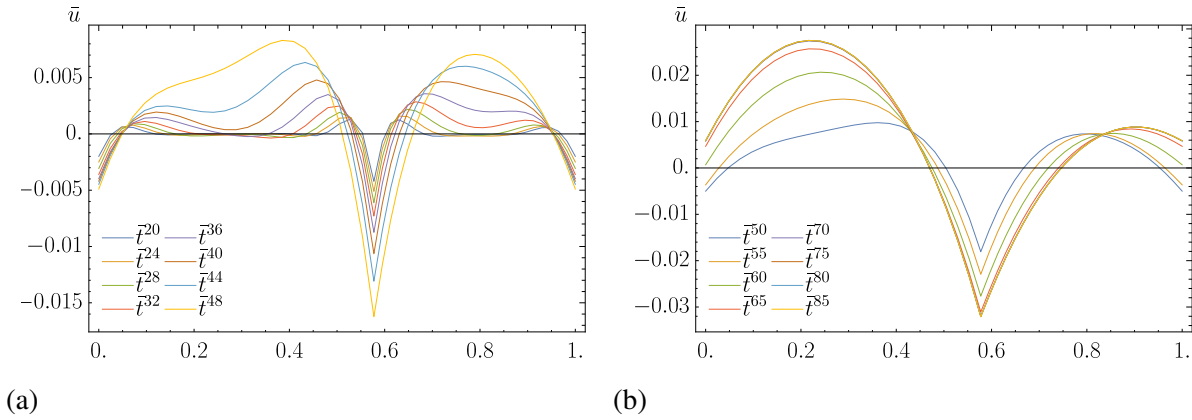
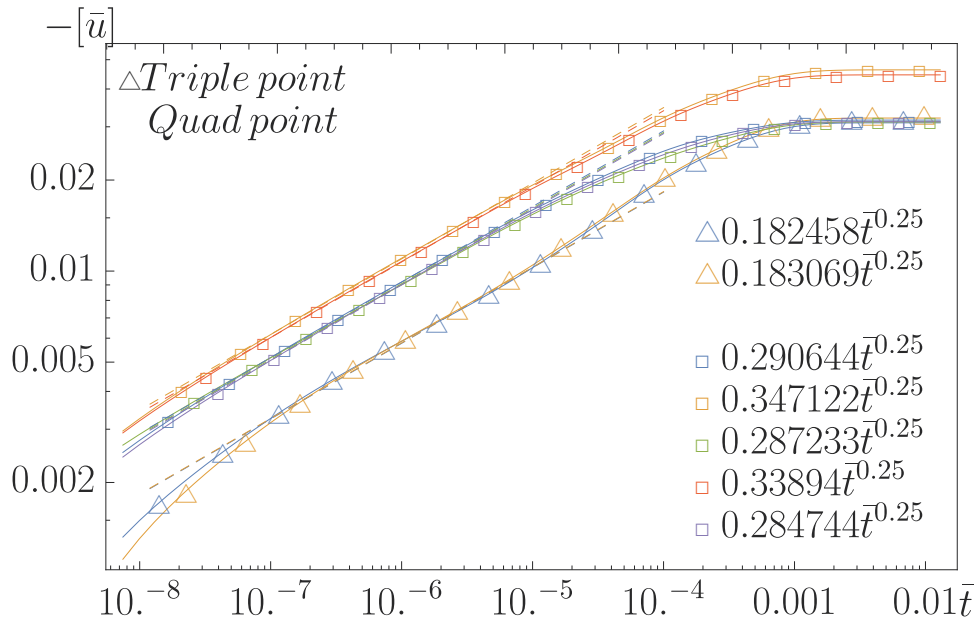


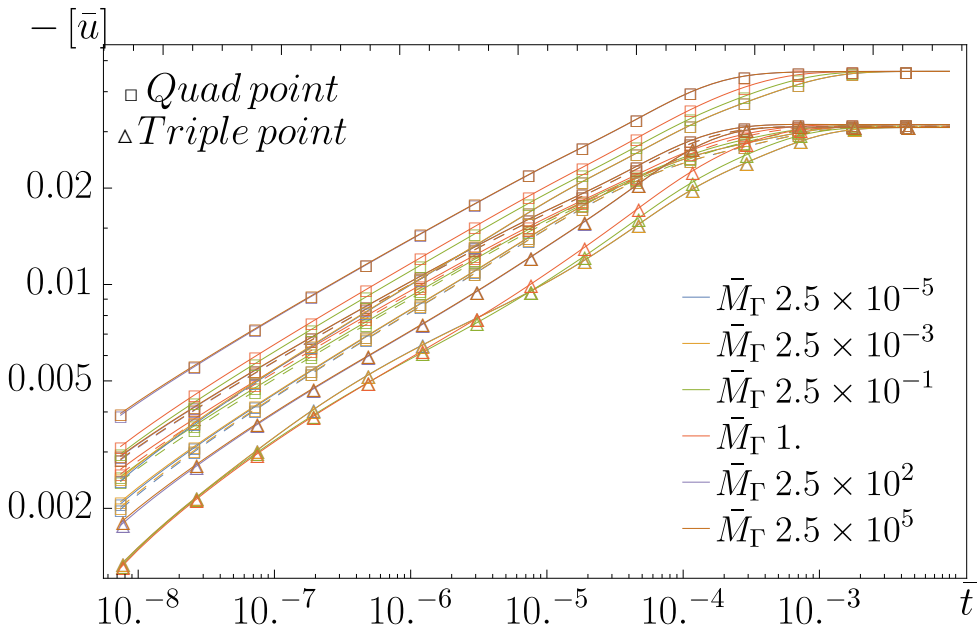
Figure 5.22.: Evolution of grooves along the horizontal boundary between  $\omega_2$  and  $\omega_3$ . Evolution along this section simulate the grooving in two dimensions. We have formation of asymmetric grooves with flat surface. (b) shows grooves with continuous mean curvature and vanishing flat plateau along the free surface.

Figure (5.22) shows morphology along the horizontal edge of the RVE. This boundary is shared by  $\omega_2$  and  $\omega_3$ . As  $\omega_3$  had the lowest energy, there must be maximum flow of flux to this grain. This cross section demonstrate two dimensions thermal grooving with anisotropic surface energy. We had formation of asymmetric groove profiles with different inclination with the horizontal.

Overall growth rates in different parts of the RVE were constant. Figure (5.23) shows the growth rates of pit depths at quadruple points and groove depths along the triple lines. Up to moderate range of anisotropy in the surface energy, we had approximately similar growth rates for symmetric elements. We also observed slight variations in the groove depth as shown in Fig. (5.23a) for the triple lines. These fluctuations were also observed in some experiments in the literature. Figure (5.23b) plots a comparison for varying relative diffusion coefficients  $\bar{M}_\Gamma$ . The system reached to constant equilibrium depths with different kinetics at different values of  $\bar{M}_\Gamma$ .



(a)



(b)

Figure 5.23.: Growth rate of quadruple points and triple points. (a) shows growth rate for  $\bar{M}_\Gamma = 2.5 \times 10^{-3}$  on log-log scale. The fitted curves shows that grooving took place with  $\bar{t}^{0.25}$  growth law. (b) shows growth kinetics of  $P_i$  and points on  $\Gamma_i$  for different values of  $\bar{M}_\Gamma$ . The overall steady state have constant grooves and pit depths with varying growth rates.

### $\{110\}$ oriented grains with moderate to critical anisotropy.

In section (5.4.2.2), we observed grooves without any singularity for low to moderate surface energy anisotropy in  $\{110\}$  textured RVE. It is evident from the results that groove profiles showed continuous curvature along the surfaces of the grains. With increase in the anisotropy factor  $c$  of the surface energy, we observed formation of intersecting regions in the polar plots as shown in Fig. (5.7). These volumes restricted the surface to some particular lowest energy faces over the range of orientations in the intersecting regions.

The increase of  $c$  in surface energy function cause increase in the volume of overlapping region, thus adding wide range of orientation vectors in the set of missing range. In this section, we will discuss the results for the moderate to the critical range of  $c$  in the surface energy function. In these results, we fixed the anisotropies,  $c_{\omega\{1,2,3\}} = \{0.8, 0.75, 0.82\}$  for three grains respectively. In reference with section (5.3), grains  $\omega_1$  and  $\omega_3$  lied in the critical range of anisotropy, while  $\omega_2$  had mild range of anisotropy in surface energy. With this energetic configuration,  $\omega_3$  had the lowest energy and  $\omega_2$  had the highest energy. It was expected that  $\omega_3$  and  $\omega_1$  observed some increase in reference with  $\omega_2$  on the basis of energetic arguments. Other model parameters grain boundary energies, external and internal triple lines had same values in accordance with the previous simulations.

Figure (5.24) shows the grooves formations due to surface diffusion and flux vectors field at different instants of  $\bar{t}^n$ . In initial settling steps, surface flux vectors orientated themselves in accordance with the surface gradient of chemical potential,  $\nabla_s \mu$ . The formations of grooves began at the locations of relatively high chemical potential, ultimately they were showing the highest value of flux vector at these sites. Figure (5.24a) shows initiation of grooves along the boundaries and at quadruple points for  $\bar{t}^{20}$ . As the diffusion progressed, the depths at grooves increased at different rates. At  $\bar{t}^{30}$ , planar faces appeared along  $\Gamma_1$  and  $\Gamma_3$ , triple lines between  $\omega_1$  and  $\omega_3$ . The lengths and as well as heights of these singular planar faces increased with proceeding time  $\bar{t}^n$ . Two more planar faces emerged along  $\Gamma_4$ , and  $\Gamma_7$ , are shown in Fig. (5.25), from the different perspective.  $\Gamma_4$  is the triple line between  $\omega_1$  and  $\omega_3$  and  $\Gamma_7$  lies between  $\omega_2$  and  $\omega_3$ . These faces have unequal depth along the grain boundaries with maximum height at common quadruple point  $P_6$ . The height of all other planar faces also varied longitudinally. Planar faces along cross sections  $\overline{SS}$  &  $\overline{VV}$  in Fig. (5.24) showed maximum height in the mid plane. It was observed experimentally that if crystalline orientations are in a window around  $45^\circ$  from the initial flat surface i.e.  $\{110\}$  with normal, we expect formations of planar facets in some part of the thin film (Zhang et al., 2004).

Surface morphology with singular grooves renders different growth kinetics to the grooving process. The quadruple points and triple lines attached to the region of singular grooves show faster growth rates with deeper grooves. Figures (5.26a) and (5.26b) show growth kinetics at section  $\overline{SS}$ . This section starts from the free boundary in  $\omega_3$  and ends in the middle of  $\omega_1$ . Along this section, the planar face has maximum height. Planar facets formed in  $\omega_3$ , while  $\omega_1$  observed normal groove profiles. There was increase in length of the face with progressing depth of the groove. It was also observed that there was no change in the dihedral angle formed along this boundary. Figures (5.26c) and (5.26d) show groove growth kinetics along section  $\overline{tt}$ . This section existed over  $\omega_1$  and  $\omega_2$  as shown in Fig. (5.25b). Planar groove was formed at the  $\omega_2$  side, while face shared by  $\omega_1$  evolved with normal continuous profile. Length of the planar low energy face also increased with grooving. There was also no change in the dihedral angle. After  $\bar{t}^{65}$ , it was observed that these groove profiles had more than one planar face.

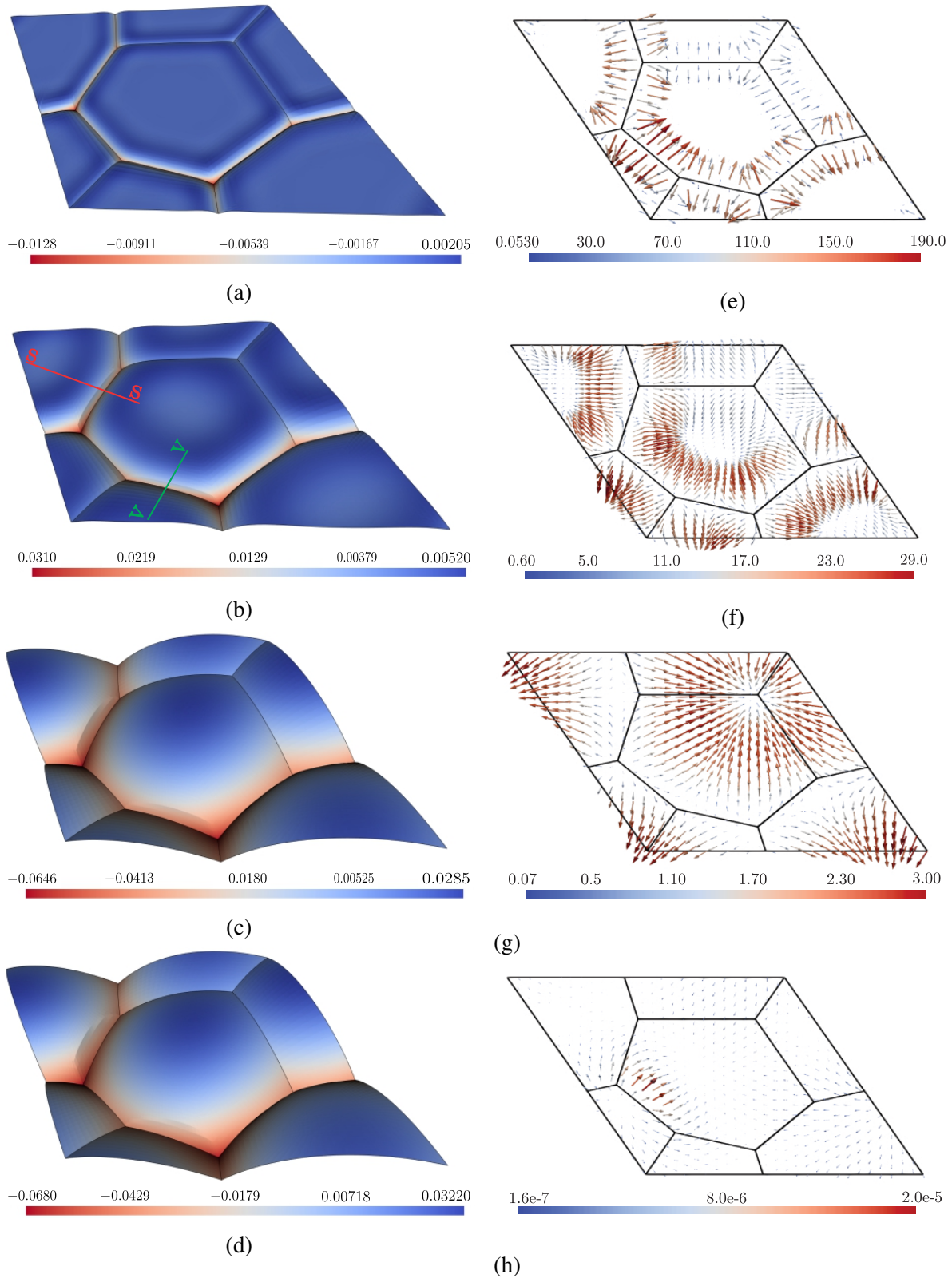


Figure 5.24.: Evolution of  $\bar{u}$  and  $J_i$  fields along the surface. In these results,  $c_{\omega_{1,2,3}} = \{0.8, 0.75, 0.82\}$  respectively and  $\bar{M}_\Gamma = 2.5 \times 10^{-3}$ . Figures (5.24a–d) show the contour plots of  $\bar{u}$  at  $\bar{t}^{20}$ ,  $\bar{t}^{40}$ ,  $\bar{t}^{60}$  and at  $\bar{t}^{75}$ , the equilibrium state. We observed formation of grooves with flat faces along the cross sections  $\overline{SS}$  and  $\overline{VV}$ . These planar faces proceeds both in longitudinal and lateral directions with increasing length and width. Figures (5.24e–h) show  $J_i$  vector field at  $\bar{t}^{20}$ ,  $\bar{t}^{40}$ ,  $\bar{t}^{60}$  and  $\bar{t}^{70}$ , near to the equilibrium state. Initially, the flux directions are along the both sides of the grooves. The flux flow is higher in the region of planar grain boundaries, thus ultimately causing accelerated growth kinetics in these parts of the geometry.

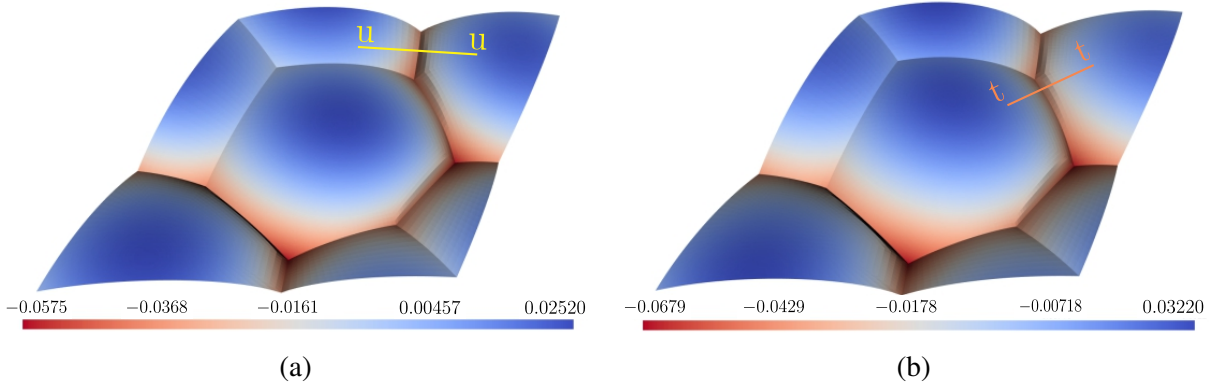


Figure 5.25.: Contour plots for  $\bar{u}$  from another view to show the other two planar grooves along  $\Gamma_4$  and  $\Gamma_7$ . (a) is at  $\bar{t}^{60}$ . (b) is at  $\bar{t}^{75}$ . It is also clear in this perspective view that two planar faces merge at  $\Gamma_i$  junction, and causes accelerated growth rate.

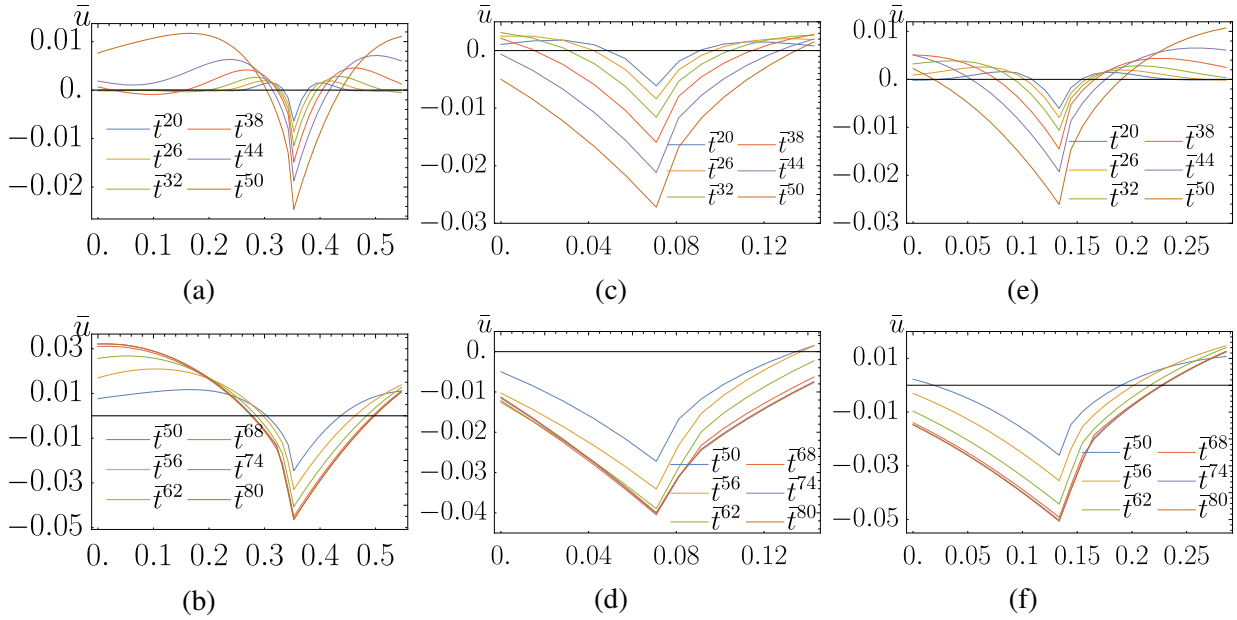


Figure 5.26.: Evolution of grooves with planar faces along the different cross sections. (a),(b) show evolution of grooves along  $\bar{s}\bar{s}$ . Similarly, (c),(d) show groove formation along  $\bar{t}\bar{t}$ , and (e),(f) show groove shape along  $\bar{v}\bar{v}$ . The length of these planar faces increases with progressing time. It is observed that these planar faces move parallel, as the depth of the grooves increase.

This situation arose due to combine effect of the facets in the neighboring boundaries. These two planar grooves met with each other and produced multi facet profile (see cross section  $\bar{u}\bar{u}$  in Fig. (5.25a), which merged at the quadruple point  $P_6$ ). Figures (5.26e) and (5.26f) show kinetics along cross section  $\bar{v}\bar{v}$ . This section is chosen along the  $\Gamma_4$ , between  $\omega_1$  and  $\omega_3$ . We observed planar facet formation for the face shared by  $\omega_3$  and normal groove profile along  $\omega_1$ . We had maximum facet length along this cross section with  $\bar{u} = 0.05$ . After establishing a state of equilibrium between grain boundary energy and the surface with lowest energy in this orientation, there was no change in the dihedral angle for proceeding grooving process.

It was also observed that overall growth kinetics slowed down in these simulations in compar-

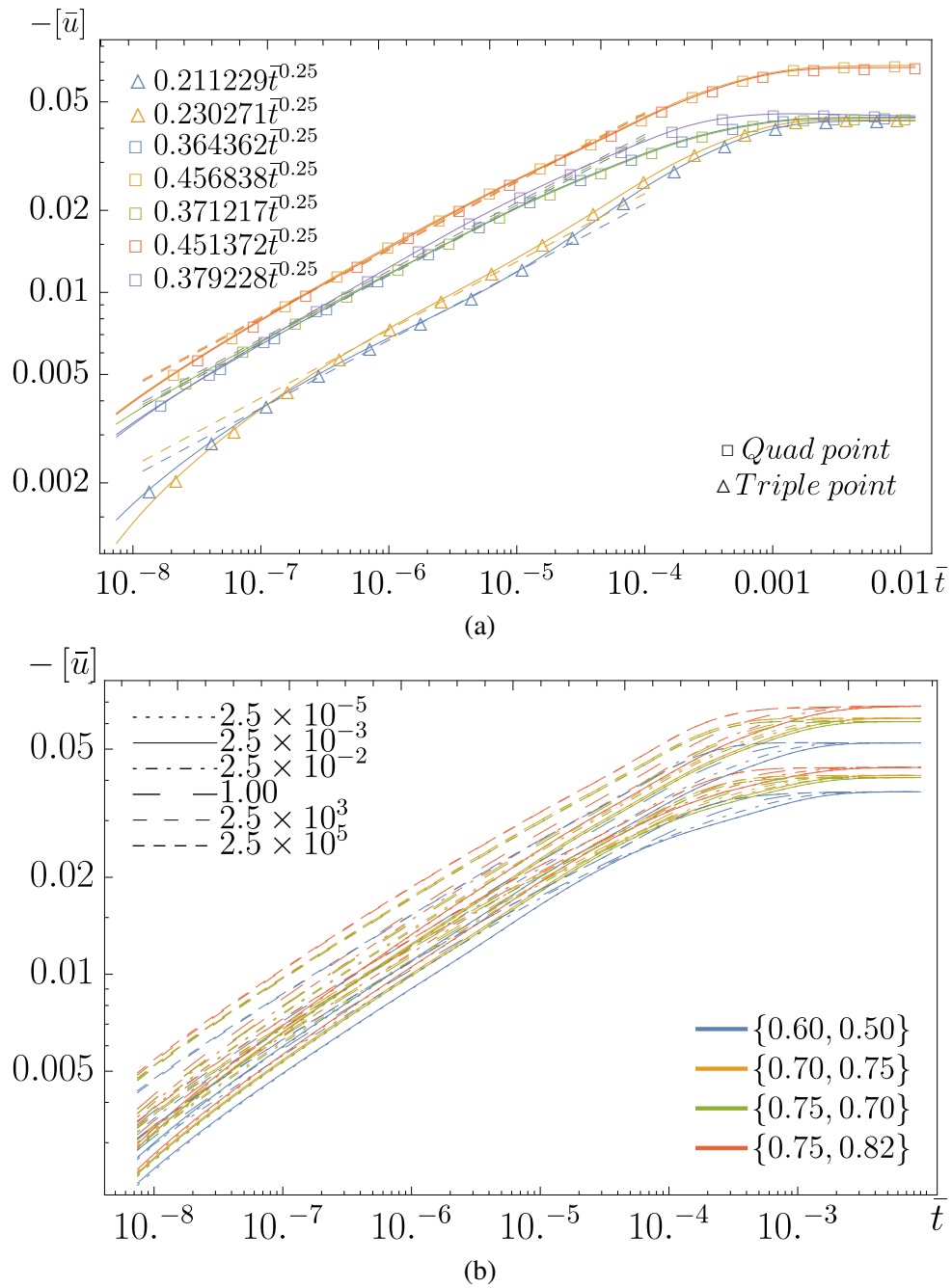


Figure 5.27.: Growth kinetics of  $P_i$  and points on  $\Gamma_i$  using log-log scale. (a): the depth evolution for selected points at  $\bar{M}_\Gamma = 2.5 \times 10^{-2}$  for  $\{110\}$  oriented grains. We observed symmetric growth in correlation with the structure symmetry. The depth evolutions are fitted for  $1/4$  power law. The growth of  $P_i$  are faster in comparison with the rest of the geometry. (b): comparison of pits depths growth for different set of  $c_{\omega_{2,3}}$  in the peripheral grains. The central grain has constant  $c = 0.8$ . We observe thermodynamically consistent behavior. The behavior is consistent for any change in  $\bar{M}_\Gamma$  with different set of  $c_{\omega_{2,3}}$ .

ison with  $\{100\}$ . The depths of quadruple points were deeper than  $\{100\}$  oriented structure. Figure (5.27) shows overall growth rates and depths of quadruple and triple points in this numerical experiment. The depths of both triple and quadruple points were deeper than  $\{100\}$  results, but the growth rates were 30~50 percent slower. We also observed some oscillatory behaviors in groove depths of some triple lines due to in flux of matter to attain the equilibrium state. Figure (5.27a) shows that over all kinetics took place under 1/4 power law for diffusion dominated processes.

As it was observed in the previous cases that overall effects of changing  $\bar{M}_\Gamma$  reflected by the variations in growth rates, but ultimately the system reached to common equilibrium state. Figure (5.27b) shows comparison for combine effects of change in  $\bar{M}_\Gamma$  and anisotropies in the polycrystalline. The kinetics of quadruple points are compared for different sets of  $c$  in  $\omega_2$  and  $\omega_3$ . With increasing anisotropies in the peripheral grains, pits depths also increased.

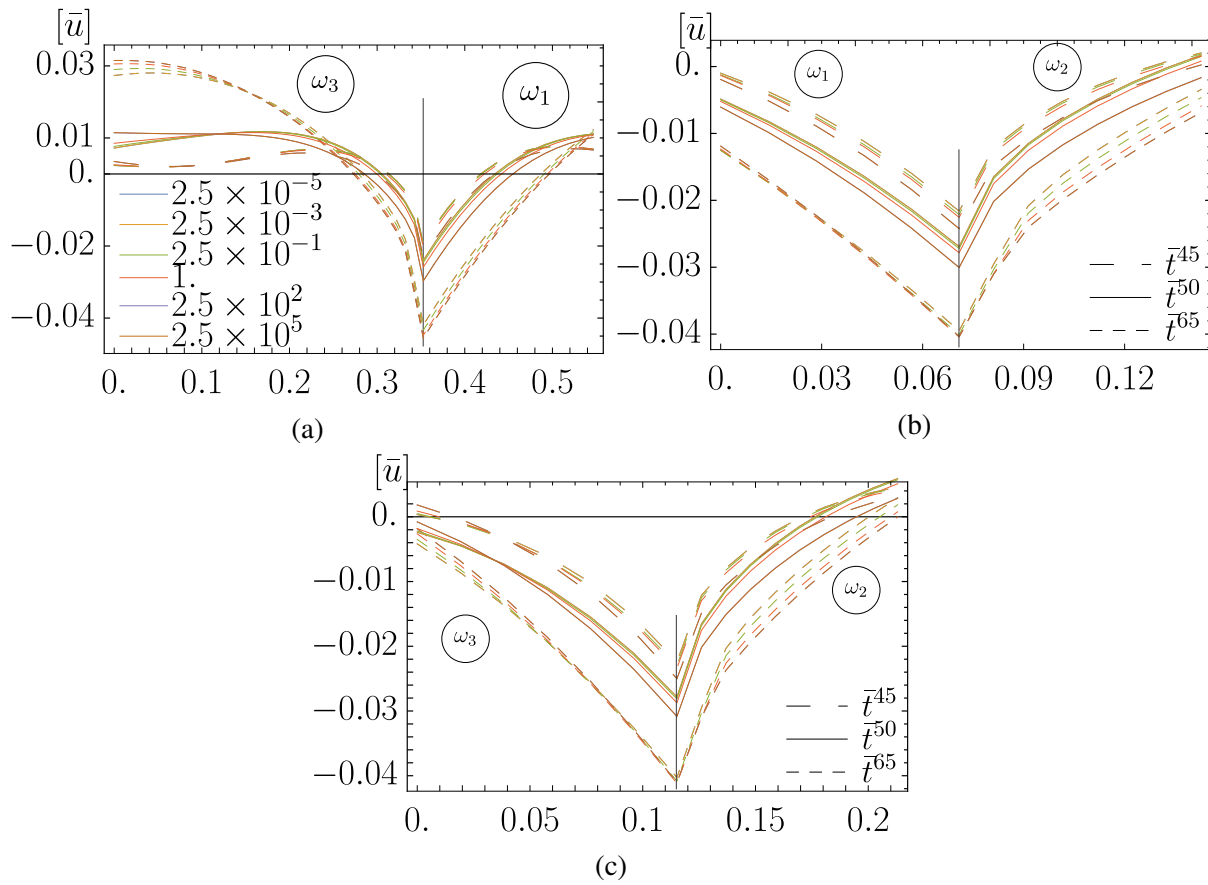


Figure 5.28.: Evolution of surface along different cross sections for varying  $\bar{M}_\Gamma$ . (a) is evolution along  $\bar{s}\bar{s}$ , (b) is evolution along  $\bar{t}\bar{t}$ , and (c) is evolution along  $\bar{u}\bar{u}$ . With varying growth rate, we observe decrease in the length of planar face of decreasing value of  $\bar{M}_\Gamma$ , due to  $M_{\Gamma_i}$  dominated process.

To compare the morphological changes due to variations in  $\bar{M}_\Gamma$ , Fig. (5.28) makes comparisons between groove profiles at different cross sections. Low value of  $\bar{M}_\Gamma$  corresponds to high surface diffusion coefficient, and within this configuration, we observed faster grooves formations, which caused smooth surface profiles. In case of planar facets, higher diffusion rate along the surface, should increase the height of planar edges. Similar behaviors were observed in these numerical experiments.

Figures (5.28a–c) show groove profiles along  $\overline{ss}$ ,  $\overline{tt}$  and  $\overline{uu}$  cross sections. The angular differences between surfaces of infinite curvatures to continuous curvatures profiles decreased with increasing value of  $\overline{M}_\Gamma$ . These effects reflect the smooth transition and dominating surface diffusion process in topographic growth. Evidently for low value of surface mobility  $M_i$ , planar faces showed slow kinetics but the steady state shapes of these profiles remained unchanged.

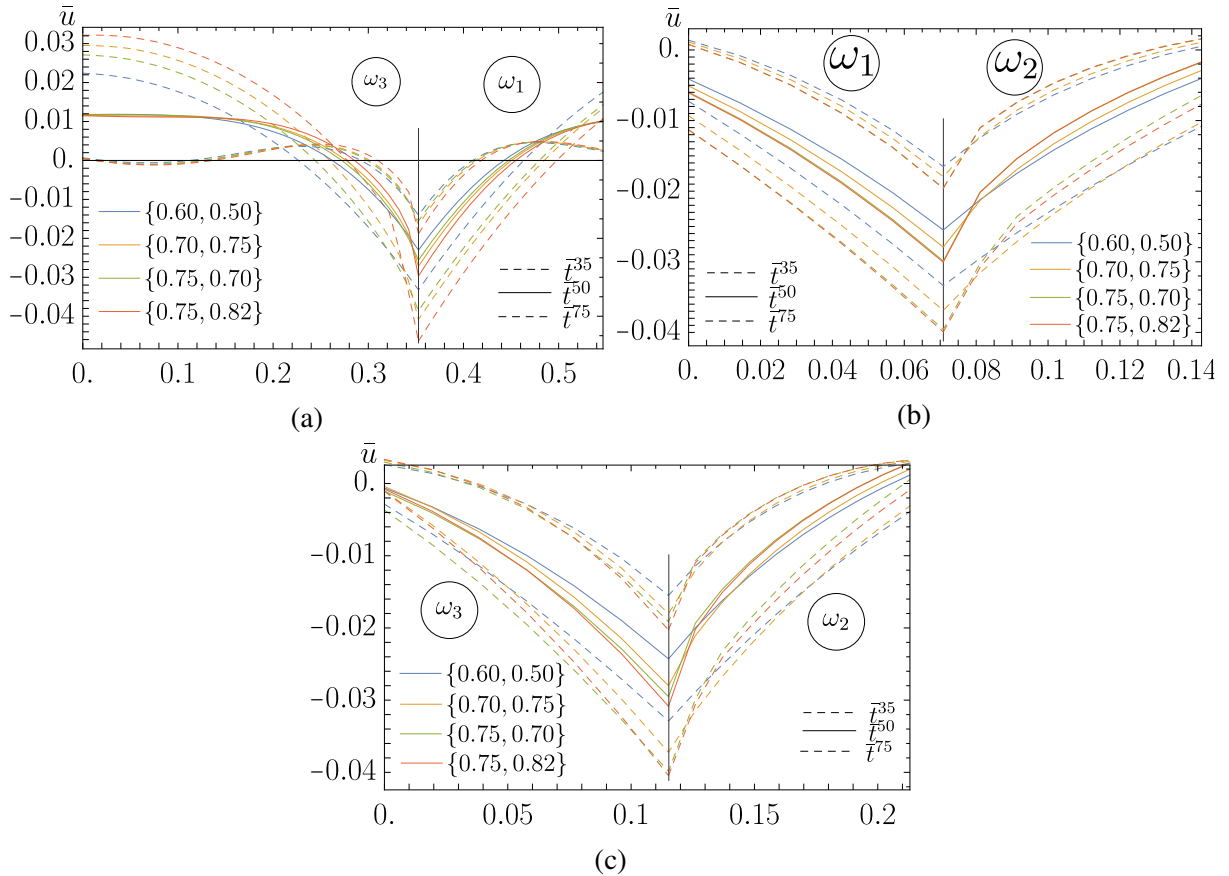


Figure 5.29.: Evolution of surface along different cross sections with varying  $c_{\omega_{2,3}}$  and constant  $c_{\omega_1} = 0.8$ . (a) Evolution along  $\overline{ss}$ , section between  $\omega_1$  &  $\omega_3$ , (b) evolution along  $\overline{tt}$ , between  $\omega_1$  &  $\omega_2$  and (c) evolution along  $\overline{uu}$ , section between  $\omega_2$  &  $\omega_3$

Figure (5.29) reveals growth kinetics for varying anisotropy,  $c$  in the circumferential grains ( $\omega_2$  and  $\omega_3$ ). In these simulations, the central grain  $\omega_1$  had  $c = 0.8$ . With the increasing anisotropies, not only the depth of grooves and quadruple points increased, but also the longitudinal lengths of the planar faces increased. It was also observed that with the increasing anisotropies, there were small changes in the dihedral angles along the grain boundaries and increased in the face length of the planar faces. These simulations with mild anisotropies showed groove profiles without any planar facet formations.

### 5.4.2.3. Three grains with $\{111\}$ orientation.

$\xi$  plot for anisotropic surface energy function, Fig. (5.7) showed that for the increasing value of  $c$  beyond  $2/9$ , ears like augmented regions extend in  $\{111\}$  directions. These regions encompass the set of orientations termed under missing orientation for the particular value of anisotropy in the surface energy function. The objective of these simulations is to study the morphologies for grains orientated in this direction with the normal. Set of Euler angles to fix the grains in  $\{111\}$  with the normal are tabulated in table (5.3). Other simulation parameters grain boundary energies, internal and external triple line energies were kept consistent in accordance with the previous simulations.

Table 5.3.: Three grains  $\{111\}$  orientation with the normal direction

Grain	Angle		
	$\phi_1$	$\phi_2$	$\phi_3$
$\omega_1$	$-45.0^\circ$	$45.0^\circ$	$45.0^\circ$
$\omega_2$	$-40.0^\circ$	$40.0^\circ$	$45.0^\circ$
$\omega_3$	$40.0^\circ$	$-40.0^\circ$	$-45.0^\circ$

Surface free energy of each grain was calculated using equation (5.10). As stated earlier in section (5.3) that for  $c > 1/3$ , areas of intersection  $\xi$  vectors, extend in  $\{111\}$ . We observed formation of ear like regions at the corners. Thus grains with surface energy of  $c > 1/3$  include missing orientations. In congruence with the section (5.4.2.2), we will discuss two particular case for  $\{111\}$  oriented RVE in the fore coming sections.

#### $\{111\}$ oriented grains with low to moderate anisotropy.

The prime objective of this section is to discuss the morphology and growth kinetics for  $\{111\}$  oriented grains with the normal. We will discuss the results for low to moderate values of anisotropic surface energy of the grains in the RVE. The Euler angles of the grains with the surfaces are given in table (5.3). These orientations engender  $\{111\}$  textured RVE. Grain boundary energies, and both internal and external triple line energies were kept constant as described in section (5.4). The scalar factors in the surface energy function had  $c_{\omega\{1,2,3\}} = \{0.3, 0.4, 0.6\}$  respectively. With this configuration for three grains periodic model shown in Fig. (5.8),  $\omega_2$  and  $\omega_3$  had surface energy with the moderate anisotropy, whereas the central grain lied with no anisotropy in the surface energy function.

The grooves evolutions and pits formations always initiate at the sites of relatively higher chemical potentials in accordance with the under laying physics of the model. Different orientations of the grains effect groove shapes and growth rates. Figure (5.30) shows  $\bar{u}$  and  $J_i$  fields along the free surface at different instants of  $\bar{t}^n$ . Figures (5.30e–g) focus the  $J_i$  vector fields with progressing time. It is clear from these vector plots that initially with the deepening of grooves along the grain boundaries, the matter started depositing on the both sides at the surfaces of the grains along the grooves. The vector lines in figures (5.30e) and (5.30f) show aligned movements of the fluxes. Consequently, we had formations of grooves along these grain boundaries as shown in figures (5.30a) and (5.30b). Formation of diffusional humps and accelerated pits formations at the quadruple points are also visible in these figures. With the progressing time, system tried to establish a state of an equilibrium with maximum dissipation. Consequently, the

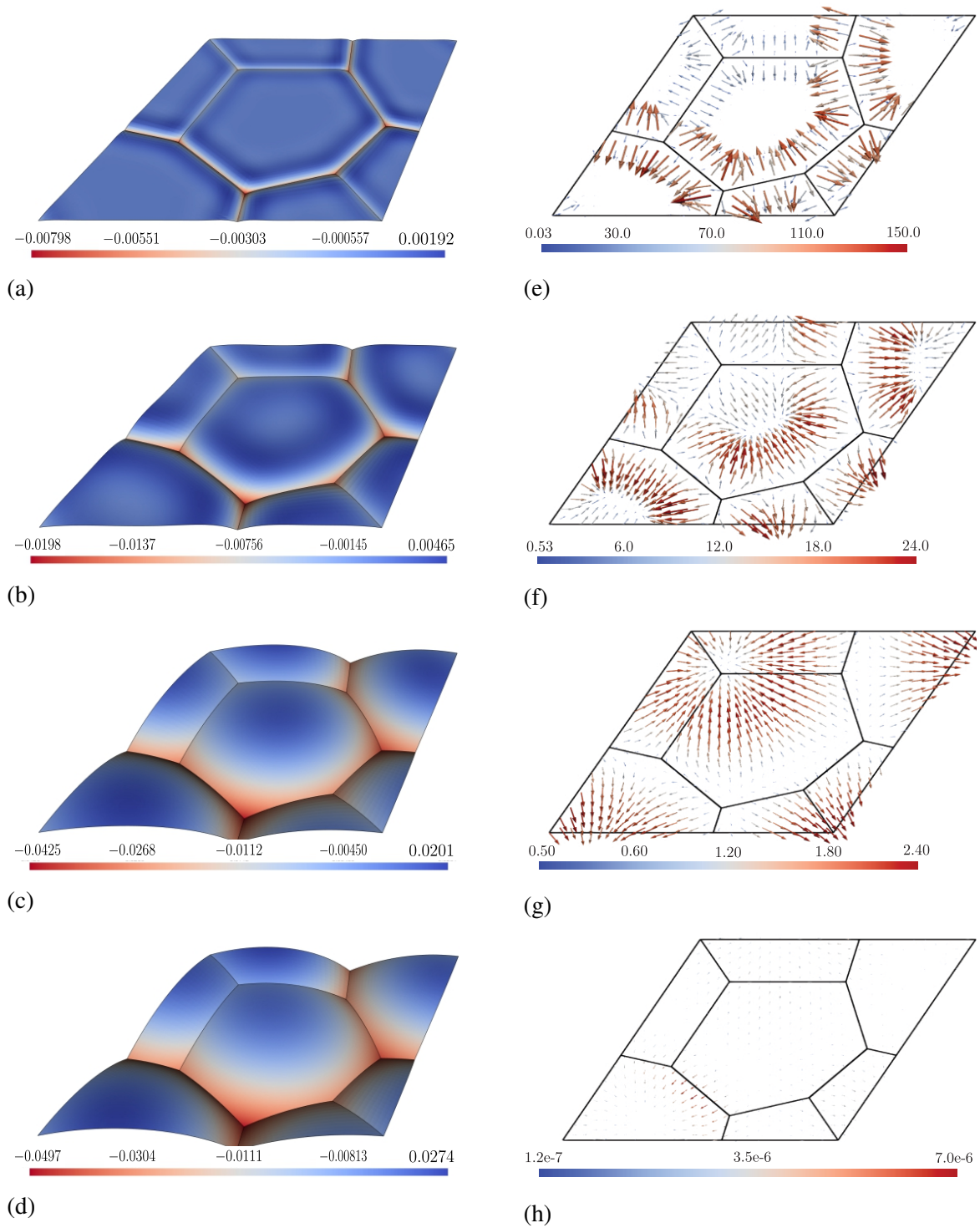
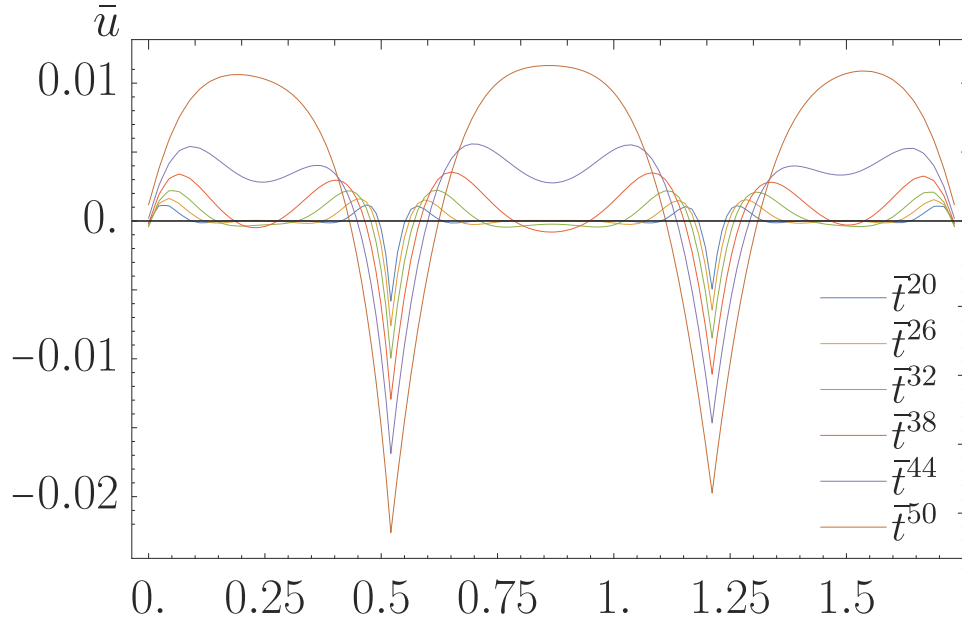
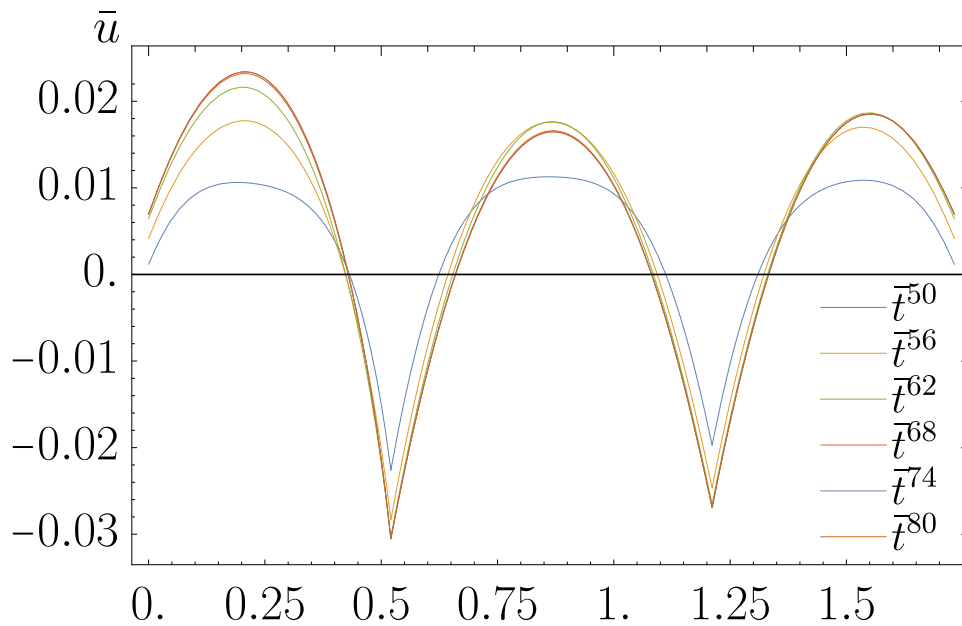


Figure 5.30.: Contour plot for  $\bar{u}$  and  $J_i$  fields. In these results  $c_{\omega_{1,2,3}} = \{0.3, 0.4, 0.6\}$  respectively with  $\bar{M}_\Gamma = 2.5 \times 10^{-3}$ . (a),(b),(c), and (d) show  $\bar{u}$  plots, we observe normal growth kinetics in this configurations. Formations of diffusional humps are clearly visible in these evolution plots. (e),(f),(g), and (h) show vector plots,  $J_i$  at  $\bar{t}^{20}$ ,  $\bar{t}^{40}$ ,  $\bar{t}^{60}$ , and  $\bar{t}^{80}$  near to the equilibrium, respectively. In the beginning of grooving process, the direction of flux vectors are normal to the grain boundary plane, but with proceeding steps, all vectors orientated to establish a constant value of  $\bar{\mu}$  over the complete domain.

flux vectors orientated themselves in the appropriate directions to minimize the total energy of the system. Figure (5.30g) shows that some of these vectors made themselves directed in the directions parallel to  $\Gamma_6$  and  $\Gamma_8$  planes. So afterward we found the upward motion at  $P_1$  in the RVE. Figure (5.30h) shows vanishing flux at  $\bar{t}^{75}$ , near to equilibrium state. Overall difference in  $\mu$  is of the order  $\times 10^{-6}$ .



(a)

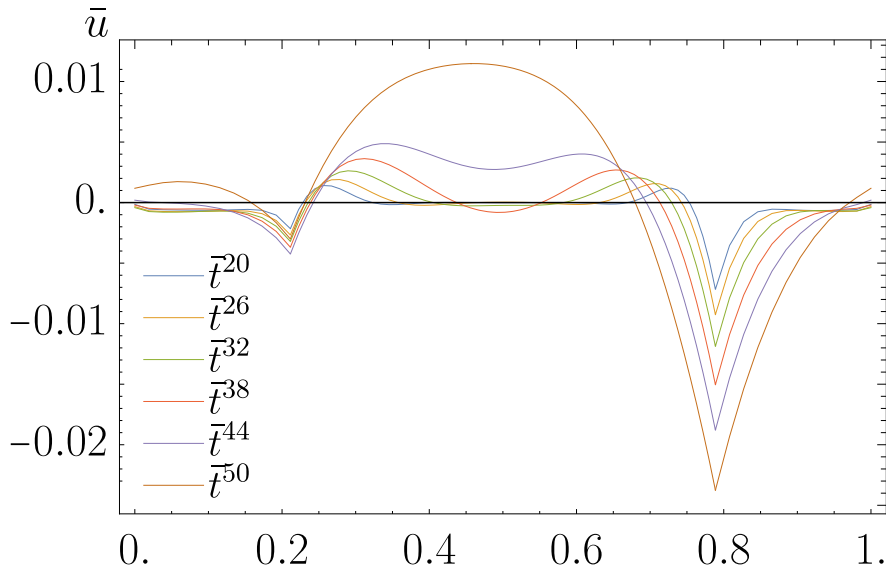


(b)

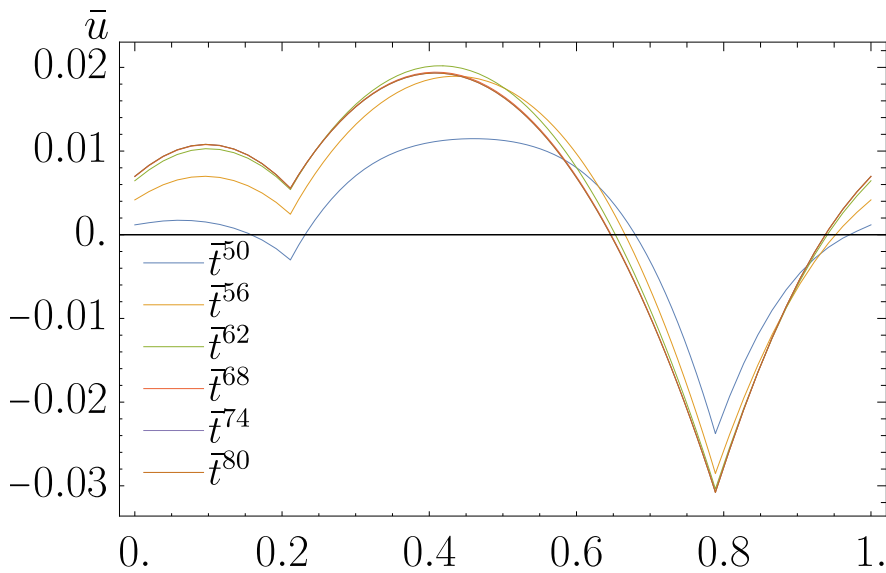
Figure 5.31.: Evolution of grooves along the major diagonal with low to moderate anisotropy in  $\{111\}$  oriented grains. (a) shows formation of observable secondary diffusional humps. The grooves depth are deeper in comparison with the previous cases. (b) shows the formation of grooves after the merging of the diffusional humps from all sides of the grains. The height of humps show thermodynamically coherent results as a function of surface energy.

The thermal grooves with  $\{111\}$  oriented grains were deeper than the  $\{110\}$  textured surface.

The main reason of the higher depth values is the higher surface energies of the grains in  $\{111\}$  directions. These grooves evolved with constant mean curvatures with different growth kinetics. Figures (5.31–.33) show morphologies of surfaces at different cross sections. Figures (5.31a) and (5.31b) show evolution along the major diagonal. We had asymmetric groove profiles with comparatively deeper grooves. Due to these pronounced effects, we also observed variations in



(a)

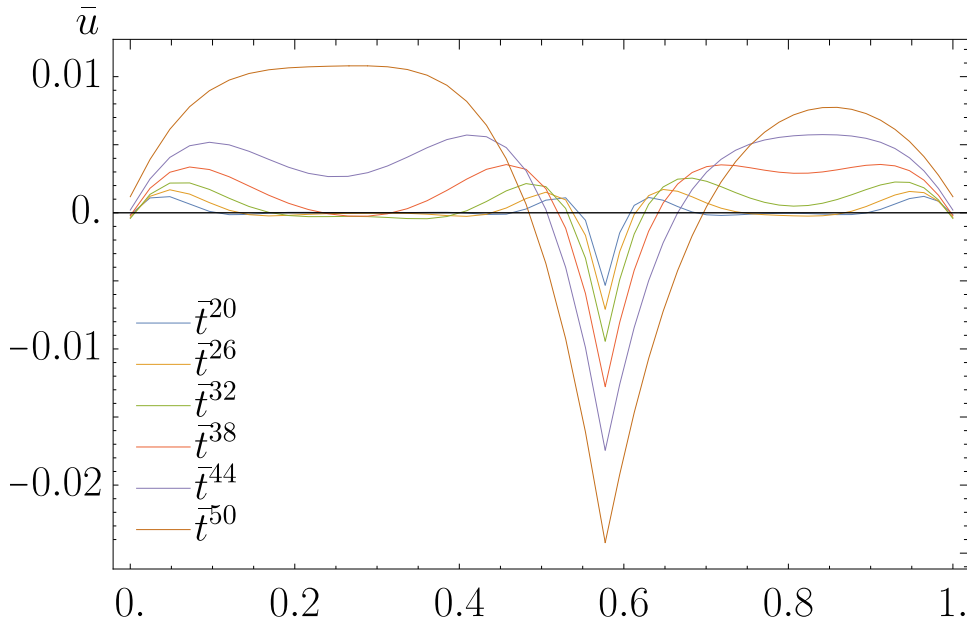


(b)

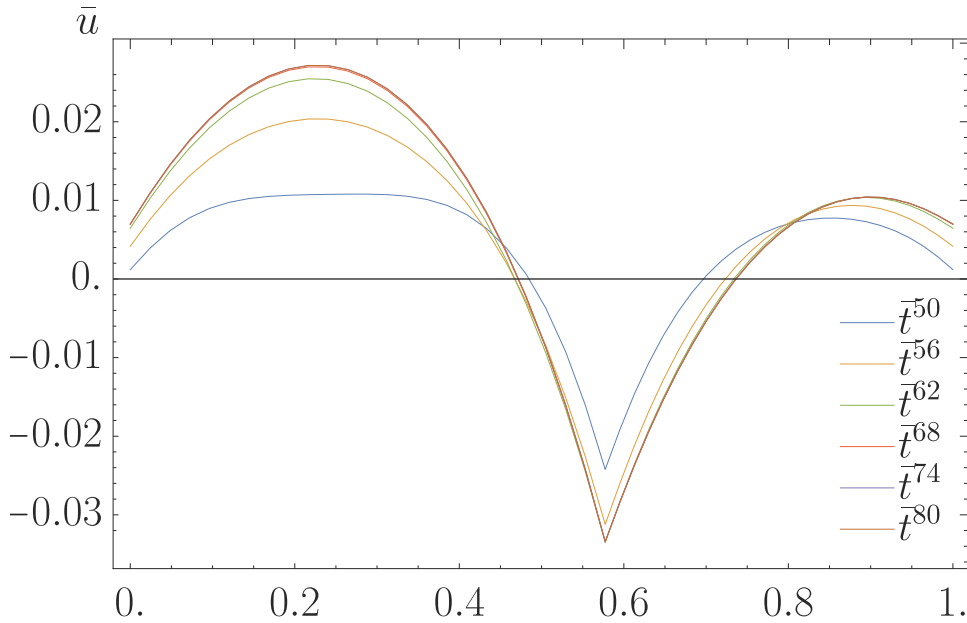
Figure 5.32.: Figures show evolution along the minor diagonal with low to moderate anisotropy in equation (5.10) for  $\{111\}$  oriented grains.  $\bar{M}_\Gamma$  is  $2.5 \times 10^{-3}$ . The pit growth at  $P_1$ , a dip on left in (a), is much slower due to higher rate of flux along the surface. While on the other side of the grain, a deeper pit is formed. (b) shows evolution of grooves with the formation of protrude region due to influx of the materials to attain the equilibrium state.

the surface morphologies along this cross section. Diffusional humps were higher than  $\{110\}$

oriented model and the formations of secondary humps were also more evident in these orientations. If we look in the plot, the difference between the maximum depth of the groove along this sections is 0.01 with  $\{110\}$  results. The differences in the growth kinetics are much more clearly observable along the triple lines /grain boundaries. Figure (5.32) shows the growth kinetics along the minor diagonal. In these orientations, it is clear that the formation of pit at quadruple point  $P_1$  took place with relatively slower rate. This slow decrease in the depth of grooves and pits along this sections displayed low value of chemical potential. There was high influx of matters from rest parts of the geometry with groove formations. Figure (5.33) shows



(a)



(b)

Figure 5.33.: Evolution of horizontal periodic boundary shared by  $\omega_2$  and  $\omega_3$ . This section illustrate grooving in two dimensions. (a) shows formation of secondary diffusional humps with a symmetric groove profiles. (b) shows evolution of the grooves in the equilibrium state.

surface morphology along the horizontal boundaries encompassed by  $\omega_2$  and  $\omega_3$ . The motion growth kinetic was different from Fig. (5.22). It is evident from this figure, that groove depth increased at faster rate along the triple line. The formation of secondary diffusional humps are also clear along this cross section.

In these simulations, we observed fast growth rates at groove pits with different groove profiles. Periodic surfaces far away from the grain boundaries showed stagnation growth kinetics in the beginning of process. Different parts in the geometry observed variations in the growth kinetics. Figure (5.34) shows evolution of quadruple points and triple points in the RVE. The increase in the pit depth took place at faster rate in comparison with the  $\{110\}$  oriented grains. Also, the grooves depth along the triple lines were similar with  $\{110\}$  oriented grains. The region influenced by the influx of matter to attain the equilibrium state showed formation of the plateau at the boundary junction, which expressed the state of grains merging at this point to form one big grain and also categorized as stable junction.

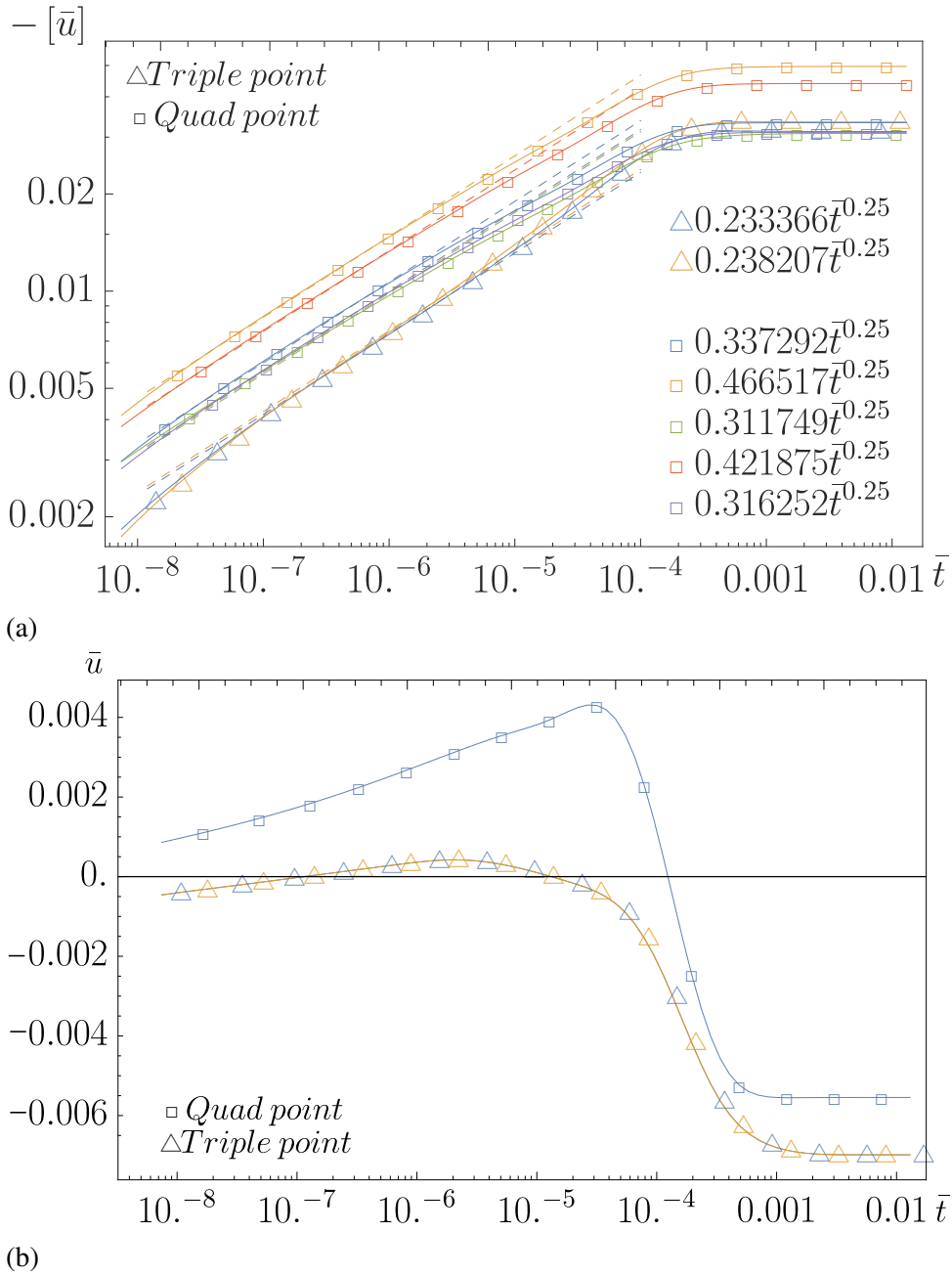


Figure 5.34.: Evolution of  $P_i$  and triple points for  $\{1\ 1\ 1\}$  oriented grains. In these results  $\bar{M}_\Gamma = 2.5 \times 10^{-3}$ . (a) shows negative depth on log-log scale. Overall growth along these points are symmetric due to low anisotropy. (b) shows slower growth in the initial diffusion process, but the influx of material is faster in comparison with the previous simulations results.

**$\{111\}$  oriented grains with moderate to critical anisotropy.**

Section (5.4.2.3) discussed the results for  $c_{\omega\{1,2,3\}} = \{0.3, 0.4, 0.6\}$ . For these low to moderate ranges of anisotropies in  $\{111\}$  textured polycrystalline model, we observed grooves profiles without any formation of low energy planes at any location. In comparison, with  $\{110\}$  oriented grains with analogous anisotropy,  $\{111\}$  oriented grains showed slower morphological growth.

In this section, we will focus our discussion for moderate to critical range of anisotropy in the surface energy function. We had  $c \geq 0.75$  and it was expected that we had formations of planar grooves with low energy planes. Figure (5.35) shows  $\bar{u}$  and  $-\bar{\mu}$  fields for  $c_{\omega\{1,2,3\}} = \{0.8, 0.75, 0.82\}$  in equation (5.10). Under these settings, two grains  $\omega_1$  and  $\omega_3$  had anisotropy coefficients above the critical range whereas  $\omega_2$  had coefficient at critical value. Initially, the surface morphological evolution followed similar trends as had been observed in the previous numerical experiments with different orientations. The diffusion started with the pits formations at the quadruple points and grooves along the grain boundaries. Figures (5.35a) and (5.35b) show  $\bar{u}$  along the surface at  $\bar{t}^{20}$  and  $\bar{t}^{40}$  respectively. In figures (5.35e) and (5.35f), we observed the distribution of  $\bar{\mu}$  at these instances of  $\bar{t}^n$ , and we found that maximum chemical potential was along the triple lines  $\Gamma_1$  and  $\Gamma_7$ . Initiation of thermal grooves at these positions is evident in the corresponding  $\bar{u}$  plots. In contrast with  $\{110\}$  oriented grains, in this configuration we observed formations of grooves with planar low energy edges on both faces of the groove.

As we have already discussed in section (5.3), that these formations are due to the existence of low energy vector,  $\xi_0$  in the range of orientations which are in the intersecting regions formed in  $\{110\}$  and  $\{111\}$  directions. We must have continuous value of the chemical potential along the surface as the basic requirement for continuity of the flux over the domain equation (3.29). In accordance with the definition of chemical potential  $\mu_i = K_i \gamma_i$ , we have high value of curvature at these grooving sites. There is maximum flow of flux at the faster rate to establish the state of the equilibrium. The matter should follow the direction in accordance with equation (3.29). From the Fig. (5.35g), the distribution of  $-\bar{\mu}$  along the surface has maximum value near to  $P_1$ . We observed the surface fluxes directed them in this direction to establish the equilibrium state. With this influx of matter, the quadruple point showed the positive motion along with the fluctuation in the depth of the triple line grooves attached to this quadruple point. Also along  $\Gamma_7$  between  $\omega_2$  and  $\omega_3$ , there was formation of a planar groove of comparatively smaller size. In rest of the geometry, we had evolution of grooves profiles with relatively slower kinetics. Planar grooves grow with faster rates in compression with the rest parts of the geometry. The quadruple points in near vicinity of these low energy planes, showed accelerated growth in their depths.

A semi planar groove at  $\Gamma_7$  showed low energy face along  $\omega_2$ , whereas surface along  $\omega_3$  grew with constant mean curvature. Figure (5.36) shows a qualitative comparison between this groove shape and AFM image of the groove profile from Derkach et al. (2014). At  $\bar{t}^{56}$ , groove depth is 0.055, which is approximately equivalent to experimental observations.

Munoz et al. (2004) observed such sharp changing of angles during the diffusion process in silver. They found that these grooves formations were due to low-surface energy faces profiles which although increase the overall surface area but reduce the total energy contribution as explained in section (5.2).

Figure (5.37) shows the morphological evolution of the surface along the major diagonal of the

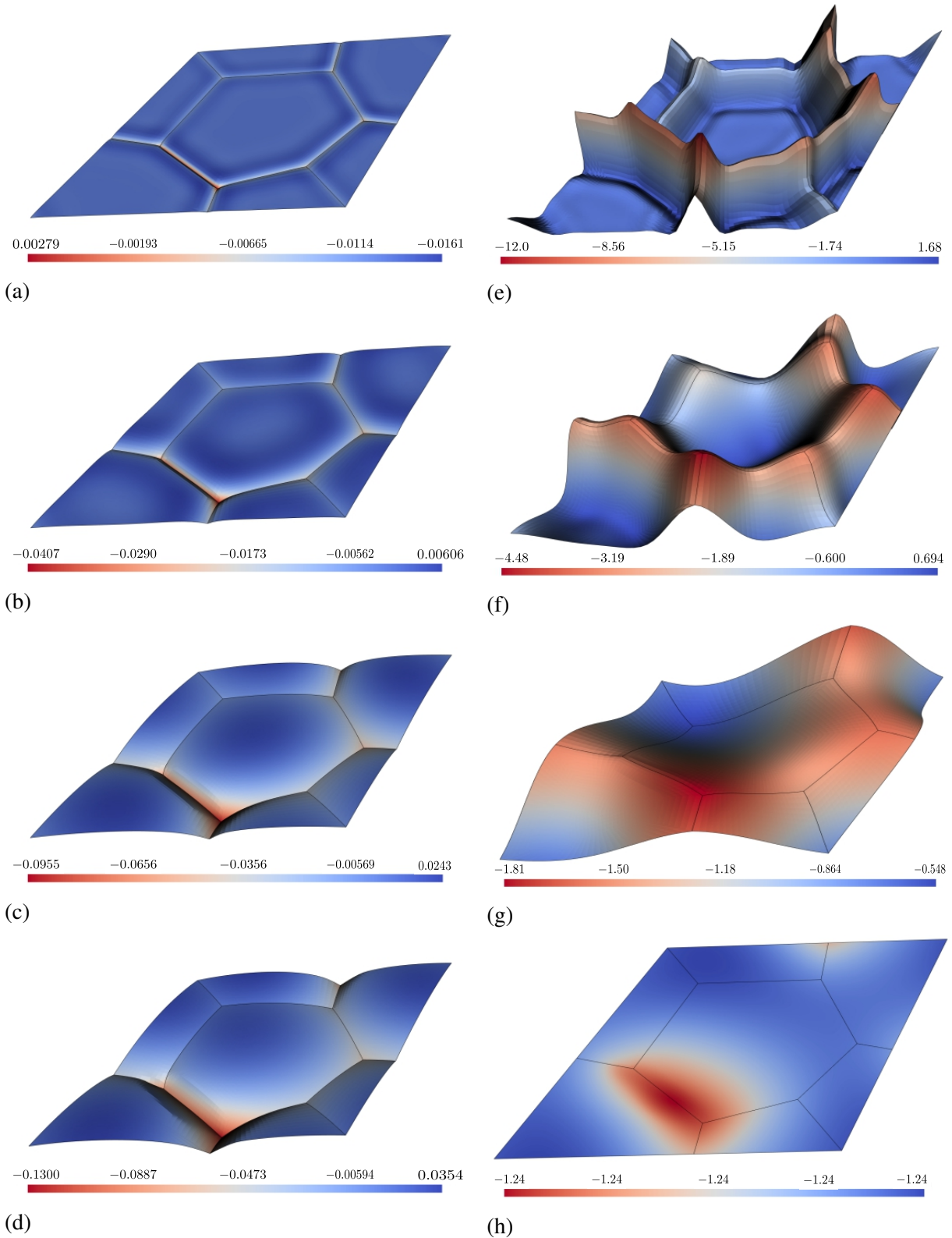


Figure 5.35.: Contour plots of  $\bar{u}$  and  $-\bar{\mu}$  with  $c_{\omega_{1,2,3}} = \{0.8, 0.75, 0.82\}$  in  $\{111\}$  oriented grains. (a),(b),(c), and (d) are  $\bar{u}$  field and (e),(f),(g), and (h) are  $-\bar{\mu}$  distributions at  $\bar{t}^{20}$ ,  $\bar{t}^{40}$ ,  $\bar{t}^{60}$ , and  $\bar{t}^{80}$  respectively. Initially the flux is relatively higher along the grain boundaries with the grooves start forming along these locations. With the progressing time, we have formation of planar faces along one of the grain boundaries. The corresponding site has discontinuity in the Gaussian curvature. Secondly, the formation of low energy faces have high curvature in accordance with relation  $(\mu = K\gamma)$  to maintain the constant value of  $\bar{\mu}$  along the surface.

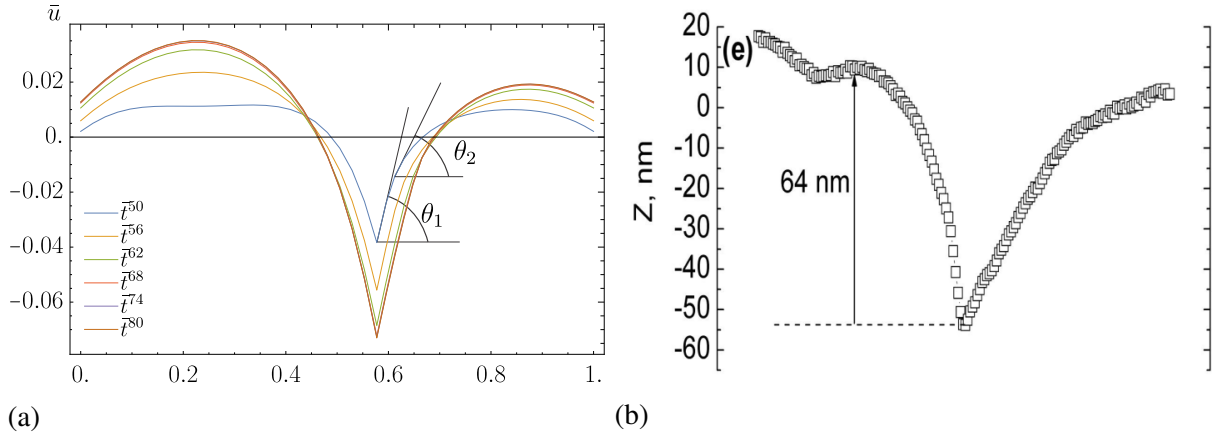


Figure 5.36.: Qualitative comparison between numerical simulations and experimental results. (a) is evolution of surface along horizontal free edge with planar face of two different angle. (b) is an AFM image of Cu thin film after second annealing (Derkach et al., 2014). Both figures shows non-symmetric groove profile with the facet formations along the grain boundary, while on the other side, we have normal groove profiles. At  $\bar{t}^{56}$ , we have the depth of 0.055, which is in good approximation with 50nm experimental observations.

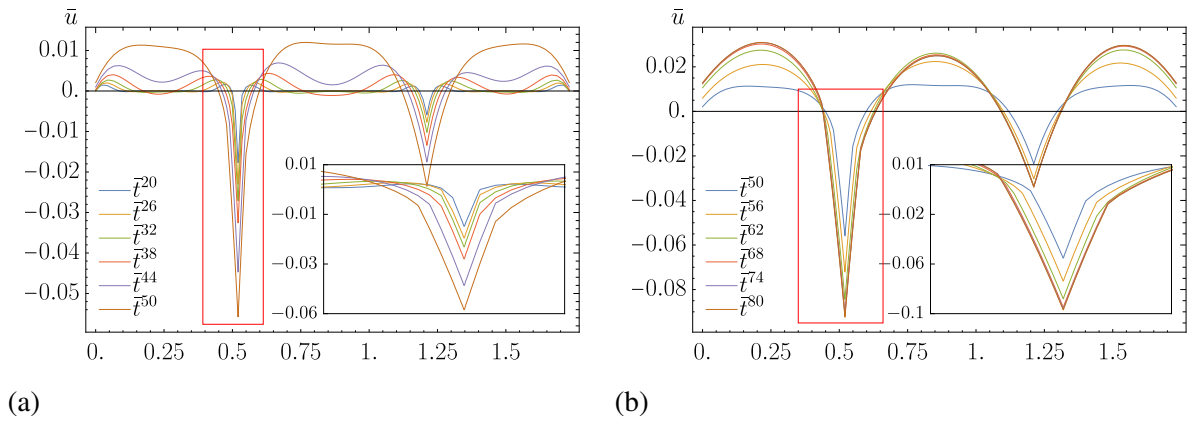


Figure 5.37.: Evolution of planar grooves using  $c_{\omega_{1,2,3}} = \{0.8, 0.75, 0.82\}$  for  $\{1\ 1\ 1\}$  oriented grains. For these results  $\bar{M}_\Gamma = 2.5 \times 10^{-3}$ . We observe these planar faces moves parallel with the increasing depth. Additionally, the secondary diffusional humps are prominent in the initial grooving process ( $\bar{t}^{26}$  to  $\bar{t}^{38}$ ) and diminish with progressing time.

RVE. It is clear from these plots that these formations are not numerical artifacts due to discretization error, but exist over more than one element length. We observed the parallel motion of singular faces with progressing time. It was due to fact, that once for the critical range of anisotropy, we had formation of low energy singular faces along the groove, it retained the angle without any change with the progressing grooving phenomena. Additionally, the grooving process started with the formation of diffusional humps as in the previous cases. Angular difference between the planar face and diffusion hump curvature attached to it, reduced as system proceeded towards the equilibrium groove profiles.

Figure (5.38) shows  $\bar{u}$  along the minor diagonal. Along this cross section, initially depth rate at  $P_1$  was slower in comparison with rest of the geometry. As shown in figures (5.35e-g),

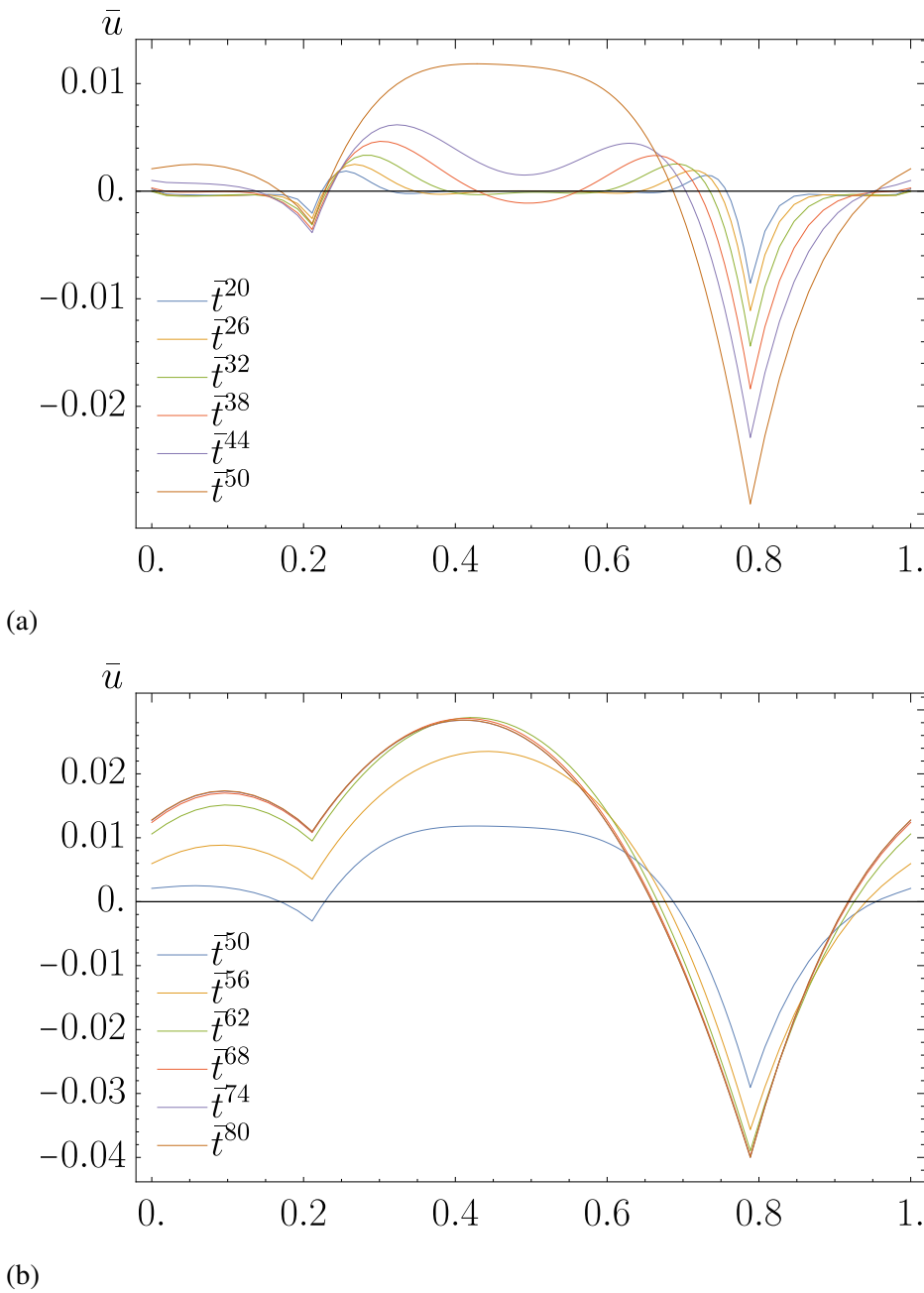


Figure 5.38.: Evolution of surface along the minor diagonal of RVE. We observe slower pit formation along the quadruple point on the left. This stagnation behavior is due to high in flux of matter from the groove with planar edge. The central part represents the  $\omega_1$  free surface, the oscillatory behavior is visible along the surface in the initial groove formation phase. The ends along this sections are representing periodic triple line.

this junction was comparatively at higher chemical potential so the rate of flow flux should be slower in accordance with the equation (3.29). Secondly, all three grain boundaries are  $120^\circ$  far apart, so this quadruple point is in most stable condition with the lowest grain boundary energies. Later on, influx of matter towards this junction incited upward motion at this part of the geometry (see Fig. (5.35g)).

Figure (5.39) compares the groove growth kinetics at different points in the RVE. Overall

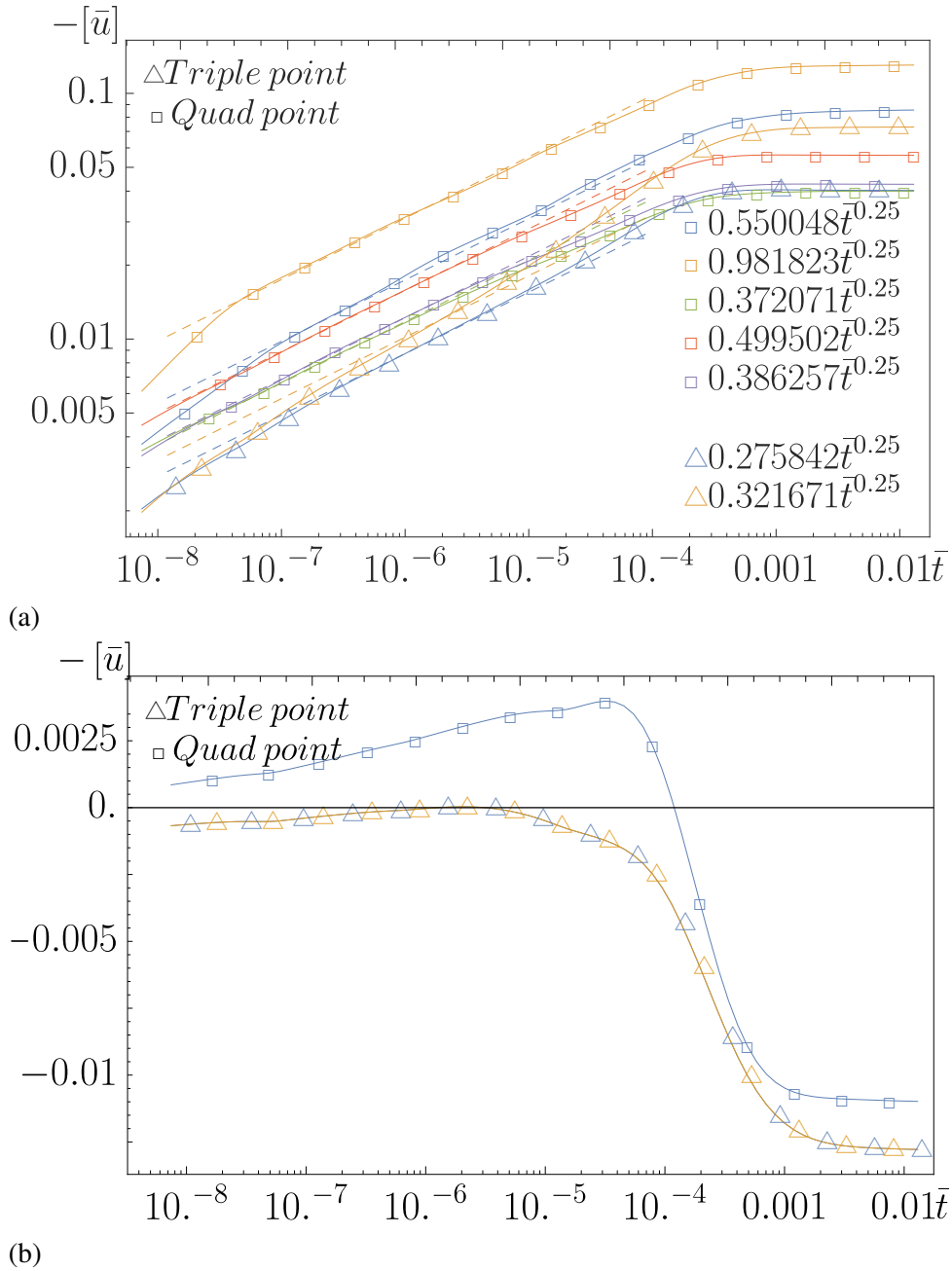


Figure 5.39.: Evolution of pit and grooves depth for  $\{111\}$  oriented grain with critical anisotropy. The depths at  $P_i$  are increasing much faster than the previous cases. (a) shows depth evolution on log-log scale. We also observe some fluctuations in the growth rate along the grooves. This behavior is dominant in the areas of planar grooves. (b) shows evolution of points depicting turnabout behavior. The protrusion height and growth rate is double than  $\{110\}$  textured model.

growth must follow the  $1/4$  power law with normal grooving behavior. As discussed earlier that we observed influx of matter in some parts of the geometry to attain the equilibrium. Figure (5.39b) shows the depth of  $P_1$ 's and point on  $\Gamma_8$  using semi log scale. It is evident that there was no groove formation along the  $\Gamma_8$  also the upward motion of quadruple point revealed merging of grains due to stable triple junction with minimum grain boundary energies of the meeting boundaries. Figure (5.39a) shows the overall trends of growth kinetics at triple and quadruple points in the RVE. In contrast with the previous sets of simulations, the quadruple

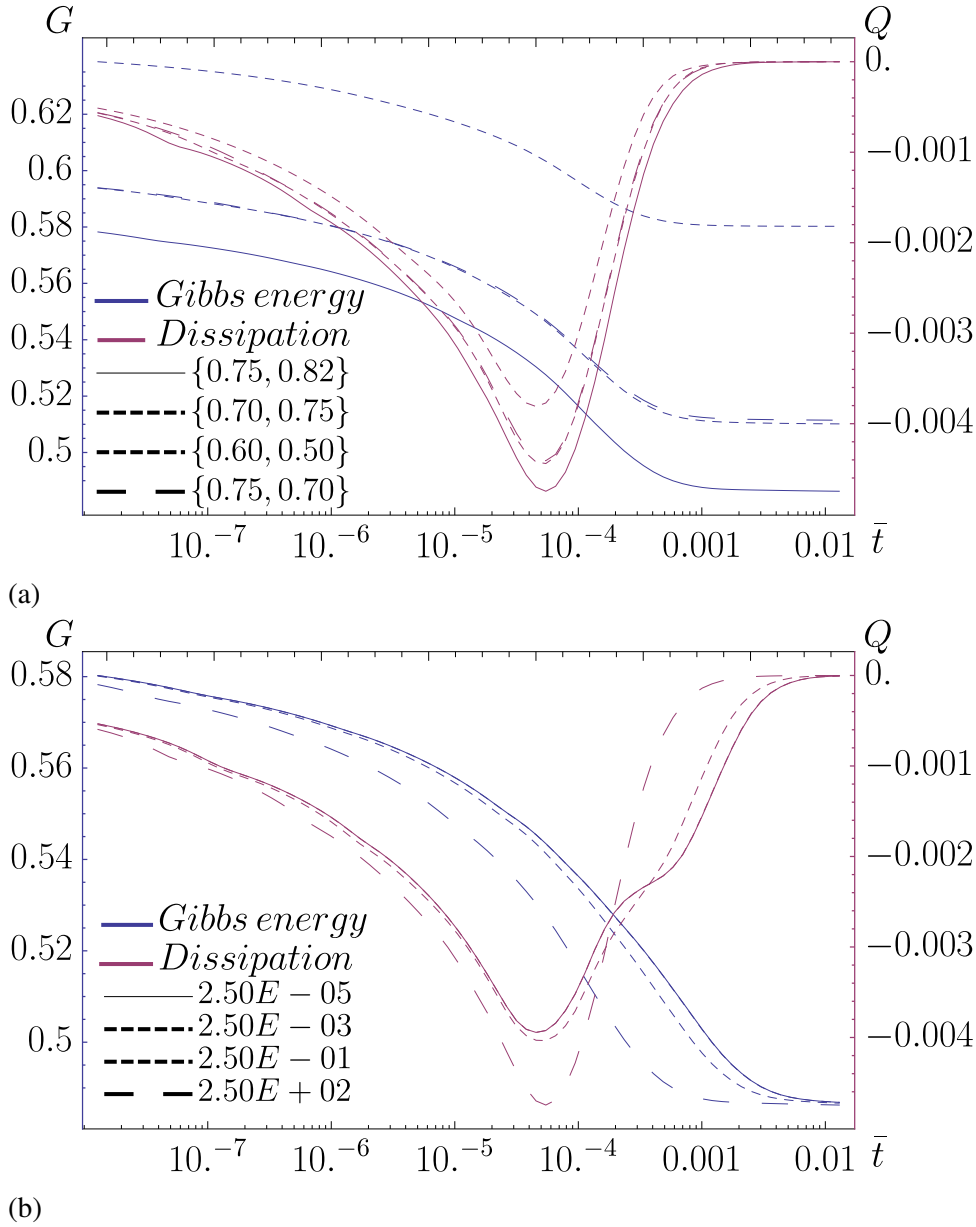


Figure 5.40.: System behavior to establish the state of an equilibrium for different set of  $c_{\omega_{1,2,3}}$  and  $\bar{M}_{\Gamma}$ . (a) shows the dissipation path and minimum energy of the system for different set of  $c_{\omega_{2,3}}$  with  $c_{\omega_1} = 0.8$ . With an increasing  $c$ , the total energy of the system also reduces and dissipation process slows down. (b) shows dissipation and energy path for different values of  $\bar{M}_{\Gamma}$ . With an increasing value of  $\bar{M}_{\Gamma}$ , the process is governed by diffusion along the surface, and we have slow dissipation rate but ultimately system attain the constant value of minimum total energy.

points kinetics took place with different rates. Initially we had relatively slower trends in the pits formations. At the later stage, a point in near vicinity of the planar groove showed approximately double growth rate in comparison with the rest part of the geometry. The other pits growths took place with normal comparable coefficients.

Génin et al. (1992) analytical model showed that quadruple points evolutions obey  $1/4$  power law in the annealing time but with relatively larger coefficients. We have similar results for our fitted curve to evolution kinetics. Munoz et al. (2004) observed experimentally that overall

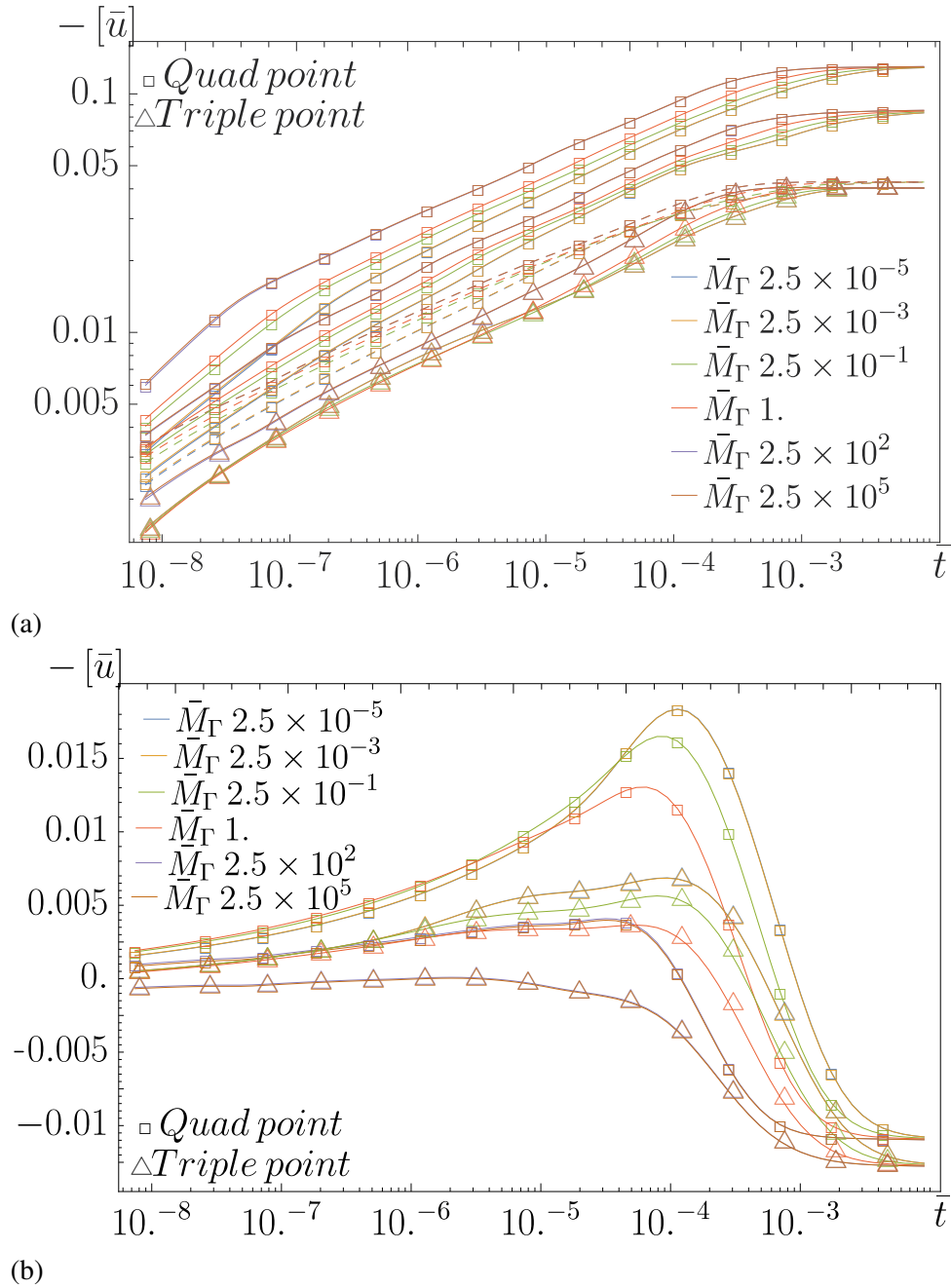


Figure 5.41.: Effect of different values of  $\bar{M}_\Gamma$  on the growth rate of  $P_i$  and points on  $\Gamma_i$ . Figure shows two behavior in two different plots. The effect of decreasing value of  $\bar{M}_\Gamma$  shows  $M_{\Gamma_i}$  controlled evolution. The growth along the quadruple points slows down, but ultimately achieve constant steady state position.

morphological growth slowed down at critical anisotropy which is also evident from the growth kinetics of the triple points. The fitted curves for triple points are multiple of smaller coefficients in  $\{111\}$  textured RVE. Zhang (2006) showed in simulation experiments that overall energy minimization rate slows down with an increasing surface energy anisotropy. This behavior is due to formation of low energy faces, which increase the overall area of the surface but total energy of the system is lower than initial condition. Figure (5.40a) shows dissipation rates and overall decrease in total energy of the system for different sets of anisotropies in the peripheral grains. In these results,  $c_{\omega 1}$  was constant. With the increase in anisotropy, overall surface free

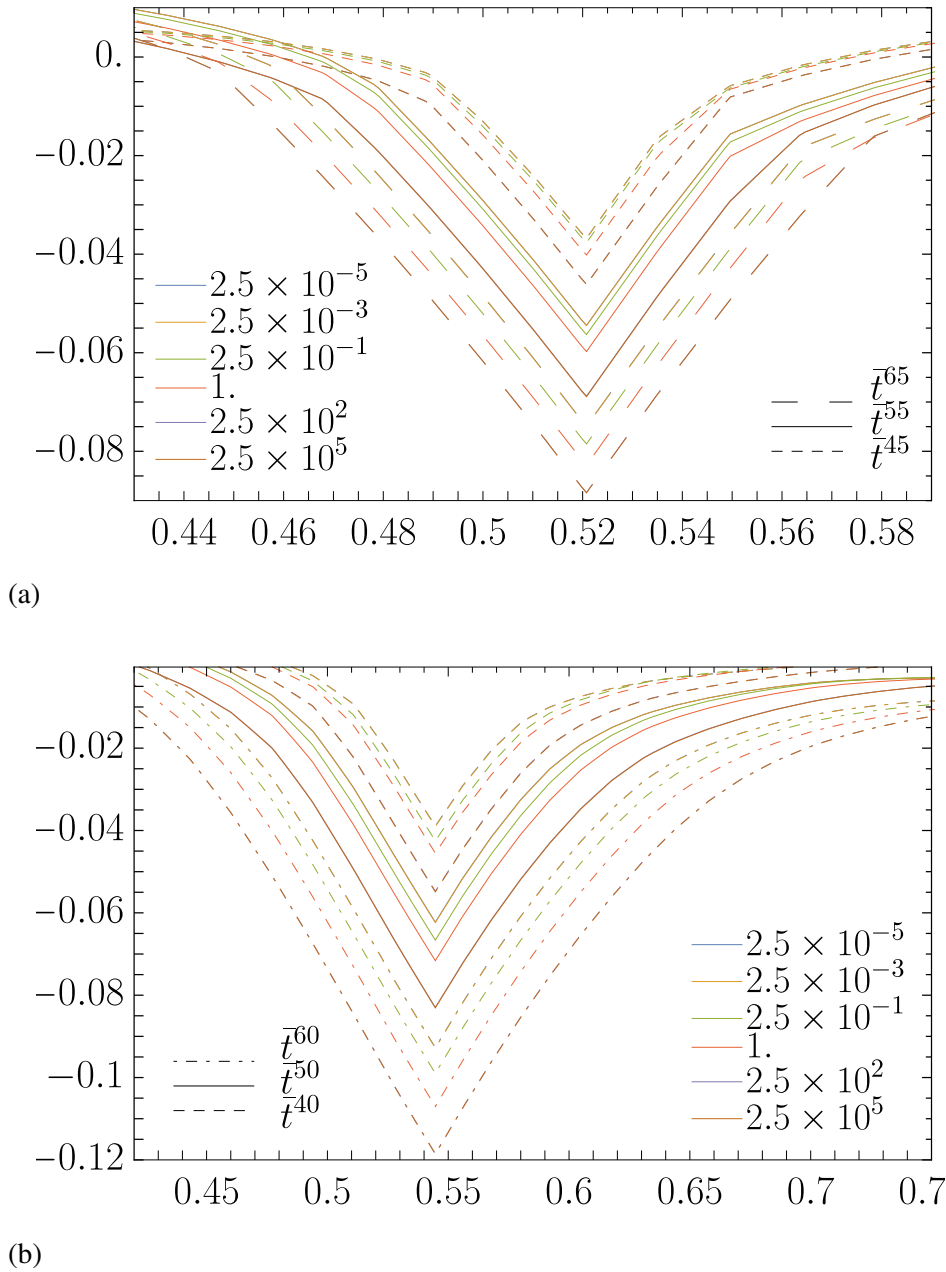


Figure 5.42.: Effect of increasing  $\bar{M}_\Gamma$  on the planar groove shapes and equilibrium dihedral angles. (a) shows evolution of the planar grooves. For any increasing in the surface diffusion coefficient, we have decreasing dihedral angle, and also length of planar face decrease. The difference of angle between the planar and normal profile decreases at the meeting edge. (b) shows evolution of normal groove. We observe the congruent effects for any variation in the diffusion coefficient in the model.

energy of the system also decreases. With this, the total reduction in the system energy was relatively lower, and overall dissipation rates slowed down. Dissipation rates and reductions in total energy of system with varying  $\bar{M}_\Gamma$  are shown in Fig. (5.40b).

As already shown in earlier sections, that system always attained a constant steady state profile for different  $\bar{M}_\Gamma$ . Consistent behaviours were also observed for the overall entropy production flux and total energy reductions in the system. For surface diffusion dominated process, we

observed faster dissipation rate in comparison with diffusion along triple line controlled process. Entropy production flux was calculated in accordance with equivalence criterion between dissipation and energy rate, i.e.  $Q + \dot{G} = 0$ .

It is necessary to compare the growth kinetics of quadruple points and points lies far away on the triple lines for different  $\bar{M}_\Gamma$  in the numerical simulations. Figure (5.41) shows the quadruple and triple points depths for different  $\bar{M}_\Gamma$  in the problem. We observed concurrence behaviors as with the dissipation rates and overall reductions of total energy of the system.

We have already seen in previous sections that  $\bar{M}_\Gamma$  also influence the groove shapes at constant instance of  $\bar{t}^n$ . Figure (5.42) shows comparative studies of small cross sections in the RVE. Figure (5.42a) compares a planar groove profiles at three different instances with varying  $\bar{M}_\Gamma$ . The overall effect of decreasing value of this parameter is increase in the planar face length and the dihedral angle. These effects are aftermath of the ease of material flow along the surface. Where as at higher value of this parameters, the depth of the quadruple points increase with an equal ease and groove shapes are dominated by diffusion along the triple lines channels. Analogous behaviors were also observed in other grooves and quadruple points (see Fig. (5.42b)).



## 6. Conclusion

Thermal grooving at the surface of solids is an important phenomenon, being studied since decades. The morphology of the polycrystal surface varies with the grain misorientation and the boundary plane inclination. There are much research works reporting the formations of grooves with continuous curvature in general and planar low energy faces in particular orientations at certain part of the geometry with progressing time. These morphologies are functions of anisotropy in grain boundary and surface energies. The contribution of torque in boundary plane due to the anisotropy in its energy causes formations of serrated grain boundary planes to minimize the total energy potential. Whereas high anisotropy in the surface energy produces the planar grooves with low energy faces along the thermal grooves or hillocks formations at the free surface of the grain. In this report, I studied two different types of anisotropy separately, ranging from the effects of grain boundary plane inclination to the effect of grain orientations on the shapes of thermal grooves and their growth kinetics.

Thermodynamic extremal principles are excellent tools to model the irreversible process. These principles are also useful in formulating the weak form for the finite element modeling of the process kinetics. In this sharp interface model, the two conditions, the balance of thermodynamic forces and fluxes established the equilibrium state. The balance of thermodynamic forces determined the groove dihedral angle as a function of triple line energy and its curvature, whereas the motion of flux determined the domain morphology. With curvature based formulation, this model converged without any constraint for time step size, even with the domain of discontinuous surface curvatures. The chemical potential was continuous and solution converged without any regularization for the surfaces with singular grooves. [Zhang and Gladwell \(2005\)](#) used the strong form of diffusion equation to study the kinetics of thermal grooving. They solved their model using finite difference method but their numerical simulations did not converge for the critical range of anisotropy and solution terminated due to high numerical error. This curvature based finite element formulations produced converging solution for any number of grains without any geometrical constraints.

In chapter (4), a method to calculate the grain boundary energies using the ansatz function was purposed under the local equilibrium condition at each triple junction. For two different set of scalar parameters, the relative values of the grain boundary energy were in good agreement with [100] tilt boundaries for Cu and Al reported in [Rohrer \(2011a\)](#). Under the assumption of isotropic surface energy, the groove formed with the low diffusional humps. The growth kinetics varied linearly with increasing value of scalar coefficient  $A$  in the ansatz function. For the set of grain boundaries with higher values, the depth of grooves and pits also increased linearly. This study demonstrated the behavior of different materials under the geometrical constraints. We are able to select the optimum manufacturing material for maximum stability and workability of thin sheet objects and protective coatings.

In chapter (5), the thermal grooving phenomena was studied using an orientation dependent surface energy. The growth kinetics and grooves shape varied as a function of anisotropy for each fixed orientation. For the highly textured RVE, we observed the formation of surfaces with constant mean curvature and singular grooves with low surface energy. Anisotropy in sur-

face energy also influenced the pits shape and growth rate at the quadruple points. For low oriented textured RVE, surfaces of constant mean curvature were formed. The kinetics of thermal grooving for low oriented textured RVE showed faster rate in comparison with  $\{110\}$  and  $\{111\}$  textured RVE. Formations of singular grooves were sensitive to the grain orientations and anisotropy in the surface energy. In case of  $\{110\}$  and  $\{111\}$ , we observed different kinetics. For low to moderate anisotropy ( $c \leq 0.6$ ) in the surface energy function, thermal grooves formed with constant mean curvature profile. The growth rate of groove and pit formation decreased in these orientations in comparison with  $\{100\}$  textured RVE. For the critical range of anisotropy ( $c > 0.6$ ) in  $\{110\}$  and  $\{111\}$  textured RVE, we observed formation of low energy faces with planer profiles in some part of the geometry. The kinetics of the process was different from the remaining part of the geometry. These grooves showed deeper profiles at faster growth rate. The width of planer grooves increased at slower rates in comparison with the normal grooves in the remaining parts. Deeper pits were formed at the ends of the grain boundaries with planer grooves. The growth rate of these pits showed tremendous increase. In addition to these, groove with varying curvature formed along the grain boundary. The variation caused formation of groove with varying dihedral angle to establish the state of equilibrium between the thermodynamic forces at the boundary junction.

Some additional numerical simulations e.g. on the effect of relative diffusion coefficient  $\bar{M}_\Gamma$  for groove shapes and process kinetics engender additional useful information. For the high value of  $\bar{M}_\Gamma$ , the surface diffusion coefficients has a low value and kinetics was dominated by the diffusion along the free surface. The groove formed with low height diffusional humps and planer surfaces appeared along the free surface of the grain. The pits growth took place at slower rate. It is important to mention that for the planer groove formations at higher value of  $\bar{M}_\Gamma$ , we observed decrease in the angular difference at the junction between singular and continuous surface curvature. For the low value of  $\bar{M}_\Gamma$ , opposite was true. Concluding, for different set of relative diffusion coefficient, the system followed different growth kinetics but it ultimately reached to the constant equilibrium state following different paths.

Our simulation model is stable over the complete range of anisotropy in the surface energy. The curvature based formulation reproduce many of the experimentally observed morphologies during the secondary annealing process reported in the literature. This model has the potential for further exploration. Diffusion along the triple line is important aspect. The role of triple line energy become significant in determining the equilibrium dihedral angle with increasing groove curvature. A constant value of triple line energy was used in these simulations and preliminary studies for the stability of the model were completed. The effects of relative values of triple line energy are still to be investigated in detail. Both the role of positive and negative values of triple line energy under the limiting case is of prime interest in the research community for the morphological stability of the polycrystal.

Secondly in  $\{111\}$  orientation, the surface energy varies in both direction. The numerical experimentations were performed with the assumption of isotropic grain boundary energies. There is need to include the anisotropic grain boundary energies with moving triple junction due to recrystallization. [Hackl et al. \(2019\)](#) model for interface kinetics explains the effect moving triple lines along the free surface. A coupled model will enable us to study the complete anisotropic system. We can study the kinetics of the polycrystalline structure with moving grain boundaries to establish a state of equilibrium.

Our simulation experiments exhibit good agreement with the experimentally observed morphologies, but the quantification of characteristic material parameters requires additional nu-

merical simulations with bulk diffusion. By introducing the additional dissipation in the variational model and by identifying suitable numerical methods, we can use a thermodynamic extremal principle for grain growth with coupled bulk and surface diffusion.



## Bibliography

- Adams, B. L., Kinderlehrer, D., Mullins, W. W., and Rollett, A. D. (1998). Extracting the relative grain boundary free energy and mobility functions from the geometry of microstructures. *Scr. Mater.*, 38:531–536.
- Adams, B. L., Ta'Asan, S., Kinderlehrer, D., Livshits, I., Mason, D. E., Wu, C.-T., Mullins, W. W., Rohrer, G. S., Rollett, A. D., and Saylor, D. M. (1999). Extracting Grain Boundary and Surface Energy from Measurement of Triple Junction Geometry. *Interface Sci.*, 7(3):321–337.
- Akyildiz, O. and Ogurtani, T. O. (2011). Grain boundary grooving induced by the anisotropic surface drift diffusion driven by the capillary and electromigration forces: Simulations. *J. Appl. Phys.*, 110.
- Akyildiz, O. and Ogurtani, T. O. (2017). Thermal Grooving by Surface Diffusion: a Review of Classical Thermo-Kinetics Approach. *Hittite J. Sci. Eng.*, 4:7–16.
- Akyildiz, O., Oren, E. E., and Ogurtani, T. O. (2011). Mesoscopic nonequilibrium thermodynamics treatment of the grain boundary thermal grooving induced by the anisotropic surface drift diffusion. *J. Mater. Sci.*, 46:6054–6064.
- Akyildiz, O., Oren, E. E., and Ogurtani, T. O. (2012). Grain boundary grooving in bi-crystal thin films induced by surface drift-diffusion driven by capillary forces and applied uniaxial tensile stresses. *Philos. Mag.*, 92:804–829.
- Allen, D. J. (1982). Thermal Grooving at migrating grain boundaries. *Scr. Metall.*, 16:5–9.
- Amouyal, Y., Divinski, S. V., Klinger, L., and Rabkin, E. (2008). Grain boundary diffusion and recrystallization in ultrafine grain copper produced by equal channel angular pressing. *Acta Mater.*, 56:5500–5513.
- Amouyal, Y., Rabkin, E., and Mishin, Y. (2005). Correlation between grain boundary energy and geometry in Ni-rich NiAl. *Acta Mater.*, 53:3795–3805.
- Amram, D., Klinger, L., Gazit, N., Gluska, H., and Rabkin, E. (2014). Grain boundary grooving in thin films revisited: The role of interface diffusion. *Acta Mater.*, 69:386–396.
- Archibald, W. E., Rollett, A. D., Ta'asan, S., and Kinderlehrer, D. (2004). Grain Boundary Properties and Grain Growth: Al Foils, Al Films. *MRS Proc.*, 819:N6.6.
- Ashby, M., Spaepen, F., and Williams, S. (1978). The structure of grain boundaries described as a packing of polyhedra. *Acta Metallurgica*, 26(11):1647 – 1663.
- Balluffi, R. W., Allen, S. M., and Carter, W. C. (2005). *Kinetics of Materials*. John Wiley & Sons, Inc.
- Barbe, F. and Quey, R. (2011). A numerical modelling of 3D polycrystal-to-polycrystal diffu-

- sive phase transformations involving crystal plasticity. *Int. J. Plast.*, 27:823–840.
- Barmak, K., Eggeling, E., Kinderlehrer, D., Sharp, R., Ta'asan, S., Rollett, A. D., and Coffey, K. R. (2013). Grain growth and the puzzle of its stagnation in thin films: The curious tale of a tail and an ear. *Prog. Mater. Sci.*, 58:987–1055.
- Barmak, K., Kim, J., Kim, C.-S., Archibald, W. E., Rohrer, G. S., Rollett, A. D., Kinderlehrer, D., Ta'asan, S., Zhang, H., and Srolovitz, D. J. (2006). Grain boundary energy and grain growth in Al films: Comparison of experiments and simulations. *Scr. Mater.*, 54:1059–1063.
- Barrales Mora, L. A., Gottstein, G., and Shvindlerman, L. S. (2012). Effect of finite boundary junction mobility on the growth rate of grains in 3D polycrystals. *Philos. Mag.*, 92:1046–1057.
- Barrales Mora, L. A., Mohles, V., Shvindlerman, L. S., and Gottstein, G. (2008). Effect of a finite quadruple junction mobility on grain microstructure evolution: Theory and simulation. *Acta Mater.*, 56:1151–1164.
- Barrett, J. W., Garcke, H., and Nürnberg, R. (2008). A variational formulation of anisotropic geometric evolution equations in higher dimensions. *Numer. Math.*, 109:1–44.
- Barrett, J. W., Garcke, H., and Nürnberg, R. (2010a). Parametric approximation of surface clusters driven by isotropic and anisotropic surface energies. *Interfaces Free Boundaries*, 12:187–234.
- Barrett, J. W., Garcke, H., and Nürnberg, R. (2010b). Finite-element approximation of coupled surface and grain boundary motion with applications to thermal grooving and sintering. *Eur. J. Appl. Math.*, 21:519–556.
- Beck, M., Pan, Z., and Wetton, B. (2010). Stability of travelling wave solutions for coupled surface and grain boundary motion. *Phys. D Nonlinear Phenom.*, 239:1730–1740.
- Blakely, J. M. (1963). Surface Diffusion. *Prog. Mater. Sci.*, 10:395–437.
- Brailsford, A. D. and Gjostein, N. A. (1975). Influence of surface energy anisotropy on morphological changes occurring by surface diffusion. *J. Appl. Phys.*, 46:2390–2397.
- Bulatov, V. V., Reed, B. W., and Kumar, M. (2013). Anisotropy of Interfacial Energy in Five Dimensions. *arXiv.org*.
- Bulatov, V. V., Reed, B. W., and Kumar, M. (2014). Grain boundary energy function for fcc metals. *Acta Mater.*, 65:161–175.
- Cahn, J. W. and Hoffman, D. W. (1974). A vector thermodynamics for anisotropic surfaces—II. Curved and faceted surfaces. *Acta Metall.*, 22:1205–1214.
- Cahn, J. W. and Taylor, J. E. (1994). Overview no. 113 surface motion by surface diffusion. *Acta Metall. Mater.*, 42:1045–1063.
- Cantwell, P. R., Tang, M., Dillon, S. J., Luo, J., Rohrer, G. S., and Harmer, M. P. (2014). Grain boundary complexions. *Acta Mater.*, 62:1–48.
- Carter, W. C., Roosen, A. R., Cahn, J. W., and Taylor, J. E. (1995). Shape evolution by surface

- diffusion and surface attachment limited kinetics on completely faceted surfaces. *Acta Metall. Mater.*, 43:4309–4323.
- Chakraborty, S., Kumar, P., and Choudhury, A. (2018). Phase-field modeling of grain-boundary grooving and migration under electric current and thermal gradient. *Acta Materialia*, 153:377–390.
- Cocks, A. and Gill, S. (1996). A variational approach to two dimensional grain growth–i. theory. *Acta Materialia*, 44(12):4765–4775.
- Coleman, B. D. and Noll, W. (1963). The thermodynamics of elastic materials with heat conduction and viscosity. *Arch. of Rational Mechanics and Analysis*, 13:167–178.
- Dantzig, J. A. Equilibrium Shapes for Crystalline Solids ( Wulff Shapes for Dummies ). 1:1–12.
- DeHoff, R. T. (2006). *Thermodynamics in Materials Sciences*. CRC/Taylor & Francis, Boca Raton, 2 edition.
- Derkach, V., Novick-Cohen, A., and Vilenkin, A. (2016). Grain Boundary Migration with Thermal Grooving Effects: A Numerical Approach. *J. Elliptic Parabol. Equations*, 2:389–413.
- Derkach, V., Novick-Cohen, A., Vilenkin, A., and Rabkin, E. (2014). Grain boundary migration and grooving in thin 3-D systems. *Acta Mater.*, 65:194–206.
- Dietz, D. and Iseri, H. Calculus and Differential Geometry : An Introduction to Curvature.
- Du, P. and Wong, H. (2006). A delta-function model for axially symmetric crystals. *Scr. Mater.*, 55:1171–1174.
- Einstein, T. (2015). Equilibrium Shape of Crystals. In *Handb. Cryst. Growth*, volume 31, pages 215–264. Elsevier.
- Fischer, F. D., Svoboda, J., and Fratzl, P. (2003). A thermodynamic approach to grain growth and coarsening. *Philos. Mag.*, 83:1075–1093.
- Fischer, F. D., Svoboda, J., and Hackl, K. (2012). Modelling the kinetics of a triple junction. *Acta Mater.*, 60:4704–4711.
- Fischer, F. D., Svoboda, J., and Petryk, H. (2014). Thermodynamic extremal principles for irreversible processes in materials science. *Acta Mater.*, 67:1–20.
- Fortier, P., Palumbo, G., Bruce, G., Miller, W., and Aust, K. (1991). Triple line energy determination by scanning tunneling microscopy. *Scr. Metall. Mater.*, 25:177–182.
- Frost, H. J., Thompson, C. V., and Walton, D. T. (1990). Simulation of thin film grain structures–I. Grain growth stagnation. *Acta Metall. Mater.*, 38:1455–1462.
- Gamsjäger, E. (2007). A note on the contact conditions at migrating interfaces. *Acta Mater.*, 55:4823–4833.
- Génin, F. Y., Mullins, W. W., and Wynblatt, P. (1992). Capillary instabilities in thin films: A model of thermal pitting at grain boundary vertices. *Acta Metall. Mater.*, 40:3239–3248.

- Gibbs, J. W. The Scientific papers of J. Willard Gibbs.
- Gleiter, H. (1982). On the structure of grain boundaries in metals. *Materials Science and Engineering*, 52(2):91 – 131.
- Głowiński, K. (2015). Methods for quantitative characterization of three-dimensional grain boundary networks in polycrystalline materials.
- Gottstein, G. and Shvindlerman, L. S. (2005). A novel concept to determine the mobility of grain boundary quadruple junctions. *Scr. Mater.*, 52:863–866.
- Gottstein, G. and Shvindlerman, L. S. (2009). *Grain Boundary Migration in Metals: Thermodynamics, Kinetics, Applications*. CRC Press, 2nd edition.
- Gottstein, G., Shvindlerman, L. S., and Ma, Y. (2005). Triple junction motion and grain microstructure evolution. *Acta Mater.*, 53:1535–1544.
- Gottstein, G., Shvindlerman, L. S., and Zhao, B. (2010). Thermodynamics and kinetics of grain boundary triple junctions in metals: Recent developments. *Scr. Mater.*, 62:914–917.
- Hackl, K. (1997). Generalized standard media and variational principles in classical and finite strain elastoplasticity. *J. Mech. Phys. Solids*, 45:667–688.
- Hackl, K. and Fischer, F. D. (2008). On the relation between the principle of maximum dissipation and inelastic evolution given by dissipation potentials. *Proc. R. Soc. A Math. Phys. Eng. Sci.*, 464:117–132.
- Hackl, K., Fischer, F. D., Klevakina, K., Renner, J., and Svoboda, J. (2013). A variational approach to grooving and wetting. *Acta Mater.*, 61:1581–1591.
- Hackl, K., Fischer, F. D., and Svoboda, J. (2011). A study on the principle of maximum dissipation for coupled and non-coupled non-isothermal processes in materials. *Proc. R. Soc. A Math. Phys. Eng. Sci.*, 467:2422–2426.
- Hackl, K., Fischer, F. D., and Svoboda, J. (2017). A variational approach to the modelling of grooving in a three-dimensional setting. *Acta Mater.*, 129:331–342.
- Hackl, K. and Heinen, R. (2008). A micromechanical model for pretextured polycrystalline shape-memory alloys including elastic anisotropy. *Contin. Mech. Thermodyn.*, 19:499–510.
- Hackl, K., Khan, A., Fischer, F., and Svoboda, J. (2019). Influence of bulk energy and triple junction mobility on interface kinetics - a tool for interpretation of experiments. *Acta Materialia*, 174:310 – 318.
- Herring, C. (1951). Some Theorems on the free energies of crystal surfaces. *Phys. Rev.*, 82:87–93.
- Hoffman, D. W. and Cahn, J. W. (1972). A vector thermodynamics for anisotropic surfaces. *Surf. Sci.*, 31:368–388.
- Holm, E. A., Olmsted, D. L., and Foiles, S. M. (2010). Comparing grain boundary energies in face-centered cubic metals: Al, au, cu and ni. *Scripta Materialia*, 63(9):905 – 908.
- Holm, E. A., Rohrer, G. S., Foiles, S. M., Rollett, A. D., Miller, H. M., and Olmsted, D. L.

- (2011). Validating computed grain boundary energies in fcc metals using the grain boundary character distribution. *Acta Mater.*, 59:5250–5256.
- Holzappel, G., Gasser, T., and Stadler, M. (2002). A structural model for the viscoelastic behavior of arterial walls: Continuum formulation and finite element analysis. *European Journal of Mechanics - A/Solids*, 21(3):441 – 463.
- Jiang, W. and Zhao, Q. (2018). Sharp–interface approach for simulating solid–state dewetting in two dimensions: a Cahn–Hoffman  $\xi$  –vector formulation. *Physica D Nonlinear Phenomena*.
- Joshi, C., Abinandanan, T. A., Mukherjee, R., and Choudhury, A. (2017). Destabilisation of nanoporous membranes through GB grooving and grain growth. *Comput. Mater. Sci.*, 139:75–83.
- Jou, D., Casas-Vázquez, J., and Lebon, G. (2010). *Extended irreversible thermodynamics*. Springer International Publishing.
- Kelly, M. N., Rheinheimer, W., Hoffmann, M. J., and Rohrer, G. S. (2018). Anti-thermal grain growth in SrTiO<sub>3</sub> : Coupled reduction of the grain boundary energy and grain growth rate constant. *Acta Mater.*, 149:11–18.
- Kennefick, C. and Raj, R. (1989). Copper on sapphire: Stability of thin films at 0.7 Tm. *Acta Metall.*, 37:2947–2952.
- Kim, H.-K., Ko, W.-S., Lee, H.-J., Kim, S. G., and Lee, B.-J. (2011). An identification scheme of grain boundaries and construction of a grain boundary energy database. *Scr. Mater.*, 64:1152–1155.
- Kim, T.-Y., Dolbow, J. E., and Fried, E. (2012). Numerical study of the grain–size dependent young’s modulus and poisson’s ratio of bulk nanocrystalline materials. *International Journal of Solids and Structures*, 49(26):3942 – 3952.
- Klinge, S., Hackl, K., and Renner, J. (2015). A mechanical model for dissolution–precipitation creep based on the minimum principle of the dissipation potential. *Proc. R. Soc. A Math. Phys. Eng. Sci.*, 471:20140994.
- Klinger, L. (2002). Surface evolution in two-component system. *Acta Mater.*, 50:3385–3395.
- Klinger, L. and Rabkin, E. (2001). Effect of surface anisotropy on grain boundary grooving. *Interface Sci.*, 9:55–63.
- Kochmann, D. M. and Hackl, K. (2011). The evolution of laminates in finite crystal plasticity: a variational approach. *Contin. Mech. Thermodyn.*, 23:63–85.
- Kosinova, A., Klinger, L., Kovalenko, O., and Rabkin, E. (2014). The role of grain boundary sliding in solid-state dewetting of thin polycrystalline films. *Scr. Mater.*, 82:33–36.
- Kozic, D., Gänsler, H.-P., Brunner, R., Kiener, D., Antretter, T., and Kolednik, O. (2018). Crack arrest in thin metallic film stacks due to material and residual stress inhomogeneities. *Thin Solid Films*, 668:14 – 22.
- Kreuzer, H. J. (1981). *Nonequilibrium Thermodynamics and its statistical foundations*. Clarendon Press. Oxford.

- Lee, S. Y., Hummel, R., and Dehoff, R. (1987). On the role of indium underlays in the prevention of thermal grooving in thin gold films. *Thin Solid Films*, 149:29–48.
- Lin, S.-C., Liu, M.-W., Gururajan, M. P., and Wu, K.-A. (2016). Modified Young's equation for equilibrium dihedral angles of grain boundary grooves in thin films at the nanoscale. *Acta Mater.*, 102:364–372.
- Liu, G., Feng, H., Liu, B., Wang, Y., Liu, W., Zou, B., Alford, N. M. N., and Petrov, P. K. (2016). Formation of V-grooves in SrRuO<sub>3</sub>epitaxial film. *J. Cryst. Growth*, 455:13–18.
- Lou, C. and Player, M. A. (2002). Advection – diffusion model for the stagnation of normal grain growth in thin films. *J. Phys. D. Appl. Phys.*, 35:1805–1811.
- Ma, Y., Wei, M., Sun, C., Cao, Z., and Meng, X. (2017). Length scale effect on the thermal stability of nanoscale Cu/Ag multilayers. *Mater. Sci. Eng. A*, 686:142–149.
- Martyushev, L. and Seleznev, V. (2006). Maximum entropy production principle in physics, chemistry and biology. *Phys. Rep.*, 426:1–45.
- McFadden, G. B., Coriell, S. R., and Sekerka, R. F. (2000). Effect of surface free energy anisotropy on dendrite tip shape. *Acta Mater.*, 48:3177–3181.
- Meier, G. H. (2014). *Thermodynamics of surfaces and interfaces: Concepts in inorganic materials*. Cambridge University Press and the Materials Research Societ.
- Miller, K. T., Lange, F. F., and Marshall, D. B. (1990). The instability of polycrystalline thin films: Experiment and theory. *J. Mater. Res.*, 5:151–160.
- Min, D. and Wong, H. (2006a). Grain-boundary grooving by surface diffusion with asymmetric and strongly anisotropic surface energies. *J. Appl. Phys.*, 99.
- Min, D. and Wong, H. (2006b). The effect of strong surface energy anisotropy on migrating grain-boundary grooves. *J. Appl. Phys.*, 100.
- Mullins, W. W. (1956). Two-Dimensional Motion of Idealized Grain Boundaries. *J. Appl. Phys.*, 27:900–904.
- Mullins, W. W. (1958). The effect of thermal grooving on grain boundary motion. *Acta Metall.*, 6:414–427.
- Mullins, W. W. (1961). Theory of linear facet growth during thermal etching. *Philos. Mag.*, 6:1313–1341.
- Munoz, N., Gilliss, S., and Carter, C. (2004). Remnant grooves on alumina surfaces. *Surface Science*, 573:391 – 402.
- Nemetz, A. W., Daves, W., Klünsner, T., Ecker, W., Schäfer, J., Czettel, C., and Antretter, T. (2019). Cyclic heat-up and damage-relevant substrate plastification of single- and bilayer coated milling inserts evaluated numerically. *Surface and Coatings Technology*, 360:39 – 49.
- Ogurtani, T. O. (2007). Dirichlet extremum problem associated with the asymmetric grain-boundary thermal grooving under the Dirac  $\delta$ -type anisotropic surface stiffness in bicrystal thin solid films. *J. Appl. Phys.*, 102:063517.

- Ogurtani, T. O., Akyildiz, O., and Oren, E. E. (2008). Morphological evolution of tilted grain-boundary thermal grooving by surface diffusion in bicrystal thin solid films having strong anisotropic surface Gibbs free energies. *J. Appl. Phys.*, 104:013518.
- Ogurtani, T. O. and Oren, E. E. (2005). Irreversible thermodynamics of triple junctions during the intergranular void motion under the electromigration forces. *Int. J. Solids Struct.*, 42:3918–3952.
- Olmsted, D. L., Holm, E. A., and Foiles, S. M. (2009). Survey of computed grain boundary properties in face-centered cubic metals—II: Grain boundary mobility. *Acta Mater.*, 57:3704–3713.
- Onsager, L. (1931). Reciprocal Relations in Irreversible Processes. I. *Phys. Rev.*, 37:405–426.
- Rabkin, E., Amouyal, Y., and Klinger, L. (2004). Scanning probe microscopy study of grain boundary migration in NiAl. *Acta Mater.*, 52:4953–4959.
- Rabkin, E., Gabelev, A., Klinger, L., Semenov, V. N., and Bozhko, S. I. (2006). Grain boundary grooving in molybdenum bicrystals. *J. Mater. Sci.*, 41:5151–5160.
- Rabkin, E., Klinger, L., Izyumova, T., Berner, A., and Semenov, V. (2001). Grain boundary grooving with simultaneous grain boundary sliding in Ni-rich NiAl. *Acta Mater.*, 49:1429–1438.
- Ramasubramaniam, A. and Shenoy, V. (2005). On the evolution of faceted grain-boundary grooves by surface diffusion. *Acta Mater.*, 53:2943–2956.
- Ratanaphan, S., Olmsted, D. L., Bulatov, V. V., Holm, E. A., Rollett, A. D., and Rohrer, G. S. (2015). Grain boundary energies in body-centered cubic metals. *Acta Mater.*, 88:346–354.
- Read, W. T. and Shockley, W. (1950). Dislocation models of crystal grain boundaries. *Phys. Rev.*, 78:275–289.
- Rohrer, G. S. (2011a). Grain boundary energy anisotropy: a review. *J. Mater. Sci.*, 46:5881–5895.
- Rohrer, G. S. (2011b). Measuring and Interpreting the Structure of Grain–Boundary Networks. *J. Am. Ceram. Soc.*, 94:633–646.
- Rohrer, G. S., Holm, E. A., Rollett, A. D., Foiles, S. M., Li, J., and Olmsted, D. L. (2010). Comparing calculated and measured grain boundary energies in nickel. *Acta Mater.*, 58:5063–5069.
- Sachenko, P., Schneibel, J. H., and Zhang, W. (2002). Effect of faceting on the thermal grain-boundary grooving of tungsten. *Philos. Mag. A Phys. Condens. Matter, Struct. Defects Mech. Prop.*, 82:815–829.
- Sachenko, P., Schneibel, J. H., and Zhang, W. (2004). Observations of secondary oscillations in thermal grain boundary grooves. *Scr. Mater.*, 50(9):1253–1257.
- Savina, T. V., Golovin, A. A., Davis, S. H., Nepomnyashchy, A. A., and Voorhees, P. W. (2003). Faceting of a growing crystal surface by surface diffusion. *Phys. Rev. E*, 67:021606.

- Saylor, D. M. and Rohrer, G. S. (2001). Evaluating anisotropic surface energies using the capillarity vector reconstruction method. *Interface Sci.*, 9:35–42.
- Saylor, D. M. and Rohrer, G. S. (2004). Measuring the Influence of Grain–Boundary Misorientation on Thermal Groove Geometry in Ceramic Polycrystals. *J. Am. Ceram. Soc.*, 82:1529–1536.
- Schiedung, R., Kamachali, R. D., Steinbach, I., and Varnik, F. (2017). Multi-phase-field model for surface and phase-boundary diffusion. *Phys. Rev. E*, 96:012801.
- Sekerka, R. F. (2005). Analytical criteria for missing orientations on three–dimensional equilibrium shapes. *J. Cryst. Growth*, 275:77–82.
- Sekerka, R. F. (2015). *Thermal Physics*. Elsevier.
- Shaffir, E., Riess, I., and Kaplan, W. (2009). The mechanism of initial de-wetting and detachment of thin Au films on YSZ. *Acta Mater.*, 57:248–256.
- Shekhawat, A., Ophus, C., and Ritchie, R. O. (2016). A generalized Read–Shockley model and large scale simulations for the energy and structure of graphene grain boundaries. *RSC Adv.*, 6:44489–44497.
- Stamelou, V., Tsoutsouva, M. G., Riberi-Béridot, T., Reinhart, G., Regula, G., Baruchel, J., and Mangelinck-Noël, N. (2017).  $\{1\ 1\ 1\}$  Facet Growth Laws and Grain Competition During Silicon Crystallization. *J. Cryst. Growth*, 479:1–8.
- Stone, H. A., Aziz, M. J., and Margetis, D. (2005). Grooving of a grain boundary by evaporation–condensation below the roughening transition. *J. Appl. Phys.*, 97:113535.
- Struik, D. J. (1961). *Lectures on Classical Differential Geometry*. General Publishing Company, Ltd. Canda., New York, NY, second edition.
- Sun, R. and Bauer, C. (1970). Tilt boundary migration in NaCl bicrystals. *Acta Metallurgica*, 18(6):639 – 647.
- Suo, Z. (1997). Motions of Microscopic Surfaces in Materials. In *Adv. Appl. Mech.*, volume 33, pages 193–294. Elsevier Masson SAS.
- Sutton, A. P. and Balluffi, R. W. (2009). *Interfaces in Crystalline Materials*. Oxford University Press, 2nd edition.
- Svoboda, J., Fischer, F. D., Fratzl, P., Gamsjäger, E., and Simha, N. K. (2001). Kinetics of interfaces during diffusional transformations. *Acta Mater.*, 49:1249–1259.
- Svoboda, J., Fischer, F. D., Fratzl, P., and Kroupa, A. (2002). Diffusion in multi-component systems with no or dense sources and sinks for vacancies. *Acta Mater.*, 50:1369–1381.
- Svoboda, J., Gamsjäger, E., Fischer, F. D., and Fratzl, P. (2004). Application of the thermodynamic extremal principle to the diffusional phase transformations. *Acta Mater.*, 52:959–967.
- Svoboda, J. and Riedel, H. (1992). Pore-boundary interactions and evolution equations for the porosity and the grain size during sintering. *Acta Metall. Mater.*, 40:2829–2840.
- Svoboda, J., Turek, I., and Fischer, F. D. (2005). Application of the thermodynamic ex-

- tremal principle to modeling of thermodynamic processes in material sciences. *Philos. Mag.*, 85:3699–3707.
- Svoboda, J., Turek, I., J. Svoboda, I. Turek, Svoboda, J., and Turek, I. (1991). On diffusion-controlled evolution of closed solid-state thermodynamic systems at constant temperature and pressure. *Philos. Mag. Part B*, 64:749–759.
- Thompson, C. V. (2012). Solid-state dewetting of thin films. *Annu. Rev. Mater. Res.*, 42:399–434.
- Weatherburn, C. E. (1927). On Isometric Systems of Curves and Surfaces. *Am. J. Math.*, 49:527.
- Weins, M., Chalmers, B., Gleiter, H., and Ashby, M. (1969). Structure of high angle grain boundaries. *Scripta Metallurgica*, 3(8):601 – 603.
- Wolf, D. (1989). A read-shockley model for high-angle grain boundaries. *Scr. Metall.*, 23(10):1713–1718.
- Wolf, D. (1990a). A broken-bond model for grain boundaries in face-centered cubic metals. *J. Appl. Phys.*, 68:3221–3236.
- Wolf, D. (1990b). Correlation between energy, surface tension and structure of free surfaces in fcc metals. *Surf. Sci.*, 226:389–406.
- Wolf, D. (1990c). Structure-energy correlation for grain boundaries in f.c.c. metals–iv. asymmetrical twist (general) boundaries. *Acta Metallurgica et Materialia*, 38(5):791 – 798.
- Wulff, G. (1901). Zur Frage der Geschwindigkeit des Wachstums und der Auflösung der Kristallflächen [On the question of speed of growth and dissolution of crystal surfaces]. *Z. Krist. Miner.*, 34:449–530.
- Xin, T. and Wong, H. (2003). Grain-boundary grooving by surface diffusion with strong surface energy anisotropy. *Acta Mater.*, 51:2305–2317.
- Xin, T. and Wong, H. (2004). A spike-function model of facets. *Mater. Sci. Eng. A*, 364:287–295.
- Zhang, H. and Wong, H. (2002). Coupled grooving and migration of inclined grain boundaries: Regime I. *Acta Mater.*, 50:1995–2012.
- Zhang, W. (2006). Evolution of crystal morphologies to equilibrium by surface diffusion with anisotropic surface free energy in three dimensions. *J. Cryst. Growth*, 297:169–179.
- Zhang, W. (2009a). Surface motion of single crystals driven by anisotropic surface diffusion. *Comput. Vis. Sci.*, 12:337–343.
- Zhang, W. (2009b). Surface motion of single crystals driven by anisotropic surface diffusion. *Comput. Vis. Sci.*, 12(7):337–343.
- Zhang, W. and Gladwell, I. (2005). Thermal grain boundary grooving with anisotropic surface free energy in three dimensions. *J. Cryst. Growth*, 277:608–622.
- Zhang, W., Sachenko, P., and Gladwell, I. (2004). Thermal grain boundary grooving with anisotropic surface free energies. *Acta Mater.*, 52(1):107–116.

- Zhang, W., Sachenko, P., and Schneibel, J. H. (2002). Kinetics of thermal grain boundary grooving for changing dihedral angles. *Journal of Materials Research*, pages 1495–1501.
- Zhao, B., Shvindlerman, L. S., and Gottstein, G. (2012a). Grain Boundary Triple Line Tension in Copper. *Mater. Sci. Forum*, 715-716:843–848.
- Zhao, B., Verhasselt, J. C., Shvindlerman, L. S., and Gottstein, G. (2010). Measurement of grain boundary triple line energy in copper. *Acta Mater.*, 58:5646–5653.
- Zhao, B., Ziemons, A., Shvindlerman, L., and Gottstein, G. (2012b). Surface topography and energy of grain boundary triple junctions in copper tricrystals. *Acta Mater.*, 60:811–818.

## A. Appendix.

### A.1. $\xi$ , surface energy vector.

In order to effectively describe the anisotropic surface energy  $\gamma(\mathbf{n})$ , [Hoffman and Cahn \(1972; 1974\)](#) purposed a vector formulation for surface energy based on Gibbs vector fields approach for the surfaces. Formulation in this section are derived, based on the explanations for anisotropic surface energy in [Sekerka \(2015, chap 14 therein\)](#). The surface energy varies with orientations, which are characterized by unit normal vector,  $\mathbf{n}$ . Thus, we write  $\gamma(\mathbf{n})$ , with  $\mathbf{n}$  is surface normal vector directed outward. Since the vector components of unit vector,  $(\mathbf{n}_1, \mathbf{n}_2, \mathbf{n}_3)$  are not independent, so we cannot take the partial derivatives with respect to one of them with other two fixed. Therefore, the vector field  $\xi$  was introduced to evaluate the derivatives without any coordinate dependency.

Let introduce a three dimensional vector field  $\mathbf{r} = r\mathbf{n}$ , with  $r$  is the magnitude of  $\mathbf{r}$ . An additional field,  $\bar{\gamma}(\mathbf{r}) = r\gamma(\mathbf{n})$  defines  $\xi$  vector. Here,  $\bar{\gamma}(\mathbf{r})$  is a homogeneous function degree 1, and can also be express as

$$\bar{\gamma}(\mathbf{r}) = r_i \frac{\partial \bar{\gamma}(\mathbf{r})}{\partial r_i}. \quad (\text{A.1})$$

We define  $\xi(\mathbf{n}) = \partial \bar{\gamma}(\mathbf{r}) / \partial r_i$ , a vector function of surface normal vectors only. Equation (A.1) gives  $\bar{\gamma}(\mathbf{r}) = \mathbf{r} \cdot \xi$ . Hence we have

$$\xi_n = \gamma(\mathbf{n}) = \mathbf{n} \cdot \xi \quad (\text{A.2})$$

Additionally if we take a derivative of  $\bar{\gamma}(\mathbf{r})$ , we have

$$\begin{aligned} d\bar{\gamma} &= d(\mathbf{r} \cdot \xi) \\ &= \xi \cdot d\mathbf{r} + \mathbf{r} \cdot d\xi. \end{aligned} \quad (\text{A.3})$$

In general, if we take the derivative of a basic definition of  $\bar{\gamma}$ , we have

$$d\bar{\gamma} = \frac{\partial \bar{\gamma}(\mathbf{r})}{\partial r_i} dr_i = \xi \cdot d\mathbf{r} \quad (\text{A.4})$$

Equations (A.3) and (A.4) give the definition for  $\xi$  vector in relation with surface normal vector  $\mathbf{n}$  as

$$\mathbf{n} \cdot d\xi = 0, \quad (\text{A.5})$$

$$d\gamma(\mathbf{n}) = \xi \cdot d\mathbf{n} \quad (\text{A.6})$$

Equation (A.2) defines the normal component  $\xi_n$ , and equation (A.6) defines the tangential component of  $\xi$ . As  $d\mathbf{n}$  is normal to  $\mathbf{n}$ , it represents the rotation of a surface through an angle  $d\theta = |d\mathbf{n}|$  (see Fig. (A.1)). The derivative,  $d\mathbf{n}/d\theta$  is also in the tangential direction, parallel to  $d\mathbf{n}$ , which is different from tangential component  $\xi_t$  direction.

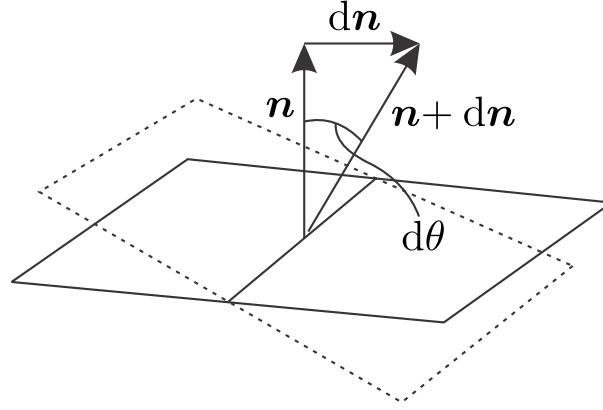


Figure A.1.: An illustrative description of surface normal vector  $\mathbf{n}$ , tangent vector  $d\mathbf{n}$ , and rotation contribution  $d\theta$  contributing to surface rotation for anisotropic surface energy.

The value of  $\xi_t$  is given by the maximum value of  $(\partial\gamma/\partial\theta)_{\max}$  pointing in the direction of maximum angular rate of increase of  $\gamma$  (Hoffman and Cahn, 1972; Sekerka, 2015). Therefore,  $\xi$  in components form is given as

$$\xi = \gamma \mathbf{n} + \left( \frac{\partial\gamma}{\partial\theta} \right)_{\max} \mathbf{t}_0, \quad (\text{A.7})$$

with  $\mathbf{t}_0$  is the component of  $d\mathbf{n}$  in the direction of maximum increase in the surface energy with orientation.

## A.2. Gaussian Curvature of a surface.

This formulation is based on the derivation given in Struik (1961). It is assumed that we have a small patch of parametric surface  $S(x, y, \mathbf{u}(x, y))$  in 2D, with  $\mathbf{u}(x, y)$  is the position vector for a point on it.  $\mathbf{T}$  is a tangent space to the surface defined at each point  $p(x, y)$  with two linearly independent orthogonal vectors,  $\mathbf{T}_x = \partial\mathbf{T}/\partial x$ , and  $\mathbf{T}_y = \partial\mathbf{T}/\partial y$ . The normal vector at each point is given by  $\mathbf{N} = \mathbf{T}_x \times \mathbf{T}_y$ . With this, we can find the unit normal vector  $\mathbf{n}(x, y)$  as

$$\mathbf{n} = \frac{\mathbf{T}_x \times \mathbf{T}_y}{|\mathbf{T}_x \times \mathbf{T}_y|} \quad (\text{A.8})$$

Divergence of surface normal vector  $(\nabla \cdot \mathbf{n})$  defined the total curvature of the surface within an algebraic sign. So, If we define

$$\begin{aligned} E &= \mathbf{T}_x \cdot \mathbf{T}_x, & F &= \mathbf{T}_x \cdot \mathbf{T}_y, & G &= \mathbf{T}_y \cdot \mathbf{T}_y \\ \text{and} \\ L &= -\mathbf{n} \cdot \mathbf{T}_{xx}, & M &= -\mathbf{n} \cdot \mathbf{T}_{xy}, & N &= -\mathbf{n} \cdot \mathbf{T}_{yy} \end{aligned} \quad (\text{A.9})$$

than the derivatives  $\mathbf{n}_x = \partial\mathbf{n}/\partial x$ , and  $\mathbf{n}_y = \partial\mathbf{n}/\partial y$  are given as

$$\begin{bmatrix} \mathbf{n}_x \\ \mathbf{n}_y \end{bmatrix} = \frac{1}{EG - F^2} \begin{bmatrix} LG - MF & MG - NF \\ ME - LF & NE - MF \end{bmatrix} \begin{bmatrix} \mathbf{T}_x \\ \mathbf{T}_y \end{bmatrix} \quad (\text{A.10})$$

In equation (A.10), coefficient matrix is called Weingarten matrix. The mean curvature and Gauss curvature are related to the trace and determinant of it [Struik \(1961\)](#). Thus mean curvature  $K$ ,

$$K = \frac{1}{2}(K_1 + K_2) = \frac{LG - 2MF + NE}{2(EG - F^2)} \quad (\text{A.11})$$

and Gaussian curvature  $G$  is

$$G = K_1 K_2 = \frac{1}{EG - F^2} ((LG - MF)(NE - MF) - (MG - NF)(ME - LF)) \quad (\text{A.12})$$

Alternative to equation (A.12), we can define it, using the derivative of normal vectors. From equation (A.10), the cross product of two derivative reads

$$\mathbf{n}_x \times \mathbf{n}_y = K_1 K_2 (\mathbf{T}_x \times \mathbf{T}_y) = K_1 K_2 H \mathbf{n} \quad (\text{A.13})$$

taking dot product with  $\mathbf{n}$ , we have

$$G = K_1 K_2 = \frac{1}{H} (\mathbf{n} \cdot \mathbf{n}_x \times \mathbf{n}_y) \quad (\text{A.14})$$



## List of Figures

2.1. Dissipative surface as function of fluxes. . . . .	16
3.1. Polycrystal geometry and its elements . . . . .	20
3.2. Contact condition along the triple line . . . . .	21
3.3. Motion of fluxes. . . . .	23
4.1. $\langle 100 \rangle$ tilt grain boundary energies in Cu. and Al. . . . .	36
4.2. Balance of energies for meeting grain boundaries. . . . .	37
4.3. Distribution of grain boundary energies, calculated using equation (4.6). . . . .	38
4.4. Geometry and meshing of four grains periodic RVE. . . . .	40
4.5. Morphological evolution of $\bar{u}$ and $\bar{\mu}$ fields at different instances of $\bar{t}^n$ . . . . .	41
4.6. Surface evolutions along different cross sections for $A = 0.30$ in the ansatz function. . . . .	43
4.7. Depth growth rates of $P_i$ and points on $\Gamma_i$ for $A = 0.30$ in an ansatz function. . . . .	44
4.8. Effect of $\bar{M}_\Gamma$ on surface morphology for $A = 0.30$ in an ansatz function. . . . .	45
4.9. Effect of change in $\bar{M}_\Gamma$ on pits and grooves depths for $A = 0.30$ in an ansatz function. . . . .	46
4.10. Effect of change in $A$ in an ansatz function, on surface morphology and groove evolution. . . . .	48
4.11. Effect of change in scalar parameter $A$ , on pit depth and growth rate at different $\bar{M}_\Gamma$ . . . . .	49
5.1. Different morphologies identified with anisotropy in the surface energy. . . . .	52
5.2. An illustrative diagram of surface formation. . . . .	54
5.3. Surface energy polar plot in two dimensions . . . . .	55
5.4. Surface energy $\gamma$ and $\xi$ plots for two different types of energy functions . . . . .	56
5.5. A schematic diagram showing the formation of planar facets. . . . .	57
5.6. Polar plot of $\gamma$ and $1/\gamma$ in two dimensions. . . . .	58
5.7. Surface energy $\gamma$ and $\xi$ plots for $\gamma(n) = 1 - c(n_1^4 + n_2^4 + n_3^4)$ . . . . .	60
5.8. Geometry and discretized of three grains periodic RVE. . . . .	61
5.9. An illustrative representation of polycrystalline with constituent grains. . . . .	63
5.10. Evolution of $\bar{u}$ and $J_i$ fields along the surface for $c \geq 0.70$ in $\{100\}$ orientated structure. . . . .	64
5.11. Evolution of surface along two cross sections for $\{100\}$ oriented grains. . . . .	65
5.12. Growth rate of $P_i$ and triple points in $\{100\}$ oriented grains. . . . .	66
5.13. Effect of $\bar{M}_\Gamma$ on pits and grooves depths. . . . .	67
5.14. Effect of change in $\bar{M}_\Gamma$ on surface morphologies in $\{100\}$ oriented grains. . . . .	68
5.15. Effect of increase in anisotropy of peripheral grains, on surface morphology in $\{100\}$ oriented RVE. . . . .	69
5.16. Effect of change in anisotropy on P depth. . . . .	70
5.17. Classification of different groove profiles. . . . .	72
5.18. Distribution of $\bar{u}$ and $\bar{\mu}$ along the $\Gamma_i$ for $\{111\}$ oriented grains with moderate anisotropies. . . . .	73

5.19. Evolution of $\bar{u}$ and $\bar{\mu}$ along the surface of $\{111\}$ oriented grain with low to moderate anisotropy. . . . .	74
5.20. Evolution of surface along the major diagonal. . . . .	75
5.21. Evolution along the minor diagonal with low to moderate anisotropy. . . . .	75
5.22. Evolution of a surface along the horizontal boundary. . . . .	76
5.23. Growth rate of quadruple points at moderate anisotropy for $\{111\}$ oriented grains. . . . .	77
5.24. Evolution of $\bar{u}$ and $J_i$ fields along the surface for $\{110\}$ oriented grains with critical values of $c_{\omega_{1,2,3}}$ . . . . .	79
5.25. Contour plots of $\bar{u}$ at $\bar{t}^{60}$ and $\bar{t}^{75}$ . . . . .	80
5.26. Grooves shapes along different cross sections with planar faces. . . . .	80
5.27. Growth kinetics of $P_i$ and points on $\Gamma_i$ for $\{110\}$ oriented grains. . . . .	81
5.28. Evolution of surface at different $\bar{M}_\Gamma$ . . . . .	82
5.29. Evolution of surface for varying $c_{\omega_{2,3}}$ in peripheral grains. . . . .	83
5.30. Contour plot for $\bar{u}$ and $J_i$ field along the surface for $\{111\}$ oriented grains. . . . .	85
5.31. Evolution of surface along the major diagonal. . . . .	86
5.32. Evolution along the minor diagonal for $\{111\}$ oriented grains. . . . .	87
5.33. Evolution along the horizontal periodic boundary. . . . .	88
5.34. Growth rates of $P_i$ and points on $\Gamma_i$ . . . . .	90
5.35. Contour plots for $\bar{u}$ and $\bar{\mu}$ along the surface for $\{111\}$ oriented grains. . . . .	92
5.36. A comparison to experimental result from literature. . . . .	93
5.37. Evolution of planar grooves for critical value of $c$ in $\{111\}$ oriented grains. . . . .	93
5.38. Evolution along minor diagonal for $c_{\omega_{1,2,3}} \geq 0.75$ in $\{111\}$ oriented grains. . . . .	94
5.39. Growth rate of $P_i$ and points on $\Gamma_i$ for $\{111\}$ oriented grains. . . . .	95
5.40. Rate of dissipation and minimization of energy. . . . .	96
5.41. Effect of different values $\bar{M}_\Gamma$ on growth rate. . . . .	97
5.42. Effect of different value of $\bar{M}_\Gamma$ on planar grooves. . . . .	98
A.1. Description of $n$ and $dn$ . . . . .	116

## Curriculum vitae

Name: Asim ullah Khan

Date of Birth: 16-02-1977

### Education

---

Secondary School (1992)	Metric with Distinction, Faiz ul Islam Model High School, Rawalpindi, Pakistan.
High School (1992-1994)	F.Sc. (Pre Engineering), Gordon College, Rawalpindi, Pakistan
Bachelor Degree (1995-2000)	B.Sc. Mechanical Engineering with honors, University of Engineering and Technology, Taxila, Pakistan.
Master Degree (Oct. ,2013-Sep. ,2015)	M.Sc. Computational Engineering, with honors Ruhr university, Bochum,Germany.
Ph.D. (Oct. 2015-Jul. 2019)	Institute of Mechanics of Materials Ruhr university, Bochum, Germany.

**Mitteilungen aus dem Institut für Mechanik  
RUHR-UNIVERSITÄT BOCHUM  
Nr. 181**

**ISBN 978-3-935892-59-9**